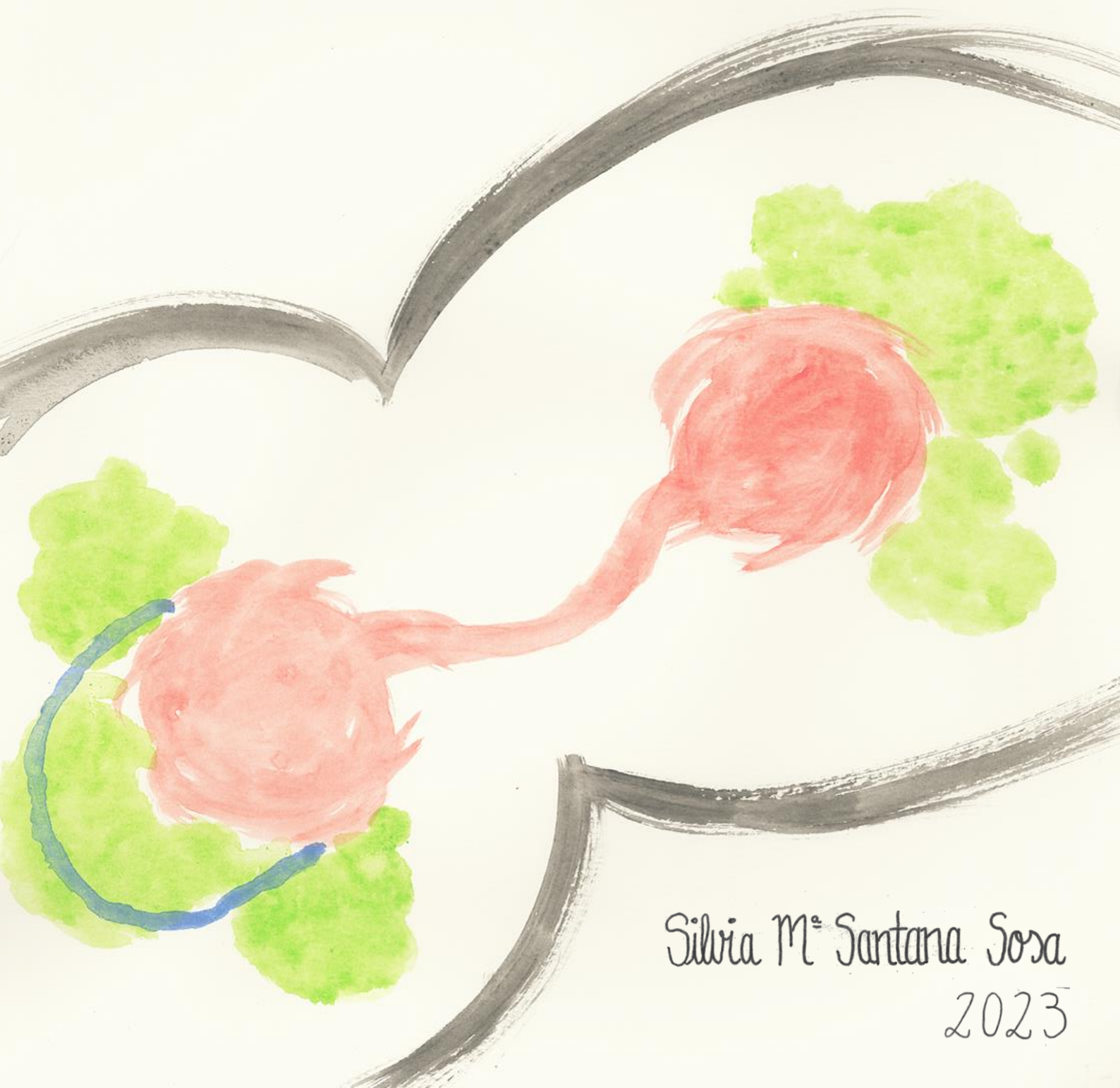


Study of the formation and resolution of non-
spherical nuclear morphologies upon
mitotic delays in *Saccharomyces cerevisiae*



Silvia M^o Santana Sosa
2023

Study of the formation and resolution of non-
spherical nuclear morphologies upon
mitotic delays in *Saccharomyces cerevisiae*



Silvia M^e Santana Sosa
2023

AUTORIZACIÓN DEL DIRECTOR DE TESIS

Dr. Félix M. Machín Concepción, director de la tesis doctoral presentada por la Graduada en Biología Silvia M. Santana Sosa,

Certifica que:

La memoria presentada por la Graduada en Biología Dña. Silvia M. Santana Sosa titulada “Estudio de la formación y resolución de morfologías nucleares no esféricas por retrasos mitóticos en *Saccharomyces cerevisiae* || Study of the formation and resolution of non-spherical nuclear morphologies upon mitotic delays in *Saccharomyces cerevisiae*”, ha sido realizada bajo mi dirección en la Unidad de Investigación del Hospital Universitario Nuestra Señora de Candelaria y, considerando que reúne las condiciones de calidad y rigor científico, autorizo para que pueda ser presentada y defendida ante la comisión nombrada al efecto para optar al grado de Doctor con Mención Internacional por la Universidad de La Laguna.

San Cristóbal de La Laguna, a 25 de noviembre de 2022



Fdo. **Dr. Félix Machín Concepción**

This work has been funded by:

- Ministerio de Ciencia e Investigación (MICIIN) / Agencia Estatal de Investigación (AEI). Research grants to Félix Machín:
 - BFU2015-63902-R
 - BFU2017-83954-R
 - PID2021-123716OB-I00
- A predoctoral contract for Silvia M. Santana Sosa (TESIS2018010034) from April 2018 to April 2022 was granted by the Agencia Canaria de Investigación, Innovación y Sociedad de la Información (ACIISI), cofinanced by the European Social Fund (ESF). || Tesis (TESIS2018010034) cofinanciada por la Agencia Canaria de Investigación, Innovación y Sociedad de la Información de la Conserjería de Economía, Industria, Comercio y Conocimiento y por el Fondo Social Europeo (FSE). Programa Operativo Integrado de Canarias 2014-2020, Eje 3 Tema Prioritario 74 (85%).



Consejería de Economía,
Industria, Comercio y Conocimiento
Agencia Canaria de Investigación,
Innovación y Sociedad
de la Información



UNIÓN EUROPEA

Fondo Social Europeo

el FSE invierte en tu futuro



This work has been carried out under the supervision of Dr. Félix M. Machín Concepción at the Research Unit of Hospital Universitario Nuestra Señora de Candelaria, Santa Cruz de Tenerife, Spain.

Silvia M. Santana Sosa performed this thesis while being affiliated with the Institute of Biomedical Technologies (ITB) of the University of La Laguna (ULL) and the Canary Health Research Institute Foundation (FCIISC), Santa Cruz de Tenerife, Spain.

A part of this work was carried out at Dr. Kerry Bloom's lab, at the Department of Biology of the University of North Carolina at Chapel Hill (USA). This research stay was funded by the University of La Laguna (ULL) and an Excellence Fellowship provided by the International Mentoring Foundation (IMFAHE). Besides, collaborative work was done with Dr. Thomas Petes' lab from the Molecular Genetics and Microbiology Department at Duke University School of Medicine (USA).



Instituto de Tecnologías
Biomédicas
Universidad de La Laguna

Duke
UNIVERSITY



DOCTORADO
CIENCIAS DE LA SALUD



To my family

An abstract painting featuring a central blue, textured shape that resembles a stylized flower or a cluster of petals. This blue shape is surrounded by several large, rounded, red shapes, also with a textured, brush-painted appearance. The composition is set against a light, off-white background. Several thick, grey, expressive brushstrokes are visible, some curving across the top and bottom of the frame, and others extending from the left and right sides. A thin, solid red horizontal line is positioned below the word 'ABSTRACT'.

ABSTRACT

The morphology of the nucleus is mostly spherical in many organisms across eukaryotes. However, this organelle needs to adapt when the cell is subjected to challenging physiological conditions, such as cell migration in higher eukaryotes, to travel through the narrow intercellular spaces, or cell division in organisms which perform closed mitosis (i.e. without dismantling the nuclear envelope), like yeast, to transform a single nucleus into the two daughter nuclei in mitosis. In addition, the nuclear morphology can be modified in pathological conditions too, being a hallmark of cancer cells. Strikingly, recent evidence in cell lines have linked aberrant nuclear morphology with defects in lysosomal function, related to the recycling process called autophagy, and with genome instability too. These data evidence a close relationship between nuclear morphology and function. Thus, understanding nuclear morphology dynamism and stability is of uttermost importance, as pathways and proteins involved in nuclear shaping may be key to develop targeted anticancer and antifungal drugs.

Previously, our group and others have described, using the budding yeast *Saccharomyces cerevisiae* as model, that in a metaphase (mid-M) block triggered by microtubule depletion the nucleus and the nucleolus drastically change their shape. The spherical morphology is lost in favor of the appearance of a single finger-like projection which can bend to the point of forming a handle or loop. Furthermore, this projection affects the nucleolar domain, which allocates the ribosomal DNA (rDNA), ribosomal RNAs (rRNAs), the rRNA processing machinery, as well as ribosomal proteins and ribosome assembly factors.

In this work, using the yeast model and fluorescence microscopy, we have observed that the rDNA loop in a mid-M block makes the nucleus resemble a toroid, as the ones recently and independently observed in higher eukaryotes, with the space under the rDNA loop occupied by the vacuole, which is the equivalent of the human lysosome. Besides, the establishment of this configuration depends on factors such as phospholipid synthesis and the absence of microtubules, as it does not form in the mid-M block caused by other mid-M blocks that preserve microtubules. Furthermore, we studied how these non-canonical nuclear morphologies evolve once cells are released from the mid-M blocks, which appear to eventually recover a rounded shape by telophase, without apparently having a negative impact on genome stability. Interestingly, there seems to be an increase in autophagy levels, which may be triggered to recycle the excess of nuclear membrane accumulated during the mitotic block.

TABLE OF CONTENTS

Abstract.....	13
Table of contents	17
List of figures	21
List of tables	25
List of abbreviations	27
1. Introduction	31
1.1. Nuclear morphology and architecture.....	33
1.1.1. Nuclear envelope components.....	33
1.1.2. Organization inside the nucleus.....	35
1.1.3. Nuclear morphology dynamics.....	37
1.1.4. Mitotic control of chromosome segregation.....	42
1.2. The nucleolus and the rDNA	45
1.3. Factors that influence nuclear shape	51
1.3.1. Chromatin	51
1.3.2. Proteins associated to the NE	52
1.3.3. Lipid homeostasis	54
1.3.4. Nuclear size	57
1.3.5. The vacuole, TOR and nucleophagy	58
1.4. <i>Saccharomyces cerevisiae</i> as a model organism	65
2. Aims	67
3. Material and methods	71
3.1. Strains	73
3.2. Culture conditions.....	74
3.2.1. Bacteria culture conditions	74
3.2.2. Yeast culture conditions	74
3.3. Transformation procedures	78
3.3.1. Transformation of <i>Escherichia coli</i>	78
3.3.2. Transformation of <i>Saccharomyces cerevisiae</i>	79
3.4. Plasmid construction using Modular Cloning (MoClo)	80
3.5. DNA preparations	83
3.5.1. Plasmid DNA preparation from <i>E. coli</i>	83

3.5.2.	Genomic DNA preparation from <i>S. cerevisiae</i>	84
3.5.3.	High molecular weight DNA preparation	84
3.6.	Polymerase Chain Reaction (PCR).....	85
3.7.	DNA electrophoresis.....	86
3.7.1.	Conventional agarose gel electrophoresis	86
3.7.2.	Pulsed-Field Gel Electrophoresis (PFGE).....	87
3.8.	Western blot.....	87
3.8.1.	Protein extraction.....	88
3.8.2.	SDS-PAGE	88
3.8.3.	Protein transfer and immunodetection.....	88
3.9.	Microscopy	90
3.9.1.	Wide-Field Microscopy (WFM).....	91
3.9.2.	Confocal Super-resolution Microscopy (CSM).....	93
4.	Results and discussion	95
4.1.	Cytological characterization of metaphase cell cycle blocks with non-spherical nuclear morphologies	97
4.1.1.	The rDNA acquires a wide range of morphologies in a metaphase block induced by microtubule depletion	97
4.1.2.	The space under the loop is occupied by the vacuole.....	102
4.1.3.	Small loops and protruding bars grow and bend around vacuoles to give rise to the rDNA horseshoe loop	105
4.1.4.	The absence of microtubules is required for the rDNA horseshoe loop development	108
4.1.5.	The horseshoe loop requires phospholipid synthesis and membrane overexpansion.....	113
4.2.	Cytological characterization of cells released from a metaphase cell cycle block	121
4.2.1.	Cells released from a Nz-induced mid-M block tend to restore normal nuclear shape	121
4.2.2.	Remaining nuclear projections in a Nz release colocalize with vacuoles	130
4.2.3.	The exit from a Nz-induced mid-M block triggers autophagy activation	131
4.2.4.	The metaphase to end of mitosis transition occurs faster after a mitotic delay without microtubule depletion.....	134

4.2.5. Effect of nuclear membrane excess and defect in survival and genome integrity	137
4.3. Study of chemical compounds with potential to alter nuclear shape and cell cycle progression	143
5. Conclusions	149
6. References	153
Appendix I. Media and solutions.....	179
Media	181
Solutions	183
Appendix II. Scientific contributions	187

LIST OF FIGURES

Figure 1.1. Rab1-like organization of the budding yeast nucleus	36
Figure 1.2. Nuclear envelope remodeling in mitosis is considered as a spectrum, ranging from closed to open mitosis.....	38
Figure 1.3. Changes in nuclear shape through the budding yeast cell cycle	40
Figure 1.4. Processes that alter the spherical nuclear shape in budding yeast	42
Figure 1.5. SAC and SPOC regulate correct mitotic progression	44
Figure 1.6. Budding yeast rDNA structure.....	47
Figure 1.7. The rDNA tethering to the INM requires the RENT, cohibin and CLIP complexes	49
Figure 1.8. rDNA morphological changes through the cell cycle and in mid-M blocks....	50
Figure 1.9. Regulatory network of the yeast lipin/Pah1.....	55
Figure 1.10. Possible outcomes upon nuclear membrane accumulation.....	58
Figure 1.11. Proposed model for nucleophagy in budding yeast	62
Figure 1.12. <i>S. cerevisiae</i> life cycle.....	66
Figure 3.1. Cell synchronization procedures used in this work.....	75
Figure 3.2. Hierarchy of MoClo assembly designed for yeast	80
Figure 3.3. Assembly vector designed for integration in the HO locus in yeast.	82
Figure 4.1. The rDNA acquires many morphologies in a metaphase arrest induced by microtubule depletion	98
Figure 4.2. The length of the rDNA increases in the metaphase arrest, accompanied by a shift in the main rDNA morphology observed in G2/M cells.....	99
Figure 4.3. There are zones devoid of Net1 signal in the flanks of the rDNA horseshoe loop	100
Figure 4.4. The space between the rDNA handle and the bulk chromatin is not nuclear	101
Figure 4.5. The nucleus acquires a toroidal shape with two lobes in the mid-M arrest achieved by Nz exposure.....	102
Figure 4.6. Vacuolar stains colocalize with the SUL	103
Figure 4.7. Flares and loops are associated to the vacuole since the beginning of the metaphase block	105

Figure 4.8. The rDNA horseshoe loop stems from small loops and bars that grow and bend around vacuoles	107
Figure 4.9. The <i>cdc16-aid</i> mutant represents a good tool to study a mid-M block by APC inhibition, alternative to thermosensitive alleles	109
Figure 4.10. A conditional <i>cdc16aid</i> mutant reproduces the phenotype observed in thermosensitive mutants of the APC. Vacuoles are associated to nuclear projections observed in the mid-M arrest induced by APC inhibition.....	111
Figure 4.11. The rDNA in the <i>cdc16aid</i> mutant acquires mainly a bar morphology, being loops present in lower proportions than Nz-driven mid-M blocks.....	113
Figure 4.12. Inducible mutants of Nem1 maintain their fitness as compared to a WT.....	114
Figure 4.13. The vacuole shapes nuclear projections caused by mutations of the lipin axis	115
Figure 4.14. Lipid synthesis is a requisite for rDNA horseshoe loop formation.....	117
Figure 4.15. Model of the rDNA horseshoe loop origin and development upon Nz-driven mid-M cell cycle blocks	119
Figure 4.16. Cells released from a Nz mid-M block maintain NE non-spherical morphologies	122
Figure 4.17. Nuclear morphology and chromosome segregation timing in a Nz release	125
Figure 4.18. Short spindles characterize cells with nuclear projections in a Nz release	127
Figure 4.19. The rDNA horseshoe loop can remain until late stages of mitosis.....	128
Figure 4.20. Cells in a Nz release exhibit morphologies reminiscent to the ones observed after APC inhibition	129
Figure 4.21. Vacuoles still associate with flares and loops after Nz removal.....	130
Figure 4.22. A Nz release triggers autophagy activation	133
Figure 4.23. <i>Cdc16aid</i> cells complete segregation faster than Nz released cells.....	135
Figure 4.24. Nuclear projections containing the rDNA in a <i>cdc16aid</i> block-and-release are present mainly in MN cells.....	137
Figure 4.25. Effect of Nz and cerulenin on cellular survival in diploid cells.....	139
Figure 4.26. Genomic rearrangements in diploid cells apparently increase in Nz and Cer cotreatment	140

Figure 4.27. Chromosome integrity appears to be compromised in haploid yeasts after Nz and Cer combined exposure	142
Figure 4.28. Exposure to CM-568 and CM-768 at 100 μ M is toxic for yeast cells	144
Figure 4.29. Concentrations of CM-568 and CM-728 lower than 1 μ M allowed cells to reach telophase and achieve correct cXII segregation.....	146

LIST OF TABLES

Table 3.1. List of strains used in this work.....	73
Table 3.2. Stock and usage concentrations of drugs used in this work.....	77
Table 3.3. Stock and usage concentrations of antibiotics used for bacteria selection....	78
Table 3.4. Stock and usage concentrations of antibiotics used for yeast selection	80
Table 3.5. MoClo reaction setup for BsaI-HF®v2.....	82
Table 3.6. MoClo thermal cycler program for BsaI-HF®v2.....	83
Table 3.7. List of primers used in this work.....	85
Table 3.8. Running conditions for PFGE used in this work.....	87
Table 3.9. List of antibodies used in this work.....	89
Table 3.10. List of filter cubes used within the Leica DMI600B microscope	91
Table 3.11. List of filters and LED lines used within the Zeiss Axio Observer.Z1/7 microscope.....	92
Table 3.12. List of microscopy stains used in this work	92
Table 3.13. List of beam splitters and lasers used within the LSM980 microscope with an Airyscan 2 detector.....	93
Table I. Nutrient concentration to prepare drop out media.....	182

LIST OF ABBREVIATIONS

- AID: auxin-inducible degron
- APC: anaphase-promoting complex
- BF: bright field
- BN: binucleated
- bp: base pair
- CDK: cyclin-dependent kinase
- CDS: coding sequence
- Cer: cerulenin
- CFP: cyan fluorescent protein
- CFU: colony-forming unit
- CLIP: chromosome linkage INM proteins
- CML: chronic myeloid leukemia
- ConA: concanavalin A
- CSM: confocal super-resolution microscopy
- cXII: chromosome XII
- cXIIr: chromosome XII right arm
- DAG: diacylglycerol
- DNA: deoxyribonucleic acid
- DSB: DNA double strand break
- ER: endoplasmic reticulum
- FAS: fatty acid synthetase
- FEAR: Cdc14 early anaphase release
- FISH: fluorescence in situ hybridization
- GFP: green fluorescent protein
- HR: homologous recombination
- IAA: indole acetic acid
- INM: inner nuclear membrane
- KASH: Klarsicht, Anc-1, Syne-1 homology
- kb: kilobase
- LD: lipid droplet

- LEM: LAP2, Emerin, MAN1
- LINC: linker of nucleoskeleton and cytoskeleton complex
- LMPA: low melting point agarose
- Mb: megabase
- MCS: membrane contact site
- MEN: mitotic exit network
- Mid-M: mid-mitosis, metaphase
- MN: mononucleated
- MoClo: modular cloning
- N/C: nuclear to cytoplasm or karyoplasmic ratio
- NE: nuclear envelope
- NLS: nuclear localization sequence
- NPC: nuclear pore complex
- NVJ: nucleus-vacuole junction
- Nz: nocodazole
- OD: optical density
- ONM: outer nuclear membrane
- PA: phosphatidic acid
- PAS: phagophore assembly site
- PFGE: pulsed-field gel electrophoresis
- Phle: phleomycin
- PKA: protein kinase A
- PMN: piecemeal microautophagy of the nucleus
- pnER: perinuclear ER
- Pol I: RNA polymerase I
- rDNA: ribosomal DNA
- RENT: regulator of nucleolar silencing and telophase exit
- RFB: replication fork block or barrier site
- RNA: ribonucleic acid
- rRNA: ribosomal RNA
- RT: room temperature
- SAC: spindle assembly checkpoint

- SEM: standard error of the mean
- SPB: spindle pole body
- SPOC: spindle position checkpoint
- SUL: space under the loop
- SUN: Sad1, UNC-84 proteins
- TAG: triacylglycerol
- TCA: trichloroacetic acid
- *tetO*: tetracycline operator sequence
- TetR: tetracycline repressor protein
- TOR: target of rapamycin
- TORC1: target of rapamycin complex 1
- TORC2: target of rapamycin complex 2
- ts: thermosensitive
- v/v: volume/volume
- VM: vacuolar membrane
- WFM: widefield microscopy
- w/v: weight/volume
- WT: wild type
- YFP: yellow fluorescent protein

A watercolor illustration featuring a central blue bird-like figure with a long neck, surrounded by red, textured floral or cloud-like shapes. Grey, brush-stroke-like branches frame the composition. The background is a light, textured white.

1. INTRODUCTION

1.1. Nuclear morphology and architecture

The main feature that characterizes eukaryotes is the presence of the nucleus, a membranous organelle which protects the genetic material from the rest of the processes carried out in the cytoplasm while allowing selective communication between both through nuclear pores. However, the procedures that involve its formation and dynamics, as well as the factors that influence them are not fully understood, being extensively researched nowadays.

1.1.1. Nuclear envelope components

The nucleoplasm is separated from the rest of the cell by two concentric bilayers known as the nuclear envelope (NE), which nevertheless allows communication with the cytoplasm through nuclear pores, where both inner and outer membranes are fused in the core of a toroid. The outer layer of the NE (the outer nuclear membrane, ONM) is a continuum with the endoplasmic reticulum (ER) and it is also referred to as the perinuclear ER (pnER), although the ONM possesses unique proteins that mark the difference between them, evidencing different functions (Deolal & Mishra, 2021).

In most eukaryotes, there is a network of proteins underlying the inner nuclear membrane (INM) which constitute a mesh named the **nuclear lamina**, which confers structural support to the nucleus and contributes to chromatin organization among other processes, like DNA repair and transcription regulation. This nuclear lamina is made of different types of proteins: a variety of filamentous lamins as main components and lamin-associated proteins, including the ones embedded in the INM (Dechat et al., 2008; Wilhelmsen et al., 2006).

However, unicellular organisms and plants do not have lamins, even though they have other **INM proteins that resemble lamins**, either structurally or functionally, like CRWN proteins in plants and Esc1 in budding yeast (Deolal & Mishra, 2021). Although Esc1 is only present in yeast, Ebp2 and Rrs1, which are also lamin-related proteins playing key roles in telomere clustering and ribosome biogenesis in budding yeast, are universally conserved and are related to various human diseases (Horigome et al., 2011).

Communication between the nucleoplasm and the cytoplasm occurs through the nuclear pores, in which the **nuclear pore complexes (NPCs)** are assembled to control

1. Introduction

molecule trafficking. These are massive assemblies of approximately 550 nucleoporins of ~ 30 different types in budding yeast, which form a toroidal structure symmetric around a central channel with flexible filaments towards both sides, which serve as chromatin and cargo binding sites (Alber et al., 2007; D'Angelo & Hetzer, 2008; S. J. Kim et al., 2018; Rout et al., 2000). The number of NPCs suffers a variation throughout the cell cycle together with the nuclear surface, ranging from ~ 65 in G1 to ~ 200 in mitotic cells in *S. cerevisiae* haploid strains (Winey et al., 1997). Their general structure and part of its components remain conserved from yeast to humans, although recent evidence remark that some elements vary substantially between species (Aitchison & Rout, 2012; De Magistris & Antonin, 2018; S. J. Kim et al., 2018). Far from being merely supportive structures of the NE, they have been shown to be involved in processes like alternative DNA recombination/repair, recombination-mediated telomere elongation and gene expression regulation, among others, suggesting that NPCs act as regulatory hubs for processes including coordination of transcript elongation, processing and export (Gomar-Alba et al., 2022; Nagai et al., 2008; Schmid et al., 2006). However, the effort to dissect the NPC fine structure is still present nowadays, using cutting-edge techniques to gain a better understanding of the form and function relationship (Hinterndorfer et al., 2022; S. J. Kim et al., 2018; Z. Li et al., 2022). Furthermore, recent evidence remark that there is heterogeneity regarding their configuration, which implies structural plasticity, correlated with different export dynamics (Akey et al., 2022; Bensidoun et al., 2022).

The **spindle pole bodies (SPBs)** constitute the yeast analogue to centrosomes and in contrast to the latter, they are embedded in the NE, from which intranuclear microtubules and the mitotic spindle arise towards the nucleoplasm while astral microtubules nucleate outwards into the cytoplasm (Prunuske & Ullman, 2006; Ungricht & Kutay, 2017). During interphase, the centromeres of yeast chromosomes are attached to the SPB by short interphase microtubules, creating the centromere cluster around it, although treatment with the microtubule depolymerizing drug nocodazole (Nz) allows centromeres to move away from it (Bystricky et al., 2004; Guacci et al., 1997; Heun et al., 2001; Q. W. Jin et al., 1998). Furthermore, the SPB is located opposite to the nucleolus and is aligned with the site of new bud emergence (Bystricky et al., 2004, 2005; L. Lee et al., 1999; Yang et al., 1989). The yeast SPB duplicates in S phase and partitions during mitosis, migrating to the opposite poles across the nuclear membrane in the mother-

daughter axis, while pulling the chromosomes with them, promoting sister chromatid segregation (Jaspersen & Winey, 2004).

The **linker of nucleoskeleton and cytoskeleton (LINC) complex** joins nuclear and cytosolic elements and is highly conserved from yeast to mammals. It consists of SUN (Sad1, UNC-84) and KASH (Klarsicht, Anc-1, Syne-1 homology) domain containing proteins, being the first group facing the nucleoplasmic side while the latter face the cytoplasmic flank. In yeast only one SUN-domain protein has been identified, Mps3, which constitutes a chromatin tether of the INM, besides its structural role in the SPB (Bupp et al., 2007; Jaspersen et al., 2002). It is believed to pair with Csm4 or Mps2, which are KASH-like proteins, thus constituting the cytoskeletal link (Fan et al., 2020). It is the cohibin complex, composed of Csm1 and Lrs4, which mediates the interaction between Mps3 and the telomeres (Chan et al., 2011; Taddei & Gasser, 2012).

There is a group of proteins of the INM which interact with lamins or lamin-like proteins through a helix-extension-helix motif containing **LEM domain** (LAP2, Emerin, MAN1), providing structural stability to the nucleus, chromosome attachment and silencing regulation (Banday et al., 2016). In the budding yeast the MAN1 homologs Heh1 (also known as Src1) and Heh2 regulate NPC quality and stability (Webster et al., 2014, 2016). Furthermore, Heh1 belongs to the CLIP (chromosome linkage INM proteins) complex which, together with the cohibin and RENT (regulator of nucleolar silencing and telophase exit) complexes, attach the ribosomal DNA to the nucleolar periphery (Chan et al., 2011; Mekhail et al., 2008).

1.1.2. Organization inside the nucleus

Interphase nuclei of *S. cerevisiae* are characterized by a **Rabl-like disposition of chromosomes** as a consequence of chromosome positioning in late anaphase (**Fig. 1.1**). The centromeres are clustered adjacent to the SPB, opposite to the single nucleolus, while the telomeres are tethered to the NE in 3 – 8 clusters at distances dictated by the length of the chromosome arms (Duan et al., 2010; Palladino et al., 1993; Yang et al., 1989). Despite chromosomes displaying this characteristic organization, chromatin is subjected to constant motion, which is consistently reduced in telomeres, centromeres and silent chromatin when compared to coding and non-coding regions along the longer

1. Introduction

chromosome arms, as they are tethered through protein-protein interactions to the NE (Dion et al., 2012; Gasser, 2002; Marshall et al., 1997).

Within the nucleus we differentiate several **non-membrane-bound domains**, generated by the combination of physical constraints on chromatin movement as well as interactions among different proteins and RNAs. Thus, they allow the existence of different microenvironments within the organelle, favoring or preventing certain activities. These domains are enriched in specific DNA sequences and factors, and carry out specific enzymatic activities, among which we find the nucleolus, the telomere clusters and sites of DNA repair (Taddei & Gasser, 2012). The assembly of these subcompartments is described as a self-driven process, initiated by production of ribosomal RNA, SIR (silent information regulator) proteins activity and accumulation of DNA repair proteins, respectively (Hernandez-Verdun et al., 2002; Lisby et al., 2004; Meister & Taddei, 2013; Miné-Hattab & Taddei, 2019; Trumtel et al., 2000). This highly regulated organization implies functional consequences, so its loss could affect processes such as gene expression and genome stability, via DSB (DNA double strand break) mobility, chromatin anchorage and recombination regulation (Taddei & Gasser, 2012).

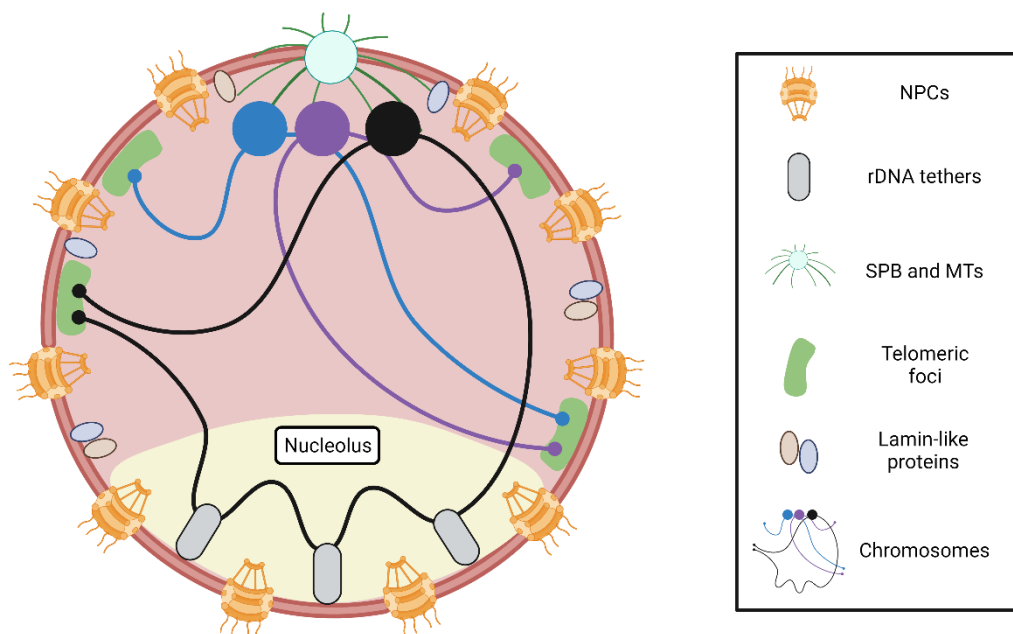


Figure 1.1. Rab1-like organization of the budding yeast nucleus. Centromeres are attached to the SPB through short microtubules, while telomeres form several foci, thus keeping these regions at the nuclear periphery. Opposite to the SPB, there is the nucleolus (in yellow), containing the ribosomal DNA repeats anchored to the NE by specific protein tethers. The NPCs allow communication and passage of molecules between the nucleus and the cytoplasm, while

lamin-like proteins provide structural support. NPCs, nuclear pore complexes; SPB, spindle pole body; MTs, microtubules (modified from Deolal et al., 2021 and created with BioRender.com).

1.1.3. Nuclear morphology dynamics

One of the main processes that cause a change in nuclear morphology is cell division. Organisms rely on mitosis to generate new cells, allowing growth and regeneration of tissues in multicellular organisms and population maintenance in single cell organisms. There are two main strategies throughout evolution to carry out this function: open and closed mitosis (**Fig. 1.2**). Open mitosis takes place in most eukaryotic cells, in which the NE is completely disassembled at the beginning of M phase to allow microtubule attachment to chromosomes and promote their segregation. Once chromosomes have reached each daughter cell, the NE needs to reassemble around them to constitute the two daughter nuclei. On the other hand, closed mitosis is performed by certain species of fungi and protists, in which the NE maintains its integrity, so chromosome segregation takes place entirely within the organelle (Güttinger et al., 2009). However, there are several NE remodeling strategies among different species (and even between cells which belong to the same organism), resembling intermediate forms of these two extremes, creating a spectrum of possibilities between open and closed mitosis. In fact, it is currently speculated that proper open and closed mitoses may not occur as such, highlighting the plasticity of the NE mitotic remodeling process (Dey & Baum, 2021; Makarova & Oliferenko, 2016; Mori & Oliferenko, 2020). This is supported by recent evidence in fission yeast, which show that this classic model of closed mitosis actually experiences partial NE disassembly in the later stages of nuclear division, localized at the bridge midzone (Dey et al., 2020; Expósito-Serrano et al., 2020).

1. Introduction

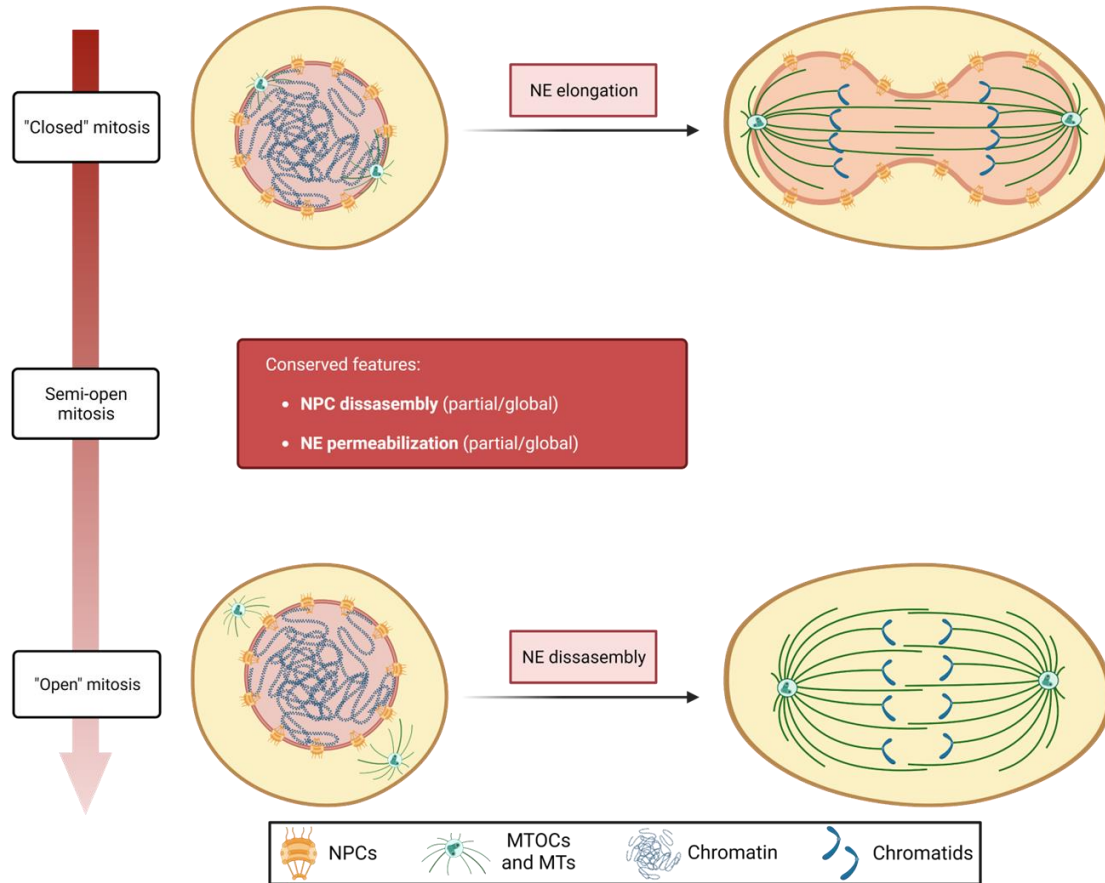


Figure 1.2. Nuclear envelope remodeling in mitosis is considered as a spectrum, ranging from closed to open mitosis. This figure shows the main characteristics of both extremes of the mitotic spectrum according to NE remodeling. In closed mitosis, the NE maintains its integrity at all times, while in open mitosis the NE and the NPCs disassemble upon mitosis onset. Semi-open mitosis shares features of both, considered as an intermediate state which represents more accurately what happens in nature. However, this spectrum shares some key conserved features, such as NPC disassembly (whether it is partial or global) and NE permeabilization (i.e. local fenestrations to allow insertion of SPBs and NPCs or, on the other hand, complete breakdown). The cytoplasm is depicted in yellow, while the nucleoplasm is depicted in pink. NPCs, nuclear pore complexes; MTOCs, microtubule organizing centers; MTs, microtubules (created with BioRender.com).

Nevertheless, what the different forms of mitotic remodeling of the NE across this spectrum have in common, is that they undergo remarkable structural changes. Towards "open" mitosis, the NE needs to be completely rebuilt around all of the chromosomes to avoid deleterious effects, such as the appearance of micronuclei, while in "closed" mitosis the NE need to increase its size and restructure to accommodate two nuclei, including being severed and sealed (karyokinesis) to be properly divided in a precise manner to avoid negatively affecting the integrity and number of chromosomes (S. Liu et al., 2018; Raab et al., 2016; Ungricht & Kutay, 2017; Varshney & Sanyal, 2019). To put it shortly, the nucleus experiences dramatic changes in shape in many organisms due to

physiological reasons, such as the aforementioned nuclear division, but also through processes not caused by the scheduled passage through the cell cycle, such as nuclear fusion during mating in yeast and development, differentiation and cell migration across higher eukaryotes (Manley et al., 2018; Stone et al., 2000; R. Wang et al., 2016).

Most nuclei in eukaryotes are rounded/oval shaped, and it has been observed that the loss of sphericity is associated with various diseases, such as cancer (Zink et al., 2004), and also with the natural deterioration caused by aging (Scaffidi & Misteli, 2006). In contrast, altered nuclear shape is essential in certain cell types to exert their function, such as cells of the immune system. Precisely, neutrophils are a widespread example of this. They possess a multilobulated (from three to four lobes in humans) nuclei, which is associated with a different chromatin organization and gene expression and is in turn correlated to their ability to migrate through the vascular endothelium and reach the potential hazard. This change in the pattern of lamin expression, together with a different NE lipid composition, is key to attain this shape which is presumed to increase NE plasticity (Denholtz et al., 2020; Manley et al., 2018; Rowat et al., 2013). The physiological impact that nuclear shape has in this example is evidenced by work showing correlation between loss of this characteristic feature and the appearance of pathologies, such as the Pelger–Huët anomaly (Hoffmann et al., 2002; Rowat et al., 2013). Hence, it is important to understand the mechanisms that govern nuclear shape and the implications of changes in morphology in health and disease.

In budding yeast, during exponential growth the nucleus is mostly spherical, until it gets enlarged and stretched through the bud neck in mitosis to accommodate chromosome segregation, finally requiring excision of the two daughter nuclei to complete the cell cycle (**Fig. 1.3**).

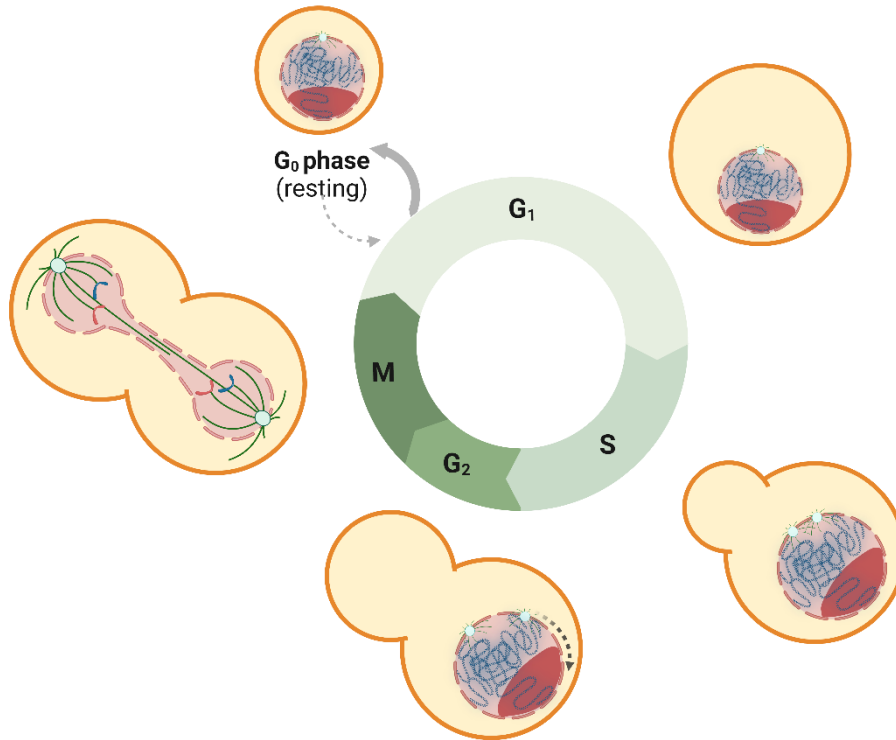


Figure 1.3. Changes in nuclear shape through the budding yeast cell cycle. In G₁, yeast nuclei (pink) are rounded, and the nucleolus (dark red) is opposite to the SPB (light green), while chromatin acquires the Rab1-like conformation. Then, nuclei grow in size as the genome replicates in S phase, accompanied by the maturation of the daughter SPB, which starts to pull away from the mother SPB (as shown by the dashed arrow). Once cells reach mitosis onset, the nucleus acquires a bowtie or dumbbell like shape, which becomes elongated as segregation takes place towards the so-called hourglass morphology, finally producing two spheric nuclei once karyokinesis and cytokinesis take place to start a new cycle (created with BioRender.com).

Another physiological change in nuclear shape is observed when yeasts are in the presence of the mating pheromone, which arrests cells in G₁ in preparation for mating and thus for nuclear fusion, and cause the nucleus to adopt a bilobed shape with a distinct “pocket” enclosing the rDNA separated from the bulk of the DNA (**Fig. 1.4**); sphericity is also affected when carbon source is changed or when cells are quiescent (Laporte et al., 2013; Stone et al., 2000; R. Wang et al., 2016). In addition, an increase in the number and contact area between the nucleus and the vacuoles (the yeast equivalent of the lysosome), known as NVJs (nucleus-vacuole junctions), has been described upon different stress cues, such as glucose deprivation and failed NPC assembly (Hariri et al., 2018; Lord & Went, 2020; Pan et al., 2000; Tosal-Castano et al., 2021). This increase in the contact surface between both organelles is thought to facilitate communication between the pnER, where most of lipid metabolism takes place, and the vacuoles, the main catabolic cellular compartment, to emit a proper and coordinated cellular response

(Kohler & Büttner, 2021). Furthermore, these contact sites are a requisite for a specific branch of nucleolar and perinuclear material degradation known as piecemeal microautophagy of the nucleus (PMN), in which a portion of the nucleus is pinched off, forming a teardrop-like protrusion towards the vacuole (Otto & Thumm, 2020; Roberts et al., 2003).

Besides, other deviations from the spherical shape of the yeast nucleus, due to defects in certain processes, have been described (**Fig. 1.4**). On the one hand, it has been described that during a mitotic delay membrane synthesis is not hampered, giving rise to membrane expansions specifically at the membrane adjacent to the nucleolus, which extends away from the bulk of the chromatin and are referred to as flares (Witkin et al., 2012). These nuclear projections which appear upon mitotic delays depend on an active Cdc5 to maintain their selectivity towards the nucleolar region, as its absence under a mitotic arrest produces an isometric NE growth instead (Walters et al., 2014). Consequently, this protein is implicated in the compartmentalization of the NE, and thus in regulating nuclear morphology. In addition, mutants of the Nem1/Spo7-Pah1/lipin axis, which regulate conversion of phosphatidic acid into diacylglycerol, also trigger an increase in nuclear size confined to the nucleolar area (Campbell et al., 2006; Santos-Rosa et al., 2005; Siniossoglou, 2009). However, when vesicle trafficking is impaired in conditions of membrane proliferation, the NE extension is no longer localized exclusively at the nucleolar region, producing highly deformed nuclei (M. T. Webster et al., 2010). Also an increased nucleolar volume is associated with a NE deformation which localizes adjacent to the nucleolus, although it does not always include it, that depends on rDNA tethering proteins and increased phospholipid synthesis (Male et al., 2020). Recently, Moriel-Carretero's lab has described two interesting phenotypes in which the NE is altered. On the one hand, they describe that oxidative stress elicits a pnER deformation probably by inducing lipid stress while, on the other hand, they report the uptake of cytoplasm portions inside the nucleus due to genotoxic stress, coupled with an autophagy boost and with preference for the nucleolar NE proximity (Garcia et al., 2022; Torán-Vilarrubias & Moriel-Carretero, 2021).

1. Introduction

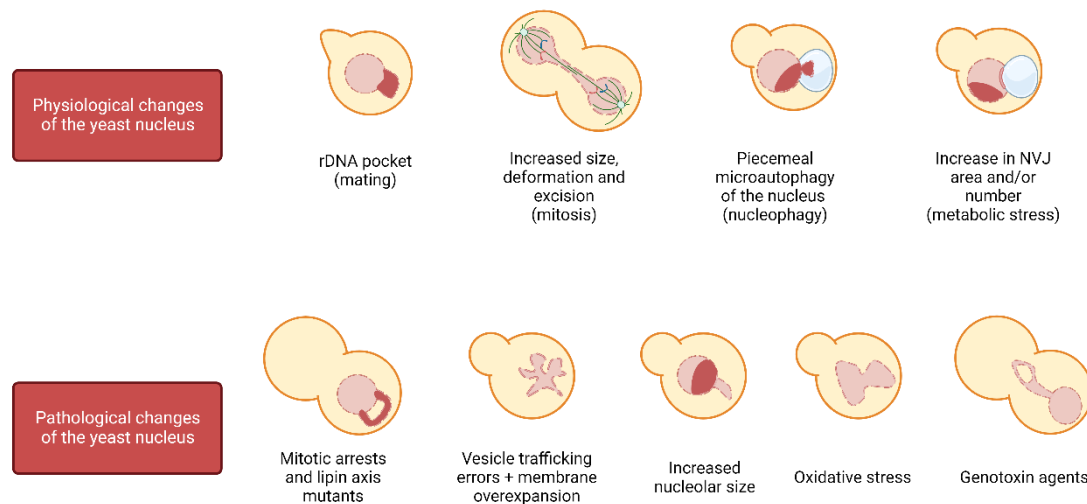


Figure 1.4. Processes that alter the spherical nuclear shape in budding yeast. The yeast nucleus experiments several changes in morphology due to physiological reasons, among which we find the appearance of a distinct rDNA pocket when cells prepare for mating, the increase in size and deformation through mitosis, teardrop protrusions towards the vacuole in PMN and an increase in NVJs size and/or number. Furthermore, other events trigger non-physiological changes, such as the appearance of flares (NE elongation confined to the nucleolar area) in mitotic arrests and lipin axis mutants, non-localized deformation when vesicle trafficking is disturbed in membrane overexpansion conditions, upon oxidative or genotoxic stress and when nucleolar volume is increased (created with BioRender.com).

In conclusion, the yeast nucleus experiments several changes in shape in response to different cues, demonstrating that it is a highly adaptable organelle. More specifically, it seems that the nucleolar region has several traits which pose an advantage to cope with NE deformation more efficiently than the rest of the NE, overall protecting the nuclear contents (Meseroll & Cohen-Fix, 2016).

1.1.4. Mitotic control of chromosome segregation

After DNA replication and until anaphase onset the **cohesin** ring-like complex, conformed by Smc1, Smc3, Scc1 and Scc3, keeps sister chromatids together and well aligned by protecting them from the opposing pulling forces exerted by microtubules. The cohesin complex is of uttermost importance for the proper alignment of chromosomes in metaphase, but must be removed at anaphase onset to allow chromosome segregation (Hirano, 2000; Laloraya et al., 2000; Michaelis et al., 1997; Strunnikov et al., 1993).

Apart from cohesin removal, the proper compaction of chromosomes needs to be achieved to ensure segregation, so chromosomal arms are short enough that the spindle is able to pull of them entirely. The **condensin** complex, composed of Smc2, Smc4, Ycs4,

Ycg1 and Brn1 is in charge of this task, regulated by the Aurora B kinase Ipl1 (Guacci et al., 1994; Machín et al., 2005; Ouspenski et al., 2000; Strunnikov et al., 1995; Vas et al., 2007).

Once chromosomes are duplicated and sister chromatids are properly aligned and condensed, it is time to equally divide them between the two daughter cells. The **anaphase promoting complex** (APC) is a ubiquitin ligase composed of more than a dozen different subunits (the essential Cdc16p among them) that exerts a variety of essential functions from yeast to humans, including separation of sister chromatids in anaphase and exit from mitosis, all regulated by specific cofactor binding (Hwang et al., 1998; Irniger et al., 1995; Lara-Gonzalez et al., 2012; Passmore et al., 2003, 2005; Peters, 2006). It is when the APC binds to its regulatory cofactor Cdc20 that APC^{Cdc20} targets securin (Pds1) for degradation, allowing separase (Esp1) to cleave the cohesin ring subunit Scc1 and therefore releasing sister chromatids for segregation (**Fig. 1.5**) (Cohen-Fix et al., 1996; Peters, 2006; Uhlmann, 2001; Yamamoto et al., 1996). Because of this, blocking the APC function causes a metaphase arrest from yeast to mammal cells (Michaelis et al., 1997). Together with the APC, Cdc5 (the single Polo-like kinase in yeast) promotes removal of the cohesin ring by phosphorylating Scc1 to enhance its cleavage (Alexandru et al., 2001).

To prevent the APC^{Cdc20} from releasing sister chromatids before all pairs are properly bioriented on the mitotic spindle, with all kinetochores attached to spindle microtubules and under tension, there is a control mechanism called the **spindle assembly checkpoint** (SAC), whose components in yeast are Mad1, Mad2, Mad3, Bub1, Bub3 and Mps1. Some of these proteins, namely Mad2, Mad3 and Bub3 constitute, together with Cdc20, the **mitotic checkpoint complex** (MCC), sequestering Cdc20 and thus controlling APC timely activation (Lara-Gonzalez et al., 2012). Despite previous literature described that degradation of Cdc16 inactivates the APC without interfering with the spindle and avoiding triggering the SAC, it has been reported that this may not be the case, hence APC inactivation may activate the SAC (Lai et al., 2003).

While the SAC is involved in the metaphase to anaphase transition, there is another surveillance mechanism for proper mitotic progression, which regulates the transition between anaphase to mitotic exit (transition to a new G1) by sensing spindle misalignment in relation to the division axis, known as the **spindle position checkpoint** (SPOC)

1. Introduction

(Caydasi & Pereira, 2012). The central SPOC kinase is Kin4, which counterbalances the mitotic exit network (MEN) activation by the Cdc14 early anaphase release (FEAR) network. Because FEAR promotes MEN after sister chromatid separation, regardless of the spindle orientation, Kin4 has been proposed to prevent mitotic exit when the spindle remains within the mother cell (Caydasi et al., 2017; Caydasi & Pereira, 2012). Additionally, Cdc5 acts as a central hub in the regulation of FEAR and MEN, and also for the functionality of the mitotic checkpoints mentioned above, as they require inhibition of mitotic exit signaling to achieve their purpose (Matellán & Monje-Casas, 2020).

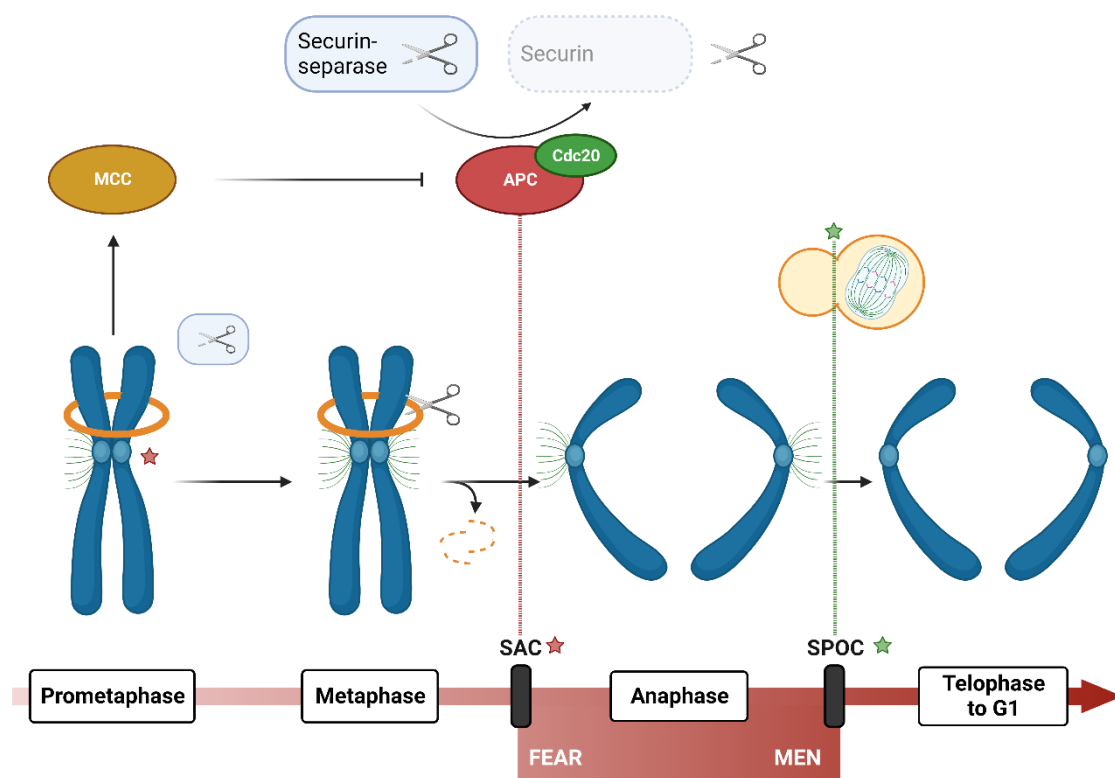


Figure 1.5. SAC and SPOC regulate correct mitotic progression. After replication, the cohesin ring (orange) keeps the sister chromatids together. At this point, securin keeps separase (scissors) inactive to inhibit early chromosome separation. The red star marks the unilateral attachment of a chromosome, the signal to keep the SAC active, so that the MCC inhibits APC^{Cdc20} and thus mitotic progression. Once all chromosomes are properly attached, the SAC is inactivated and APC^{Cdc20} releases separase from securin, which in turn degrades the cohesin ring and allows anaphase progression. Within anaphase we find two complex signaling cascades name FEAR and MEN, which regulate this critical step in mitosis and is mainly controlled by the master phosphatase Cdc14. To complete the anaphase to telophase transition and the entry into a new cell cycle, the spindle needs to be properly oriented in the mother-daughter axis, which is surveilled by the SPOC (the green star depicts an incorrect spindle orientation, which does not traverse the bud neck and is entirely within the mother cell). MCC, mitotic checkpoint complex; SAC, spindle assembly checkpoint; SPOC, spindle orientation checkpoint; APC^{Cdc20}, anaphase promoting complex bound to its cofactor Cdc20 (modified from Peters, 2006 and created with BioRender.com)

When these control mechanisms are activated, the cells delay the progression of the cycle to permit the correction of the cell insult which triggered them. Biochemically, metaphase or mid-M blocks are characterized by high cyclin dependent kinase (CDK/Cdc28) activity and inactive Cdc14 (the yeast master cell cycle phosphatase), a balance that is inverted upon anaphase onset through Cdc28 inactivation by Cdc14, along with dephosphorylation of many of its targets (D'Amours & Amon, 2004). There are several ways to achieve a mitotic arrest in metaphase and allow cell synchronization to ease interpretation of cell cycle studies, being the most commonly used microtubule depletion caused by the drug nocodazole (Nz), which promotes microtubule depolymerization and inhibit assembly dynamics (Jacobs et al., 1988). This triggers the SAC and inhibits the APC^{Cdc20}, and direct APC^{Cdc20} inactivation through inducible mutants. The morphological traits among them are slightly different, presumably by the lack of microtubules in Nz, but both arrest as mononucleated dumbbell shaped cells. In Nz treated cells, the nucleus stays in the mother cell and presents a handbag structure, with the bulk of the chromatin in one big pocket and the rDNA as a handle (Guacci et al., 1994; Machín et al., 2005). On the other hand, in APC inactive cells (either *cdc20* or *cdc16* defective), the nucleus traverses through the bud neck, leaving the right arm of cXII in the mother (although the centromere is predominantly located in the daughter, presumably within the centromere cluster) and hence defining the polarity of the nucleus (Guacci et al., 1994; Palmer et al., 1989, 1992). Interestingly, in *cdc20* depleted cells under arrest, the nucleoporin Nup49 was missing from the bud neck, along with high mobility of the chromatin between both cellular bodies, together with high dynamism of the spindle (Palmer et al., 1989; Rai et al., 2017).

1.2. The nucleolus and the rDNA

The nucleolus is the most prominent functional compartment within the nucleus, where transcription and processing of ribosomal RNA (rRNA), as well as the first steps of ribosome assembly, take place in eukaryotic organisms (Klinge & Woolford, 2018). It is assembled around the rDNA locus, composed of the genes encoding rRNA, which are organized in tandem repeats that can be physically together in a single chromosome or spread throughout the genome. In budding yeast, there is a single nucleolus characterized by a crescent shape at the periphery of the nucleus, occupying roughly one third of the organelle volume, while in mammals, several nucleoli are close to the center of the organelle (Mekhail & Moazed, 2010). This crescent shape is severely lost in favor of

1. Introduction

several granules called mininucleolar bodies when the RNA polymerase I (Pol I) gene is deleted or conditionally removed, meaning that Pol I plays a role in the maintenance of an intact nucleolar structure (Oakes et al., 1993).

Furthermore, besides its role as ribosome factory, this domain also stores factors involved in other cellular functions, acting as a reservoir to control their timely release. This has been well described for the yeast master phosphatase Cdc14, that is sequestered by its inhibitor Net1 in the nucleolus until anaphase; its release allows mitotic progression and exit (Shou et al., 1999; Traverso et al., 2001; Visintin et al., 1999). Additionally, it has been considered that the assembly of this domain is a self-driven process initiated by production of rRNA, and that the spatial constraint of Pol I transcription is a critical feature of nucleolar assembly (Albert et al., 2011; Trumtel et al., 2000). Moreover, the processes in which the nucleolus is involved have increased in number, discarding the concept of this domain as only a ribosome factory. Among these we find that it has been proposed as a stress sensor, controlling the maintenance of genome stability, the response towards nutrient availability and cell senescence (Boisvert et al., 2007; Lindström et al., 2018; Matos-Perdomo & Machín, 2019; Mayer et al., 2005).

In budding yeast, the nucleolus is assembled around the single rDNA locus on the right arm of chromosome XII (cXII), which contains 150 – 200 copies of a 9.1 kb repeat, making it the largest yeast chromosome (**Fig. 1.6**). Also, this region is the last to segregate, making cXII an indicator of the end of anaphase. In each repeat we find, both 35S (precursor of the 25S, 5.8S and 18S rRNAs) and 5S rRNA precursors, which are transcribed by RNA polymerases I and III, respectively, and two intergenic spacers (IGS1 and IGS2) separating them (Pasero & Marilley, 1993). The autonomous replication sequence (ARS) is found in IGS2. Within IGS1 we find a cryptic non-coding bidirectional promoter (E-pro) transcribed by RNA polymerase II, which is regulated by Sir2, being active only when the rDNA copy number drops below the homeostatic range, so that rDNA amplification can occur. Besides, in IGS1 there is the replication fork block or barrier site (RFB), where the protein Fob1 binds to prevent replication and transcription machinery collapse between different rDNA repeats, as it is a highly active locus in which replication and transcription occur simultaneously (Brewer et al., 1992; Kobayashi, 2003; Kobayashi et al., 1992, 1998; Kobayashi & Horiuchi, 1996; Muller et al., 2000; Takeuchi et al., 2003).

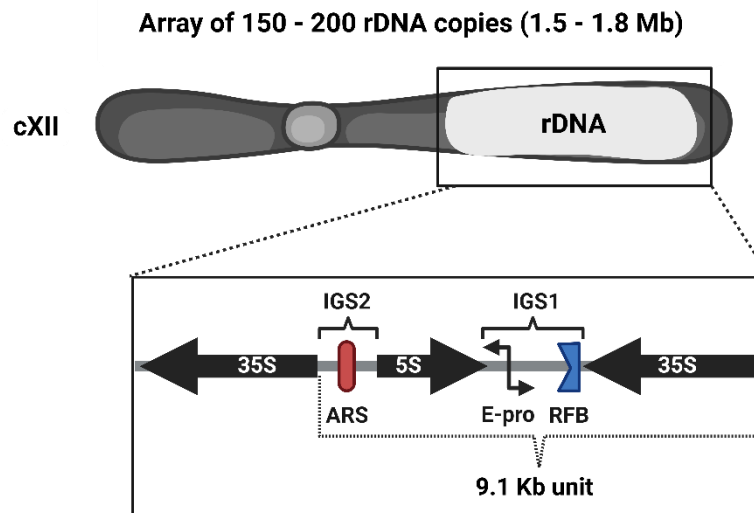


Figure 1.6. Budding yeast rDNA structure. This unscaled schematic represents the organization of the basic 9,1 kb rDNA repeat, on the right arm of chromosome XII. 35S and 5S: genes for the corresponding pre-rRNAs; IGS 1 and 2: intergenic spacer 1 and 2; ARS: autonomous replication sequence; RFB: replication fork barrier; E-pro: a cryptic non-coding bidirectional promoter (modified from Matos-Perdomo et al., 2022 and created with BioRender.com).

Cohesin, condensin and Sir2 are involved in rDNA compaction during the cell cycle, presumably helping to pack this piece of roughly 2 Mb of DNA within this compartment (Guacci et al., 1994; Lavoie et al., 2002, 2004). Besides the general need for chromosome compaction to allow mitotic exit, condensation of the rDNA is specifically required in late anaphase to allow cXII segregation. But first, to allow condensin loading, Cdc14 must shut down transcription of ribosomal genes. It does so by excluding Pol I subunits from the rDNA array by dephosphorylating its essential subunit Rpa43, thus inhibiting RNA Pol I activity (Clemente-Blanco et al., 2009; Machín et al., 2006; B.-D. Wang et al., 2006).

The mechanism behind copy number maintenance is mostly homologous recombination (HR) between the rDNA repeats, although an alternative and HR independent replication-based mechanism which causes a copy number increase has also been described (Houseley & Tollervy, 2011; Kobayashi & Nagata, 2014). A highly repetitive region like this is at high risk of unscheduled recombination. And thus, the generation of extrachromosomal rDNA circles excised from the locus has been shown to cause replicative senescence, implying that rDNA stability is critical for growth and survival (Sinclair & Guarente, 1997). However, HR is also suppressed at this locus up to a certain level, which was confirmed by Torres-Rosell et al. by showing nucleolar

1. Introduction

exclusion of HR proteins (but not sensors of DSBs), being dependent on the Smc5/6 complex (Petes, 1980; Torres-Rosell et al., 2007). In addition, work with cell cultures has evidenced that rDNA which presents DSBs also move towards the nuclear periphery, thus we observe this feature occurs not only in yeast, but in higher eukaryotes (Marnef et al., 2019).

To prevent this critical event, a subset of rDNA repeats is tethered to the NE (**Fig. 1.7**) by the **CLIP** (chromosome linkage INM proteins) and **cohibin** complexes, keeping the rDNA tightly associated with the nuclear periphery -associated to silenced DNA- (and thus being partly responsible for its characteristic shape) and more importantly, contributing to genome stability. The CLIP complex is composed of the aforementioned Man1 homolog Heh1 and Nur1, both proteins inserted in the NE. Cohibin, composed of Lrs4 and Csm1, connects the rDNA and silent chromatin to the NE by linking the chromatin-bound **RENT** complex and either CLIP (for the rDNA) or Mps3 (for non-rDNA regions) (Chan et al., 2011; Mekhail et al., 2008). RENT stands for regulator of nucleolar silencing and telophase exit, thus mediating transcriptional silencing at the rDNA locus, and its components are Sir2, Cdc14 and Net1, although the Net1 paralog Tof2 has been identified to interact with it as well (Straight et al., 1999; Tanny et al., 2004). Net1 is in fact responsible for tethering the RENT complex to the rDNA through interaction with Fob1 (Huang & Moazed, 2003). During interphase, Net1 and Sir2 colocalize with the nucleolus but, at the end of mitosis, a fraction of Sir2 leaves the nucleolus and disperses forming foci throughout the nucleus, indicating that the structure of silent rDNA changes during the cell cycle (Straight et al., 1999). However, if damage occurs at the rDNA, it needs to be detached from the NE tethers to allow relocation of the break outside the nucleolus and be able to be repaired. This is regulated by post-translational modifications in CLIP and cohibin components (mostly driven by Nur1 phosphorylation), indicating the need of dynamism in anchoring/dislodgment to response to different necessities, not only in yeast, but in a similar fashion in human cell cultures (Capella et al., 2021).

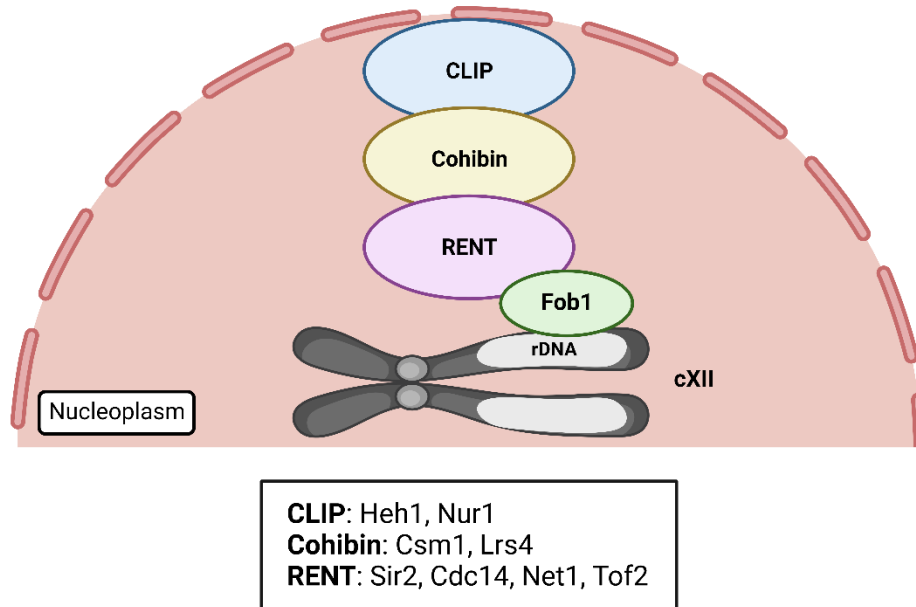


Figure 1.7. The rDNA tethering to the INM requires the RENT, cohibin and CLIP complexes. This schematic shows the interaction between the three complexes involved in rDNA attachment to the nuclear envelope and its protein components. It is the RENT complex that binds the RFB protein Fob1, while cohibin mediates RENT and CLIP interaction, being the latter attached to the NE (modified from Mostofa et al., 2018 and created with BioRender.com).

S. cerevisiae represents a unique genetic model to dissect chromosome behavior. Because precisely the rDNA is the only visible chromosome structure under the microscope, the locus has been widely used to unveil chromosome dynamics, including segregation and condensation events (Ayra-Plasencia & Machín, 2019; Clemente-Blanco et al., 2009; Machín et al., 2006; Miyazaki & Kobayashi, 2011; Torres-Rosell et al., 2005).

This locus experiments drastic morphological modifications through the cell cycle, defined by changes in compaction and condensation (**Fig. 1.8**). During interphase, the rDNA acquires a loosely organized structure that has been referred to as puffs, which evolves into a highly organized state on G2/M, attaining a line or arc-like morphology at the nuclear periphery (Guacci et al., 1994; Lavoie et al., 2002, 2004). As described above, Nz exposure and consequent microtubule depletion entails a mid-M arrest, where the rDNA adopts a remarkably complex loop shape mediated by condensin, and thus considered a condensed state of the repetitive locus (Freeman et al., 2000; Lavoie et al., 2002, 2004; Matos-Perdomo & Machín, 2017). Additionally, cohesin, the Polo-like kinase Cdc5 and TORC1 (Target of rapamycin complex 1) are also involved in the establishment and maintenance of the rDNA loop (Harris et al., 2014; Lamothe et al.,

1. Introduction

2020; Matos-Perdomo & Machín, 2018; St-Pierre et al., 2009). As explained earlier, in mid-M blocks due to APC disturbance, such as the *cdc16* mutant, the nucleus traverses the bud neck, being the rDNA elongated forming a line or hook (Guacci et al., 1994; Palmer et al., 1989, 1992). The relation of TOR, which involves TORC1 and TORC2, the master growth switch in response to nutrient availability, with nucleolar regulation is not surprising, because transcription of the rDNA genes require high levels of energy and cellular resources, thus needing to shut it down upon nutrient deprivation (H. Li et al., 2006; Martin et al., 2006). Additionally, the TOR pathway is also implicated in rDNA chromatin structure apparently by regulating the localization of RNA pol I and the Rpd3 histone deacetylase to rDNA (Tsang et al., 2003).

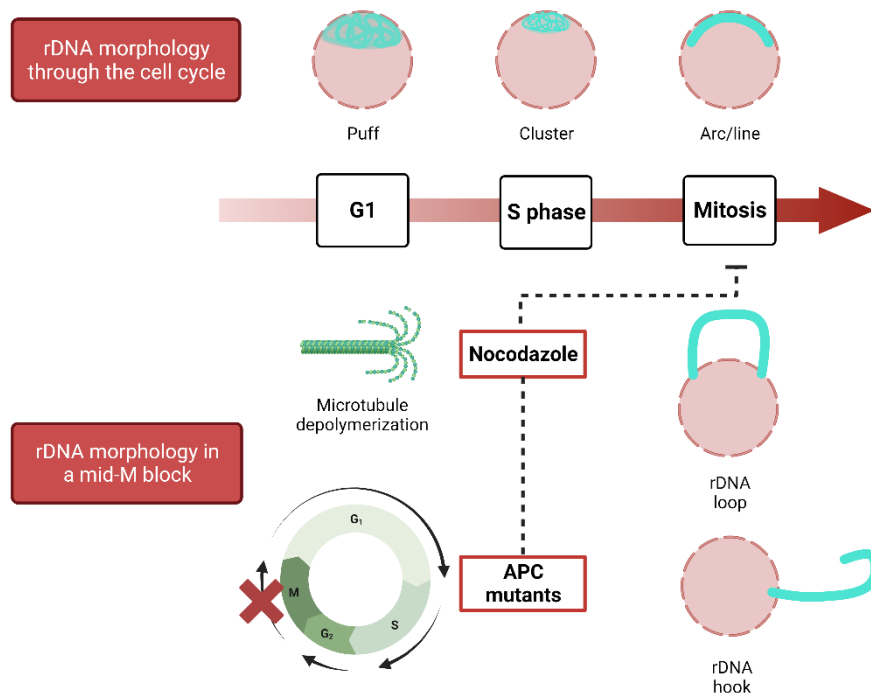


Figure 1.8. rDNA morphological changes through the cell cycle and in mid-M blocks. The rDNA (in cyan, while the rest of the nucleus is depicted in pink) acquires different morphologies through a normal cell cycle, from a disorganized puff in interphase which gradually transforms into a condensed and organized arc or line in early mitosis. Nevertheless, in mid-M blocks caused by the microtubule depolymerizing drug nocodazole or APC inducible mutants, the rDNA develops nucleolar extensions around the rDNA array (created with BioRender.com).

A connection between the nucleolus and NE morphological alterations has been established in the last years as various groups, including ours, have shown that abnormal structures of the NE triggered by membrane overextension arise adjacent to the nucleolus, being proposed as a membrane sink by Witkin et al. thanks to its ability to resist deformation (Barbosa et al., 2019; Campbell et al., 2006; Male et al., 2020; Matos-Perdomo & Machín, 2018; Witkin et al., 2012). However, nuclear flares in fission yeast

and *S. japonicus* are not associated to the nucleolus, suggesting either that nuclear domains have species-specific effects on nuclear morphology or that they differ in the sites of new membrane synthesis, because symmetrical addition of new membrane differs from the phenotype observed in *S. cerevisiae*, producing an increase in nuclear area without the appearance of nuclear projections (Deolal & Mishra, 2021; Makarova et al., 2016). Strikingly, besides the nucleolar ability to protrude, it has been recently reported that upon lipid stress, NE inward ingressions arise in association to the nucleolar subdomain and juxtaposed to vacuoles (yeast lysosome equivalents), evidencing the plastic nature of the nucleus and the nucleolus (Garcia et al., 2022).

1.3. Factors that influence nuclear shape

Considering the complexity of the nucleus and the wide variety of components and processes involved, from the lipids and proteins of the NE to the content enclosed within, it is likely that altering any of them might influence the morphology of the nucleus.

1.3.1. Chromatin

One of the factors expected to have an impact on nuclear shape is one of its main constituents, which is chromatin, because the size of the nucleus may be directly proportional to the amount of DNA it contains and its compaction degree. Species with larger genomes generally have larger nuclear and cellular volumes, supporting this idea, especially in plants (Cavalier-Smith, 2005; Jovtchev et al., 2006). Nonetheless, DNA content per se does not strictly affect nuclear shape, although ploidy differences induce nuclear shape changes during development (Jevtić & Levy, 2014; Jorgensen et al., 2007; Neumann & Nurse, 2007; M. Webster et al., 2009). Also, the size of the nucleus experiences a gradual increase in size from G1 to M, as the doubling of chromatin in S phase occurs (Jorgensen et al., 2007; Neumann & Nurse, 2007)

However, architecture and packaging of chromosomes has been shown to contribute significantly to morphology in yeast studies. For example, forcing untethering of chromosomes from the INM increases chromatin mobility and nuclei susceptibility to deformation, mostly in response to cytoskeletal forces. Furthermore, RSC chromatin remodeling complex loss of function in *sth1* mutants results in perturbed NPC localization along with NE aberrant organization (Schreiner et al., 2015; Stephens et al., 2019; Titus et al., 2010).

1. Introduction

1.3.2. Proteins associated to the NE

Proteins associated to the NE excluding chromatin tethers

In several organisms including human cells, *Drosophila* and *C. elegans*, **lamin** dysfunction has been linked to nuclear morphology alterations and several health disorders under the umbrella term laminopathies (Lenz-Böhme et al., 1997; J. Liu et al., 2000; Taimen et al., 2009).

NPC assembly entails an intricate process in which inner and outer nuclear membranes must fuse, and disruption (absence by deletion or changes in regulation) of their components have been reported to result in distorted nuclear shape (Bogerd et al., 1994; Goldstein et al., 1996; Titus et al., 2010; Webster et al., 2014; Wentz & Blobel, 1993). Some nucleoporins possess an amphipathic helix which can drive nuclear insertion and then NPC assembly (Drin et al., 2007; S. J. Kim et al., 2014; Mészáros et al., 2015; Patel & Rexach, 2008). Thus, NPC components have the ability to impact nuclear morphology by inducing NE deformations, which can lead to aberrant forms upon nucleoporin stoichiometric imbalance, such as lamellae, which consists of stacked flattened membranes that are structurally similar to the NE, but lack NPCs (Marelli et al., 2001; Wentz & Blobel, 1993). It is speculated that the aberrant morphologies observed in these mutants may be due to interactions between the NE and the nuclear content, because an altered NPC composition may disrupt chromatin attachment to the NE (Walters et al., 2012). Additionally, disturbing the evolutionary conserved reticulon proteins of the ER (like Rtn1 and Yop1), which regulate membrane curvature and expansion, result in aberrant NE, as they influence NPC insertion and hence nuclear import (Dawson et al., 2009).

As microtubules nucleate from the **SPBs**, they exert force on the NE, comparable to nucleo-cytoskeletal components and thus influencing nuclear size and shape. When spindle positioning or separation is impaired, the NE loses its natural form in fission yeast, failing to segregate chromosomes properly. This happens also when microtubule attachment to SPBs or kinetochore proteins is altered due to excessive elongation of the spindle (Cantwell & Nurse, 2019a; Zheng et al., 2007). Besides, we have already described above that nuclear morphology is extensively altered when microtubules are depleted.

Proteins involved in chromatin tethering

The attachment of chromatin to the NE comprises a mechanical link between nuclear components while also providing stiffness to the nucleus, meaning that a change in chromosome structure may affect the NE by altering the tethering (Male et al., 2020; Taddei & Gasser, 2012).

Regarding **INM lamin-like proteins**, the coiled-coil domain containing protein Esc1 (establishes silent chromatin) in *S. cerevisiae* is involved in anchoring silenced telomeres to the NE through its high affinity for Sir4 (silent information regulator) (Andrulis et al., 2002; Hattier et al., 2007; Male et al., 2020). Its overexpression triggers NE projections referred to as “escapades”, which include NPCs but exclude chromatin, and arise adjacent to the nucleolus, hence opposite the SPB. Additionally, they are not inherited by daughter nuclei during mitotic growth (Andrulis et al., 2002; Hattier et al., 2007).

Proteins that belong to the **LINC** complex have been established to provide shape and stability to the nucleus, and its disruption provokes distorted nuclear shape and organization because of disturbed cytoskeletal forces acting on the nucleus. Mps3, together with Esc1, anchor telomeres at the nuclear periphery, favoring telomere silencing and recombination suppression (Garapati & Mishra, 2018; D. I. Kim et al., 2015; Rothballer & Kutay, 2013; Taddei & Gasser, 2012). The overexpression of the toxic mutation *MPS3-G186K* causes mitotic arrest due to SPB insertion defects, together with INM over proliferation and NE aberrations, thus the authors proposed that this protein promotes SPB insertion into the NE by modulating NE lipid composition. In this mutant, membrane expanded symmetrically, not restricted to the nucleolar area, although this region was often partitioned away from the bulk of the nucleus either by a membrane or by the formation of a lobe (Friederichs et al., 2011). The overexpression of this mutant always led to extensions and protrusions, while the overexpression of the WT led to altered nuclear morphology in 50% of the cells even though they do not suffer from membrane overexpansion (Friederichs et al., 2011; Rothballer & Kutay, 2013). Additionally, mutations in Mps3 or the related proteins Ebp2 and Rrs1 hamper ribosome biogenesis and disrupt telomeric silencing and clustering, not affecting anchoring to NE but deforming the nucleus, suggesting a connection between NE proteins, nuclear shape and chromatin function (Garapati & Mishra, 2018; Horigome & Mizuta, 2012).

1. Introduction

Regarding **LEM domain proteins**, NE deformations are not triggered in budding yeast by loss of Heh1, despite nuclei are larger in size, while absence of MAN1 and LEM2 in fission yeast causes blebbing of the nucleus and discontinuous membrane distribution (Gonzalez et al., 2012; Male et al., 2020). Heh1 or Heh2 null mutants are viable, but the double mutant is inviable or displays a growth defect. However, loss of the cohibin-CLIP anchoring pathway (including *heh1* single mutant) leads to rDNA repeat instability, cell cycle arrest and premature senescence (Chan et al., 2011).

To sum up, an extensive group of proteins and complexes stabilize nuclear structure by creating protein-protein interactions, but also interacting with the lipids of the membrane and the chromosomes inside the nucleus, as well as cytoskeletal elements, evidencing the complexity of nuclear morphology maintenance.

1.3.3. Lipid homeostasis

As the NE is mainly composed of phospholipids, it is to be expected that lipid regulation is involved in nuclear size and shape. According to Makarova *et al.*, NE expansion is dependent on phospholipid biosynthesis, as defects in these pathways result in misshapen nuclei in *S. pombe* and *S. japonicus* (Makarova et al., 2016). Likewise, deletion mutants of genes involved in regulation of lipid homeostasis in *S. cerevisiae* also exhibit aberrant nuclear shape (Han et al., 2008; Santos-Rosa et al., 2005; Siniossoglou, 1998). Because the ONM is a continuum with the ER, one may think that ER overexpansion could affect nuclear morphology. Indeed, even though there are mutants in which membrane excess arise in both compartments, there are also examples in which they are independent (*pah1*, *spo7*, *nem1*, *MPS3-G186K* and certain *sec* mutants), suggesting the existence of a barrier to membrane expansion between the peripheral ER and the NE (Campbell et al., 2006; Friederichs et al., 2011; O'Hara et al., 2006; Siniossoglou, 1998; Walters et al., 2019; Wright et al., 1988).

Lipid precursors are used for phospholipid synthesis under nutrient rich conditions to maintain rapid proliferation but are redirected to triacylglycerol (TAG) production during starvation, which are stored in lipid droplets (LDs). Phosphatidic acid (PA) is the precursor used in the synthesis of membrane phospholipids used for membrane expansion and also LDs, and its fate is largely controlled by nutrient availability and the correspondent regulatory pathways (Carman & Han, 2019; Han et al., 2006; Henry et al., 2012; Kwiatek et al., 2020; Makarova et al., 2016; Siniossoglou, 2009). The evolutionary

conserved lipin, Pah1 in budding yeast, generates diacylglycerol (DAG) from PA and has been proposed as a metabolic switch in response to growth and environmental signals, controlling the balance between lipid storage as LDs and membrane biogenesis (Barbosa et al., 2015; Carman & Han, 2018; Han et al., 2006) (**Fig. 1.9**). Lipins are kept inhibited in the cytosol by multisite phosphorylation, mediated by Pho85, Cdc28 and protein kinase A in yeast (Choi et al., 2011, 2012; Su et al., 2012) and target of rapamycin (TOR) and mitotic kinases in mammals (Grimsey et al., 2008; T. E. Harris et al., 2007; Huffman et al., 2002). Pah1 translocation onto the ER membrane is achieved after activation by dephosphorylation catalyzed by the transmembrane Nem1 (catalytic subunit)-Spo7 (regulatory subunit) complex, which is subjected to TOR regulation (H.-S. Choi et al., 2011; Dubots et al., 2014; Karanasios et al., 2010; O'Hara et al., 2006; Santos-Rosa et al., 2005; Siniossoglou, 1998). Additionally, the activation of the DAG kinase Dgk1 counteracts the action of Pah1 by resynthesizing PA from DAGs, rerouting the pathway towards membrane biogenesis (Han et al., 2008).

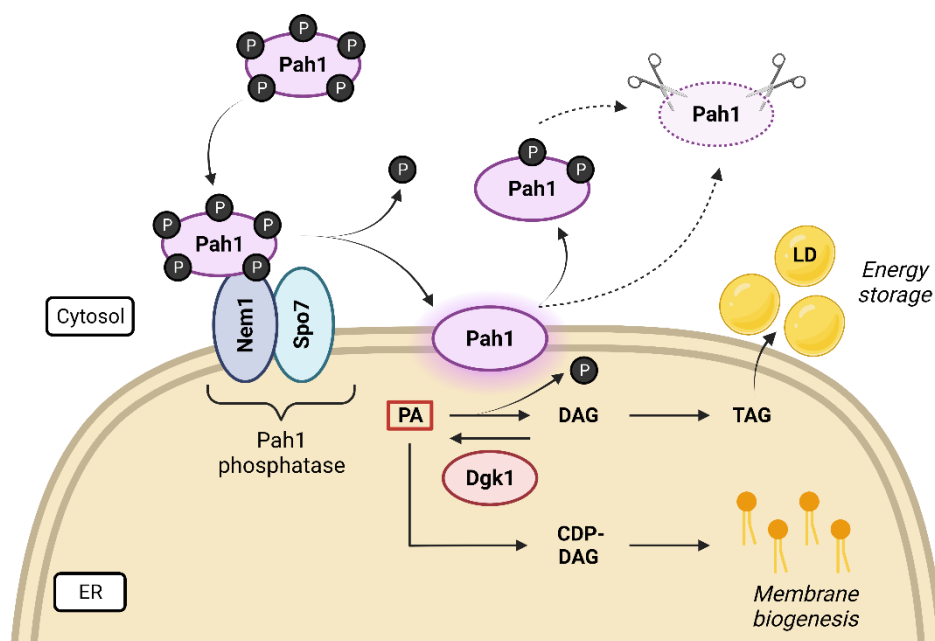


Figure 1.9. Regulatory network of the yeast lipin/Pah1. Phosphatidic acid (PA) is the central precursor in lipid biosynthesis. Pah1, the PA phosphatase, remains phosphorylated (inactive) in the cytosol under growth conditions to favor phospholipid biosynthesis needed for membrane expansion through the CDP-DAG pathway. However, when nutrients are depleted the Nem1-Spo7 complex, which is embedded at the ER membrane, dephosphorylates Pah1 to activate it and promote PA into DAG conversion, which are acylated and converted into TAG, stored in lipid droplets (LD). Dephosphorylated (or partially dephosphorylated) Pah1 is targeted for proteasomal degradation (modified from Carman & Han, 2019 and created with BioRender.com).

Cells lacking any of these 3 proteins (Pah1, Spo7 and Nem1) exhibit aberrant nuclear shape due to a reciprocal increase in membrane biogenesis, which gives rise to nuclear

1. Introduction

flares in the nucleolar region, suggesting that Pah1 regulation may be important for nuclear remodeling (Campbell et al., 2006; Santos-Rosa et al., 2005; Siniosoglou, 2009). Furthermore, not only NE morphology is altered. Cells with an impaired Nem1/Spo7-Pah1 axis display defects in lipid droplet formation, vacuole morphology and autophagy (Rahman, Mostofa, et al., 2018; Xu & Okamoto, 2018). However, some of the phenotypes observed in the *pah1Δ* mutant are suppressed by the loss of Dgk1, suggesting that a proper balance of PA/DAG is required for lipid metabolism and cell fitness (Han et al., 2008; Pascual & Carman, 2013).

The work from Witkin *et al.* suggests that nuclear expansion in closed mitosis is independent of spindle elongation and occurs in response to a cell cycle cue that signals mitotic entry (Witkin et al., 2012). The flare induced by mitotic arrests shares similarities to nuclear expansions caused by misregulation of the yeast lipin/Pah1 pathway (including its regulators Nem1/Spo7) (Campbell et al., 2006; Pascual & Carman, 2013). Using a mutant of this pathway, Campbell et al. demonstrated that nucleolar expansion is not enough to drive flare formation. Additionally, *spo7Δ* cells combined with mutations in vesicle-trafficking genes give rise to multiple flares around the entire nucleus instead, indicating that the spatial confinement of a single nuclear flare is dependent on vesicle trafficking (Webster et al., 2010). It has been proposed that there is a mechanism that favors nuclear elongation next to the nucleolus to prevent disruption of nuclear inner chromosomal architecture, thus protecting the rest of the genome. Altogether, these works support the idea that the budding yeast nuclear envelope has domains of different properties (Arnone et al., 2013). Besides nuclear protrusions after lipid stress have been extensively shown, NE inward ingressions associated with the nucleolus also arise after lipid regulation impairment (Garcia et al., 2022).

Lipid metabolism processes take place mainly at the ER lumen, however recent studies in budding yeast have spotted lipid droplet synthesis inside the nucleus too, providing a possible connection between membrane remodeling, lipid metabolism and genome function (Barbosa et al., 2019; Romanauska & Köhler, 2018). Barbosa et al. show a translocation event of the phospholipid:DAG acyltransferase Lro1 from the ER to the INM, resulting in local TAG increase. Lro1 localization at the INM depends on cell cycle and nutrient availability signals, as it is excluded from the nucleolar territory under nuclear expansion but recruited there upon starvation, promoting LD biogenesis at the pnER adjacent to the nucleolus and allowing cell survival during starvation (Barbosa et

al., 2019; Barbosa & Siniosoglou, 2020). Likewise, recent evidence also confirms nucleus-vacuole junctions (NVJs) as a site for LD budding in response to nutritional stress, consistent with previous evidence showing Pah1 close to NVJs, and implicating the NE-vacuole tether Mdm1 in their biogenesis by interacting with enzymes of the fatty acid synthesis pathway (Barbosa et al., 2015; Barbosa & Siniosoglou, 2017; Hariri et al., 2018; Henne et al., 2015; Kohler & Büttner, 2021; Kvam et al., 2005; Kvam & Goldfarb, 2007; Otto & Thumm, 2020).

1.3.4. Nuclear size

Furthermore, not only nuclear shape must be controlled, but also the size plays an important role, given that nuclear volume is kept at 8-10% of cell volume in all organisms (Deolal et al., 2021; Jorgensen et al., 2007). Previous evidence supports that nuclear and cytoplasmic volumes are correlated and maintain a relationship known as the karyoplasmic ratio (N/C). This proportion remains constant in yeast through the cell cycle as growth increases its size, suggesting a mechanism which links nuclear and cellular volumes (Gregory, 2005; Jorgensen et al., 2007; Neumann & Nurse, 2007).

In experiments done using *sec* mutants to stop cell growth without disturbing cell cycle biochemistry, nuclear extension was not hampered and it was observed that the ratio was kept constant by disturbing nuclear morphology in the form of flares (Walters et al., 2012, 2019). Indeed, it has been shown that in single and multi-flared nuclei the NE surface area is increased, though they maintain the N/C ratio constant as in wild type cells, suggesting that flares may help to keep this ratio constant when NE proliferation is overstimulated (Webster et al., 2010). Nonetheless, disturbance of nuclear transport did lead to increased nuclear volume in *S. pombe* and also correlated with shape defects due to membrane excess (Kume et al., 2017). This difference between both organisms has been attributed by Walters et al. as a difference in the way of measuring cell and nuclear volumes.

Recently, it has been observed that increased nucleolar size in budding yeast triggers a non-isometric NE expansion concomitant with abnormal nuclear morphology, where NE projections arise preferentially adjacent to the nucleolus. These extensions require rDNA tethering to the NE, as cells display symmetric NE growth when the attachment is impaired. Additionally, this phenotype can be suppressed by reducing nucleolar size using low rDNA copy number strains (Male et al., 2020). This phenotype differs in the

1. Introduction

flares observed in *cdc5* mutants, as these are unaffected by rDNA copy number and rDNA tethering to the INM (Walters et al., 2014).

Taken all together, when over expansion of the NE takes place, the cell can take two approaches: either changing nuclear shape at specific locations to keep the N/C ratio constant or evenly expanding the NE leading to an increased nuclear volume without distortions in shape, and both also depend on the tethering of chromosomes to the INM (**Fig. 1.10**) (Deolal & Mishra, 2021).

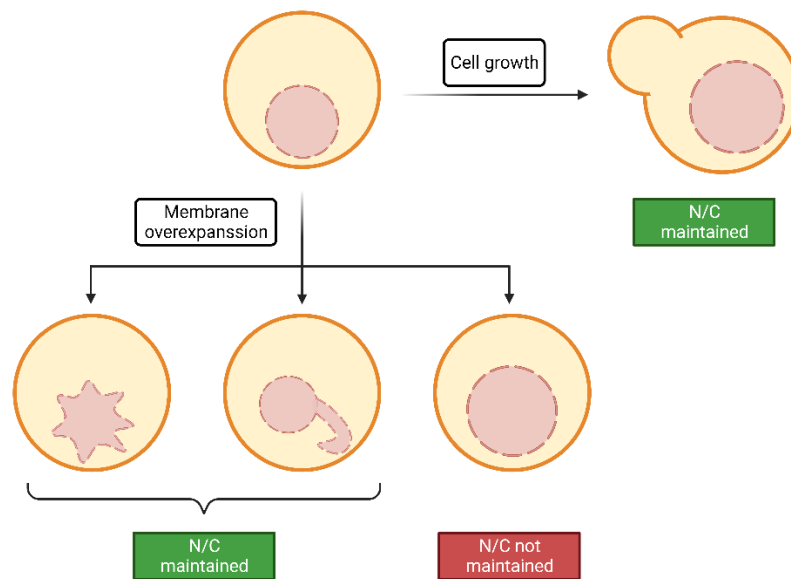


Figure 1.10. Possible outcomes upon nuclear membrane accumulation. Because cells tend to maintain a constant nuclear volume relative to the cytoplasm (known as the karyoplasmic ratio), upon membrane overexpansion conditions when the cell does not continue growing in size, loss of circularity due to altered nuclear morphology (single or multi-flared cells) can keep this ratio constant by increasing the nuclear surface (modified from Walters et al., 2019 and created with BioRender.com).

1.3.5. The vacuole, TOR and nucleophagy

Additionally, interaction of the NE with other organelles, including the vacuole and ER, may affect the NE capacity of expansion (Pan et al., 2000; Tomioka et al., 2020). Furthermore, the process of membrane remodeling involves membrane contact sites (MCS), which are characterized by physical proximity between different endomembrane systems, as it happens at the interface between the nucleus and the vacuole (Scorrano et al., 2019).

The vacuole is the yeast equivalent of the lysosome, and is frequently associated with the nuclear envelope adjacent to the nucleolus (Kvam & Goldfarb, 2007). WT cells under normal growth conditions contain between one and four vacuoles, depending on the strain background (Banta et al., 1988). It is critical for yeast viability, as it is required to perform multiple roles in response to cellular stressors and it has been demonstrated that this organelle is required for cell cycle progression, and thus, when vacuole inheritance to the daughter cell is prevented, it results lethal to the progeny (Jin & Weisman, 2015).

Among its main functions we encounter the turnover of cellular components via autophagy, storage of certain components, including phosphate, and the buffering of cellular pH, playing a role in water and ion homeostasis (Weisman, 2003). Under nutrient deficiency, cells form a single vacuole, expanding their volume and probably facilitating autophagy (Baba et al., 1994). The fusion of vacuoles require DAGs and it is hampered in lipin axis mutants because DAG synthesis is abolished, leading to vacuole fragmentation (Michaillat & Mayer, 2013; Sasser et al., 2012). Strikingly, this phenotype is surpassed upon rapamycin induced TORC1 inactivation, after which these mutants display a single vacuole, suggesting that autophagy itself is dispensable for vacuole fusion after TORC1 inactivation (Rahman, Mostofa, et al., 2018).

Autophagy is the general term to define a group of processes of import of a wide range of cargos, from portions of cytoplasm to entire organelles, into the vacuole/lysosome lumen for degradation by vacuolar hydrolases. We differentiate mainly between macroautophagy, in which the cargo is wrapped into a vesicle named autophagosome (which arises from expansion of the isolation membrane or phagophore) that fuses with the vacuole, and microautophagy, in which cargo is directly engulfed by the vacuole. Those two processes can be divided into selective or non-selective macro and microautophagy respectively, depending on whether a specific cargo or bulk cytosol is affected. The specificity in macroautophagy is achieved through the binding of specific receptors to the specific cargo to degrade and the protein Atg8, involved in autophagosome formation. Briefly, autophagy initiation requires the Atg1 kinase and Atg13 to trigger phagophore formation followed by vesicle nucleation and recruitment of Atg8, a ubiquitin like protein required for phagophore expansion during autophagosome biogenesis, among many other proteins (Papandreou & Tavernarakis, 2020). In a WT strain we consider a baseline level in which 30% of the cells display a PAS (phagophore assembly site), which is where the autophagy related proteins, Atg, assemble adjacent to

1. Introduction

the vacuole, as measured by GFP-Atg8 foci location (Backues & Klionsky, 2022; Geng et al., 2008; Nair et al., 2011; Shintani & Klionsky, 2004). However, proteins involved in PAS formation may be dynamic and the PAS could also be a transient structure (Reggiori & Klionsky, 2013).

In organisms which undergo closed mitosis, because the NE remains intact through the cell cycle, misfolded and aggregated proteins from the nucleus must be eliminated somehow. Thus, cells must allow access to potential nuclear cargo by the autophagic machinery. Two mechanisms have been proposed: proteasomal degradation (either nuclear or after export to the cytoplasm) and autophagy of the nucleus (Chen & Madura, 2014; Krick et al., 2009; Roberts et al., 2003). Regarding the selective degradation of nuclear components, until recently only microautophagic processes had been described in yeast. Up to date, we differentiate between macronucleophagy and two microautophagic processes, referred to as piecemeal microautophagy of the nucleus (PMN) and late nucleophagy, respectively (Mijaljica et al., 2012; Roberts et al., 2003).

Macronucleophagy depends on the outer nuclear membrane receptor Atg39 (a homologue has not been found in mammals yet), which promotes selective engulfment of nuclear cargos by the phagophores by binding Atg8 (involved in autophagosome expansion) and Atg11, which recruits the autophagosome formation machinery onto receptor-target complexes, but it is independent of Nvj1 (essential in PMN) (**Fig. 1.11**). Additionally, the ER receptor Atg40 is partially involved in this process. These experiments identified as cargos portions of NE, including proteins of the INM and ONM, along with the nucleolar protein Nop1, which were found inside the autophagic vesicles. However, it is not known if nuclear partitioning of the cargo occurs before autophagosome formation or if these two processes are synchronized (Mochida et al., 2015). Prolonged nitrogen starvation conditions trigger macronucleophagy, and in turn nuclear shape changes (Papandreou & Tavernarakis, 2020). Deletion mutants of *ATG39* also displayed aberrant nuclear morphology, and were less viable than WT cells after prolonged nitrogen starvation, envisioning the relevance of nucleophagy in this conditions, as non-selective autophagy was not affected (Mochida et al., 2015).

PMN was the first mechanism of nucleophagy described in budding yeast by Roberts et al., 2003 and remains the best described. It takes place through direct contact between the two organelles at the NVJs, established by the Velcro-like interaction of the vacuolar protein Vac8 and ONM protein Nvj1, regulated by Snd3 upon nutrient stress (Pan et al.,

2000; Tosal-Castano et al., 2021). The cargo is pinched off the nucleus directly to the vacuolar lumen thanks to an electrochemical gradient generated by the vacuolar ATPase. (Dawaliby & Mayer, 2010; Kvam et al., 2005; Pan et al., 2000; Roberts et al., 2003). Besides, there are other NE-vacuole contact sites established as sites for lipid droplet biogenesis which do not intervene in PMN that contain the tethers Mdm1, Nvj2 and Nvj3 (Hariri et al., 2018; Henne et al., 2015). It was recently described that Atg39 was also required in PMN, making this autophagic cargo receptor a common feature of macro and micronucleophagy to target degradation, along with the core autophagic machinery and the additional requirement of Atg11. One difference between both autophagy modes is the size of the cargo, which is significantly bigger in PMN (Otto & Thumm, 2020, 2021). Within the PMN process, we differentiate two stages: the initial protrusion of nuclear membrane at the NVJ and the late step of vesicle scission (Dawaliby & Mayer, 2010). This pathway requires the core autophagic machinery for the latter, although not for the NVJ establishment (Krick et al., 2008). Through PMN several cargo are degraded, including NE components and parts of the nucleolus containing pre-ribosomes and RNA, but importantly NPCs and SPBs are excluded (Millen et al., 2009). Interestingly, there is a specific autophagy pathway to selectively degrade NPCs upon TORC1 inactivation, divided into two branches referred to as NPC-phagy and nucleoporinophagy, mediated by Atg8–Nup159 interaction but Atg39 independent (Lee et al., 2020; Tomioka et al., 2020). Because parts of the nucleolus are targeted for PMN, it is crucial to prevent rDNA degradation. To avoid rDNA inclusion in the PMN nuclear projections, the CLIP and cohibin complexes drive the DNA away from the NVJ upon TORC1 inactivation to physically separate it from nucleolar protein degradation (Mostofa et al., 2018, 2019). This process of separation and repositioning of nucleolar proteins and rDNA is promoted by rDNA condensation after TORC1 inactivation (Mostofa et al., 2019).

1. Introduction

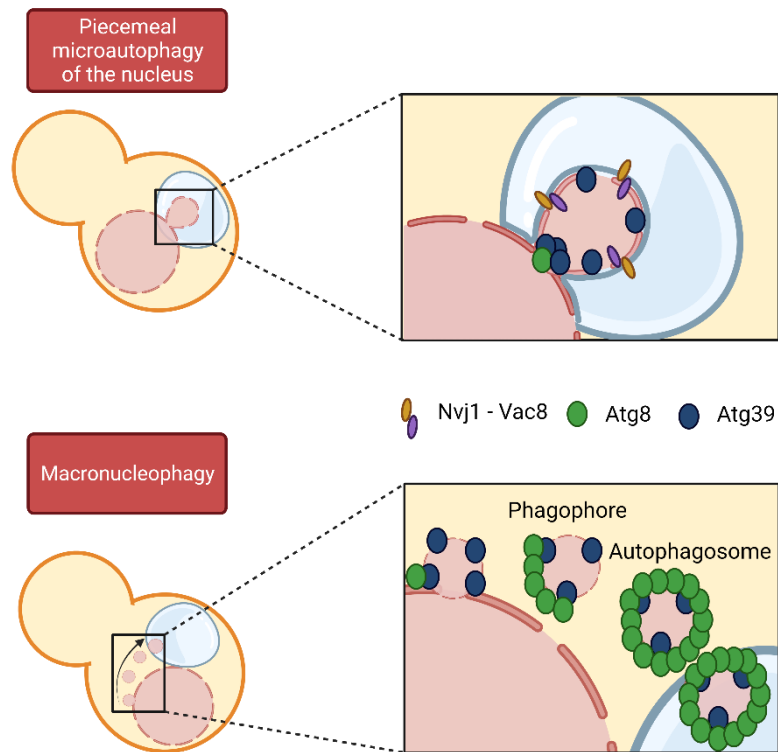


Figure 1.11. Proposed model for nucleophagy in budding yeast. Both macro and micronucleophagy depend on the interaction of Atg8 and the specific cargo receptor Atg39, although Nvj1 is only detected in PMN vesicles. As described above, macronucleophagy involves autophagosome formation, depicted by Atg8, which recruits the rest of the autophagic machinery, in contrast to PMN, whose vesicles are not coated with Atg8 except for a focus which arises at the neck of nuclear protrusion into the vacuole. Remarkably, PMN cargo is bigger in size than macronucleophagic vesicles (modified from Otto & Thumm, 2021 and created with BioRender.com).

The third type of nucleophagy described until now (only acknowledged by a subset of authors in nucleophagy reviews) is referred to as **late nucleophagy**, which is a form of micronucleophagy that differs in time and space from PMN. First, in contrast to PMN, it is independent of NVJs and some Atg core components, and second it is only observed after prolonged nitrogen starvation (20 – 24 h), while PMN is detectable in exponentially growing cells at a baseline level and at higher rates upon shorter nutrient deprivation (3 h). Interestingly, inhibition of late nucleophagy caused by certain Atg mutations under nitrogen starvation conditions led to aberrant nuclear morphology, despite they recovered a rounded shape when exposed to enriched medium (Mijaljica et al., 2012).

In contrast to other eukaryotes, in which several cues can activate autophagy, in yeast is nutrient depletion the main stimulus that triggers autophagy, although PMN is active at baseline levels in exponential growth under medium rich conditions as well (Mijaljica &

Klionsky, 2022; Papandreou & Tavernarakis, 2019; Reggiori & Klionsky, 2013; Roberts et al., 2003). It is the evolutionary conserved **TOR** complex that regulates growth by coupling nutrient sensing and cell metabolism. In yeast, unlike almost all other eukaryotes which only carry one, there are two TOR genes, which in turn form two different complexes: TORC1 (which contains either Tor1 or Tor2) and TORC2 (which contains Tor2 exclusively). Both complexes play a central role in regulating cell growth through two separate signaling branches. There is a TOR shared function redundant in both complexes, which is the one nutrient and rapamycin responsive that controls protein synthesis and degradation, mRNA synthesis and degradation, ribosome biogenesis, nutrient transport and autophagy; but there is also a TORC2 unique function, which controls polarization of the actin cytoskeleton, endocytosis and sphingolipid synthesis. The TOR shared branch executed by TORC1 is considered to mediate temporal control of cell growth (Loewith & Hall, 2011).

TORC1 localizes mainly on the limiting membrane of the vacuoles (of note, the yeast vacuole acts as a nutrient reservoir) and acts as a metabolic switch in response to nutrient availability, being the primary sensor of nitrogen and amino acids, negatively regulating autophagy when they are present at sufficient concentrations, hence promoting cell growth. It does so by keeping Atg13 (among other proteins) phosphorylated, which inhibits the downstream cascade triggered by this protein to assemble the Atg1 kinase complex (Noda & Ohsumi, 1998). Additionally, it has been proposed that autophagy regulation by TORC1 requires at least a partial relocalization, in which it detaches from the vacuolar membrane upon inactivation, to allow Atg13 dephosphorylation and PAS recruitment (Noda, 2017). Another way to activate autophagy in mammal cells and yeast is rapamycin exposure because it is a TOR inhibitor and thus influences TOR signaling pathways, mimicking what happens under nitrogen deprivation. Furthermore, glucose deprivation can trigger autophagy too. Under higher concentrations of glucose protein kinase A (PKA) is active and inhibits macroautophagy by phosphorylating Atg1 and Atg13, at different sites from those targeted by TOR, inhibiting downstream reactions as well (Budovskaya et al., 2005; Stephan et al., 2009). Nonetheless, this complex process is regulated through many other different cue-specific mechanisms.

Besides inducing general autophagy, when TORC1 is inactivated under different kinds of stress, it promotes macro and micronucleophagy through the Nem1/Spo7-Pah1 axis, as it properly localizes Nvj1 to the NVJ and the specific nucleophagy receptor Atg39

1. Introduction

(Morshed et al., 2020; Mostofa et al., 2018; Rahman, Mostofa, et al., 2018; Rahman, Terasawa, et al., 2018; Ueda et al., 2019). Additionally, the yeast lipin/Pah1 is recruited to the nuclear membrane domain in contact with the vacuole when glucose is consumed from the media in the post-diauxic shift, suggesting it might play a role in lipid remodeling to promote PMN (Barbosa et al., 2015). Furthermore, other proteins involved in lipid biosynthesis (Tsc13 and Osh1) are targeted to the NVJs by Nvj1 and have been implicated in PMN, suggesting a connection between lipid composition and the ability to form NE extensions towards the vacuole (Dawaliby & Mayer, 2010; Kvam et al., 2005; Kvam & Goldfarb, 2006; Tosal-Castano et al., 2021). Additionally, TORC1 inhibition reduces nucleolar size both in interphase and mitosis, while also impinging on its morphology (Ha & Huh, 2011; Matos-Perdomo & Machín, 2018; Tsang et al., 2003). Cerulenin-induced fatty acid synthesis inhibition prevents the formation of these NE extensions, impairing PMN, implicating that enough lipid synthesis is needed to create these membrane protrusions (Inokoshi et al., 1994; Kvam et al., 2005). In mammalian cells, TORC1 phosphorylates lipin to keep it inactive and prevent it from binding the nuclear membrane in favorable conditions (T. E. Harris et al., 2007; Huffman et al., 2002). However, yeast TORC1 helps to keep Pah1 inactive by preventing its dephosphorylation by Nem1, keeping the latter phosphorylated (Dubots et al., 2014). It was suggested that abnormal nuclear morphology in these mutants could be worsened by nucleophagy impairment, as the cell could not recycle the excess of membrane created (Krick et al., 2008; Nakatogawa & Mochida, 2015). TAGs present in LDs act as donors for autophagosome membrane formation, implying that impaired TAG synthesis has a negative impact in autophagy induction. This has been observed in yeast mutants of TAG synthesis or lipolysis, which show inhibited autophagosome formation and macroautophagy after nitrogen starvation (Shpilka et al., 2015). Furthermore, altering the lipin axis and impairing DAG production compromises bulk autophagy, and especially nucleophagy, after TORC1 inactivation (Rahman, Mostofa, et al., 2018; Rahman, Terasawa, et al., 2018).

It is evident that impairing nucleophagic mechanisms must have implications for the organism health, as has been reported in many human pathologies, including cancer, type II diabetes and several illnesses of the central nervous system, such as Parkinson's disease (Nakatogawa et al., 2009; Papandreou & Tavernarakis, 2019; Schneider & Cuervo, 2014). Furthermore, we can envision how intricate the balance of the NE is, taking into account

processes such as lipid composition and degradation of nuclear components via nucleophagy, connection to other organelles such as the vacuole and lipid droplets, which are in turn regulated by different pathways, such as TOR-mediated surveillance. This tight regulation might evidence that nuclear morphology is essential for proper cell survival.

1.4. *Saccharomyces cerevisiae* as a model organism

The yeast *Saccharomyces cerevisiae*, commonly known as baker's or budding yeast, represents one of the main model organisms used in biological research. This non-pathogenic unicellular fungus from the phylum *Ascomycota* has a size of 4 – 6 μM and has been used to study processes like cell cycle, maintenance of genomic stability, DNA damage and stress responses, including autophagy, within the eukaryotic domain because they are highly conserved through evolution and thus, unlike bacteria, being comparable to humans.

Thanks to a series of traits, its use presents many advantages compared to higher eukaryotes, being especially suitable for genetic, biochemical and cell biology studies. Some of its attributes include rapid growth with low requirements of media and temperature (generation time of approximately 90 – 120 min under optimal conditions), highly efficient genetic engineering thanks to a high rate of HR and a stable life cycle either as haploid or diploid cells. When they exist in haploid form, we distinguish two different mating types, so-called MAT α or MAT a , which are able to mate to produce a diploid cell. Nonetheless, when diploids face stressful conditions like nitrogen deprivation, they undergo meiosis and produce four haploid spores contained within an ascus, which will germinate under favorable conditions (**Fig. 1.12**). The different mating types produce different pheromones, a-factor and α -factor respectively, which block the cells of the opposite sex in G1 to prepare them for mating and start a new diploid cycle (Schrick et al., 1997). Also, the stages of the cell cycle are morphologically distinguishable under a simple bright field microscope by the existence and size of the bud.

1. Introduction

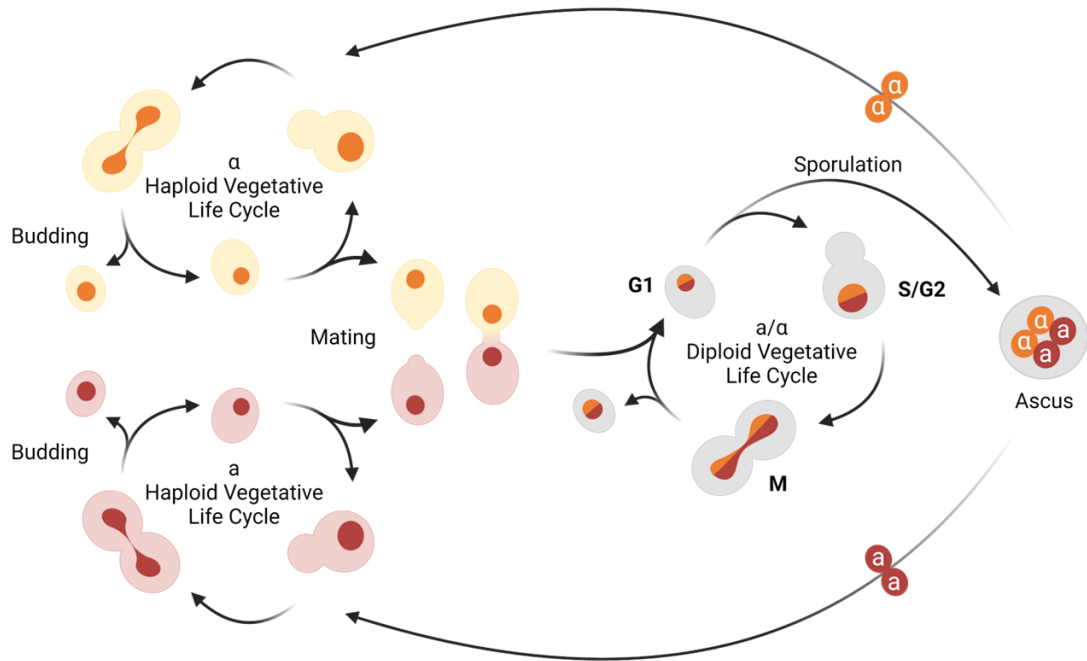


Figure 1.12. *S. cerevisiae* life cycle. MAT α and MAT α cells mate to give rise to a diploid cell, which will undergo meiosis and sporulate under stressful conditions, forming an ascus containing four ascospores. Both, haploids and diploids, double by mitosis in a vegetative life cycle (modified from <https://www.singerinstruments.com/resource/what-is-yeast/> and created with BioRender.com).

An important advantage over other model organisms is that the yeast genome organization is far simpler, it was the first eukaryote entirely sequenced, and all related information is publicly available online at Saccharomyces Genome Database (Cherry et al., 2012). The size of the genome is 12.1 million base-pairs (bp), containing about 6000 genes (of which about 4000 are not essential) with barely any introns distributed in 16 chromosomes (Goffeau et al., 1996).

A watercolor illustration of a blue, bird-like creature with a long neck and a small head. It is surrounded by several red, fluffy flowers. A green line is drawn around the creature's head, forming a smile. The background is white with some grey brushstrokes.

2. AIMS

As explained above, there are multiple scenarios which cause nuclear envelope morphological alterations, either caused by genetical or chemical means. There is a gap in the knowledge regarding how these non-spherical nuclear morphologies might affect chromosome segregation and if they compromise genomic integrity. Likewise, it is not well described the mechanism by which cells get rid of nuclear membrane imbalances to achieve proper mitotic exit and entry into a new cell cycle, reshaping the nucleus to reestablish an accurate nuclear/cytoplasmic volume ratio.

The aims addressed in this work are:

1. To characterize how different chemical and genetic factors affect nuclear morphology and architecture in mid-M delays.
2. To evaluate the possible consequences of such mitotic delays on nuclear morphology and genome stability upon cell cycle reentry.
3. To study the possible role of autophagy in the correction of nuclear membrane imbalances caused by mitotic delays.
4. To evaluate the effect of toxic compounds from CEAMED S.A. in nuclear shape and chromosome segregation.

A watercolor illustration of a tree with a blue trunk and red foliage. The trunk is a thick, textured blue line that curves from the bottom left towards the top right. The foliage consists of several large, textured red shapes that resemble flowers or leaves. A thin green line is drawn around the bottom of the foliage. The background is white with some faint grey brushstrokes.

3. MATERIAL AND METHODS

3.1. Strains

Yeast strains used in this work are listed below on **Table 3.1**. The genetic backgrounds of these cells are W303 (Thomas & Rothstein, 1989), YJM789 (Wei et al., 2007) and YPH499, derived from the S288C background (Sikorski & Hieter, 1989).

Table 3.1. List of strains used in this work.

Strain	Relevant genotype	Origin
AS499 (YPH499)	<i>MATa ura3-52 lys2-801 ade2-101 trp1-Δ63 his3-Δ200 leu2-Δ1 bar1-Δ</i>	A. Strunnikov
W303	<i>MATa leu2-3,112 trp1-1 can1-100 ura3-1 ade2-1 his3-11,15</i>	R. Rothstein
CCG771	[AS499] <i>NET1-GFP::LEU2</i>	CCG ^a
CCG1326	[AS499] <i>TetR-YFP::ADE2 tetO(5.6Kb)::194Kb-ChrXII::HIS3 NET1-CFP::KanMX4</i>	CCG ^a
CCG1327	[AS499] <i>TetR-YFP::ADE2 tetO(5.6Kb)::450Kb-ChrXII::URA3 NET1-CFP::KanMX4</i>	CCG ^a
CCG1328	[AS499] <i>TetR-YFP::ADE2 tetO(5.6Kb)::487Kb-ChrXII::HIS3 NET1-CFP::KanMX4</i>	CCG ^a
CCG1329	[AS499] <i>TetR-YFP::ADE2 tetO(5.6Kb)::1061Kb-ChrXII::HIS3 NET1-CFP::KanMX4</i>	CCG ^a
CCG1582	[AS499] <i>NET1-CFP::HygB NUP49-GFP::URA3</i>	CCG ^a
FM2010-2012	<i>Mata/α ade2-1/ade2-1 can1-100/Δcan1::SUP4-o his3-11,15/HIS3 ura3-1/ura3-1 trp1-1/TRP1 V9229::HYG/V V261553::LEU2/V</i>	Our lab ^b
FM2013-2015	<i>Mata/α leu2-1,112/LEU2 his3-11,15/HIS3 ura3-1/ura3-1 ade2-1/ade2-1 trp1-1/TRP1 Δcan1::NAT/Δcan1::NAT IV1510386::KANMX::can1-100/IV1510386::SUP4-o</i>	Our lab ^b
FM2396	[W303] <i>ADH1-OsTIR1-9Myc::URA3 NET1-GFP::LEU2 cdc16-aid*-9myc::hphNT</i>	Our lab
FM2614	[W303] <i>HTA2-mCherry::URA3 NET1-GFP::LEU2</i>	Our lab
FM2637	[W303] <i>ura3-1::ADH1-OsTIR1-9Myc::URA3 SEC61-ECFP::kanMX4 NET1-mCherry::natNT2 trp1-1::P_{ADH1}-IAA17-EGFP-NLS::TRP1</i>	Our lab
FM2639	[W303] <i>ura3-1::ADH1-OsTIR1-9Myc::URA3 SEC61-ECFP::kanMX4 NET1-mCherry::natNT2 trp1-1::P_{ADH1}-EGFP-IAA17-NLS::TRP1</i>	Our lab
FM2658	[AS499] <i>TetR-YFP::ADE2 tetO(5.6Kb)::450Kb-ChrXII::URA3 tetO(5.6Kb)::1061Kb-ChrXII::HIS3 SEC61-ECFP::kanMX4 NET1-mCherry::natNT2</i>	Our lab

3. Material and methods

FM2676	[AS499] TetR-YFP::ADE2 tetO(5.6Kb)::1061Kb-ChrXII::HIS3 cdc15-2::9Myc::HphNT1 ADH1-OsTIR1-9Myc::URA3 SPC42-mCherry::natNT2	Our lab
FM2707	[AS499] TetR-YFP::ADE2 tetO(5.6Kb)::1061Kb-ChrXII::HIS3 cdc15-2::9Myc::HphNT1 ADH1-OsTIR1-9Myc::URA3 HTA2-mCherry::natNT2 NET1-ECFP::kITRP1	Our lab
FM2732	[AS499] pep4::HIS3 GFP-TUB1::URA3 cdc15-2::9myc::HphNT1 SPC42-mCherry::natNT2	Our lab
FM2735	[FM2707] cdc16-aid*-9myc::KanMX	Our lab
FM2748	[FM2707] nem1-aid*-9myc::KanMX	Our lab
FM2795	[AS499] pep4::HIS3 GFP-TUB1::URA3 cdc15-2::9myc::HphNT1 P _{PGK1} -mRuby2-3xNLS-T _{ADH1} ::LEU2 NET1-ECFP::kITRP1	Our lab
FM2799	[W303] HTA2-mCherry::URA3 NET1-ECFP::kITRP1 SEC61-EYFP::kanMX4	Our lab
FM2829	[W303] HTA2-mCherry::URA3 NET1-ECFP::KanMX4 GFP-ATG8::TRP1	Our lab
FM2965	[W303] HTA2-mCherry::URA3 NET1-ECFP::KanMX4 VPH1-GFP::HIS3	Our lab

a. Strains courtesy of Dr. Luis Aragón (MRC, London, UK). b. Haploid strains used to create the diploid courtesy of Dr. Thomas Petes (Duke University, NC, USA).

3.2. Culture conditions

3.2.1. Bacteria culture conditions

Bacterial strains DH5 α and XL1-Blue were routinely used for cloning purposes or to amplify preexisting plasmids. To prepare competent cells and to amplify plasmid DNA, bacteria were grown in LB media at 37°C with moderate shaking (150 – 200 rpm).

3.2.2. Yeast culture conditions

Strain stocks were kept at -80°C in YPD + 20% glycerol in cryogenic tubes. When needed, they were grown for 2 – 3 days on YPDA plates at 25°C, due to the presence of thermosensitive alleles such as *cdc15-2*, allowing ~ 32 – 48 cell divisions. The colonies obtained were used to inoculate liquid cultures. That is, cells were grown overnight in liquid YPD at 25°C in an orbital shaker incubator at 150 – 200 rpm before every experiment, unless stated otherwise. Adenine was added to the media at 75 μ g/mL if they were aimed for microscopy experiments to avoid autofluorescence due to accumulation of colored metabolic intermediates of the adenine synthesis pathway, as some strains used were *ade2*. Also, for some conditional depletion experiments, cells were grown overnight in the presence of IAA 5 mM.

The day after, exponentially growing cells were adjusted to an OD₆₀₀ between 0.4 – 0.7 to perform the experiment. If the culture had an OD₆₀₀ slightly over 1, it was adjusted to 0.4 diluting in fresh media and grown in the orbital shaker for 1h before starting the experiment. In the case of nocodazole (Nz) arrest experiments aimed to study the rDNA loop, cultures were not diluted in fresh media, and they were grown to late exponential phase to favor loop formation.

Auxin-mediated protein degradation

We routinely used conditional depletion of proteins within different experiments to assess the effect of their absence in certain situations. The chosen method is based on proteasomal degradation of AID-tagged proteins mediated by the auxin-binding receptor (TIR1) when the plant hormone auxin (indole-3-acetic acid, IAA) is present in the media (Morawska & Ulrich, 2013). A concentration of 5 mM was used between 1 – 3 h, and its efficiency was examined by microscopy, Western blot and/or spot assays.

Synchronization procedures

For most experiments, synchronization of the cell population at different stages of the cell cycle was required. This was generally achieved after a 3h incubation under the effect of a specific drug or temperature (in the case of *ts* alleles) once the optical density of the culture was adjusted as described above (**Fig. 3.1**).

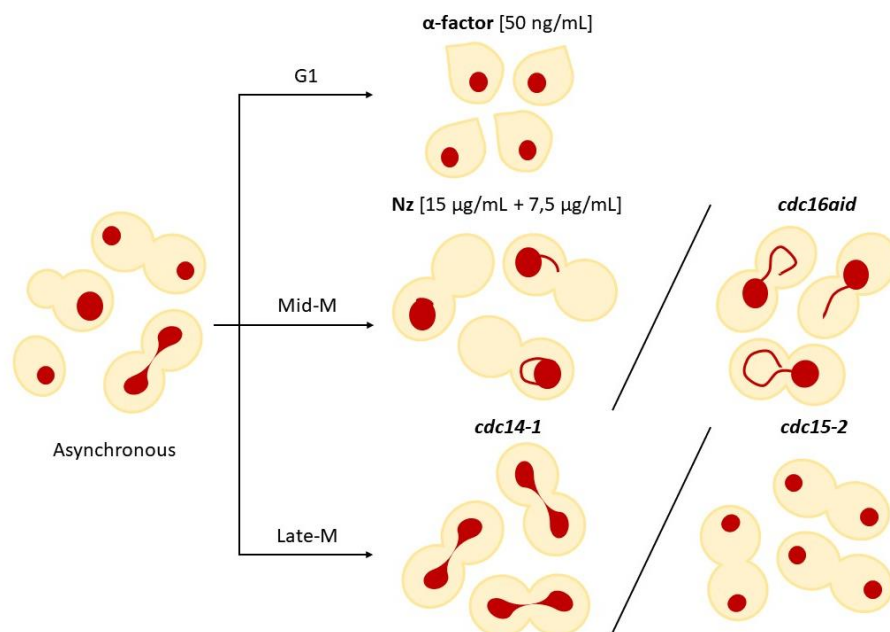


Figure 3.1. Cell synchronization procedures used in this work. Cell boundaries and nucleoplasm are depicted in yellow while nuclei are indicated in red. To synchronize in G1, the

3. Material and methods

pheromone α -factor was used at 50 ng/mL. For mid-M blocks, two approaches were used: the microtubule depolymerizing drug nocodazole or the inducible mutant of the APC *cdc16aid*. For late mitosis arrests, the ts alleles *cdc14-1* or *cdc15-2* were used. All these procedures were maintained for 3 h to achieve full synchronization of cultures. Note how different procedures render different nuclear morphologies among cell cycle blocks.

Asynchronous cultures were blocked in G1 by adding 50 ng/mL of the pheromone α -factor to the medium and a following incubation of 3h, since all yeast strains used in this work belong to the sexual type MATa. As the Bar1 protease cleaves α -factor in the extracellular space, thus inactivating it, (Sprague et al., 1983), all strains used carried *BARI* deletions, so that small amounts of pheromone are required for an efficient treatment. When cells were required to resume cycling after synchronization, the culture was spun down and resuspended in fresh media containing 0.1 mg/mL of pronase E (mixture of proteolytic enzymes obtained from *Streptomyces griseus* used to hydrolyze proteins into individual amino acids) to wash and degrade the remaining α -factor.

Mid-M or G2/M arrests were achieved through different methods. Mostly, the microtubule depolymerizing drug nocodazole (Nz) was used for this purpose, allowing DNA replication but not segregation. It was added to asynchronous cultures at a concentration of 15 μ g/mL followed by a 2h incubation, and then supplemented again with 7.5 μ g/mL to maintain the arrest, followed by a 1h incubation before cell cycle block completion. When cells were required to resume cycling after synchronization, the culture was spun down and resuspended in fresh media, because when Nz is no longer present, cells are able to start segregation. In some experiments, we depleted an essential component of the anaphase promoting complex (APC) through the conditional allele *cdc16-aid*. To achieve mid-M arrests in *cdc16-aid* strains, we added IAA 5 mM to the culture and incubated for 3h.

Late anaphase or telophase blocks were accomplished by 3h incubations at restrictive temperature (34 – 37°C) of strains bearing the ts alleles *cdc14-1* or *cdc15-2* respectively. Cdc14 phosphatase is involved in FEAR and MEN networks, while Cdc15 kinase exerts its role in MEN. Therefore, inactivating each of these proteins cause a cell cycle block before cytokinesis.

Occasionally, the experimental design required the use of drugs with different purposes, either alone or combined with the aforementioned synchronization procedures. A list of those drugs and their concentration is shown below (**Table 3.2**).

Table 3.2. Stock and usage concentrations of drugs used in this work.

<i>Drug</i>	<i>Stock concentration</i>	<i>Working concentration</i>
α-factor	5 mg/mL in H ₂ O	50 ng/mL
Cerulenin	5 mg/mL in EtOH	2 μ g/mL
IAA	500 mM in DMSO	5 mM
Nocodazole	1.5 mg/mL in DMSO	15 μ g/mL
Pronase E	10 mg/mL in H ₂ O	100 μ g/mL
Rapamycin	2.2 mM in DMSO	200 nM

Clonogenic assays

To assess the survival rate of a population under certain circumstances, we used clonogenic assays, plating a known number of cells after specific treatments and comparing the amount of CFUs grown vs an untreated control. We routinely diluted cells 1:1,000 or 1:2,000, then 100 μ L from that dilution were spread onto YPDA plates and incubated at 25°C for 2 – 4 days until colonies were easily visible.

Cell viability assessment

Spot dilution assays were used to evaluate the effect of certain chemicals on yeast populations. Yeast cultures optical density was adjusted to 0.5 and then serially diluted 5 times in 10-fold steps on YPD in a 96 well plate. Then, a microplate replicator was used to apply the drops onto a Petri dish containing media plus the chemical product to test (usually IAA), and then they were incubated at 25°C for 3 – 4 days.

Growth curves

To assess the growth dynamics of WT and mutant strains exposed to IAA at different concentrations we used the microplate reader TECAN Spark®. This machine recorded the OD₆₀₀ of individual wells of a 96-well plate incubated at 96 rpm at room temperature for 24 h, measuring every 15 min.

3.3. Transformation procedures

3.3.1. Transformation of *Escherichia coli*

A standard protocol (Seidman, C.E., Struhl, K., Sheen, J., and Jessen, 1997), with slight modifications, was used to transform *E. coli* and thus to amplify plasmid DNA.

First, competent cells were prepared as follows. A single colony was inoculated in liquid LB medium and incubated at 37°C with moderate shaking until cells reached stationary phase. After this, they were diluted 1:400 and grown until they reached an $OD_{590} = 0.375$ (early or mid-log phase). Cells were aliquoted into eight 50 mL prechilled tubes and incubated on ice for 5 – 10 min. In all subsequent steps, cells were kept cold by incubating them on ice or performing centrifugation steps at 4°C. Next, they were centrifuged at 1,600 g for 7 minutes, the pellet was resuspended in 10 mL of ice-cold $CaCl_2$ solution and centrifuged at 1,100 g for 5 minutes. The pellet was resuspended again in 10 mL of ice-cold $CaCl_2$ solution and incubated on ice for 30 minutes. Finally, cells were centrifuged again at 1,100 g for 5 minutes, the pellet was resuspended in 2 mL of ice-cold $CaCl_2$ solution and then aliquoted and stored at -80°C until needed.

For bacterial transformation, 50 μ L of competent cells were mixed with 1 – 5 μ L of plasmid DNA from a miniprep, a midiprep (diluted 1:100) or a MoClo reaction. Then, the mixture was incubated on ice for 30 minutes and subjected to heat shock in a water bath at 42°C for 45 seconds. After that, cells were shortly incubated on ice again for 2 minutes before adding 950 μ L of prewarmed LB medium. Cells were incubated for 1 hour 30 minutes at 37°C with mild shaking before plating on selective medium (LB + selection antibiotic). Concentrations of all antibiotics used for selection are listed below (**Table 3.3**).

Table 3.3. Stock and usage concentrations of antibiotics used for bacteria selection.

<i>Antibiotic</i>	<i>Stock concentration</i>	<i>Final Concentration</i>
Ampicillin (Amp)	50 mg/mL	100 μ g/mL
Kanamycin (Kan)	50 mg/mL	50 μ g/mL
Chloramphenicol (Cm)	25 mg/mL	25 μ g/mL

3.3.2. Transformation of *Saccharomyces cerevisiae*

Yeast strains created in this work were made following an adapted version from the original published by (Janke et al., 2004; Knop et al., 1999). Thus, many yeast constructs relied on the preparation of PCR-based transformation products, which are introduced into the cell by lithium acetate transformation.

To prepare competent cells, a single yeast colony was grown overnight in 40 mL of YPD until an OD₆₀₀ of 0.7 - 1. Then, cells were harvested by centrifugation at room temperature and washed, first with 25 mL of sterile distilled water and then with 1 mL of SORB. Finally, cells were resuspended in 350 µL of SORB + 50 µL of carrier DNA (sonicated and denatured herring or salmon sperm). These stocks were stored at -80°C until needed.

The transformation procedure starts by thawing yeast stocks on ice, and then mixing 27 µL of competent cells with 3 µL of DNA obtained from a PCR, an enzymatic digestion, or a plasmid DNA preparation. Then, 180 µL of PEG solution were added before a 30 min incubation at room temperature. After that, 33.3 µL of DMSO were added prior the heat shock step in a water bath at 42°C for 15 min. Next, cells were harvested by centrifugation at 2,000 rpm for 3 min and treated as follows, regarding the selection process required:

- **Auxotrophic markers:** the pellet was resuspended in 150 µL of distilled milli-Q water and then plated on the corresponding minimum media, which consisted of Synthetic Complete (SC) medium lacking particular amino acids or nucleotides. The media is made from Yeast Nitrogen Base (YNB), glucose at 2% (w/v) and a dropout of amino acids and nucleotides.
- **Antibiotic-resistance markers:** the pellet was resuspended in 150 µL of YPD and incubated at 25°C for 3h before plating, to allow cells to express the resistance gene product before exposing cells to the antibiotic on the selection plate, which consisted of YPDA + the selection antibiotic. Concentrations used for each drug are listed below on **Table 3.4**.

Table 3.4. Stock and usage concentrations of antibiotics used for yeast selection.

<i>Antibiotic</i>	<i>Stock concentration</i>	<i>Final Concentration</i>
Geneticin (G-418)	50 mg/mL	300 µg/mL
Hygromycin B (Hph)	50 mg/mL	300 µg/mL
Nourseothricin (Nat)	200 mg/mL	100 µg/mL

3.4. Plasmid construction using Modular Cloning (MoClo)

To create new complex constructs to be expressed in yeast, we used the Modular Cloning (MoClo) hierarchical strategy designed for *S. cerevisiae* (M. E. Lee et al., 2015). In this hierarchy, modules are categorized according to their function – such as promoters, CDS, tags, terminators, etc – and can be interchanged with other of the same type while maintaining the transcriptional unit structure (**Fig. 3.2**).

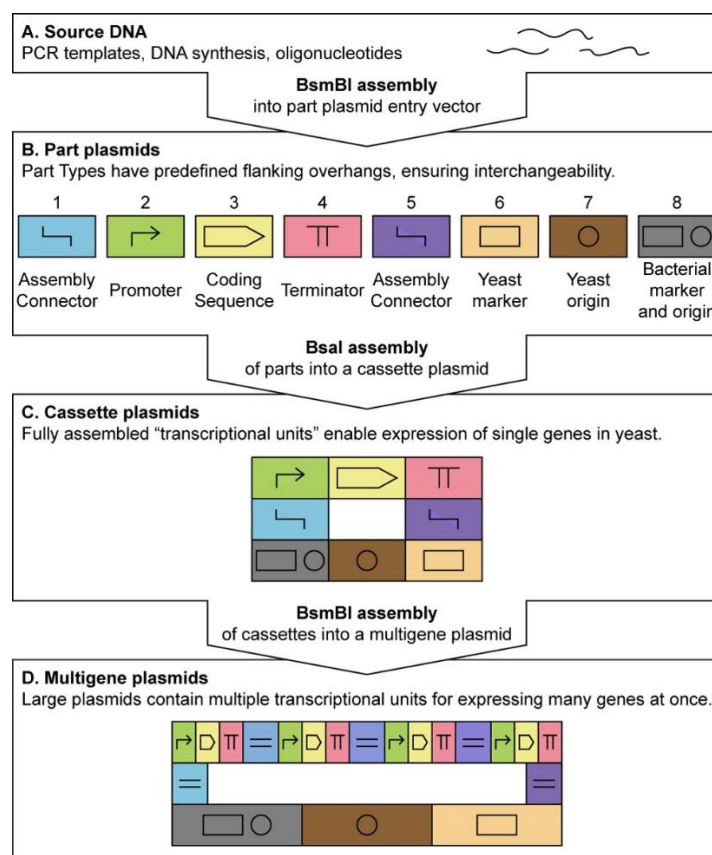


Figure 3.2. Hierarchy of MoClo assembly designed for yeast. Taken from M. E. Lee et al., 2015.

This approach is based on Golden Gate assembly, an efficient way to assemble multiple DNA sequences (called modules or parts in Synthetic Biology) into a plasmid in a single reaction (Engler et al., 2008, 2009). The method relies on Type II restriction enzymes (in this work we used BsaI-HF®v2 and BsmBI from NEB), which cut DNA outside of their recognition sequences, creating specific overhangs that allow simultaneous and directional assembly of the desired DNA fragments by a DNA ligase (in this work we used the T4 DNA ligase from Promega).

The website <https://spleonard1.shinyapps.io/paRting/> was used for primer design to amplify parts with the desired tails, adding the appropriate restriction enzyme target sequences and the bases that will constitute the desired overhang to achieve directional assembly, through PCR from yeast gDNA or other plasmids as templates. This hierarchical process can be divided into the following steps. First, the creation of dsDNA encoding the part for cloning. This was achieved by PCR, adding the appropriate flanking region (specific to the type of module) by using tailed oligos or by ordering synthetic dsDNA with the desired sequence ready for cloning. These sequences can be inserted into a part plasmid entry vector, to be further amplified in bacteria and stored as bacteria DNA preps. Then, the assembly of first-stage plasmids which contain one transcriptional unit. We created the vector pSS2, designed to be integrated in the yeast HO locus, using LEU2 as selection marker for yeast and KanR for bacteria (**Fig. 3.3**). This vector contains a GFP stuffer sequence to be replaced with parts corresponding to promoters, CDS, tags and terminators, simplifying following cloning reactions by diminishing the number of modules to assemble at once.

3. Material and methods

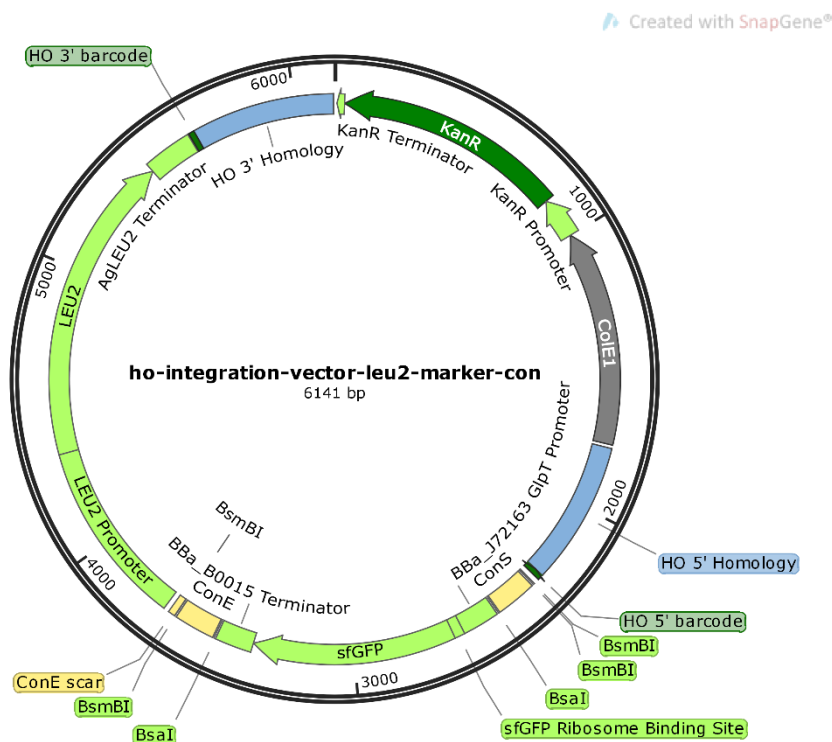


Figure 3.3. Assembly vector designed for integration in the HO locus in yeast.

The Golden Gate Assembly Wizard from the website <https://www.benchling.com/> was used to verify *in silico* assembly and correct design before ordering oligos and synthetic dsDNA from Thermo Fisher Scientific as GeneArt Strings. Reactions were prepared (**Table 3.5**) and incubated (**Table 3.6**) in a thermal cycler as follows, alternating between temperatures which allow cut and ligation processes.

Table 3.5. MoClo reaction setup for BsaI-HF®v2.

<i>Reagent</i>	<i>Amount</i>
dsDNA parts	1 µL of each part
10x T4 DNA ligase buffer (Promega)	2 µL
T4 DNA ligase (Promega)	1 µL
BsaI-HF®v2 (NEB)	1 µL
Milli-Q water	Up to 20 µL total

Table 3.6. MoClo thermal cycler program for Bsal-HF®v2.

Step	Temperature	Time
1	37°C	1.5 min
2	16°C	3 min
Cycles 1-2	Repeat 25x	
3	37°C	5 min
4	80°C	10 min

Once the assembly reaction was finished, 2 – 5 μ L were used to transform competent *E. coli* as described above. A first screening was done visually by discarding green colonies on the plate (as they still harbor plasmids containing the GFP stuffer), indicating an improper assembly or uncut pSS2. Plasmid minipreps were prepared from WT colored colonies to survey accurate constructions through diagnostic restriction digestion with different enzymes, comparing with predictions obtained using SnapGene® or Benchling. Plasmids were linearized by NotI digestion, which also eliminates bacteria replication origin and selection marker, and then transformed in yeast as explained above, allowing the integration into the yeast genome in a stable manner.

For this work, we created a plasmid which contains a construct that consists of *P_{PGKI}-mRuby2-3xNLS-T_{ADHI}::LEU2* integrated in the HO locus (strain FM2795) to allow nucleoplasm visualization.

3.5. DNA preparations

3.5.1. Plasmid DNA preparation from *E. coli*

Plasmid DNA extraction from *E. coli* was performed i) to obtain the amplified plasmid after bacterial transformation or ii) to check transformants carrying the appropriate plasmid ligation product after MoClo.

According to these purposes, different commercial kits were used. For i), a plasmid DNA mid-scale preparation was performed using the PureYield™ Plasmid Midiprep System (Promega), while in case ii) the kit PureYield™ Plasmid Miniprep System (Promega) was used instead, always following manufacturer's instructions.

3. Material and methods

These DNA preparations were subjected to a conventional agarose gel electrophoresis. In the case ii), restriction enzyme digestions were also needed to analyze the band pattern obtained compared to the expected regarding the sequence predicted using Benchling and SnapGene® software.

3.5.2. Genomic DNA preparation from *S. cerevisiae*

Genomic DNA from yeast was obtained from liquid cultures or colonies grown on solid media, either to screen positive clones after yeast transformation or to obtain templates for PCR.

In the first case, 1 mL of culture was harvested and resuspended in 200 µL of breaking buffer, while yeasts from plates were directly resuspended in the same amount of buffer. Next, 200 µL of ice-cold phenol:chloroform:isoamyl alcohol (25:24:1) and ~ 200 mg of glass beads were added, and the mix was vortexed for 2 min 30 s to break cells mechanically. To separate the organic and aqueous layers, 200 µL of 1x TE buffer were added and then centrifuged at 13,000 rpm for 5 min. The top aqueous layer (~ 300 µL) containing the DNA was transferred to a new Eppendorf tube and precipitated by adding 1 mL of ice-cold 95% ethanol, letting stand for 10 minutes. Next, the sample was centrifuged at maximum speed for 2 minutes, the pellet was air dried or dried in a vacuum concentrator and finally resuspended in 50 µL of 1x TE buffer. Samples were stored at -20°C until use.

3.5.3. High molecular weight DNA preparation

To preserve the integrity of large DNA molecules, such as whole yeast chromosomes, we used a specific protocol to prepare samples for PFGE.

Before DNA extraction, we embedded cells taken from liquid cultures in low melting point agarose (LMPA) as follows. First, a sample of 4 mL was washed twice with ice-cold 50 mM EDTA, then the pellet was resuspended in 10 µL of ice-cold 50 mM EDTA. After that, we added 20 µL of Solution I (containing zymolyase to digest cell walls) and then 60 µL of pre-heated LMPA (kept at 50°C). Swiftly, the mix was transferred into plug molds placed on ice, and let polymerize for 10 min.

Once all the plugs were ready, they were transferred to 2 mL tubes filled with Solution II (containing RNaseA) and incubated overnight at 37°C to allow enzyme digestion. The day after, Solution II was removed and replaced with Solution III

(containing proteinase K), followed by another overnight incubation at the same temperature. Next day, Solution III was removed, and plugs were washed twice with 1x TE buffer for 1 h each, keeping the tubes on ice. Finally, TE was replaced with storage solution and DNA preparations were kept at -20°C until use.

3.6. Polymerase Chain Reaction (PCR)

Amplifications of DNA were done following enzymes manufacturer's instructions, using a T100™ Thermal Cycle (Bio-Rad). To check transformants, the PCR BIO Taq Mix (PCR Biosystems) was mainly used, while the PCR BIO HiFi polymerase (PCR Biosystems) was used to create amplified DNA products aimed for transformations, either from plasmids or genomic DNA. For amplifications longer than 5 kb, PCR BIO Ultra Mix (PCR Biosystems) was used instead. The table below contains the list of primers used during this work (**Table 3.7**).

Table 3.7. List of primers used in this work.

<i>Primer name</i>	<i>Purpose</i>	<i>Sequence (5' → 3')</i>
CDC15-S3	C-terminal tagging Cdc15	AAGTGACGGCTTTTCCGTCCCCATTACAACATTTCA AAACACGTACGCTGCAGGTCGAC
CDC15-S2	C-terminal tagging Cdc15	TATTCTCTATATATGTATGTATGCACATGCAATTCC TACAATCGATGAATTCGAGCTCG
CDC15-F (-132)	Verify integration of tagged Cdc15	AAAGGCTTGGCGCATTATCG
CDC15-R (+3023)	Verify integration of tagged Cdc15	CGGAAGACTGTGCCACTGC
CDC16-S3	C-terminal tagging Cdc16	TAATGCCGACGATGATTTTGACGCAGATATGGAAC TGGAACGTACGCTGCAGGTCGAC
CDC16-S2	C-terminal tagging Cdc16	CTAAGTCGTGTCTTTATTCTCGCCCCGCTTCGTA CTTTAATCGATGAATTCGAGCTCG
CDC16 C' tag CHK F	Verify integration of tagged Cdc16	ATGTTTTAGATGCGTTTTGG
HO 5' forward	Verify integration of MoClo constructs at HO locus	CACATCATTTTCGTGGATCC
HO 5' reverse	Verify integration of MoClo constructs at HO locus	ACAGCGATGGAAGTACGGC
HO 3' forward	Verify integration of MoClo constructs at HO locus	TATCGTGTTCATCTGCGGC
HO 3' reverse	Verify integration of MoClo constructs at HO locus	CTTTGGACTTAAAATGGCGT
HTA2-S3	C-terminal tagging Hta2	TTGCCAAAGAAGTCTGCCAAGACTGCCAAAGCTTC TCAAGAAGTACGCTGCAGGTCGAC

3. Material and methods

HTA2-S2	C-terminal tagging Hta2	ACAAGAATGTTTGATTGCTTTGTTTCTTTTCAACT CAGTTCTTAATCGATGAATTCGAGCTCG
HTA2-F (-382)	Verify integration of tagged Hta2	GAGAACACCGCTTTATTAGG
HTA2-R (+732)	Verify integration of tagged Hta2	CATGAAAAGGATGAAAATGG
NEM1-S3	C-terminal tagging Nem1	ACTGGCATTGAAACATGGAGAGAAGGCATTCAAC ATAAACCGTACGCTGCAGGTCGAC
NEM1-S2	C-terminal tagging Nem1	AATTCTCATCTTTTTTGAAGGACACAATAACAATT GTCAATCGATGAATTCGAGCTCG
NEM1 C' tag CHK F	Verify integration of tagged Nem1	AAGAATACGCTGATCCTGTG
NET1-S2	C-terminal tagging Net1	ACTAGCTTTCTGTGACGTGTATTCTACTGAGACTT TCTGGTATCAATCGATGAATTCGAGCTCG
NET1-S3	C-terminal tagging Net1	CCAAGTGGTGGATTTGCATCATTAAATAAAGATTT CAAGAAAAACGTACGCTGCAGGTCGAC
NET1 5'UTR CHK F	Verify integration of tagged Net1	TGTTTGTAGACGAGGGAAAG
SEC61-S3	C-terminal tagging Sec61	GTTTACTAAGAACCTCGTTCCAGGATTTTCTGATTT GATGCGTACGCTGCAGGTCGAC
SEC61-S2	C-terminal tagging Sec61	ATTTTTTTTTCTTTGGATATTATTTTCATTTTATATT CAATCGATGAATTCGAGCTCG
SEC61 C' tag CHK F	Verify integration of tagged Sec61	AAGCTCTTCTGGACCCTATC
SPC42-S2	C-terminal tagging Spc42	AGAACGCTTTAAGAATGCGCCATACTCCTTAAC TG CTTTTTAAATCATCAATCGATGAATTCGAGCTCG
SPC42-S3	C-terminal tagging Spc42	CTGAAAATAATATGTCAGAAACATTCGCAACTCCC ACTCCAATAATCGACGTACGCTGCAGGTCGAC
SPC42-F (+770)	Verify integration of tagged Spc42	AGCTGAAGCGTGTGCGAAGAA
SPC42-R (+1530)	Verify integration of tagged Spc42	ACTTAGATGAAAGTTGTTGGT
Vph1-F (-673)	Amplify Vph1-GFP	TCTCGGTGTGCAAACCTTTGG
Vph1-R (+2767)	Amplify Vph1-GFP	CCCCAAGGCAAATGATGGTC

*The number in brackets corresponds to the 5' nucleotide position relative to the ATG start codon of the gene. That is, negative values for upstream nucleotides and positive for downstream. F: Forward. R: Reverse. S3 and S2: Forward and reverse in Janke's tagging and deletion system respectively. (Janke et al., 2004).

3.7. DNA electrophoresis

3.7.1. Conventional agarose gel electrophoresis

Agarose gel electrophoresis was routinely used to i) verify DNA amplification through PCR, ii) check transformant colonies and iii) confirm restriction enzyme digestion patterns.

Most electrophoreses were done using agarose at a final concentration of 1% (w/v) dissolved in 1x TBE buffer, using 0.5x TBE as running buffer. To separate small fragments from enzyme digestions, agarose concentration in the gel could be as high as 3%. Running conditions were approximately 90 V for 1 hour. Before loading, 5 μ L of the sample were mixed with 1 μ L of EZ-Vision® One DNA stain loading dye (Amresco), allowing us to visualize the bands directly after running under UV light on a Gel Doc system (Bio-Rad). The GeneRuler 1 kb DNA Ladder (ThermoFisher Scientific), peqGOLD 1 kb DNA Ladder (VWR) and peqGOLD 50 bp DNA Ladder (VWR) were employed as molecular weight markers depending on fragment size.

3.7.2. Pulsed-Field Gel Electrophoresis (PFGE)

To visualize whole chromosome integrity, we ran PFGE on a CHEF-DR III System (Bio-Rad). Gels were prepared at 1% (w/v) agarose in 0.5x TBE buffer, then loaded with 1/3 of a DNA plug and then ran in 0.5x TBE buffer at 12°C according to the parameters shown in **Table 3.8** to maximize cXII resolution.

Table 3.8. Running conditions for PFGE used in this work.

<i>Parameter</i>	<i>Settings used</i>
Voltage	3 V/cm
Switching time	300 – 900 s
Angle	120°
Running time	68 h

After the run, gels were stained with a 0.5 μ g/mL ethidium bromide solution in milli-Q water for 40 min and de-stained for 20 min in milli-Q water to visualize DNA bands under UV light using a Gel Doc system (Bio-Rad).

3.8. Western blot

In this thesis, Western blot analysis was used to assess the presence and expression level of certain proteins, detect post-translational modifications such as phosphorylation and to verify auxin-mediated protein degradation.

3. Material and methods

3.8.1. Protein extraction

The trichloroacetic acid (TCA) method was used to extract whole-cell proteins from yeast samples, as it conserves post-translational modifications. First, samples of 5 mL of liquid cultures were taken and centrifuged for 3 minutes at 3,000 rpm. The pellet was resuspended in 1 mL of TCA 20% and transferred to a 2 mL tube, which was centrifuged for 1 minute at maximum speed. Next, the pellet was resuspended in 100 μ L of TCA 20% and ~ 200 mg of glass beads were added before vortexing for 5 minutes. We added 200 μ L of TCA 5% and vortexed again before transferring the top 200 μ L of the suspension to a new Eppendorf tube, which were centrifuged for 10 minutes at 3,000 rpm. The supernatant was removed with a vacuum pump and the pellet was resuspended in 100 μ L of a mix consisting of Laemmli Sample Buffer (Bio-Rad) 1x + Tris-HCl pH 8 + β -mercaptoethanol 2.5% before being boiled at 95°C for 5 minutes. Finally, samples were centrifuged for 10 minutes at 3,000 rpm before quantification.

A Qubit 4 Fluorometer (ThermoFisher Scientific) was used to quantify proteins before normalization to have 20 – 30 μ g in ~ 20 μ L to load onto each well of the gel.

3.8.2. SDS-PAGE

Samples were subjected to one-dimension polyacrylamide gel electrophoresis under denaturing conditions (SDS-PAGE) in 7.5% acrylamide/bisacrylamide 37.5:1 (Bio-Rad) separating gels, while the stacking gels were prepared at 4%.

We used the mini-PROTEAN® Tetra Cell system from Bio-Rad. To remove undesired fragments from the polymerization remaining in the wells, gels were subjected to a pulse of 160 V for 12 minutes before sample loading. Running conditions included a gradual increase in voltage as follows: 20 min at 90 V, then 1 h at 120 V and finally 150 V until the end of the electrophoresis. The molecular weight marker used was Precision Plus Protein™ Dual Color (Bio-Rad).

3.8.3. Protein transfer and immunodetection

Gels were equilibrated in cold transfer buffer for 30 min, while Immobilon-FL PVDF membranes (Merck Millipore) were activated by soaking in methanol for 20 s. Then, membranes were rinsed in milli-Q water for 5 min and incubated in cold transfer buffer up to 30 min. Afterwards, transfer was setup in a Mini Trans-blot® Cell (Bio-Rad) in transfer buffer with 20% methanol and ran at 30 V overnight at 4°C.

Membranes were first rinsed in water and then stained with Ponceau S Solution BC (Panreac) for 5 minutes to verify proper protein transfer and sample standardization. Then, membranes were rinsed to remove staining, activated again as described above and blocked by incubating them in TBST + 5% skimmed milk + 0.1% NaAz for 1 h at 4°C. This solution was substituted by a mix of the primary antibody diluted in blocking solution, followed by an overnight incubation at 4°C.

The following day, membranes were washed 3 times in TBST for 10 min each. Then, they were incubated in a solution of TBST + 5% skimmed milk + the appropriate secondary antibody for 1 h at room temperature. The 3 washing steps were repeated, and the membranes were covered in ECL Prime Western Blotting Detection Reagent (Amersham) to be further developed in a Fusion Solo S Documentation Chamber (Vilber Lourmat). Quantifications were performed with the Bio1-D Software when needed. Antibodies used in this work are listed below in **Table 3.9**.

Table 3.9. List of antibodies used in this work.

<i>Antibody</i>	<i>Working dilution</i>	<i>Host</i>	<i>Reference</i>
α-c-Myc (clone 9E10)	1:500	Mouse	Sigma-Aldrich (M4439)
α-Rad53 (clone EL7.E1)	1:500	Mouse	Abcam (ab166859)
α-mini-AID-tag (clone 1E4)	1:500	Mouse	MBL Life Sciences (M214-3)
α-GFP	1:5,000	Rabbit	Abcam (ab6556)
α-Mouse IgG (H+L) (HRP conjugated)	1:5,000	Goat	Promega (W4021)
α-Rabbit IgG (H+L) (HRP conjugated)	1:10,000	Goat	Abcam (ab97051)

3.9. Microscopy

Most of the work hereby presented was carried out using live cell imaging of yeast as the main technique, thanks to the versatility offered by the use of double and triple tagging with fluorescent proteins.

Yeast attachment and fixation

To create 3D cellular models on a super-resolution microscope and a few other experiments, cells needed to be fixed as follows. First, 1/10th of 37% formaldehyde was added to an aliquot taken from a yeast culture. Then, it was incubated in a nutating mixer at room temperature for 15 – 30 min and spun down at 10,000 rpm for 30 s. The pellet was washed in 500 μ L of filtered PBS 1x and then resuspended in another 500 μ L of PBS 1x. Finally, suspensions were stored at 4°C for a week at most, until micrographs were taken. Right before use, suspensions were sonicated for 8 s in a bath sonicator to separate cells adhered to each other.

For long time lapse microscopy films, living yeast cells needed to be immobilized. We used the lectin-binding protein concanavalin A (ConA) as an adhesive on Nunc Lab-Tek chambered slides of 8 wells. First, 50 μ L of ConA from a 1 mg/mL stock in PBS (pH = 7.4) were applied to a well and it was kept in the dark at 25°C for 20 – 30 min. Then, it was removed and washed twice with 50 μ L of SC media. After, 500 μ L were taken from an overnight grown yeast culture in exponential phase, spun down at 2,500 rpm for 2 min and resuspended in 250 μ L of SC complete to concentrate it. 100 μ L of the suspension were applied to the well and kept at room temperature for 20 min to allow cell adhesion. Non-attached cells were washed twice with 100 μ L of SC media and finally they were covered with 250 μ L of YPDade + Nz at a final concentration of 22.5 μ g/mL to start live cell imaging. The higher concentration of Nz used in these experiments is actually equal to the initial plus the reinforcement doses applied in liquid cultures growing in an air incubator. We do this to avoid detachment of the cells by applying liquid in the middle of the experiment. Immobilized cells were photographed continuously or every 5 – 15 min for 3 h (unless stated otherwise) in single slices, or z-stacks when photobleaching and/or phototoxicity of our proteins of choice allowed it.

3.9.1. Wide-Field Microscopy (WFM)

A Leica DMI6000B epifluorescence microscope (Leica) was used, equipped with an ultrasensitive DFC350 digital camera and employing a 63x/1.30 immersion objective in combination with immersion oil (UV-transparent, fluorescence-free) with a refractive index of 1.515 – 1.517 (Fluka). Filter cubes used are listed below (**Table 3.10**).

Table 3.10. List of filter cubes used within the Leica DMI600B microscope.

<i>Fluorochrome</i>	<i>Filter cube</i>	<i>Excitation range</i>	<i>Excitation filter</i>	<i>Dichroic mirror</i>	<i>Suppression filter</i>
mCherry, mRuby2	RFP	Green	BP 546/12	560	BP 605/75
(E)YFP, (E)GFP cDCFDA	YFP	Blue	BP 500/20	515	BP 535/30
(E)CFP MDY-64, Blue CMAC	CFP	Violet-blue	BP 436/20	455	BP 480/40
DAPI	A	UV	BP 360/40	400	BP 470/40

A Zeiss Axio Observer.Z1/7 was also used, equipped with and AxioCam 702 sCMOS camera, a 63x/1.40 immersion objective in combination with Immersol™ 518 F (Carl Zeiss) and the Colibri-7 LED excitation system. A list of the filters used together with the excitation LED is shown below (**Table 3.11**).

3. Material and methods

Table 3.11. List of filters and LED lines used within the Zeiss Axio Observer.Z1/7 microscope.

Fluorochrome	Excitation range	Reflector	Beam splitter	Filter ex. wavelength	Filter em. wavelength	Excitation LED line
mCherry	Green	110 HE	405, 493, 611, 762	375-395, 455-483, 583-600, 720-750	410-440, 501-547, 618-690, 770-800	567 nm
(E)YFP, (E)GFP cDCFDA	Blue	46 HE	515	488-512	520-550	511 nm
(E)CFP MDY-64	Violet-blue	47 HE	455	424-448	460-500	430 nm

In general, for *in vivo* fluorescence microscopy, 200 – 1,000 μ L samples were collected from cultures, harvested, and ~ 1.5 μ L of the pellet were spread on microscopy slides. Sometimes, staining was required before visualization. When vacuolar stains were used, a wash in YPD (PBS 1x if fixed) was done prior to sample mounting to remove the remaining stain. A list of the stains used is shown below in **Table 3.12**.

Table 3.12. List of microscopy stains used in this work.

Stain	Stock concentration	Working concentration	Incubation time
Blue CMAC	10 mM in DMSO	100 μ M	15 – 30 min
Carboxy-DCFDA	10 mM in DMSO	10 μ M	15 – 30 min
DAPI	2 μ g/mL	1 μ g/mL	1 – 2 min
MDY-64	10 mM in DMSO	10 μ M	3 – 5 min

On one hand, series of 10 – 20 z-focal planes (0.2 – 0.6 mm depth between each slice) were routinely captured and acquisition settings were optimized before the start of every experiment. On the other hand, short time-lapse movies were taken to analyze the

dynamics of certain cell components by acquiring single slices every 0.2 – 5 min for 5 to 30 min as needed.

3.9.2. Confocal Super-resolution Microscopy (CSM)


An LSM980 with an Airyscan 2 detector, paired with a Plan-Apochromat 63x/NA 1.40 Oil M27 DIC objective was used in this work. The Airyscan detector was used for the acquisition of all fluorescent signals. The resolution provided in Airyscan mode is lateral (x/y) resolution to 120 nm for 2D and 3D data sets (z-stacks) and 350-nm axial (z) resolution for z-stacks, with an improved resolution up to 1.7X compared to standard confocal (Huff, 2015). Bright field images were acquired with T-PMT detectors instead of the Airyscan. A list of the beam splitter combinations and the excitation lasers used is shown below (**Table 3.13**).

Table 3.13. List of beam splitters and lasers used within the LSM980 microscope with an Airyscan 2 detector.

<i>Fluorochrome</i>	<i>Excitation range</i>	<i>Laser wavelength</i>	<i>Excitation wavelength</i>	<i>Emission wavelength</i>	<i>Detection wavelength</i>
mCherry	Green	561 nm	587	610	574-720
(E)YFP	Blue	514 nm	508	524	420-480, 495-550
(E)GFP	Blue	488 nm	488	509	499-557, 659-720
(E)CFP/MDY-64	Violet-blue	405 nm	433	475	380-548

For 3D reconstructions ~ 45 – 50 z-planes (0.15 μm thick) were acquired. Usually, fixed cells were used for this purpose, but when fixation conditions altered fluorescence patterns, alive cells were used instead.

Images were processed using FIJI (Schindelin et al., 2012), Zeiss Zen Blue and Zeiss Zen lite 3.5 (blue edition) software. Statistical analysis and plots were done using the Prism 8 software (GraphPad). For z-stack 2D projections, the maximum intensity (for WFM) and sum intensity (for CSM) methods were used.



4. RESULTS AND DISCUSSION

4.1. Cytological characterization of metaphase cell cycle blocks with non-spherical nuclear morphologies

4.1.1. The rDNA acquires a wide range of morphologies in a metaphase block induced by microtubule depletion

As mentioned above, there are several ways to induce a mid-M cell cycle block. The first we are going to characterize in this work is triggered by microtubule depletion caused by nocodazole (Nz), mainly focusing on nuclear and nucleolar structure. In this cell cycle arrest, the rDNA acquires a wide range of morphologies, among which we found a remarkable loop that resembles the handle of a handbag, considering the bulk chromatin as the main body. This outstanding rDNA morphology has been shown before by FISH and using fluorescent tagging of proteins which bind the rDNA, such as Net1 (Guacci et al., 1994; Lavoie et al., 2002; Machín et al., 2005; Matos-Perdomo & Machín, 2018). In these conditions, the nucleus occupies a significant amount of the cell body, leaving an apparent gap or space between the handle and the chromatin mass, which we refer to as space under the loop (SUL) (**Fig. 4.1. A**). If this SUL were indeed of nuclear nature, the N/C ratio would not be maintained, so we aimed to further characterize this feature of the metaphase nucleus (Cantwell & Nurse, 2019b; Deolal & Mishra, 2021). As we show in this figure, the rDNA in 2D single slices or z-stack projections can take many shapes (**Fig. 4.1. B**). However, these morphologies are highly dynamic and interconvert from one another in short periods of time, as observed in short time-lapse microscopy. Furthermore, 3D projections of confocal z-stacks which contain a front view of the loop evidence that 2D apparent non-horseshoe projections correspond in fact to horseshoe loops being observed from different spatial perspectives (**Fig. 4.1. C**). Considering these two features, further quantification of rDNA morphology may underestimate the amount of horseshoe loops. Due to the same reasons, loop length measurements on 2D projections should be considered as under-approximations of the real ones, because as it is shown in the 3D projection horseshoe loops might appear as a bent arc of shorter length.

4. Results and discussion

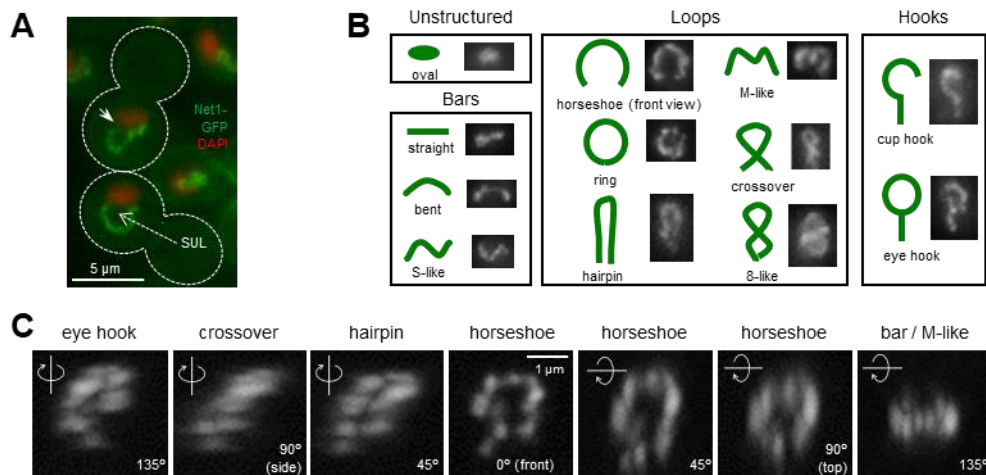


Figure 4.1. The rDNA acquires many morphologies in a metaphase arrest induced by microtubule depletion. (A) Example of cells displaying the outstanding rDNA horseshoe loop and the space under the loop (SUL, pointed with dotted arrow) in a 3h Nz arrest (15 μg/mL). The rDNA is labelled with Net1-GFP, while the mass of the chromatin is stained with DAPI (pseudocolored in red). Occasionally, there are small gaps between both signals, pointed with the white arrow in the upper cell. Acquired by WFM, borders of the cells are marked with dotted lines. **(B)** Representation of all rDNA morphologies found in a Nz arrest under 4 major categories: unstructured, bars, loops and hooks. **(C)** 3D CSM reconstruction of a horseshoe loop obtained by confocal microscopy rotated in the y axis (left) and x axis (right), respectively. Thus, a horseshoe loop might appear as different morphologies when viewed from different perspectives.

In asynchronous growing cells transiting through G2/M, the horseshoe loop arises infrequently, while most of the cells have small rDNA bars instead. However, there are small loops, mostly crossover and eight-like, which appear packed. After Nz treatment, the bars category is reduced in favor of loops (**Fig. 4.2. A**). Furthermore, there is an increase in the length of the rDNA in general, with the horseshoe loops at 3h in the metaphase arrest with a mean length of 5 μm (**Fig. 4.2. B and C**). This might indicate that the natural small loops observed under normal conditions open up and the small bars grow and bend in the Nz arrest to give rise to horseshoe loops, giving us a clue of their possible genesis mechanism. The remaining morphologies in budded cells, namely oval and resolved, correspond to cells that have not reached or have escaped the mid-M block, respectively.

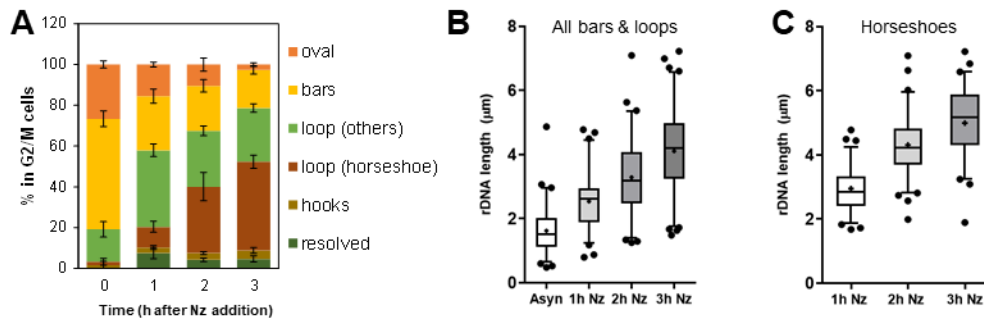


Figure 4.2. The length of the rDNA increases in the metaphase arrest, accompanied by a shift in the main rDNA morphology observed in G2/M cells. (A) Proportion of rDNA morphologies in a Nz time-course experiment (mean \pm SEM; $n = 3$). While asynchronous G2/M cells mainly display bars, this category is progressively reduced in favor of loop formation along the Nz arrest. **(B)** rDNA length in asynchronous and Nz time-course experiment, considering bars and loops ($n > 100$ cells/timepoint). **(C)** As in B, but only considering horseshoe loops. In (B) and (C), whiskers represent 5-95 percentile, mean is shown as '+' and dots represent outliers.

If we relate the position of the rDNA to the chromatin mass using the histone H2A2 (Hta2) tagged with a fluorescent protein, we observe mainly 4 categories (**Fig. 4.3. B**). In the first one, the rDNA appears as an attached or crossing bar over the mass histone signal, which may sometimes correspond to top views of loops (**video 3**, nuclei 3 and 15 and **video 4**, nuclei 3–5; videos available in supplementary materials of our LSA article following the aforementioned reference in <https://www.life-science-alliance.org/content/5/10/e202101161/tab-figures-data>). In the second it takes the shape of a bar that protrudes away from the histone mass, which we refer to as protruding bars or flares and are sometimes side views of loops (**video 3**, nucleus 5). The last two are quite similar, showing a closed handle of rDNA which encloses the SUL. The difference between both is whether the rDNA signal fully coats the handle (full loops, **Fig. 4.1. A**) or if they contain small gaps devoid of Net1 signal but marked with the histone, denoting the presence of chromatin (partial loops, **Fig. 4.3. A**), although it only happens in approximately 10% of the cases, while fully Net1 coated loops account for a 40% of rDNA morphologies in the mid-M block. Besides, time-lapse microscopy shows that these two types of loops are interchangeable (**video 3**, nuclei 2, 4, 6 and 13).

4. Results and discussion

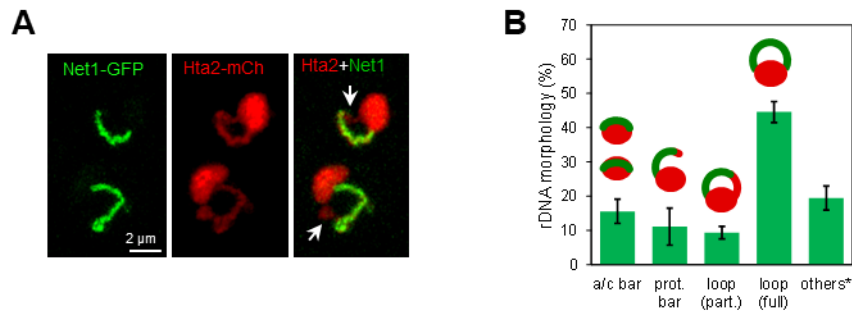


Figure 4.3. There are zones devoid of Net1 signal in the flanks of the rDNA horseshoe loop. (A) Examples of cells showing partially Net1 coated horseshoe loops, marked with white arrows at the flanks, showing only Hta2-mCherry signal. Captured by CSM. [This image was provided by Matos-Perdomo, E] **(B)** Quantification of rDNA morphologies relative to the bulk chromatin mass, using Net1-GFP and Hta2-mCherry respectively, in z-stack projections (mean \pm SEM; n = 3); a/c, attached/crossing bar; prot. bar, protruding bar. Others* mostly include oval and resolved into two rDNA signals. A/c bars may actually be top views of loops, while some protruding bars may be side views, so it is possible that the loop total proportion is higher than the ~55% accounted here.

Next, we wanted to interrogate the nature of the SUL. Taking advantage of several strains carrying the *tetO*/TetR system, in which not all TetR-YFP molecules are bound to the *tetOs*, leaving a freely circulating pool in the nucleus that allows us to visualize the nucleoplasm. This signal is always present in horseshoe loops, surrounding the Net1 signal (**Fig. 4.4. A**). In those strains, the *tetO* is inserted at a specific locus within the chromosome XII. Using a strain which contains two *tetO* loci which flank the rDNA array, one at the proximal flank of the rDNA array (450 kb) and the other one close to the right arm telomere (1061 kb), we observed that the rDNA array traverses the protrusion from side to side in a non-folded manner, as we find one *tetO* spot at every side of the handle. If the rDNA array was folded back, we would have observed the two *tetO* spots on the same side. That means that the bases of the rDNA horseshoe loop are the flanking regions of the rDNA array (**Fig. 4.4. A**). This also explains the appearance of partially Net1 coated loops, as the non-coated regions may correspond to the distal part of the right telomere of cXII. Strikingly, the nucleoplasm signal follows the loop, but it is not present in the SUL, suggesting that its nature is not nuclear. As we saw in **Fig. 4.3**, this space is not occupied by chromatin either, because it does not present histone staining. To further confirm this, we used other strains which carry a variety of nuclear markers, including Nup49 as a marker for the NPCs embedded throughout the NE, Sec61 to detect the pnER and a EGFP fused to an NLS to indicate the nucleoplasm. Despite Nup49 is a more specific reporter of the NE, its punctate nature complicates interpretation compared to Sec61, which is a marker for pnER; thus, we used the latter more throughout this work.

We observed that both Nup49 and Sec61, surround the loop on both sides, meaning that it is bordered by nuclear membrane in both its outer and inner faces (**Fig. 4.4**). However, there are certain regions which appear to show a decrease in the number of NPCs in close proximity to the loop (**Fig. 4.4. F**). With the data provided by all these markers, we conclude that the SUL is not nuclear, that the rDNA spans from side to side of the loop and that it is in fact surrounded on both sides by NE.

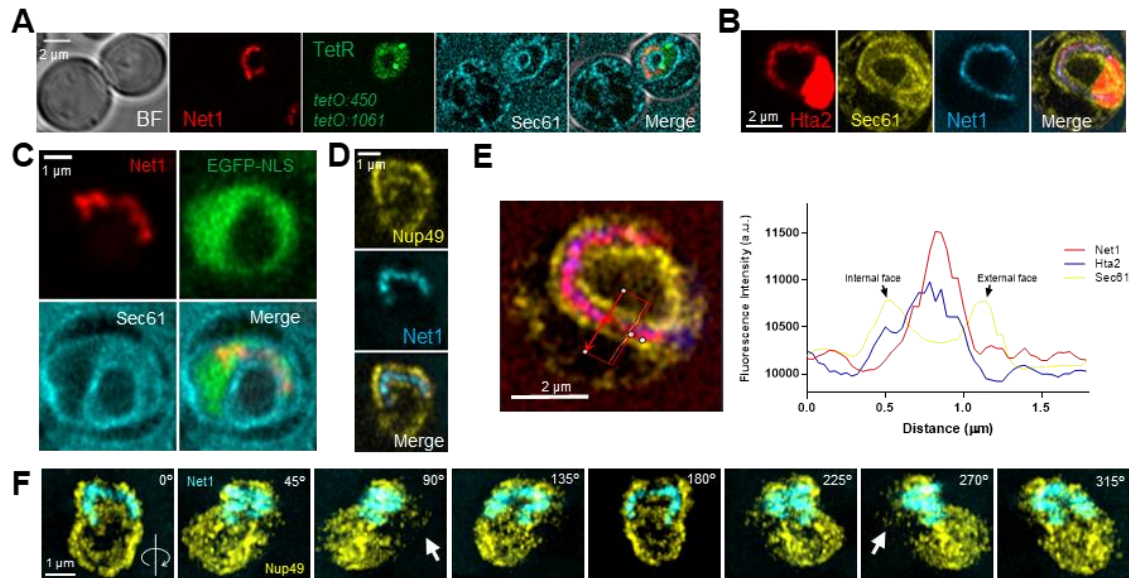


Figure 4.4. The space between the rDNA handle and the bulk chromatin is not nuclear. (A) The freely circulating TetR-YFP which marks the nucleoplasm does not label the SUL and shows a donut-like nucleus. The *tetO* are positioned at both sides of the rDNA handle, located using Net1-mCherry and the pNER using Sec61-ECFP. BF, bright field. **(B)** The Sec61-EYFP signal delimits the rDNA on the internal and external faces in a donut-like nucleus, chromatin observed using Hta2-mCherry and rDNA with Net1-ECFP. **(C)** Like in (A) but the nucleoplasm is labeled with EGFP-NLS instead of TetR. **(D)** The rDNA loop (Net1-CFP) is also coated internally and externally by the NPC protein Nup49-GFP. **(E)** Cross-section intensity profile of a z-stack depth-in-focus 2D projection of the horseshoe loop shown in (B). On the left, the cross section is depicted over the image. On the right, the intensity profile showing increase in Sec61 signal at both sides of the Net1 and Hta2 signals. Note that color pattern has been changed relative to (B), legend on the right of the graph. [This plot was provided by Matos-Perdomo, E] **(F)** CSM 3D projection of (D) rotated every 45° in the y axis. Arrows depict areas with poor Nup49 signal in the SUL compared to the rest of the NE.

The nucleoplasm and NE labelling shows that the nucleus is arranged in a ring-shape toroidal way, often distributed asymmetrically forming two lobes, where one contains most of the nucleoplasm or chromatin signal, while the other contains the rDNA (**Fig. 4.5. A-D**). These two lobes can overlap to various degrees, presumably caused by a protruding bar that bends back (**Fig. 4.5. A**). These two lobes are separated by a constriction that can be observed with NE markers like Nup49 (**Fig. 4.5. C**) as well as the

4. Results and discussion

nucleoplasm (**Fig. 4.5. D**). Interestingly, when observing the Sec61 signal in a z-stack series, sometimes we can observe a circular patch-like shape in peripheral slices (**Fig. 4.5. B**). Most 3D reconstructions show Sec61 distribution in depth as a hemisphere in the SUL, suggesting that the NE (or the ER) could be ladle shaped in lateral views despite being donut-like in frontal views (**video 6**, top 2 cells). As this ladle was also observed with Nup49, this supports that it is made of NE, being these regions characterized by a lower density of NPCs, maybe due to restrictions to access these sites (**Fig. 4.4. F**).

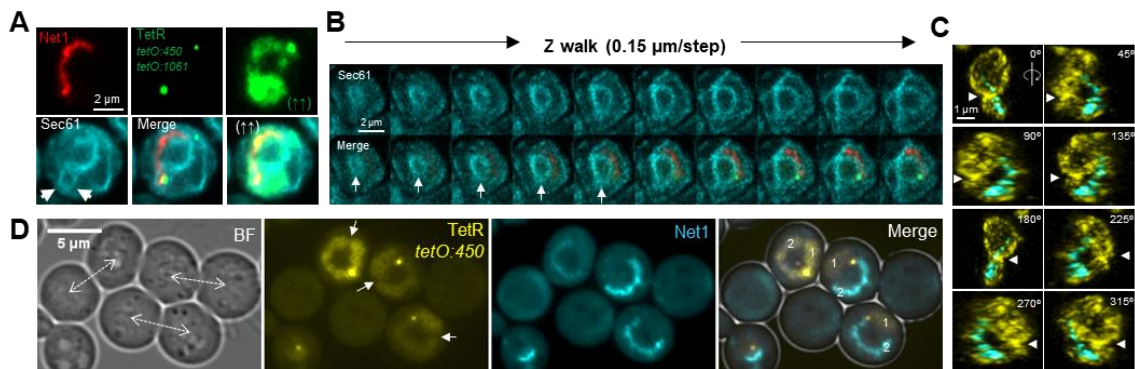


Figure 4.5. The nucleus acquires a toroidal shape with two lobes in the mid-M arrest achieved by Nz exposure. (A) A donut-like nucleus that results from the overlapping of the two nuclear lobes as seen with Sec61-ECFP, marked with two white arrows, one containing the bulk of the nucleoplasm while the other contains the rDNA. **(B)** The SUL can contain a NE/ER ladle, appearing like a closing ring while moving through a z-stack (white arrows). **(C)** CSM 3D projection of a horseshoe loop (Nup49-YFP, Net1-CFP) rotated every 45° in the y axis. The rDNA loop connects two lobes that touch each other in the constrictions marked with arrowheads. **(D)** Three cells displaying bilobed nuclei in which one of the lobes contains most of the TetR-YFP signal, marked with 1, while the other contains the rDNA (Net1-CFP), marked with 2. Arrows show constrictions where both lobes are in contact, while double dotted arrows indicate the polar axis. BF, bright field.

4.1.2. The space under the loop is occupied by the vacuole

The first hint regarding the nature of the SUL came from the observation of bright field (BF) images in which some cells showed rounded structures with different refraction pattern when compared to the rest of the cytoplasm, suggesting that it may be caused by the vacuole colocalization. Furthermore, using a strain with a cytosolic EGFP also suggests that the nature of the SUL is not cytosolic, as this area presents poor staining (**Fig. 4.6. A**). Thus, we decided to use several specific vacuolar markers, including the non-vital dye MDY-64 for the vacuolar membrane (VM), the vital dyes Blue CMAC and carboxy-DCFDA for the vacuolar lumen and fluorescent tagging of the VM protein Vph1-GFP. In all cases the SUL colocalizes with vacuoles, either one big vacuole or a

group of smaller ones (**Fig. 4.6. A-G**). Besides, the vacuole not only associates to the SUL in horseshoe loops, but it is also juxtaposed to the immense majority of protruding bars (**Fig. 4.6. D**). In some cases, the vacuole is not allocated inside the SUL when it is too big, but it still shapes the loop (**Fig. 4.6. F, left**). Of note, as we observed above, some protruding bars may actually be loops observed from a side or top view. Using 3D reconstruction of CSM images, we could observe how the vacuole occupies the SUL (**Fig. 4.6. G**).

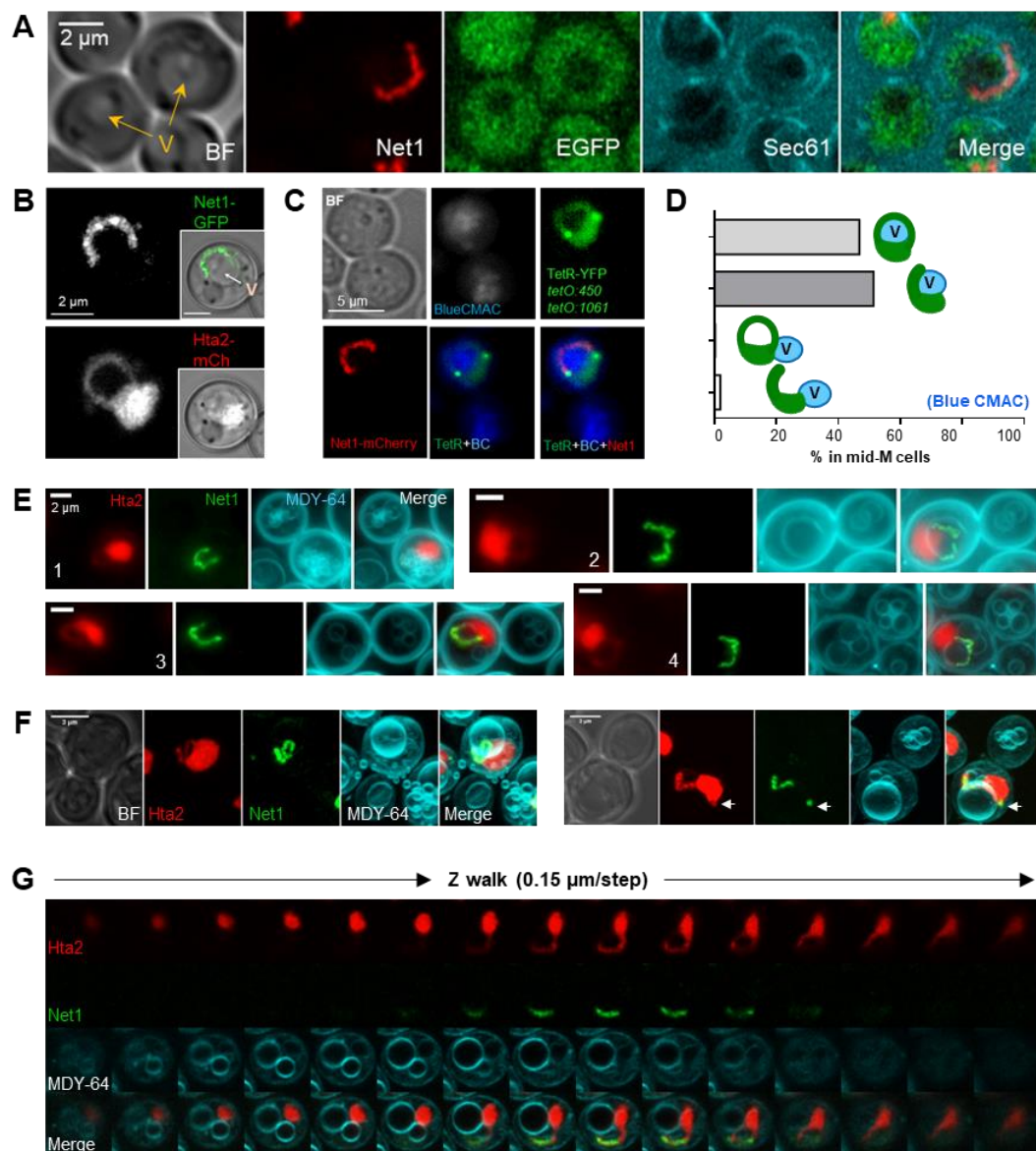


Figure 4.6. Vacuolar stains colocalize with the SUL. (A) BF imaging hinted the presence of vacuoles (V) in close proximity to the loop. Cytosolic EGFP weakly stains the SUL in a strain bearing Sec61-eCFP and Net1-mCherry to delimit the SUL, indicating this space is not cytoplasmic. (B) The handle surrounds the vacuole (V) depicted in BF when using the rDNA marker Net1-GFP and chromatin marker Hta2-mCherry. (C) Vacuolar lumen is observed in the SUL by Blue CMAC staining. (D) Quantification of experiment from where example in (C) was taken to measure loop and flare association to the vacuoles. (E) Four examples of rDNA loops

4. Results and discussion

surrounding one or multiple vacuoles in the SUL, stained with MDY-64. The size and number of accommodated vacuoles is variable, suggesting that the spatial orientation of the loop can vary in response. **(F)** Maximum projection examples of CSM images of cells stained as in (E). In both, the tridimensional shape of the vacuole appears to shape the spatial configuration of the loop. On the left, the loop appears partly collapsed because of the vacuole pushing it towards the cell border, while on the right it appears expanded because of the wider space at its disposal. Of note, a portion of the rDNA separated from the main array is observed and marked with a white arrow, which matches a decrease in signal intensity in the Hta2-mCherry channel. **(G)** The vacuole sits on the SUL as observed while moving in a CSM z-stack. [Images B and C, and quantification in D were provided by Matos-Perdomo, E]

The use of Vph1-GFP provides cleaner images while avoiding the need for extra time for staining, with a lower signal to noise ratio, higher specificity and evading the possibility of uneven staining among all cells. The results observed with the tagged version of the native VM protein validated what we saw using vacuolar stains (**Fig. 4.7. B-F**). In time-course experiments and time-lapse video-microscopy, we observed that the association of the flares and loops with the vacuole start as soon as they start to arise, showing a constant ~7:1 ratio in favor of juxtaposition through the time course (**Fig. 4.7. A and video 10**), so the influence of the vacuole may shape the protruding bar bending into the horseshoe loop from the very beginning of NE expansion. Of note, some protruding bars display a denser Hta2 signal at the tip that suggests the presence of the distal part of the right telomere of chromosome XII, confirming it is indeed a protruding bar instead of a side view of a loop (**Fig. 4.7. D**). Both z-stack walk-through and 3D projections indicate that the vacuole sits on the SUL (**Fig. 4.7. E and F**). Taken all together, it appears that vacuoles juxtapose to nascent flares at the beginning of the mid-M arrest, modulating its bending by being in its close proximity until it acquires the horseshoe loop morphology, which represents the maximum bending it shows in the Nz induced mid-M block.

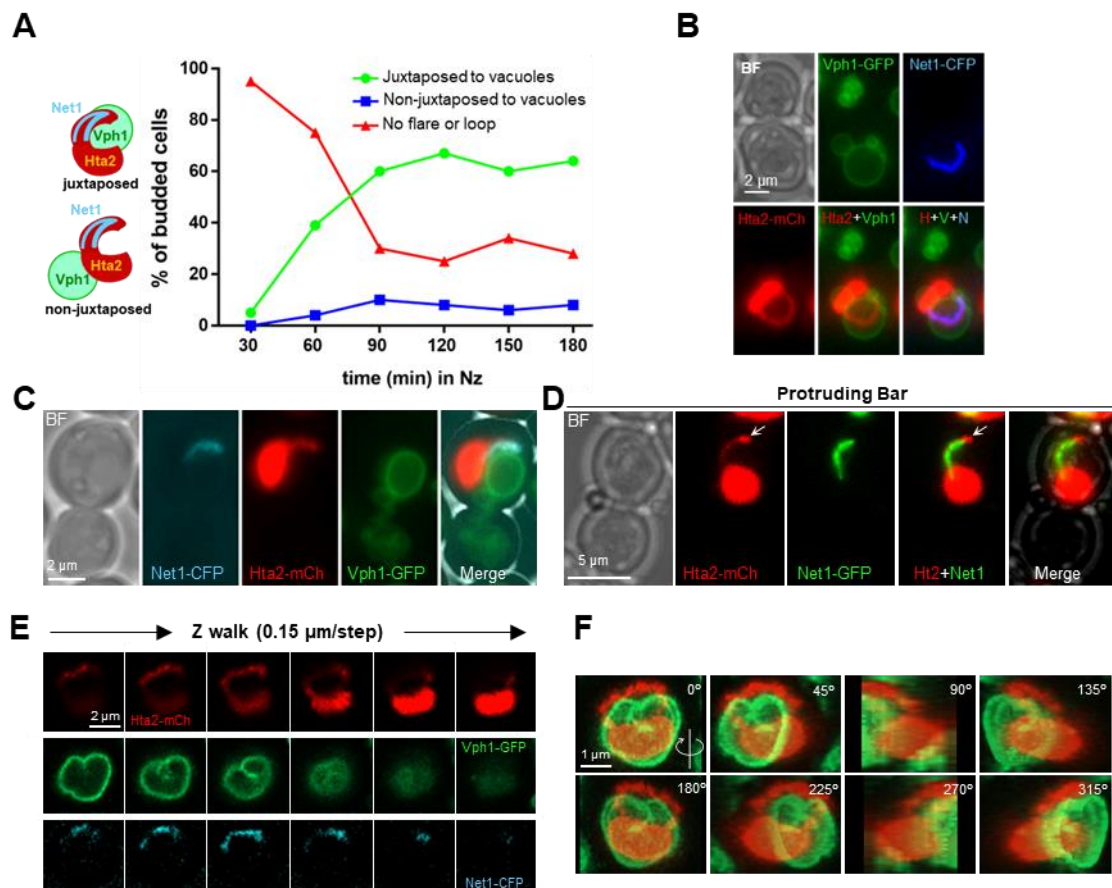


Figure 4.7. Flares and loops are associated to the vacuole since the beginning of the metaphase block. (A) Juxtaposition of growing nuclear extensions containing the rDNA and vacuoles in a Nz time-course experiment. “No flare or loop” (red triangles) indicate the absence of nucleolar extensions and SUL. As this category starts to descend, “juxtaposed to vacuoles” increase almost at the same rate, indicating that nuclear projections associate to vacuoles since they start to arise. [Experiment performed by SSS, quantified by EMP] **(B)** A horseshoe loop smaller than the vacuole diameter, so the latter partially sits on the loop rather than being entirely surrounded. Thus, in a z-stack projection it appears that the loop is crossing the vacuole. **(C)** Example of a protruding bar or side view of a loop juxtaposed to a large vacuole. **(D)** A protruding bar with a denser signal of Hta2 at the apex (white arrow), which might correspond to the distal telomeric region of cXII. [This image was provided by Matos-Perdomo, E] **(E)** The vacuole colocalizes with the SUL as observed while moving in a CSM z-stack. **(F)** A 3D reconstruction of (E) rotated every 45° in the y axis evidences how the loop leans onto the vacuole.

4.1.3. Small loops and protruding bars grow and bend around vacuoles to give rise to the rDNA horseshoe loop

Next, we decided to investigate the origin and the process of formation of the horseshoe loop by time-course and time-lapse microscopy after Nz addition. As we mentioned before, budded cells in asynchronous cultures have rounded nuclei (**Fig. 4.8. A**). Some of these appear squeezed between the vacuole and the cellular edge, suggesting that the nucleus is malleable enough to be pushed between two stiffer bodies, i.e., the

vacuole and the cell wall, as these two organelles never lose their rounded shape apparently. After Nz addition, budded cells start to expand their nuclei with different degrees of symmetry in relation to the amount of nucleoplasm and chromatin present along the extension, displaying either small handles or protruding bars (**Fig. 4.8. A and video 7**). Among extended nuclei, some display a primordial constriction that makes them resemble cashew nuts (**Fig. 4.8. C and videos 7 and 8**), indicating that bilobulation may be a primordial step in the reshaping of the nucleus after Nz exposure. Taking all these data together, the elongation of the nucleus could occur in two axes relative to the rDNA. In the first and most abundant category, the rDNA resides on one side or lobe, separating the nucleolus away from the nuclear center (**Fig. 4.8. B and C, two upper cells, videos 7 and 8, upper cell**), as the Cohen-Fix's laboratory has described before (Campbell et al., 2006; Witkin et al., 2012). The second axis leads to the formation of an rDNA bar that spans across the extended nucleus (**Fig. 4.8. B and C, lower cell, and video 8, lower cell**). Strikingly, the Sec61 ladle is visible in some cashew-like nuclei which lack a proper SUL, and even traces of nucleoplasm colocalize with it, suggesting that this ladle is formed by the close apposition of two portions of the NE (instead of ER) that excludes most of the nucleoplasm from this area (**Fig. 4.8. C, bottom cell**).

To determine the arrangement of the chromosome XII in the Nz induced mid-M block, we used a set of strains which carry the *tetO* in different positions along the chromosome XII. We looked at their location in protruding bars, as we cannot state what is an apical or basal position in a closed horseshoe loop. According to these results, in a Nz 3h block, the distal flank of the rDNA (*tetO*:487 kb) tended to be significantly present in nuclear projections (~65%), mainly in apical position, although the *tetO* of the proximal flank (*tetO*:450 kb) and the subcentromeric *tetO* (*tetO*:194 kb) were apical in ~18% and ~10% of the protruding bars, respectively (**Fig. 4.8. E**). Taken all together, the fact that the distal rDNA flank was more frequently found in the apex of projections compared to the proximal flank, suggests that this region is more prone to be within the nuclear extension. The last *tetO*, present in the subtelomeric region of the right arm of chromosome XII (*tetO*:1061 kb), was less frequently apical than the *tetO*:487, suggesting that in these cases the apparent protruding bars are actually side views of loops. Observing the position of the subtelomeric *tetO* in a time-course experiment, as time goes by its presence in the mid and apical positions of the bar becomes more frequent (**Fig. 4.8. D-F**). These rDNA bars and their surrounding nucleoplasmic flares often show extensive

bending, resembling incomplete states of the horseshoe loop, while in a few examples the nucleus traverses the bud neck reminiscent of what has been described for APC inhibition induced mid-M blocks (Fig. 4.8. D, right cell) (Palmer et al., 1989; Rai et al., 2017).

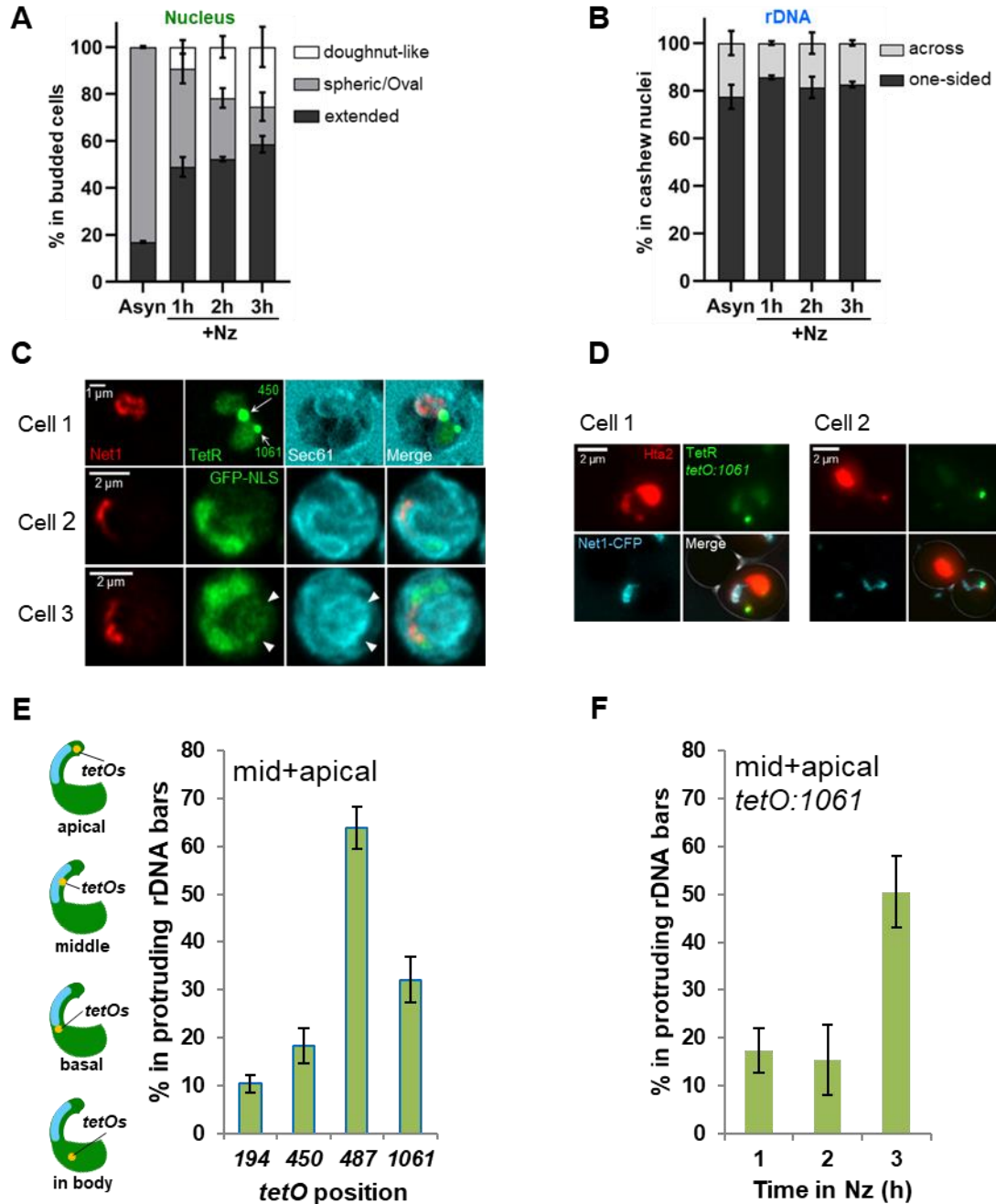


Figure 4.8. The rDNA horseshoe loop stems from small loops and bars that grow and bend around vacuoles. (A) Quantification of nuclear morphologies in a Nz time-course experiment. Donut-like nuclei include toroidal nuclei in which there is a closed hole in the center, like in horseshoe loops, while extended nuclei show nuclear projections that deviate from the spherical/oval condition, often displaying a primordial constriction that makes them resemble cashew nuts (mean \pm SEM; $n = 3$). **(B)** Proportion of the location of the rDNA in extended cashew-like nuclei, which can be allocated in one lobe (one-sided) or traversing the elongation axis (mean

4. Results and discussion

\pm SEM; $n = 3$). **(C)** Examples of major nuclear morphologies representing the category “extended” resembling cashew nuts in which the rDNA is one sided forming a small loop (cell 1) or across the elongation axis (cells 2 and 3). In cell 3, there is a Sec61 ladle which colocalizes with traces of nucleoplasm, indicated with arrowheads. **(D)** Examples where the telomeric right flank of cXII is leading the formation of the protruding rDNA bar, as depicted by the apical position of the *tetO*:1061 kb. On the left (cell 1), the whole nucleus is within the mother cell, while on the right (cell 2), the extension traverses the bud neck. **(E)** Quantification of the sum of mid and apical position of the different *tetO* across cXII in rDNA protruding bars (from a pooled Nz time-course) (mean \pm SEM; $n = 3$). **(F)** Quantification of the sum of mid and apical position of distal subtelomeric *tetO* in cXII in a Nz time-course (mean \pm SEM; $n = 3$).

4.1.4. The absence of microtubules is required for the rDNA horseshoe loop development

As explained in the introduction, the mid-M block caused by Nz exposure is triggered by the SAC activation, because cells no longer have a bipolar spindle attached to kinetochores when microtubules are depolymerized (Jacobs et al., 1988). However, Nz is the most common experimental tool to achieve the metaphase block. To gain further insight into the development of the horseshoe loop and the plethora of nuclear morphologies acquired in the process, we decided to use a different approach to achieve a mid-M block by preserving the mitotic spindle. We used a conditional mutant of the essential protein Cdc16, which is a core component of the APC, based on the AID system, creating a *cdc16-aid* fusion. With this method, we avoid the need to use thermosensitive alleles, as our group and others have described before that a temperature increase induces a heat-shock response that affects the rDNA shape (Matos-Perdomo & Machín, 2018; Shen & Skibbens, 2017). The degradation of Cdc16-aid is triggered by exposure to the auxin indole-3-acetic acid (IAA) (Nishimura et al., 2009), allowing us to inactivate the APC without interfering with the spindle and SAC (**Fig. 4.9. A**). We have monitored the behavior of this strain using growth curves and spot assays, observing that it grows equally to a WT strain in rich medium and that the response to IAA is dose-dependent, being 5 mM the concentration used in further experiments as the response to 1 mM is not that strong for an essential protein, while in the spot assay at the higher concentration growth is completely abolished, consistent with an essential protein involved in cell cycle progression (**Fig. 4.9. B and C**).

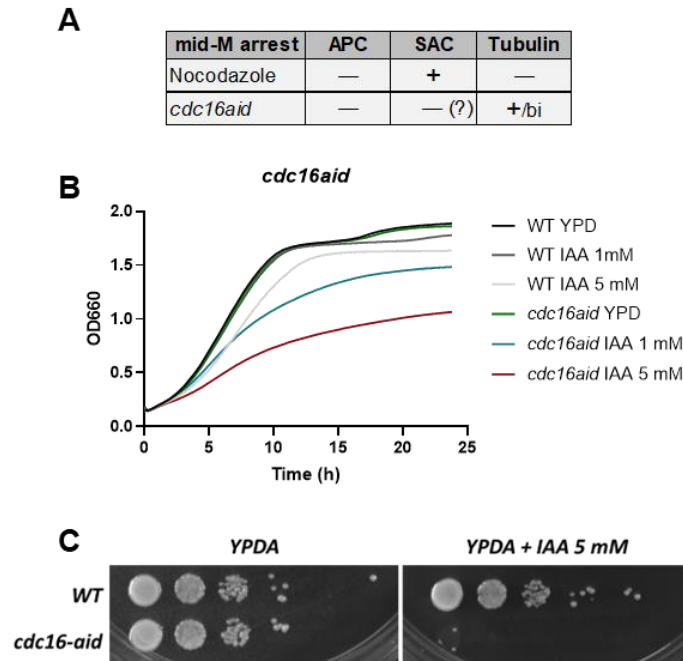


Figure 4.9. The *cdc16-aid* mutant represents a good tool to study a mid-M block by APC inhibition, alternative to thermosensitive alleles. **(A)** Nz and *cdc16aid* are two different approaches to achieve a mid-M block which differentiate in microtubule and SAC response, but both inhibit the APC. The plus sign indicates active or present, while the minus implicates the opposite. The question mark indicates contradictory data according to previous evidence. APC, anaphase promoting complex; SAC, spindle assembly checkpoint; bi, bipolar spindle. **(B)** Growth curves at 25°C of the *cdc16aid* (color lines) strain compared to a WT (grayscale lines) in YPD and different concentrations of IAA, i.e. 1 and 5 mM. Every line is the media of 3 technical replicates. **(C)** Spot assay of the *cdc16aid* strain compared to a WT in YPD and YPD + 5 mM IAA. Cdc16 is an essential protein, thus when it is depleted cell growth is abolished. However, under non-restrictive conditions, this conditional allele allows WT-like growth.

A three-hour incubation in the presence of IAA rendered the same morphological features already described for Cdc16 ts alleles, resulting in a correct mid-M block with the nucleus spanned across the bud neck leaving the rDNA in the mother cell in the shape of straight bars and bent hooks, sometimes to the point of forming a loop, while the gross of the chromatin mass resides in the daughter cell body (**Fig. 4.10. A-E**). We also observed the high dynamism in this block described before as “chromatin transits”, in which chromatin goes from the mother body to the daughter and back again in short periods of time (Palmer et al., 1989; Rai et al., 2017). Furthermore, we wanted to assess whether this characteristic morphology is related to the vacuole position, like what we observed in Nz. For that purpose, we used again the vacuole dyes carboxy-DCFDA (lumen) and MDY-64 (VM), even though our strain has a triple tagging pattern in the three fluorescent channels already. With the first dye, vacuole staining is brighter than the TetR-YFP signal, making them distinguishable, and the *tetO* signal was even brighter

4. Results and discussion

than the stain, so in this case we could assess the position of this locus along with the chromatin and rDNA signals, using Hta2-mCherry and Net1-ECFP respectively (**Fig. 4.10. A**). On the other hand, MDY-64 emits in the CFP channel and masks the Net1-ECFP signal, so we differentiate the position of nuclear extensions by the TetR-YFP signal and the histone, locating the right arm of chromosome XII thanks to the *tetO*:1061 kb (**Fig. 4.10. B**). Interestingly, despite the rDNA is in the mother body in ~80% of the cells, separated from the main Hta2 mass, the *tetO*:1061 kb is located in the rDNA in ~70% of the cases, suggesting that the rDNA might be bent in the remaining ~30%, similar to what we observed in the Nz induced horseshoe loop (**Fig. 4.10. D and E**). Indeed, in both cases the vacuole showed a high colocalization (~90%) with nucleolar projections (**Fig. 4.10. F**), suggesting a role for this organelle in nuclear reshaping, as it happens under Nz exposure. In cells that take the shape of a hook, the vacuole was allocated in the space it leaves (**Fig. 4.10. A**), similar to what we observed regarding the SUL, while in straight bars, it is the apex which is more prone to be associated to the vacuole (**Fig. 4.10. B**). We do not know if this apparent association depends on the nucleus-vacuole junctions, which remains to be studied in the *cdc16* arrest.

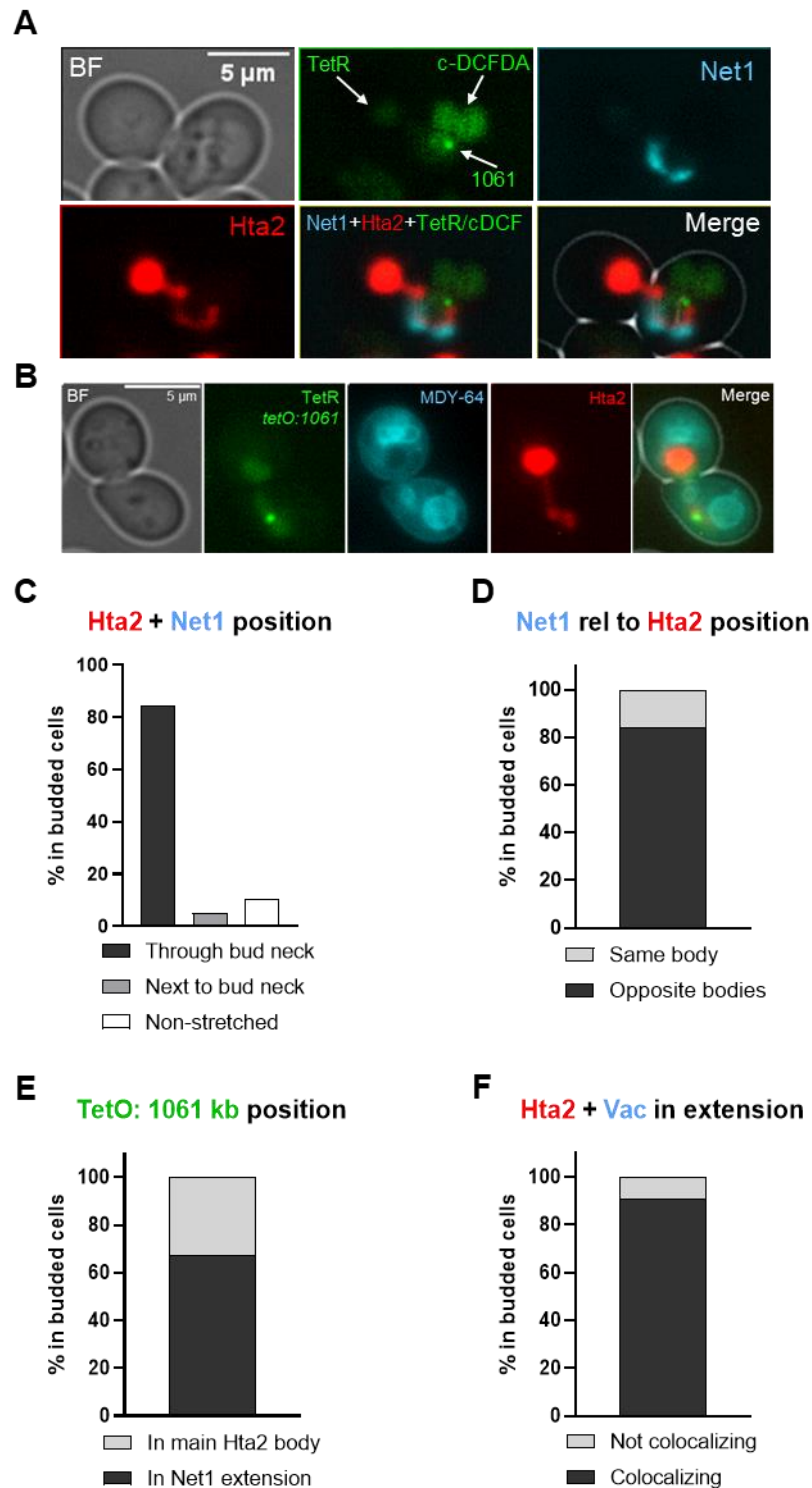


Figure 4.10. A conditional *cdc16aid* mutant reproduces the phenotype observed in thermosensitive mutants of the APC. Vacuoles are associated to nuclear projections observed in the mid-M arrest induced by APC inhibition. (A) Example of a mid-M blocked cell induced by *cdc16aid* in which the rDNA (Net1-ECFP) forms a hook enclosing the vacuole (c-DCFDA). (B) Example of *cdc16aid* cell in which the right arm of cXII (TetR-YFP/*tetO*) is stretched as a bar, touching the vacuole at the apex (MDY-64). (C) In the mid-M block induced by APC inhibition the nucleus traverses the bud neck in the vast majority of cases. (D) In this block, the rDNA resides mostly in the body of the mother cell, in contrast to the bulk of the chromatin mass,

4. Results and discussion

which is allocated in the daughter cell body. **(E)** The *tetO*:1061 kb is usually located in the nuclear projection formed by Net1, although in ~30% of the cases it is positioned in the main Hta2 body, suggesting that the projection might be bent as it happens in the horseshoe loop in Nz. In micrographs: BF, bright field.

We investigated in a time-course experiment the time of projection appearance using this mutant. If we look at the cell morphology in BF images, asynchronous culture display roughly a 40% of budded mononucleated (MN) cells, which increase up to ~85% after 3 h in IAA (**Fig. 4.11. A**). Regarding the nuclear shape of these budded MN, around 20% showed projections in asynchronous culture. However, we cannot differentiate early projections caused by IAA exposure and the ones that arise as a consequence of early nuclear division because both extend to the bud neck's direction, meaning that this 20% of cells which show projections are not equal to the ones induced by the absence of Cdc16, which correspond to complete nuclear projections due to the cell cycle block. Thus, this 20% of extensions may be considered as an overestimation in asynchronous cultures. During the time-course, between 150 and 180 min the culture peaks synchronization at mid-M, displaying the characteristic nuclear projections in ~85% of the budded MN cells (**Fig 4.11. B**). This strain still forms horseshoe loops upon Nz treatment, so the presence of the *aid* allele does not disturb this feature (**Fig. 4.11. C**). In the *cdc16aid* mid-M block, the rDNA acquires different morphologies compared to the ones we described for Nz. In contrast, the phenotype is not so variable, and we distinguish mainly four categories, being extended bars the predominant (~50%) followed by the oval shape (~30%), while the remaining ~20% consists of the sum of loops and hooks (**Fig. 4.11. D**). Additionally, the rDNA is slightly longer in the *cdc16aid* block than in the Nz-induced block (**Fig. 4.11. E**). As we see, in this mid-M block the loop is a minority morphology, thus we suggest that microtubules are required to form the rDNA horseshoe loop, in spite of a mid-M arrest being enough to modify nucleolar morphology towards a bar-like structure.

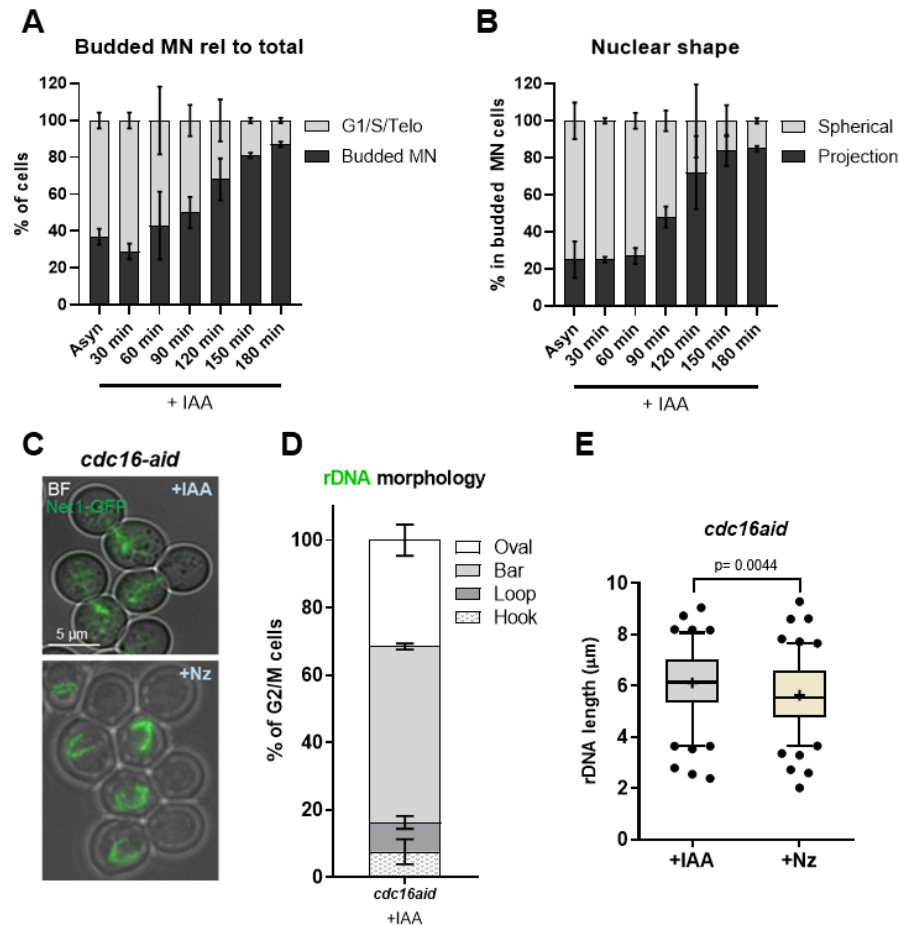


Figure 4.11. The rDNA in the *cdc16aid* mutant acquires mainly a bar morphology, being loops present in lower proportions than Nz-driven mid-M blocks. (A) Proportion of cells in G2/M compared to other cell cycle stages in an asynchronous culture exposed to IAA in a time-course experiment, assessed by the presence and size of the bud and histone signal to differentiate between mononucleated cells and anaphase-telophase cells (mean \pm SEM; $n = 2$). **(B)** Proportion of budded MN cells with nuclear projections compared to spherical nuclei in an asynchronous culture exposed to IAA in a time-course experiment (mean \pm SEM; $n = 2$). **(C)** The *cdc16aid* strain forms extended bars across the division axis when exposed to IAA (top), but still displays the rDNA horseshoe loop upon Nz exposure (bottom). BF, bright field. **(D)** Proportion of rDNA morphologies in the *cdc16aid* mid-M arrest (mean \pm SEM; $n = 3$). **(E)** rDNA length in the *cdc16aid* strain exposed to either IAA or Nz ($n > 100$ cells per condition). Whiskers represent 5-95 percentile, mean is shown as '+' and dots represent outliers. [Data in C, D and E were provided by Matos-Perdomo, E]

4.1.5. The horseshoe loop requires phospholipid synthesis and membrane overexpansion

As reviewed in the introduction, in mid-M blocks phospholipid synthesis is still active, leading to the formation of the nuclear flare (Campbell et al., 2006; Witkin et al., 2012). The Nem1-Spo7/Pah1 axis is the central hub that controls the balance between phospholipid and lipid droplet (LD) biosynthesis, by deciding the fate of its main

4. Results and discussion

precursor, PA. Thus, activation of Pah1 by Nem1 favors DAG biogenesis, which further transform into TAG and are packed in LDs (Pascual & Carman, 2013; Siniossoglou, 1998). We wondered whether mutants of this axis show and additive effect regarding nuclear morphology when blocked in mid-M. For this, we decided to use inducible mutants instead of the null mutants the literature has mainly used, to expose cells to membrane imbalances for shorter periods of time, avoiding carryover effects after growth of many generations. Using different approaches, we confirmed that the use of a *nem1aid* mutant is comparable to a wildtype strain regarding growth behavior, making this mutant useful for these studies (**Fig. 4.12**).

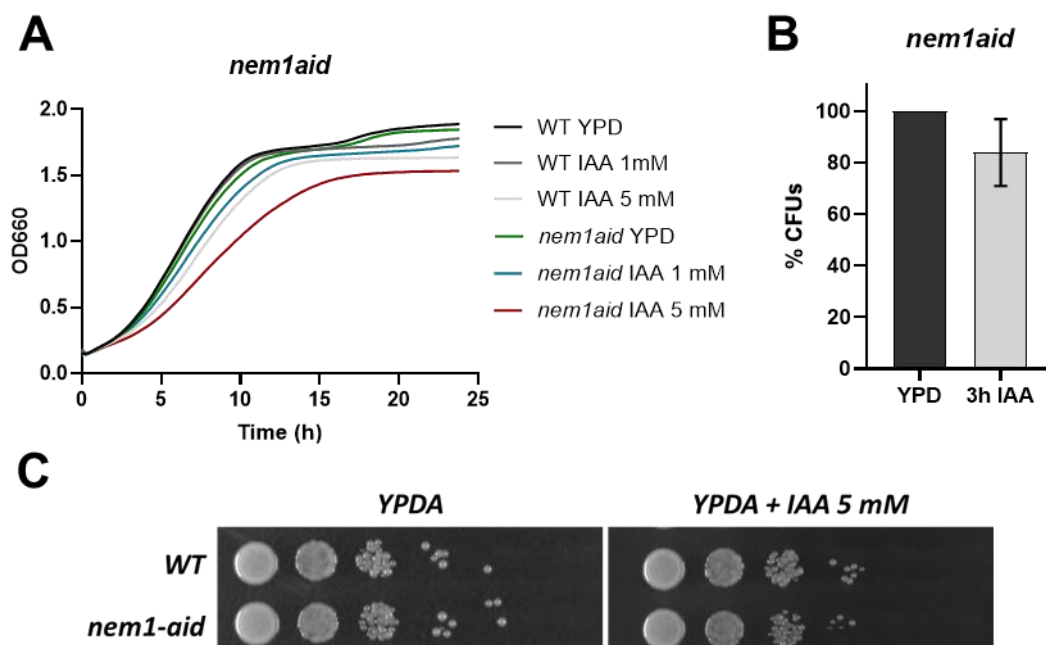


Figure 4.12. Inducible mutants of Nem1 maintain their fitness as compared to a WT. (A) Growth curves at 25°C of the *nem1aid* (color lines) strain compared to a WT (grayscale lines) in YPD and different concentrations of IAA, 1 and 5 mM. Every line is the media of 3 technical replicates. **(B)** Clonogenic assay of the *nem1aid* strain, in which survival after 3h of IAA 5mM exposure only decreases slightly (mean \pm SEM; n = 2). **(C)** Spot assay of the *nem1aid* strain compared to a WT in YPD and YPD + 5 mM IAA. Nem1 is a non-essential protein, and thus shows a growth pattern comparable to the WT.

Then, we confirmed that the *nem1aid* mutant shows nuclear projections as described for the null mutant after an overnight incubation on IAA (~6 generations), in agreement with previous knowledge of knockout mutants, and consistently Western blot showed a fast decrease in expression levels upon IAA exposure (**Fig. 4.13. A and B**). Surprisingly, when comparing rDNA morphology upon IAA addition and IAA + Nz coincubation, we observed that ~50% of budded cells present nuclear projections (sum of protruding bars

and loops) in the first case, which increased up to ~60% after Nz addition. Starting from ~10% of loops, Nz exposure raised this number up to ~25%, which is lower than expected for Nz alone in WT cells (~70%) (**Fig. 4.13. C**). Furthermore, the position of the *tetO*:1061 kb in the nuclear mass suggests that the *nem1* protruding bars are instead highly bent loops which expand after Nz exposure. Additionally, we noticed that even though loops are present in this mutant, they mostly take the shape of small hairpins. Because of that, we measured the rDNA through the Net1 signal and indeed, the mean length of the rDNA in loops and bars together is ~2.5 μm , which after Nz mid-M block increases significantly until reaching a length slightly shorter than 4 μm (similar to the sum of bars and loops in a WT Nz-induced mid-M block, **Fig. 4.2. B**) (**Fig. 4.13. D**). Like we assessed before in both models used for mid-M arrests, we wanted to know if the vacuole is associated with nuclear projections caused by impairment of the lipin axis. Indeed, the vacuole presence adjacent to nuclear flares and loops accounts for more than 90% of the cases (**Fig. 4.13. E and F**). However, no apparent additive effect arises when combining these two conditions that individually trigger changes in nuclear morphology.

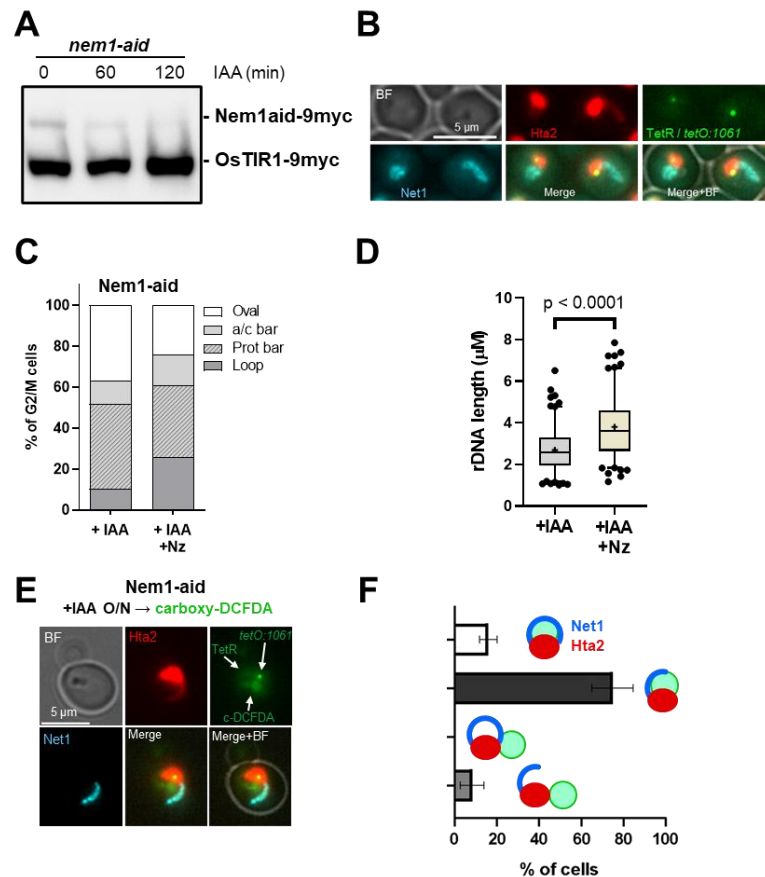


Figure 4.13. The vacuole shapes nuclear projections caused by mutations of the lipin axis. (A) Western blot of the degradation of Nem1 in the *nem1aid* mutant upon IAA incubation, in which

4. Results and discussion

the OsTIR1 band serves as a load control because it is constitutively expressed. **(B)** *Nem1aid* mutants display nuclear flares and small loops under depletion conditions (YPD+IAA overnight culture) comparable to the null mutants. In both examples the *tetO:1061* kb resides within the main Hta2 body. BF, bright field. **(C)** Quantification of the rDNA morphology of the *nem1aid* strain after IAA overnight incubation and exposed to Nz after *nem1* depletion. Note that the number of loops doubles after Nz treatment, although it does not reach the 40 – 70% observed in WT cells exposed to Nz alone. **(D)** rDNA length of the *nem1aid* strain after IAA overnight incubation and exposed to Nz after *nem1* depletion, which causes an increase in length ($n > 100$ cells each). Whiskers represent 5-95 percentile, mean is shown as '+' and dots represent outliers. **(E)** A representative example of asynchronous *nem1aid* cells grown in IAA in which the vacuole staining with carboxy-DCFDA shows that vacuoles reside adjacent to nuclear flares and rDNA bars. Five subcellular structures are labelled: bulk chromatin (Hta2-mCherry), the rDNA (Net1-ECFP), nucleoplasm (free TetR-YFP), subtelomeric right arm region of cXII (*tetO:1061* kb) and vacuolar lumen (c-DCFDA). The three signals in the green channel are differentiated by intensity, morphology and position, as the nucleoplasm is the weakest signal and colocalizes with the Hta2 signal, the *tetO* is the spot, and the vacuolar lumen is the stronger and does not coincide with the nuclear signal. **(F)** Proportion of flares and loops adjacent to the vacuole in a *nem1aid* mutant after an overnight incubation on IAA (mean \pm SEM; $n = 3$).

On the other hand, we wanted to study the nuclear morphology in the mid-M block when lipid synthesis is hampered. With that purpose we used the fatty acid synthase inhibitor drug cerulenin (Cer). Following nuclear morphology using a fluorescently tagged Sec61, we observed that the immense majority of nuclei are completely rounded, implicating that *de novo* lipid synthesis is required to form nuclear projections in a mitotic delay (**Fig. 4.14. A and B**), as has been described before by others, linking lipid synthesis and NE projections (Male et al., 2020; Walters et al., 2014, 2019; Witkin et al., 2012). There are two other minor categories in which nuclei appear squeezed, presumably between the vacuole and the cell envelope, and bowtie, which corresponds to cells escaping the mid-M arrest towards anaphase. These two categories together account for less than a 10% among budded cells in the block in the presence of Cer, evidencing the great tendency of nuclei to form a nearly perfect sphere when exposed to this drug. However, when closely examining the rDNA morphology, small loops are still frequent, mostly in the shape of hairpins, although bars are the main morphology it presents (**Fig. 4.14. C**). The horseshoe rDNA loop with a proper SUL is never observed under these conditions, and the same happens for protruding bars when taking the histone signal as reference for the chromatin mass. Strikingly, the rDNA length is considerably reduced to a mean of $\sim 2 \mu\text{m}$, compared to a Nz incubation without cerulenin in which bars and loops have a mean length of $\sim 4 \mu\text{m}$ (**Fig. 4.14. D**). Taking all this into account, phospholipid synthesis is required for the development of the rDNA horseshoe loop in the mid-M Nz arrest.

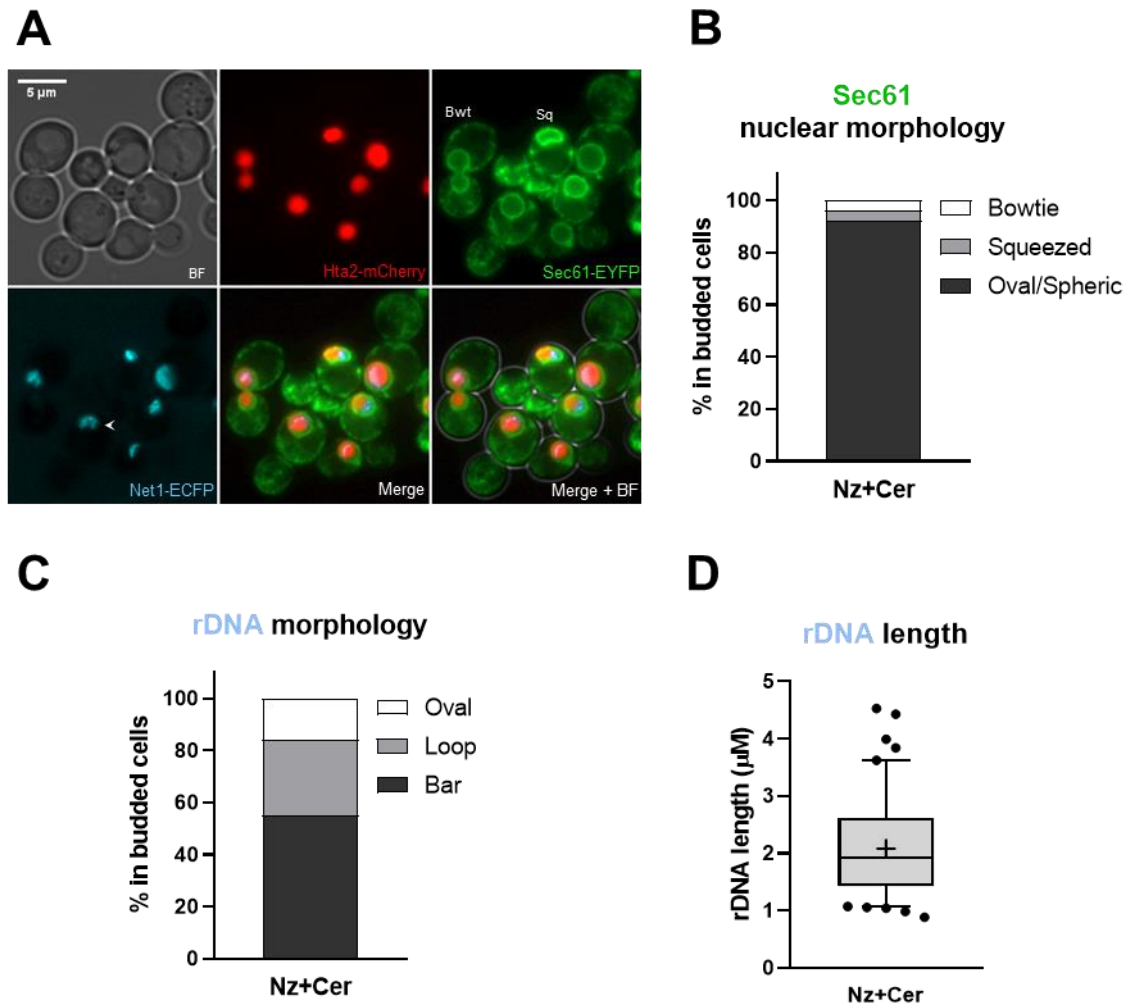


Figure 4.14. Lipid synthesis is a requisite for rDNA horseshoe loop formation. (A) Examples of NE morphologies observed by Sec61-EYFP tagging in a Nz arrest in the presence of the FAS inhibitor cerulenin. The arrowhead points to a small hairpin loop. BF, bright field; Bwt, bowtie; Sq, squeezed. **(B)** Quantification of experiment from (A). Most nuclei have a rounded shape, but nuclei through the bud neck in the shape of a bowtie and squeezed, presumably between the vacuole and the plasma membrane, are also present. **(C)** rDNA morphology quantified using Net1-ECFP maximum projections of z-stacks. Despite the lack of lipid synthesis, loops are still present, although most acquire a bar shape. Loops are smaller and have no SUL. **(D)** Measurements of rDNA length in a Nz+Cer arrest ($n = 100$ cells). Whiskers represent 5-95 percentile, mean is shown as '+' and dots represent outliers.

To conclude this first part, taking all these data into account, we propose the next model for horseshoe loop formation, in which we separate this morphology in classes I and II regarding their development and final structure. As we saw in the introduction, nuclei of asynchronous cells transiting through G2/M are characterized by a spherical shape and a crescent like nucleolus in the nuclear periphery. However, the rDNA transforms into bars and loops when the cell cycle is stalled in mid-M by microtubule depletion. Considering the plethora of morphologies we have observed, thanks to the

4. Results and discussion

information provided by several nuclear markers and the most frequent positions of the *tetO* in chromosome XII, we propose three main ways to achieve the horseshoe loop shape, being the rest intermediate states in those pathways (**Fig. 4.15. A**). These findings shed light on the origin and development of the horseshoe rDNA loop structure, including the apparent void space enclosed between the rDNA handle and the chromatin mass, actually occupied by vacuoles, and the multiple ways of formation that ultimately lead to this characteristic structural change in the nucleus. Additionally, we now differentiate between two different SULs, regarding its formation process. In one, the presence of a NE ladle hints that vacuoles may push very close two portions of NE while excluding nuclear proteins when expansion is confined to the nucleolar area (**Fig. 4.15. B**), while the other does not possess a ladle because they arise after extensive bending of one nuclear lobe until it reaches the other. In both models used for mid-M block, almost always vacuoles and nuclear extensions colocalize. The large volume that vacuoles occupy inside the cell predicts a high degree of colocalization of these two. However, data showing association of nascent projections to vacuoles, which wrap around the vacuole while they grow, suggest an intimate nucleus-vacuole connection since the begging of this morphological change. Also, in a *cdc16aid* block, the presence of microtubules apparently favors this interaction in the mother cell, where the nucleolar projection remains behind very often associated to vacuoles at its apical portion (**Fig. 4.10. A, B and F**). There may be a mechanism involved in the NVJs management to release the rDNA for segregation, explaining why this region is the only one left behind in this mid-M block where microtubules are present, despite the rest of the nuclear mass mostly being allocated in the daughter cell. Further investigation could shed light on the role of proteins involved in NVJs may have in the morphology and segregation of this locus, to envision if the role of vacuoles in nuclear and rDNA reshaping is active or passive.

It has not escaped our notice that the existence of multiple morphologies converging into one involves a certain degree of randomness, likely influenced by the number and size of the vacuoles, the degree of overexpansion of the NE and the axis of elongation regarding the nucleolus. Additionally, our model fits well with data obtained by chromosome conformation capture (Hi-C), in which both regions flanking the rDNA array do not interact (Lazar-Stefanita et al., 2017).

Strikingly, a unique phenotype in human cell lines referred to as toroidal or donut-shaped nucleus has been recently described, in which the lysosome occupies the hole left

by the nuclear content, which unequivocally resembles the nuclear shape acquired in yeast mitotic arrests by microtubule depletion or under membrane excess conditions explained above. The toroidal nuclei in this study arise from mitotic errors after lysosomal impairment, linking genome stability with accurate lysosome function through autophagic degradation (Almacellas et al., 2021). The morphologies we describe in this work highly resemble these structural observations, but it remains to be confirmed if in yeast they are also correlated with this function.

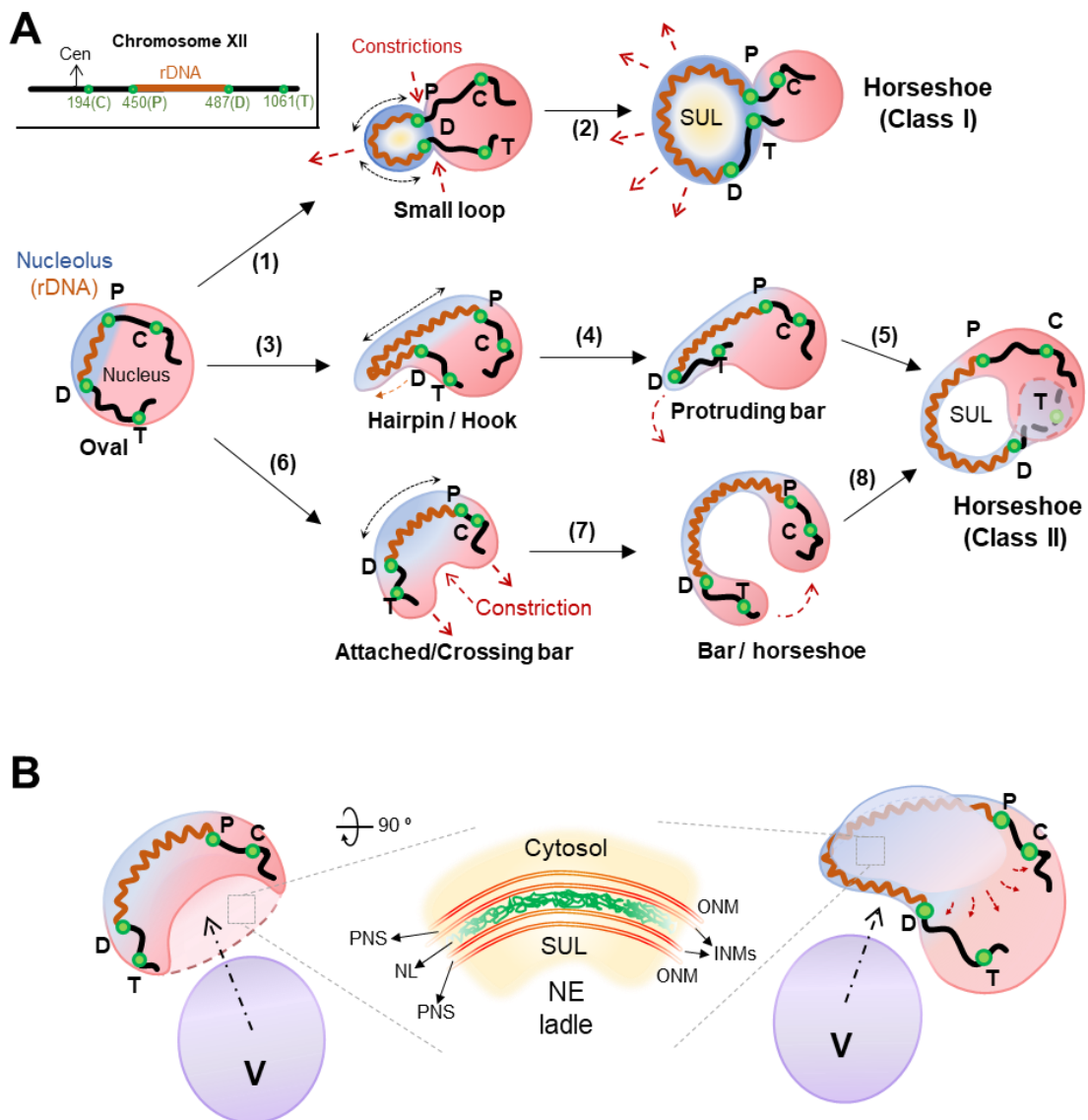


Figure 4.15. Model of the rDNA horseshoe loop origin and development upon Nz-driven mid-M cell cycle blocks. (A) Using different nuclear markers and the position the position of the *tetO* along cXII, we propose three main ways to achieve the rDNA horseshoe loop morphology in a Nz arrest, in which spherical nuclei start to expand, giving rise to small projections. In the first pathway (1), the nucleus becomes bilobulated with a primordial constriction, allocating the nucleolus in a second lobe, (2) which further elongates symmetrically in all directions until giving rise to a class I horseshoe loop around a SUL with a ladle inside (yellow). The second pathway

4. Results and discussion

(3) starts with the growth of the nucleolus as a finger-like projection, (4) which pulls the distal flank of cXIIr into the projection, (5) resulting in a bilobed nucleus that bends at different degrees, finally overlapping in a frontal view. The third pathway (6) starts with the elongation of the nucleus to both sides of the nucleolus, taking a cashew-like shape, (7) which continues to expand giving rise to an rDNA handle that connects a bilobed nucleus, (8) that can bend until both lobes overlap forming the class II horseshoe loop with a proper SUL. The main chromatin mass is depicted in red, the nucleolus in blue, the rDNA array as a red spring, while the rest of cXII is represented with a black line, with the four *tetO* positions along itself as green dots in which C refers to the subcentromeric one, P is the proximal rDNA flank, D is the distal rDNA flank and T the subtelomeric portion of cXIIr (scheme of cXII and *tetO* positions at top left inlet). Black arrows indicate morphological transitions, dashed black double arrows the directions of NE expansion and red arrows the motion of nuclear subdomains during transitions. **(B)** Diagram of how the vacuole may act as a template to create the SUL NE ladle. The first example on the left, explains the presence of a NE ladle in cashew-like nuclei (see Fig. 4.8. C). The example on the right depicts a class I horseshoe loop in which the NE ladle forms by the vacuole pushing the nucleus towards the cell membrane. At the center, a schematic of the putative ladle configuration, showing that it is comprised of two close NE sheets leaving a narrow nuclear lumen in between, excluding most of the nucleoplasm (in green) from it. SUL, space under the rDNA loop; NE, nuclear envelope; INM, inner nuclear membrane; ONM, outer nuclear membrane; NL, nuclear lumen; PNS, perinuclear space.

4.2. Cytological characterization of cells released from a metaphase cell cycle block

4.2.1. Cells released from a Nz-induced mid-M block tend to restore normal nuclear shape

To continue our study, we wondered what happens to these nuclear extensions when cells are released from Nz. We hypothesized that these projections may be maintained and inherited by one or both daughter cells or, on the other hand, that they may be corrected by an unknown mechanism based on a reorganization of the surplus of NE or removal of membrane excess by autophagy.

To start this part of the project, we observed cells transiting through late mitosis in an asynchronous culture and compared them with Nz released cultures. We used a triple labeled strain for the rDNA (Net1-mCherry), the NE (Sec61-ECFP) and nucleoplasm together with the proximal flank of the rDNA and the distal cXIIr (TetR-YFP/*tetO*:450 kb/*tetO*:1061 kb). In asynchronous cells we observe the already characterized rounded nuclei from G2/M to the bowtie and hourglass shapes in anaphase and telophase, respectively (**Fig. 4.16.** Asyn row). We categorized anaphases in this strain by the presence of three *tetO* spots, according to the expected segregation pattern described for cXII in which the rDNA separates zipper wise, and thus the *tetO* 1061 is still unresolved when rDNA segregation has started (Torres-Rosell et al., 2004). On the other hand, in telophase we observe four *tetO* spots along with the two Net1 signals being resolved, indicating complete genome segregation. From now on, when using *tetO* strains, we will refer to these two stages as mononucleated (MN) if the cells pose a single *tetO*:1061 and binucleated (BN) when they show two, as they can be unambiguously correlated with the end of the last region to segregate, i. e. the rDNA.

In several experiments we observed that cells transiting through anaphase and telophase after a Nz arrest frequently show nuclear projections derived from the arrest. Likewise, the rDNA horseshoe loops can be maintained even when the nucleus starts positioning between both cell bodies to start segregation, meaning that this feature may not be restricted to the mid-M block (**Fig. 4.16.** - Nz row, G2/M example). Also, Sec61 ladles are often observed, presumably associated to the vacuole as we observed in the mitotic block (**Fig. 4.16.** - Nz row, telophase example). In this example, we can observe

4. Results and discussion

a thin portion of nucleoplasm surrounding the Sec61 ladle, consistent with our hypothesis that the vacuole presses together two portions of NE excluding nucleoplasmic proteins from it. These non-spherical morphologies can be observed using an EGFP-NLS as well, using the same strain we used to evaluate the Nz arrest to investigate the nature of the SUL (Fig. 4.16. B).

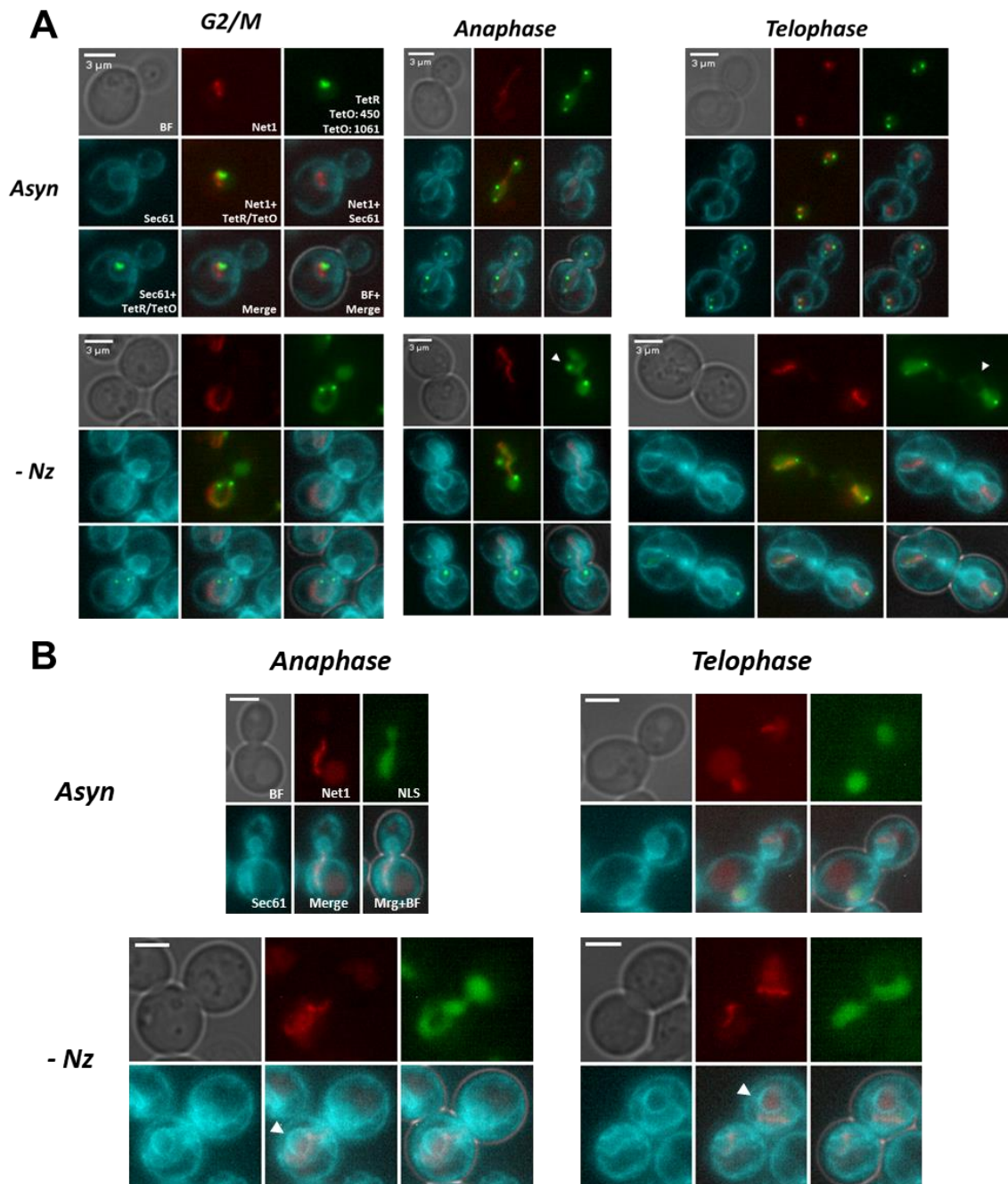


Figure 4.16. Cells released from a Nz mid-M block maintain NE non-spherical morphologies. (A and B) In this panel of micrographs, we compared cells transiting through different mitotic stages in asynchronous cycling cells (upper row, Asyn) vs cells release from a Nz induced mid-M block (bottom row, -Nz). We observed that nuclear projections and the NE

ladle are preserved after Nz removal (white arrowhead), easily observed with both nucleoplasm markers, i. e. free TetR and EGFP-NLS. In (B) bottom row, autofluorescence in the red channel is useful to hint the presence of the vacuole colocalizing with the Sec61 ladle.

We further examined nuclear morphology and cXIIr segregation in time course experiments after Nz removal. Remarkably, ~20% of the cells still possess a single *tetO:1061* even after 90 min of Nz had been cleaned from the media, indicating incomplete cXII segregation (**Fig. 4.17. A**). Furthermore, nuclear projections determined by TetR and Hta2 signal decrease in the time course, especially in the BN category (~50% within total budded cells). This suggests that cells get rid of nuclear projections in later stages of mitosis after the arrest. However, at least in the time window we covered in these experiments, the remaining 50% of cells still display nuclear projections (**Fig. 4.17. B**). This is in agreement with data from the Cohen-Fix lab, which shows that ~90% of Nz released cells proceed through mitosis, of which ~75% of one or both daughter nuclei regained a rounded shape following nuclear division (Witkin et al., 2012). The differences in our observations may rely solely in the time window observed in both time-course experiments, as Witkin et al. maintain the Nz release up to 160 min. Because an entire yeast cell cycle lasts 90 – 120 min, we would not expect such a long time to transit from mid-M to a new cycle in undisturbed cells, implying a possible checkpoint mechanism to resolve nuclear extensions before the onset of the subsequent cell cycle. Thus, nuclear projections are not apparently corrected during mitotic progression, but rather once it has finished and both cells have inherited their corresponding genetic material.

Because this mid-M block is triggered by the absence of microtubules, we decided to investigate the speed of mitotic spindle reassembly and its positioning, as it might influence nuclear morphology and segregation timing in the release. In time-course experiments we observed that microtubules (GFP-Tub1) are reassembled as soon as 15 min after Nz removal, and that SPBs, detected by Spc42-mCherry, achieve a mean straight distance of 6 μm after 75 – 90 min (**Fig. 4.17. C and D**). However, the data are highly heterogeneous, indicating lack of synchrony in Nz released cells, so we decided to categorize cells according to the number and position of *tetO* and SPB signals they exhibit. We would expect the majority of cells to range from a single *tetO* and SPB signal in the arrest to two separated *tetO* and SPB signals, one of each in both daughter cells in late mitosis. Indeed, at 90 min almost 80% of cells achieved correct *tetO* and SPB segregation (**Fig. 4.17. E**). Considering these data, nuclear projections observed in BN cells are not strictly maintained by delays through anaphase due to failures in spindle

4. Results and discussion

reorganization and SPB segregation. Interestingly, the latter process seems to be highly dynamic, because both in micrographs and short time-lapse movies there are a few apparent transition states, in which even the two SPB signals travel to the daughter cell, leaving a single *tetO* behind. We also observed a few other configurations which are probably explained by a temporal lack of cohesion, as for example happens when two *tetO* are observed when there is only one SPB signal or there are two in the same body, meaning that the spindle is not elongated as required for proper chromosome segregation. When reanalyzing SPB distance per category instead of time, variability was highly reduced, especially in the initial and transition stages towards division (**Fig. 4.17. F**).

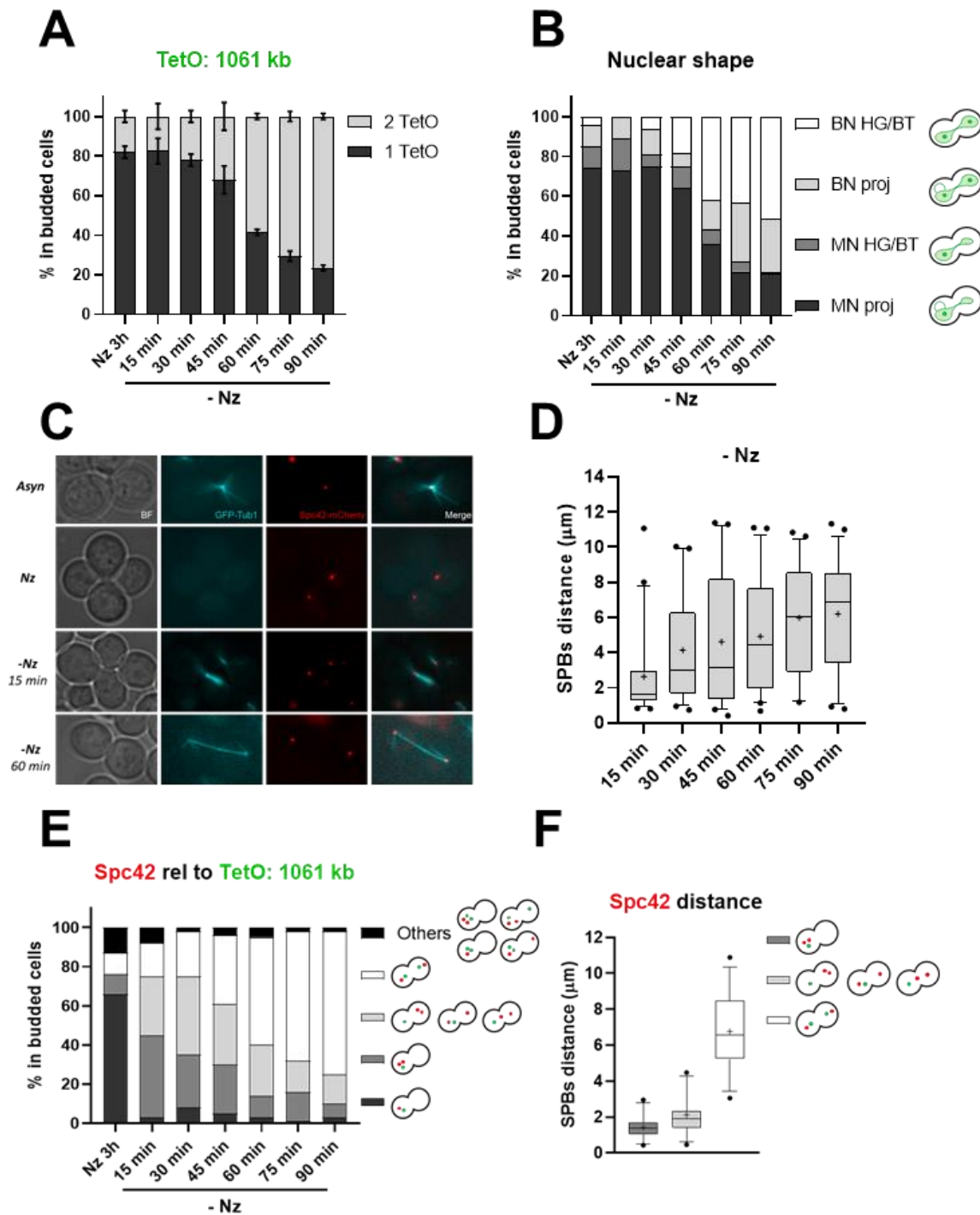


Figure 4.17. Nuclear morphology and chromosome segregation timing in a Nz release. (A) Proportion of cells displaying one or two *tetO*:1061 kb signals in a Nz release time-course (mean \pm SEM; $n = 2$). **(B)** Quantification of nuclear shape determined by TetR and Hta2 signals in a Nz release time-course. MN, mononucleated determined by 1 *tetO* signal; BN, binucleated determined by 2 *tetO* signals; HG/BT, hourglass/bowtie shape; proj., projections. **(C)** Panel of micrographs showing that microtubules are present after 15 min of Nz removal and switching temperature to 34°C (this strain carries the *ts* allele *cdc15-2* to arrest in telophase), which constitute a fully elongated spindle in many cells after 60 min. Note that the SPBs are together in the Nz arrest, as described before, but quickly start to separate in the release. Asyn, asynchronous; Nz, 3h arrest; - Nz, release; BF, bright field. **(D)** Measurements of the distance between both

4. Results and discussion

SPBs signals in a Nz release ($n = 50$ cells). Whiskers represent 5-95 percentile, mean is shown as '+' and dots represent outliers. **(E)** Quantification of Spc42 relative to the *tetO* signal as depicted in pictograms in a Nz release time-course, regarding one or two signals and presence in the same or different cell body. Most cells achieve the expected configuration of one *tetO* and one Spc42 signals in each daughter body in the final times. **(F)** Measurements of the distance between both SPBs signals in a Nz release pooling cells per category as described in (E) ($n = 30$ cells). Whiskers represent 5-95 percentile, mean is shown as '+' and dots represent outliers.

Using time-lapse microscopy and observing the position and length of the spindle in a time-course Nz release in a strain with the nucleoplasm marker mRuby2-3xNLS, we observed that in cells with horseshoe loops, the spindle is frequently positioned perpendicular to the rDNA loop (**Fig. 4.18. A**). During the time-course, most cells which still display nuclear projections are characterized by short spindles positioned at the bud neck or in the daughter cell, sometimes perpendicular relative to the division axis regardless of the timepoint (**Fig. 4.18. B**). This may explain the heterogeneity regarding SPBs distances in the Nz release in the previous figure (**Fig. 4.17. D**), because those cells are still trying to position and elongate the spindle in order to segregate, corresponding with highly dynamic microtubules, and consistent with what has been observed for *cdc20* and *cdc16* arrested cells, where the spindle is undisturbed despite the cell cycle block. When Nz is removed, cells eventually achieve proper spindle positioning and elongation, displaying equal quantities of nucleoplasm and two rDNA signals, indicating at least proper cXII division (**Fig. 4.18. C**). In agreement with Cohen-Fix data, cells apparently do not suffer segregation errors due to non-spherical nuclear morphologies caused by this mitotic delay and recover a spherical shape. Still, the timing of reaching this point differs greatly between individuals, as seen in (**Fig. 4.17. E**). However, the factors that allow a subgroup of cells to position the spindle faster than others remain elusive to us.

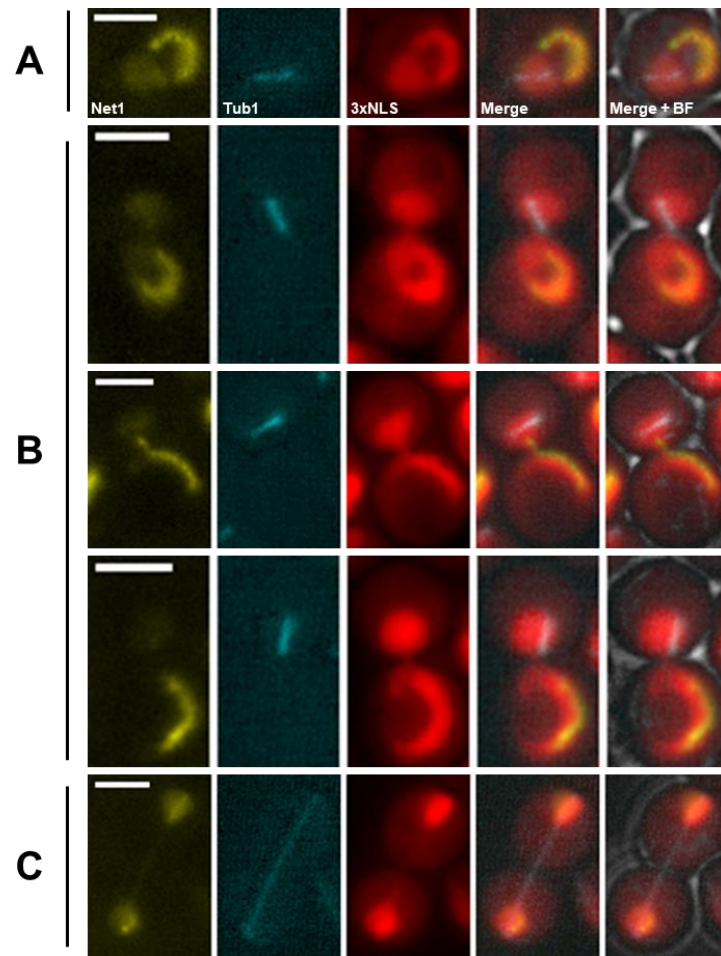


Figure 4.18. Short spindles characterize cells with nuclear projections in a Nz release. The strain in this panel possesses the following fluorescent markers: Net1-ECFP (pseudocolored in yellow), GFP-Tub1 (pseudocolored in blue) and mRuby-3xNLS. **(A)** Example where the spindle is positioned perpendicular relative to the horseshoe loop in a front view, but parallel to the division axis. **(B)** Examples of short spindles in cells with nuclear projections at different times of a Nz time course release. **(C)** Cells eventually achieve proper spindle elongation and equal division of nucleoplasm and rDNA. Scale bars, 3 μm .

Throughout the release, several nuclear morphologies arise in the transition from mid-M to late anaphase, consistent with the plethora of shapes observed in a Nz block. Strikingly, the rDNA horseshoe loop can be maintained once chromatin starts migrating through the neck, even when most of the chromatin is equally distributed between the progeny (**Fig. 4.19. A**, upper cell and **C**). Thus, nuclear projections caused by a Nz arrest can be retained in later stages of mitosis, even when both rDNA signals are resolved (**Fig. 4.19. A**, bottom cell). Occasionally, we observed uneven signal of Net1 between both daughters, although they may likely pose different degrees of compaction (**Fig. 4.19. B**). Remarkably, once the rDNA has been segregated, we frequently detected denser spots of Hta2 signal lagging behind, suggesting a high compaction of the distal part of cXIIr, from

4. Results and discussion

the rDNA distal flank to the telomere (**Fig. 4.19. C**, indicated by arrowheads). This is quite similar to the Hta2 intense spots we observed at the apex of nuclear flares in the Nz arrest, right on top of the rDNA signal of protruding bars.

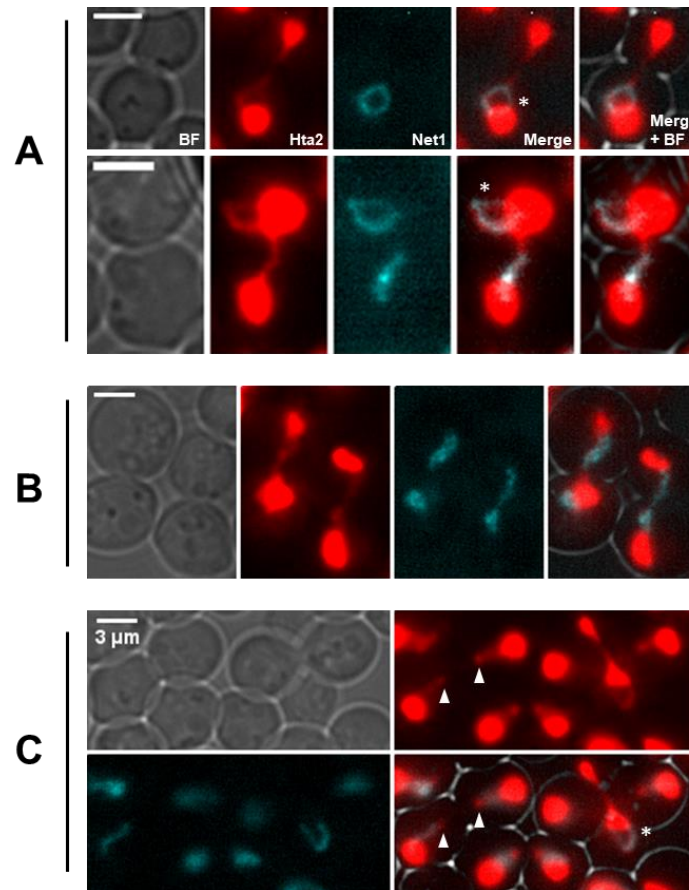


Figure 4.19. The rDNA horseshoe loop can remain until late stages of mitosis. (A) In these two examples of a Nz release, the rDNA horseshoe loop remains when most of the histone signal is evenly distributed. In the upper cell, a single rDNA signal indicates that cXII has not been segregated, while in the bottom cell, there are two Net1 signals, suggesting rDNA segregation is complete, despite both nuclear masses are still linked by a histone thread. **(B)** Eventually, rDNA segregation occurs, although in some cases the Net1 signal is unequal between both daughter cells, as in the left cell. **(C)** Spots of higher intensity histone signal are frequently observed when cXII are migrating to the opposite poles (indicated by arrowheads), presumably corresponding to the subtelomeric region. Asterisks indicate horseshoe loops. Scale bars, 3 μm.

Interestingly, in time-lapse microscopy films, we observed a pattern of movement similar to what have been described for the mid-M arrest triggered by APC inactivation, in which most of the chromatin resides in the daughter cell, while the rDNA remains in the mother, showing highly dynamic movements referred to as DNA transits (**Fig. 4.20. A**). Apparently, once cells are allowed to resume cycling after Nz removal, they continue to divide first by acquiring intermediate phenotypes characteristic of the APC inhibition induced arrest, and then continue to seek an hourglass morphology until karyokinesis is

achieved (**Fig. 4.20. B**). This would place the Nz arrest upstream to the mid-M block caused by APC inactivation regarding cell cycle timing, presumably taking longer to end mitosis. Despite the appearance of all these morphologies that deviate from the classic hourglass mitosis, including stages of uneven DNA mass proportion between mother and daughter, cells seem to be able to correct them and achieve proper segregation and proceed to the next cycle if given enough time. However, similar to what has been observed for APC mutants, cells seem to possess a mechanism to maintain the rDNA in the mother cell until most of the chromatin has been equally divided, proceeding then to rDNA segregation.

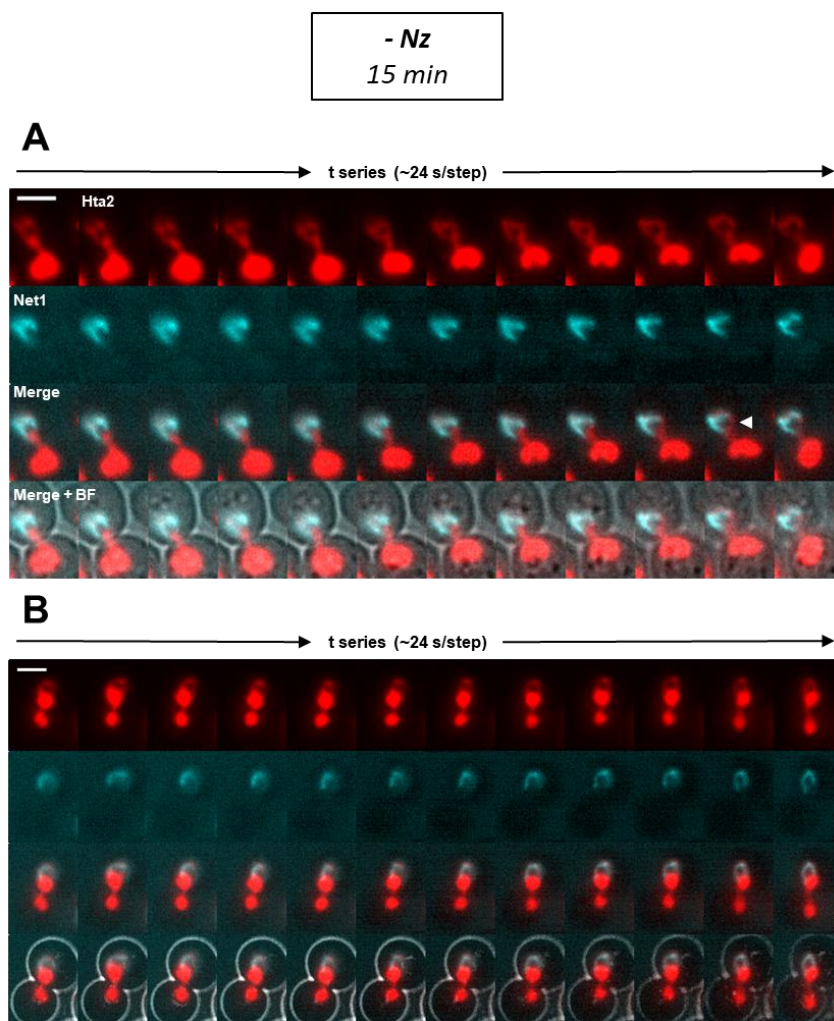


Figure 4.20. Cells in a Nz release exhibit morphologies reminiscent to the ones observed after APC inhibition. (A) Short time-lapse of a Nz released cell in which most of the chromatin resides in the daughter body, while the rDNA remains in the mother, like what we observed before in the *cdc16aid* mutant. The overlap between the histone and Net1 signals change in time, and part of the handle is non-coated by Net1, as we observed for partial loops in the first chapter (white arrowhead). In this example, the chromatin mass in the daughter cell appears to be pulled back, losing the rounded shape in favor of a kidney shape, and then released again from tension,

4. Results and discussion

recovering the previous shape. **(B)** In this example, chromatin followed by the histone signal has a general bowtie shape, expanding across the division axis in time, and is more evenly distributed, despite the mother cell having an rDNA horseshoe loop. Scale bars, 3 μm . Frames are separated by 24 s.

4.2.2. Remaining nuclear projections in a Nz release colocalize with vacuoles

Because we described that nuclear extensions in a Nz arrest colocalize with vacuoles, we investigated if this association was maintained in the release. Indeed, this was the case. Either one big vacuole or groups of small vacuoles nearly always colocalized with nuclear projections after Nz removal, regardless of their shape (**Fig. 4.21. A and B**). Even in very late stages of mitosis when rDNA has been segregated, if nuclear projections are present, they are found in close association to vacuoles (**Fig. 4.21. C**).

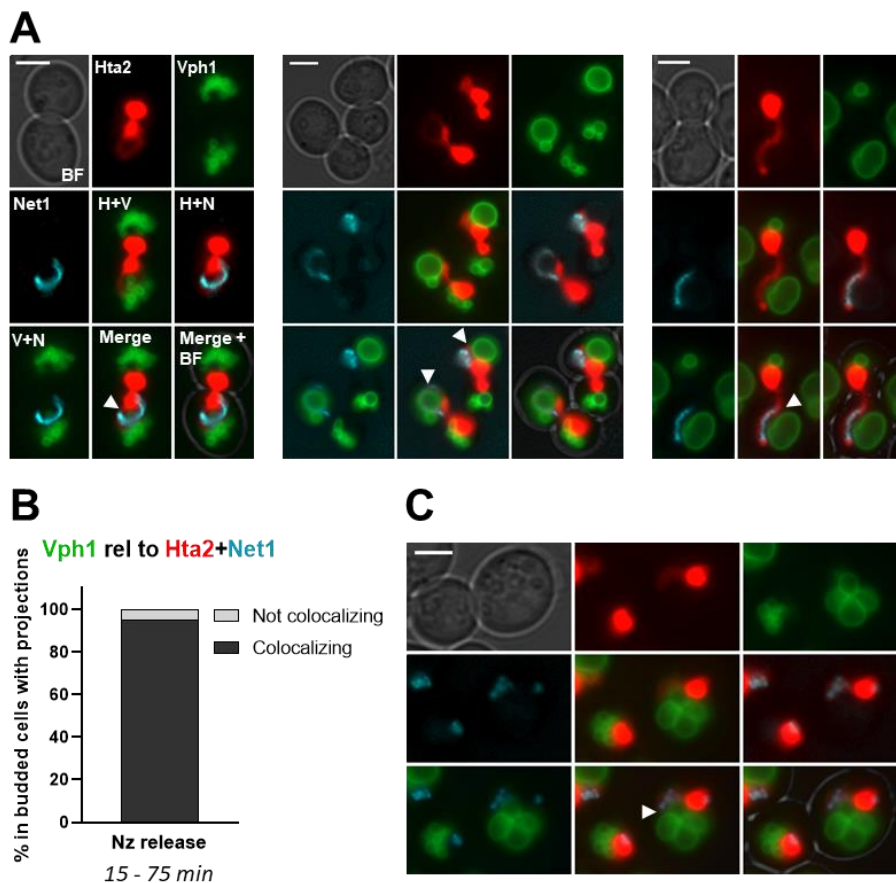


Figure 4.21. Vacuoles still associate with flares and loops after Nz removal. (A) Examples of Nz released cells with nuclear projections of different shapes, all associated to one big vacuole or a group of smaller vacuoles, indicated by arrowheads. **(B)** Quantification of Vph1 colocalization with histone and/or Net1 projections in a representative Nz release experiment. ~250 cells were pooled from timepoints between 15 and 75 min after Nz removal. **(C)** Example of a cell that presents a nuclear projection in contact with vacuoles in telophase (arrowhead). Scale bars, 3 μm .

Whether this proximity involves nuclear-vacuole junctions, or it is just a consequence of the volume vacuoles occupy within the cell, remains to be investigated. However, the closeness of rDNA loops and flares regarding vacuoles, suggest there may be a mechanism linking them. Because the nucleolar region has been described as a membrane sink upon phospholipid overproduction (Witkin et al., 2012), being apparently more capable to cope with nuclear membrane overexpansion than the rest of the NE, an increased contact area with the organelle in charge of recycling cellular components would result useful, possibly coupling the process of NE remodeling by degrading membrane excess. This increased contact may favor the PMN pathway targeting the degradation of nuclear components via NVJ uptake. However, a step of clearance of the rDNA from the NVJ would be essential to avoid DNA uptake by the vacuole and its degradation. This process has been described to be carried out by the CLIP and cohibin complexes in conjunction to separate the DNA from nucleolar proteins (Mostofa et al., 2018).

4.2.3. The exit from a Nz-induced mid-M block triggers autophagy activation

Next, we decided to investigate if autophagy was involved in the process of nuclear reshaping after Nz removal. Because this process oversees recycling of cellular materials, it would be logical that autophagy may be activated to remove the nuclear membrane excess accumulated in a mitotic arrest. For this purpose, we used the conventional GFP-Atg8 tagging for microscope visualization (Backues & Klionsky, 2022; Geng et al., 2008; Nair et al., 2011). This protein localizes at incipient phagophores as well as growing and mature autophagosomes before vacuolar uptake (thus, giving rise to foci usually at the vacuole periphery) and is used as a marker for general autophagy activation, although it is involved in macro and micronucleophagy as well, as we described in the introduction (Otto & Thumm, 2021). We used a GFP-Atg8 centromeric plasmid kindly provided by Yoshiaki Kamada (NBRP ID: BYP9641; plasmid name: pRS314[GFP-ATG8]).

Our data agrees with previous knowledge which situated a baseline level of autophagy in which approximately 30% of cells display at least one GFP-Atg8 focus (Reggiori & Klionsky, 2013). Furthermore, we noticed this level did not change in the mitotic arrest caused by Nz exposure (**Fig. 4.22. A**), which suggests that nuclear membrane accumulation keeps a steady rhythm in a mitotic arrest, not being constantly turned over while new membrane is synthesized. These foci often colocalized with the

4. Results and discussion

rDNA horseshoe loop, that we now know is shaped by the vacuole (**Fig. 4.22. B**). To determine the level of autophagy activation during the Nz release, we further divided the culture in two after Nz removal and added rapamycin to one of them to induce autophagy due to TOR inactivation. As expected, there was a rapid increase in autophagy in the rapamycin treated culture, which serves as a positive control for autophagy stimulation, in which nearly 80% of cells had at least one GFP-Atg8 focus. Strikingly, when Nz was removed in cells without rapamycin addition, the percentage of cells displaying at least one GFP-Atg8 focus gradually increased in time up to a 60% after 90 min, nearly doubling baseline levels (**Fig. 4.22. C**). These foci were found both in the mother and the daughter bodies, using the rDNA single signal presence as reference of the mother cell (**Fig. 4.22. D**).

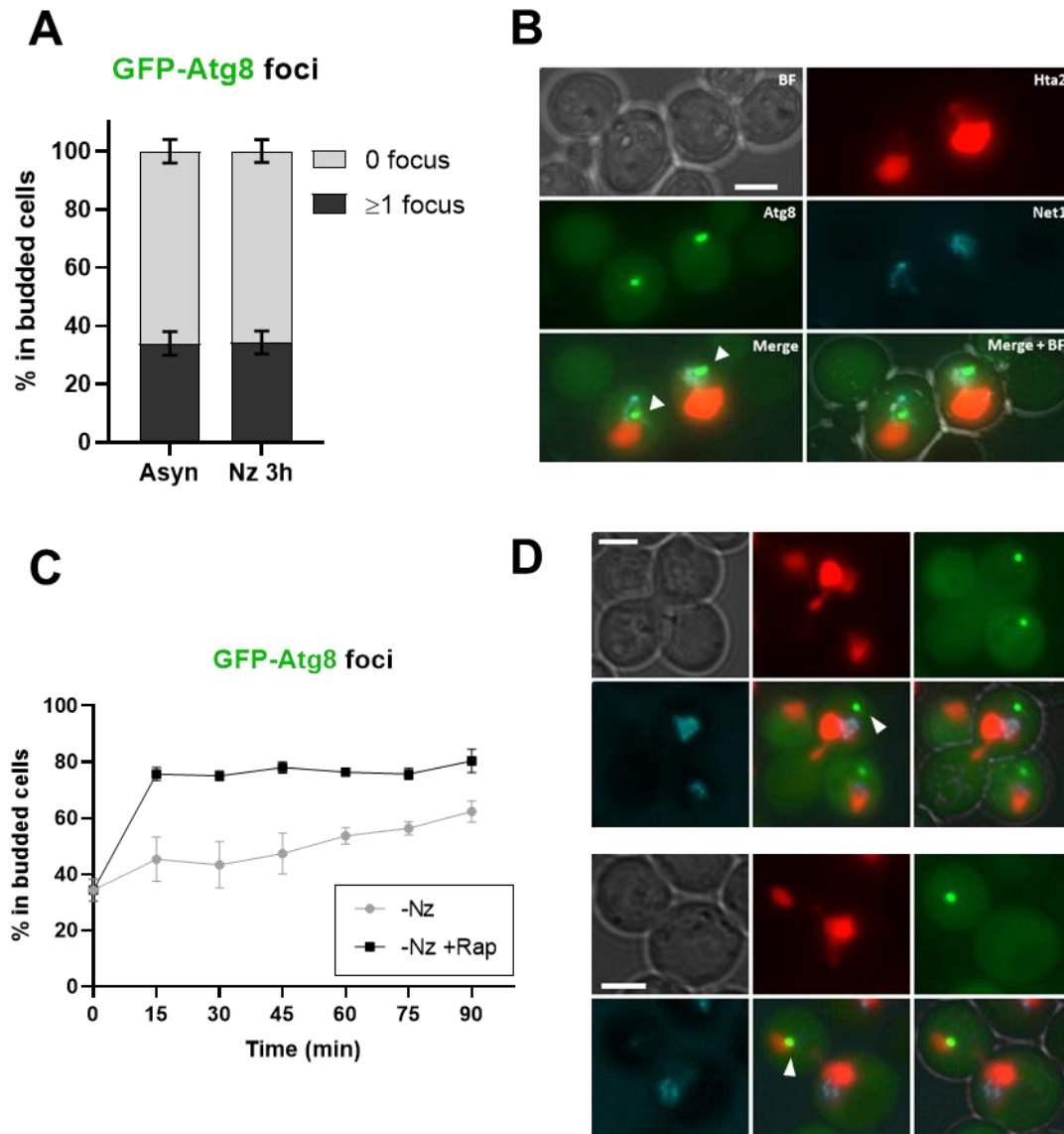


Figure 4.22. A Nz release triggers autophagy activation. (A) Proportion of cells displaying at least one GFP-Atg8 focus in asynchronous and Nz arrested cells (mean \pm SEM; $n = 3$). **(B)** Two examples of Nz arrested cells with rDNA horseshoe loops in contact with GFP-Atg8 foci (marked with arrowheads), presumably at the vacuole periphery, which allocates in the SUL. **(C)** Proportion of cells displaying at least one GFP-Atg8 focus in a Nz release time-course experiment. Nz arrested cells were split into after Nz elimination, one culture was treated with rapamycin to serve as autophagy positive control, while the other remained untreated (mean \pm SEM; $n = 3$; some error bars in the -Nz +Rap timepoints are not observable due to their small size, and thus are hidden by the software used to plot data). **(D)** Examples of Nz released cells in which the GFP-Atg8 focus can be located in the mother (top example) or daughter cell (bottom example), indicated by arrowheads. Scale bars in B and D, 3 μ m.

These results unveil a role of the autophagy pathway after a mitotic block. It would be interesting to test whether autophagy inhibition disturbs cell cycle continuation or if it has an impact in nuclear morphology. If our hypothesis that nucleophagy takes place after Nz removal to eliminate nuclear membrane excess were true, we would expect nuclear

4. Results and discussion

deformation upon autophagy abrogation. Also, to confirm that this increase in autophagy is caused by membrane overexpansion and not only because of the arrest, the study of GFP-Atg8 foci would be interesting in the release of cells arrested in mid-M upon coincubation of Nz with cerulenin, which we know renders spheric nuclei due to FAS inhibition. We cannot confirm an increase in either macro or microautophagy at this point because this tool is not specific of these branches, but rather a common feature of autophagy, so we cannot rule out that other cellular compartments participate in this process. It remains to be seen whether Atg39, the specific cargo receptor for nucleophagic processes, is essential for NE recycling after a Nz block-and-release.

4.2.4. The metaphase to end of mitosis transition occurs faster after a mitotic delay without microtubule depletion

Continuing the approach we used in the first part of the results, we used again the *cdc16aid* model to characterize the mid-M release after a mitotic block and compare it with the results obtained with Nz. Strikingly, we observed that *cdc16aid* cells continued cycling and completed cXII segregation, as indicated by *tetO*:1061 kb, much faster than Nz released cells. More precisely, after 45 min of IAA removal, approximately 90% of cells had segregated the cXIIr telomere, which is the last part of the region to segregate (**Fig. 4.23. A and B**). Furthermore, if we categorize cells by their nuclear morphology, we observe that after 60 min of IAA removal around 90% of cells have recovered the hourglass morphology besides completing DNA segregation (**Fig. 4.23. C**). Taking a closer look at the proportions showed in the time-course release experiments, we observed the biggest change between 30 and 40 min, marking the time needed to achieve the transition between the arrest and the end of mitosis. Interestingly, the category in which cells display a single *tetO* but have a bowtie or hourglass morphology (**Fig. 4.23. D**) is not represented after the 60 min, probably because this population of cells achieved the BN status as they did not need to fix nuclear membrane extensions and could proceed faster. The remaining ~10% after 60 min is split between MN and BN cells which still possess non-spherical nuclear morphologies, which possibly end up being removed in posterior steps.

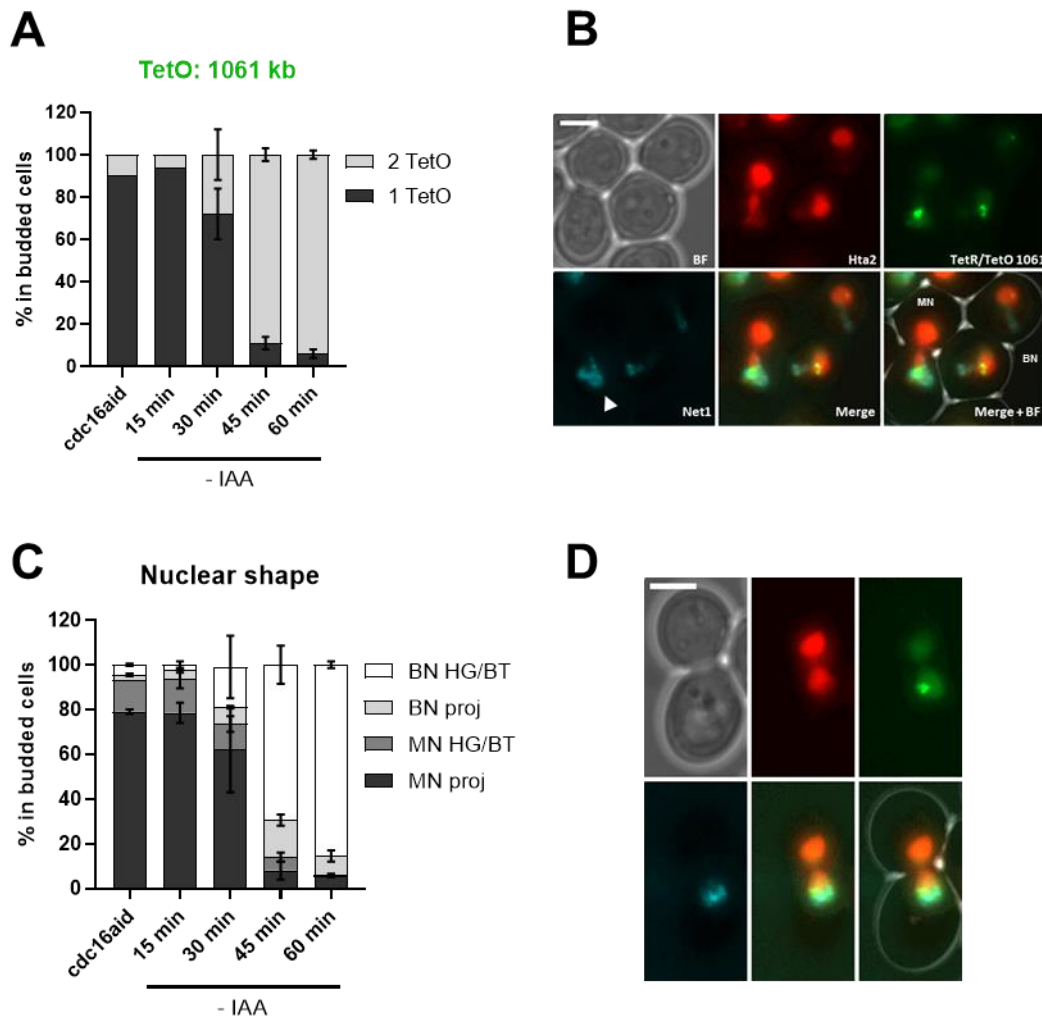


Figure 4.23. *Cdc16aid* cells complete segregation faster than Nz released cells. (A) Proportion of cells displaying one or two *tetO*:1061 kb signals in a *cdc16aid* release time-course experiment (mean \pm SEM; $n = 2$). **(B)** Representative examples of MN and BN cells with nuclear projections in the experiment quantified in (A and C). The MN cell has the histone signal spanning the bud neck and an rDNA loop in the mother body (indicated by an arrowhead), while the BN cell has already segregated cXII, as indicated by the two Net1 and *tetO* signals, in which both nuclear masses have a small hairpin loop or flare formed by the rDNA. **(C)** Quantification of nuclear shape in a *cdc16aid* release time-course experiment (mean \pm SEM; $n = 2$). MN, mononucleated determined by 1 *tetO* signal; BN, binucleated determined by 2 *tetO* signals; HG/BT, hourglass/bowtie shape; proj., projections. **(D)** Example of a MN *cdc16aid* cell from the IAA block-and-release experiment with a nearly perfect bowtie nuclear morphology, with the rDNA capping the lobe in the mother cell in a crescent like shape. Scale bars in B and D, 3 μ m.

Thus, if we compare these results with the Nz time-course release, we observe that *cdc16aid* cultures achieve segregation and recover proper nuclear morphology earlier than Nz released cells (60 min vs > 90 min). The main difference between both mid-M blocks reside in the absence of microtubules in the Nz arrest. We assume that the reason behind this difference in timing resides in the extra time needed to reassemble and correctly reposition and elongate the spindle to proceed to anaphase, as we stated before

4. Results and discussion

that nuclear projections are apparently corrected after segregation, in agreement with data from the Cohen-Fix laboratory.

We evaluated the data from the experiment in the previous figure and represented the proportion of MN and BN cells which display nuclear projections vs an hourglass/bowtie shape, which clearly shows that most cells with nuclear projections are MN. Indeed, we prepared a 2x2 contingency table, counting the MN cells from the arrest and pooling the BN cells from the release (timepoints from 30 to 60 min), and ran a two-tailed Fisher's exact test, which shows statistically significant differences between the MN and BN groups regarding nuclear shape ($p < 0.0001$) (**Fig. 4.24. A**). The choice to only select MN from the arrest and BN from the release is done to make sure we are only picking properly and timely arrested MN cells, as well as cells which are BN after they have been released from the mid-M block, thus avoiding counting cells which are MN or BN asynchronously, escaping the block. Of note, not all nuclear projections detected by nucleoplasm presence contain the rDNA (**Fig. 4.24. B**). It does not happen frequently, but we have observed cases in MN and BN cells. However, we cannot rule out that this type of extensions in MN cells are due to normal shaped nuclear division, because at early stages we cannot differentiate the finger-like projection which evolves into a bowtie shape from the ones that stay like this, as extended nuclei traverse through the bud neck in *cdc16aid* mid-M arrested cells. Thus, we decided to compare whether the presence of the rDNA in these projections differs between MN and BN cells. Again, we prepared a 2x2 contingency table and ran a two-tailed Fisher's exact test, which renders a non-statistically significant p-value ($p > 0.05$), meaning that the rDNA occupies nuclear extensions equally in pre- and post-anaphase cells (**Fig. 4.24. C**).

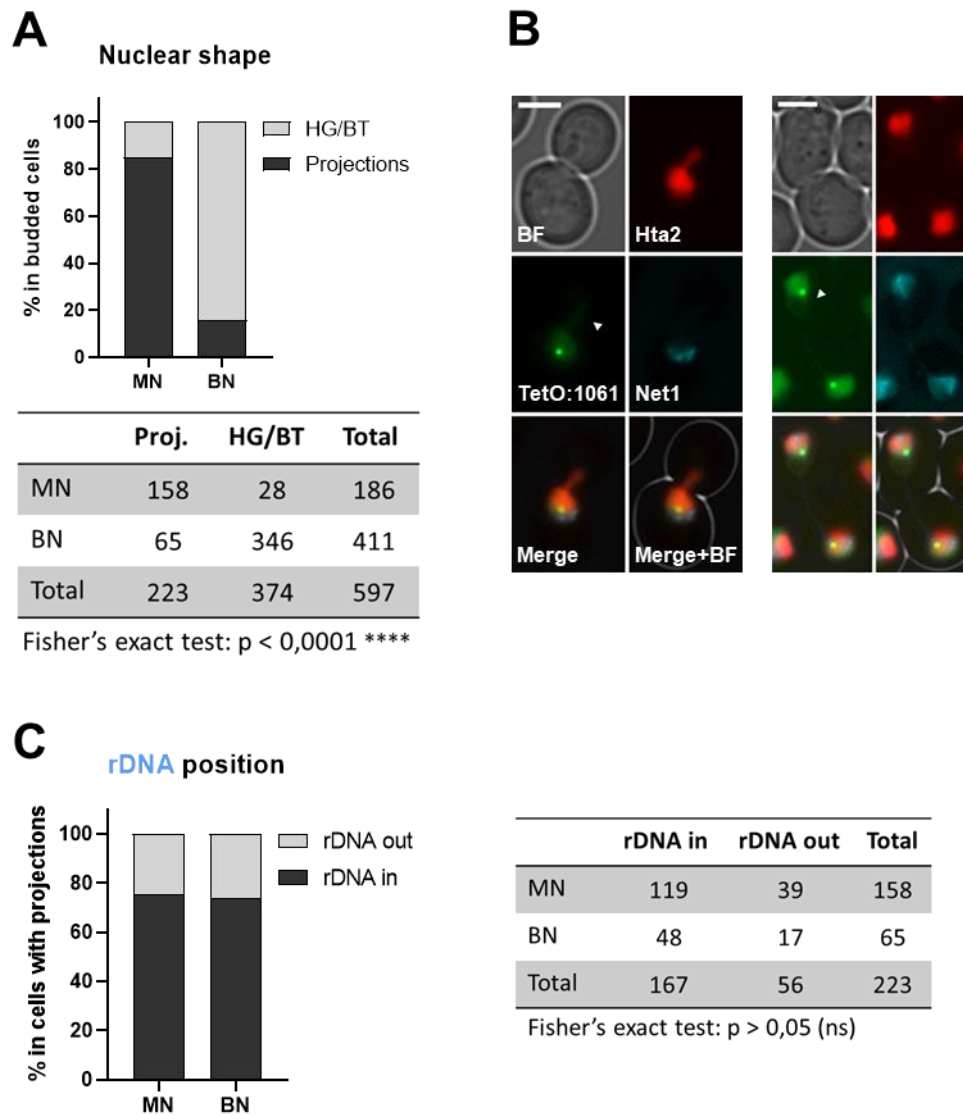


Figure 4.24. Nuclear projections containing the rDNA in a *cdc16aid* block-and-release are present mainly in MN cells. (A) Proportion of MN vs BN cells, as measured by presence of one or two *tetO:1061* kb signal(s), which exhibit bowtie/hourglass shape or nuclear projections. MN cells counted belong to the 3 h arrest timepoint, while BN are pooled from timepoints between 30 and 60 min. Below, a 2x2 contingency table of the plotted data, used to perform a two-tailed Fisher's exact test. **(B)** Microscopy examples of a MN (left) and BN (right) cell with nuclear projections in which the rDNA is not present. Scale bars, 3 μ m. **(C)** Proportion of nuclear projections which contain or not the rDNA in MN and BN cells. On the right, a 2x2 contingency table of the plotted data, used to perform a two-tailed Fisher's exact test. MN, mononucleated determined by 1 *tetO* signal; BN, binucleated determined by 2 *tetO* signals; HG/BT, hourglass/bowtie shape; proj., nuclear projections.

4.2.5. Effect of nuclear membrane excess and defect in survival and genome integrity

To further complete our study, we examined the effects of membrane imbalances on cell viability. With this purpose, we used a set of diploid strains which allow phenotypic

4. Results and discussion

evaluation of genomic rearrangements by their colony color and sectoring pattern on YPD plates. These strains were created by mating cells with two different backgrounds with ~ 0.5% sequence divergence, i.e. W303 (JSC12) and YMJ789 (JSC21) (Lee et al., 2009; Lee & Petes, 2010), which are differentiated by more than 55,000 SNPs along the genome, heterozygous in the resulting diploid strain (Wei et al., 2007). Furthermore, both parental haploid strains bear two different markers on the right arm of chromosome IV (*KanMX/can1-100* in the W303 and the *SUP4-o* allele in the YMJ789 strain), which is one of the largest chromosomes, together with cXII, at position 1,510,386 bp. Also, they both are *ade2-1* mutants, which corresponds to an ochre mutation at position 190 within the *ADE2* gene and makes haploid and diploid homozygous strains form red colored colonies. On the other hand, the allele *SUP4-o*, an ochre suppressor tRNA gene, inhibits this phenotype and colonies become white colored by suppressing the *ade2-1* mutation. In diploids bearing only one copy of *SUP4-o*, colonies are pink as an intermediate phenotype between red and white (Andersen & Petes, 2012; Barbera & Petes, 2006; St Charles & Petes, 2013). Besides the aforementioned diploid, we used another one developed by mating strains PSL2 (W303) and PSL5 (YJM789), which is similar in rationale but with the color reporting system designed for chromosome V instead (St. Charles et al., 2012).

In our experimental approach, overnight cultures from these two strains were divided in four. Each culture was treated with Nz, cerulenin, a cotreatment with Nz together with cerulenin or left untreated as reference of growth in rich medium, while a sample from YPD was plated at $t = 0$ as a starting point reference. We performed clonogenic assays by plating on YPD after the 3h in the different conditions and incubated them until colonies were easily visible. We counted CFUs on each plate (**Fig. 4.25. A**) and then referenced all conditions to our 3h asynchronous culture, as it represents the maximum growth they would achieve in normal conditions when left untreated. We observed a decrease in CFUs in all conditions when compared to the control (**Fig. 4.25. B**). However, in the treatments involving Nz we cannot say that it is caused by increased cell death, because Nz induces a cell cycle arrest, meaning that cells are not able to double as much as their control counterparts. Regarding Cer, it is known that it is an antifungal agent and indeed, it caused a survival drop of ~ 40% compared to the asynchronous culture. The coincubation of both agents reduced colony count to approximately 25%, and we decided to investigate if there was a suppressive effect of cerulenin in Nz fitness by applying the multiplicative fitness

model, comparing expected and observed frequencies (**Fig. 4.25. C**), and then testing the mean value against 0 with a one sample t test, which indicates that there is no difference between expected and observed frequencies (**Fig. 4.25. D**). Indeed, this result suggests that these two drugs act independently, with a simple additive effect, so they do not cause synergism or suppression when combined. This supports our proposal that yeast cells are able to deal with nuclear projections before it has an impact on cell survival.

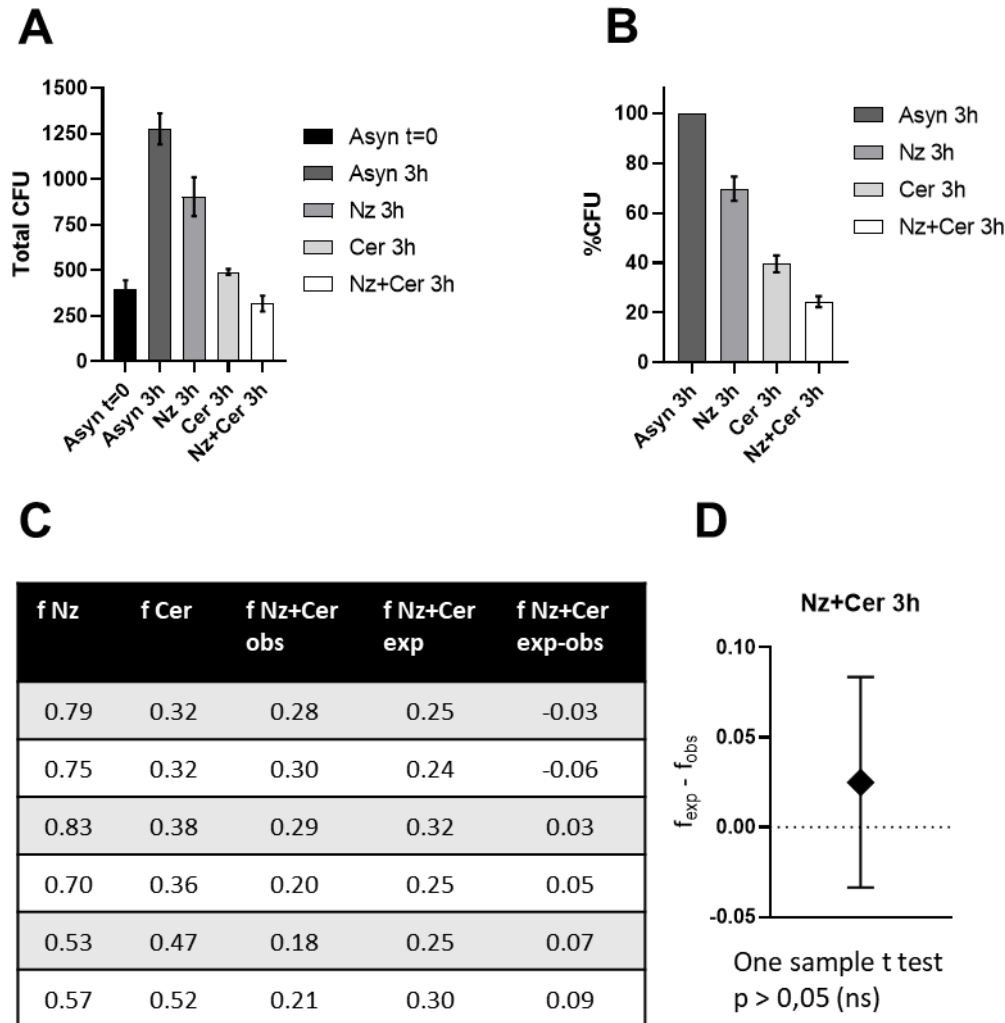


Figure 4.25. Effect of Nz and cerulenin on cellular survival in diploid cells. (A) Total CFU count of clonogenic assays from an overnight culture (t=0) treated with Nz, Cer, Nz + Cer and an untreated control for 3 h (mean \pm SEM; n = 6). **(B)** Percentage of CFUs after the 3 different treatments referenced to the 3 h asynchronous culture (same data from (A)). **(C)** Table of the observed frequencies of 6 individual replicates plotted in (B) for Nz, Cer and Nz + Cer. The expected frequency for independent contributors of Nz + Cer was calculated applying the multiplicative fitness model, and then the difference between the expected and observed values was calculated for each replicate. **(D)** The mean value of the difference between the expected and observed frequencies was tested using a one sample t test (mean \pm SD; n = 6). Asyn, asynchronous; Cer, cerulenin; obs, observed; exp, expected; f, frequency; ns, non-significant.

4. Results and discussion

Due to the difficulty to assess the color of the PSL2/PSL5 diploid, whose pink colonies were nearly white, we could only use the clonogenic assays of this strain for survival count, not to assess color categories for genomic rearrangement detection. To phenotypically evaluate genomic rearrangements, we used the clonogenic assays of the JSC21/JSC12 strain. We observed that the number of colonies which were not pink was maintained barely unchanged between all conditions; only the coincubation of Nz and Cer increased non-pink colony count (**Fig. 4.26. A**). Then, we categorized the non-pink colonies into four: white, red, and colonies which presented sectors, either white or red, each indicating different types of rearrangements which affect chromosome IV and the *SUP4-o* allele, and thus colony color acquired by the ochre *ade2-1* mutation (**Fig. 4.26. B**). Most non-pink colonies in all conditions were red or white, and sectoring was hardly ever found. In the cotreatment of Nz and Cer, the count of red colonies coincides with the other conditions, and the category that increased the total non-pink count was white colonies, which account for cells with two copies of the *SUP4-o* allele, while the red ones have lost both copies. The exact nature of these genomic rearrangements could be studied subjecting these clones to further phenotypic testing on different selective media (assessing loss and gain of different resistance to auxotrophic markers or antibiotics) and Comparative Genomic Hybridization. However, the deviation between the different replicates suggests there is not a significant increase in genome instability.

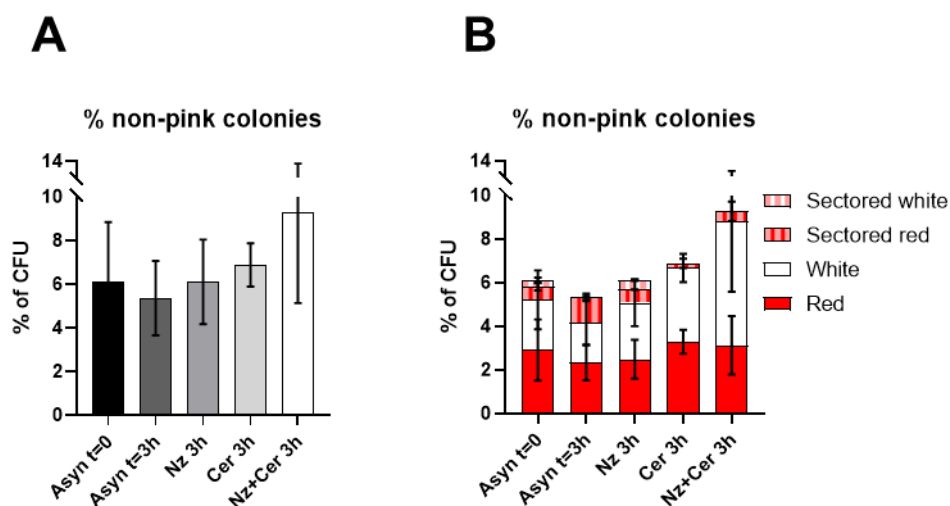


Figure 4.26. Genomic rearrangements in diploid cells apparently increase in Nz and Cer cotreatment. (A) Proportion of the sum of non-pink colonies of the clonogenic assays of Nz, Cer and cotreatment (mean \pm SEM; $n = 2$). (B) Data from (A) categorised by colony color pattern. Note that the y axis has been cut to allow better visibility of the differences between categories due to large error bars.

Because in the diploid strains we apparently found no correlation between Nz and Cer exposure with an increase in genomic rearrangements, we decided to use a haploid strain to evaluate genome integrity through PFGE and DNA damage checkpoint activation through the phosphorylation of the protein Rad53, which becomes hyperphosphorylated in response to DSBs, among other DNA insults, such as replicative stress (Sanchez et al., 1996; Santocanale & Diffley, 1998; Sun et al., 1996; Tercero & Diffley, 2001). The experimental design we used included three subcultures from an overnight asynchronous culture (**Fig. 4.27. A**), which was first divided in two, one treated with Nz and the other Nz together with cerulenin for three hours. After the mid-M block, the Nz treated cells were released and sampled at 30, 45 and 60 min (line a), while the cotreatment culture was split into two again, Nz was removed from both, but Cer was added again in one of them (lines b and c respectively), so cells were allowed to resume cycling but without FAS activity and samples were taken as described for the Nz release. The Western blot revealed that Rad53 phosphorylation levels appear to be slightly higher in Nz released cells (line a) compared to the asynchronous culture but remained constant through the release (**Fig. 4.27. B**). However, in Cer treated cells Rad53 appears not to have a clear increase in phosphorylation levels after Nz removal (the multiband presentation of phosphorylated Rad53 is not seen despite the retardation observed on the right of the gel) (**Fig. 4.27. C**). Furthermore, the PFGE revealed that in all conditions where cells have been exposed to Cer, there is a decrease in signal intensity corresponding to the largest chromosomes, while it is noticeable for neither the rest of the chromosome bands nor in all lanes of Nz only treated cells (**Fig. 4.27. D**). Apparently, yeast haploid strains do not have an increase in DSBs appearance after a Nz arrest, maintaining genome integrity despite nuclear deformation. Of note, I have only been able to perform a single replicate of these experiments due to time limitation, which need further confirmation to support these observations, which may imply interesting insights into the mechanism of action behind cerulenin antifungal activity.

4. Results and discussion

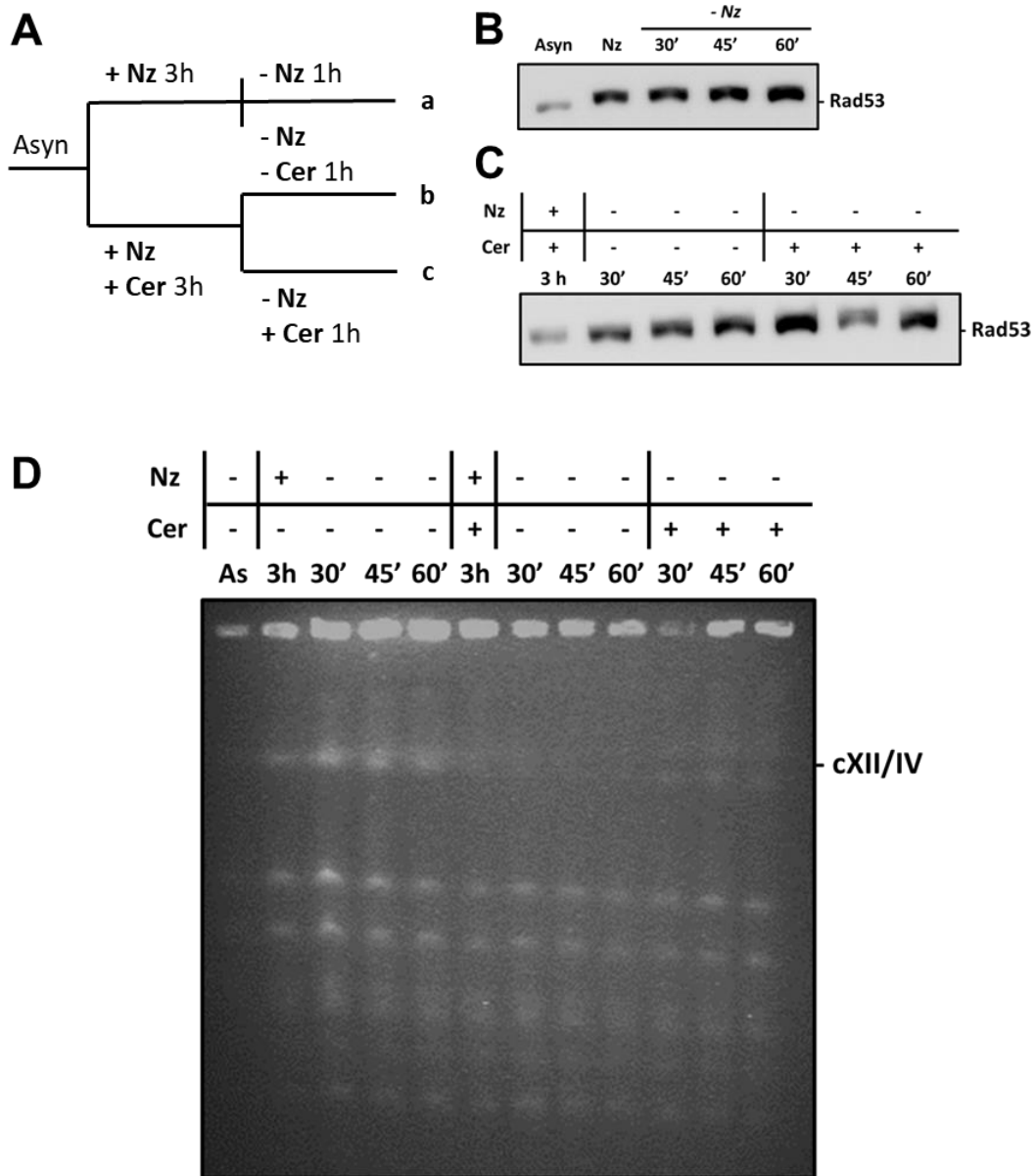


Figure 4.27. Chromosome integrity appears to be compromised in haploid yeasts after Nz and Cer combined exposure. (A) Experimental approach used in these experiments. An asynchronous culture was divided into two, one was treated only with Nz and the other with Nz combined with Cer for 3 h. After the mid-M block, Nz was removed from both, but the cotreatment culture was split again and Cer was added back to one of them after the medium had been washed. (B) Western blot against Rad53 of a Nz block-and-release, which corresponds to line a in (A), to detect phosphorylation levels. (C) Western blot against Rad53 of Nz arrested cells in the presence of Cer and their release without the readdition of Cer (line b, samples 2 – 4) or readding Cer (line c, samples 5 – 7). (D) PFGE of the experiment described in (A) using conditions to accurately resolve cXII.

In sum, cells appear to fully recover nuclear shape and complete accurate segregation despite excess nuclear membrane accumulation due to mitotic arrests, meaning that mitotic blocks which alter nuclear morphology do not pose a risk in the budding yeast genome stability and survival.

4.3. Study of chemical compounds with potential to alter nuclear shape and cell cycle progression

During the development of this work, we collaborated with the company CEAMED S.A. (Centro Atlántico del Medicamento S.A.), which provided us with newly developed chemical compounds they synthesized to be tested for toxic effects on our yeast model. The main interest of this company consists in the development of new anticancer drugs, based on natural products from the Canary Islands. More precisely, these agents were designed to find new treatments against the chronic myeloid leukemia (CML) whose patients present resistance to the treatment with Imatinib (Gleevec®), which constitutes one of the main chemotherapeutic agents used to fight this disease, and thus have the need of an alternative drug. CML is a type of cancer that starts in the myeloid cells of the bone marrow, occurs mostly in adults (average age at diagnosis is 64 years) and accounts for ~10-15 % of leukemias, according to the American Cancer Society. Consequently, we used the budding yeast as a tool to easily evaluate microscopic changes in nuclear morphology and chromatin after exposure to these new compounds designed to complement or substitute Imatinib.

In previous works undertaken by our group, two chemical agents, named CM-568 and CM-728, were found interesting due to cytotoxic effects on halo assays and growth curves, whose profiles pointed towards a mechanism of action related to oxidative stress, although this remains to be confirmed. These molecules are derived from quinones fused to oxazepins, although their specific molecular structures are protected by a patent and will be disclosed when published.

Thus, because yeast poses a cheap and easy-to-use model to screen compounds, we used it to evaluate the effect of exposure to these drugs on the yeast nuclear morphology and ability to complete a cell cycle.

Due to the high resistance yeast have to xenobiotics because of the pleiotropic drug resistance systems, and also after previous data obtained in our group with other chemical entities, in our first experiment we used a relatively high concentration, i.e. 100 μ M. The experimental rationale lies on the synchronization of a yeast culture in G1 in reach media, which is then released from the block and split into two. One of the cultures was kept as a control, in which 1% DMSO is added (the drug's vehicle), while the other was treated with either CM-568 or CM-728, and the temperature switched to 34°C to block again

4. Results and discussion

cells in telophase thanks to the *cdc15-2* ts allele (**Fig. 4.28. A**). With this approach, we pretended to evaluate the number of cells which accurately reached telophase, with segregation of the two *tetO*:1061 kb, as well as their nuclear shape after being exposed to the drug throughout a single cell cycle. After this first experiment, we observed that cells from the control culture accurately reached telophase, and they formed pseudohyphae, which is known to happen in *cdc15-2* arrests. However, in both cultures exposed to CEAMED drugs at the aforementioned concentration, cells could not exit from G1, according to cellular morphology on the bright field. There was nearly a complete loss of fluorescent signal for Net1-ECFP and the TetR-YFP, while the histone signal appeared highly packed (**Fig. 4.28. B**), suggesting a high toxicity which triggered a strong stress response or, perhaps, even cell death.

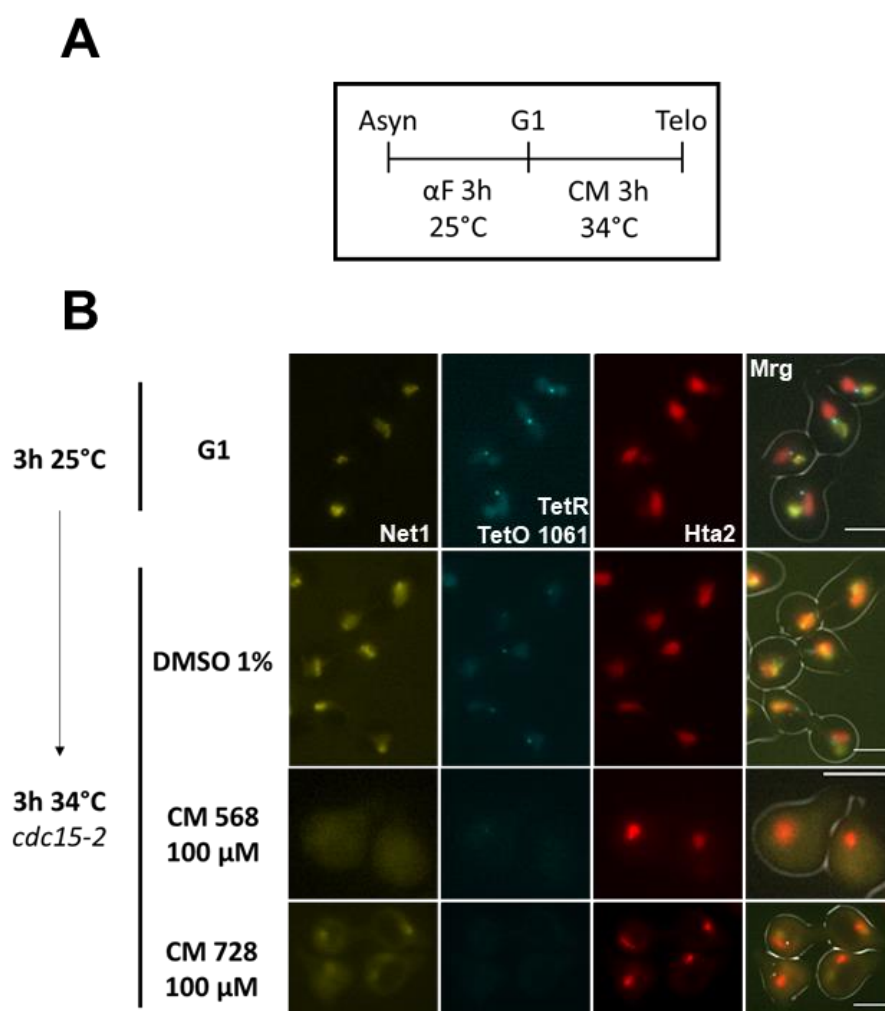


Figure 4.28. Exposure to CM-568 and CM-768 at 100 μ M is toxic for yeast cells. (A) Schematic for the experimental approach used to evaluate chemical compounds from CEAMED S.A., which consists of a G1 arrest and release to telophase. **(B)** Representative microscopy examples of the experiment described in (A). A concentration of 100 μ M inhibits exit from G1 and

provokes disturbances in microscopy signals (loss of CFP and YFP signals and Hta2 hypercompaction). Control cells exposed to the vehicle (DMSO) reached telophase despite showing pseudohyphae due to the *cdc15-2* allele. Note that micrographs are pseudocolored: Net1-ECFP (yellow), TetR-YFP (cyan) and Hta2-mCherry (red). Mrg, merge. Scale bars, 5 μm .

Hence, we confirmed that a concentration of 100 μM inhibits cell cycle progression and thus proceeded to assay a range of concentrations to evaluate the dose-response using the same experimental approach. The chosen concentrations were: 100, 10, 1, and 0.1 μM . Surprisingly, we observed for both compounds that not even a decrease in concentration of the drug down to 1 μM allowed exit from G1 (**Fig. 4.29. A and B**). However, dropping the concentration to 10 μM recovered the Net1 and TetR signals, although the histone signal was still condensed. We manually measured the chromatin area using the Hta2 signal perimeter in all assayed concentrations for CM-728, since both chemicals behaved similarly (**Fig. 4.29. C**). We observed that the histone area was recovered to normal conditions, compared to untreated asynchronous cells, when the concentration was ≤ 1 μM . Interestingly, in G1 the nuclear area is increased, as cells show nuclear projections already characterized elsewhere (Stone et al., 2000), which we also observed in panels A and B in the G1 arrest. Finally, only cells subjected to 0.1 μM were able to reach telophase and segregate the rDNA and the subtelomeric *tetO* at cXIIr, which they did nearly in a 100 % of the cases (**Fig. 4.29. D**).

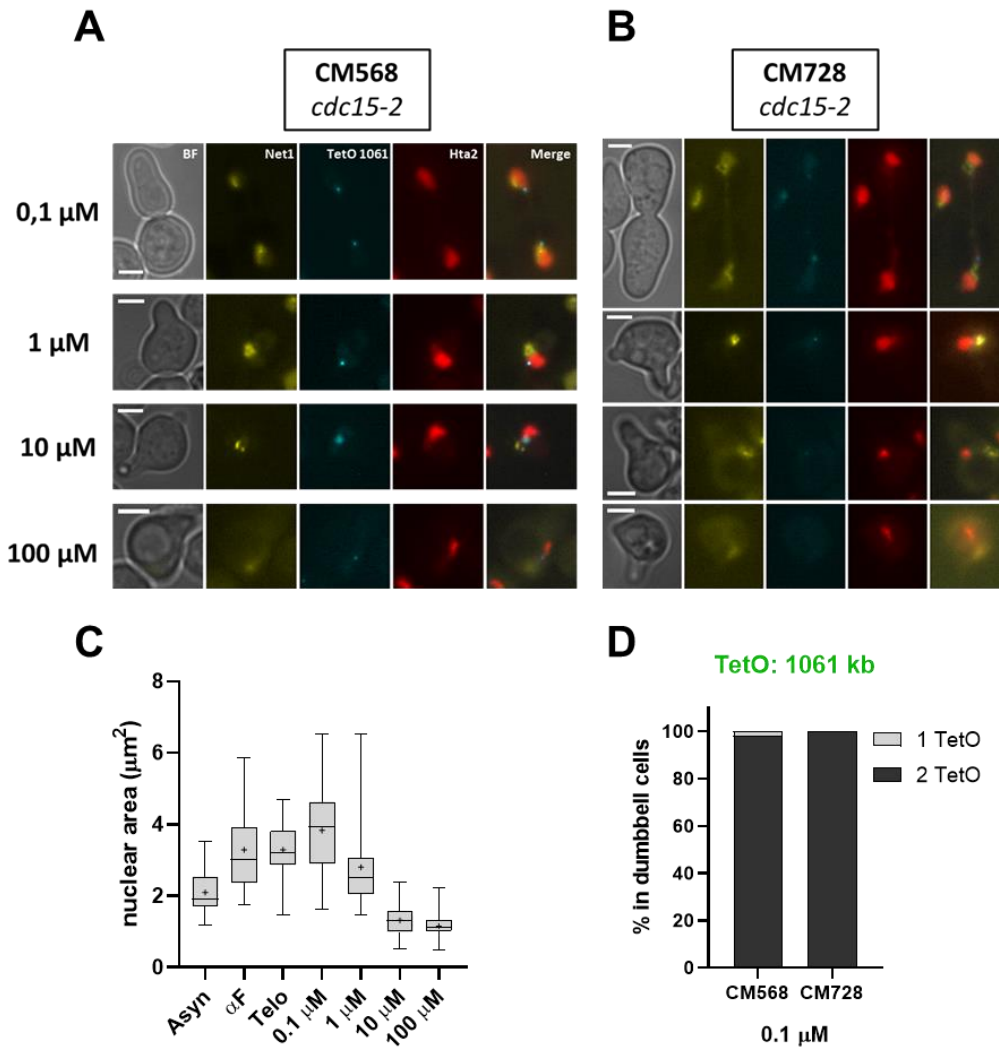


Figure 4.29. Concentrations of CM-568 and CM-728 lower than 1 μM allowed cells to reach telophase and achieve correct cXII segregation. (A) Representative micrographs of the G1 block and release to telophase final timepoint (3 h 34°C) using a series of concentrations of CM-568. BF, bright field. Scale bars, 3 μm. **(B)** As in (A) for CM-728. **(C)** Plot of nuclear areas measuring the Hta2 signal borders in experiments using CM-728 (n = 20 cells). Whiskers represent min to max values and mean is shown as '+'. Asyn, asynchronous; αF, α factor induced G1 arrest; Telo, telophase in DMSO. Concentrations indicate final timepoints' areas. **(D)** Proportion of budded cells displaying one or two *tetO*:1061 kb signals in the final timepoint as in (A), using 0.1 μM of CM-568 and CM-728 respectively, which indicates correct segregation of cXIIr.

Taking all of these into account, our model reveals that drugs CM-568 and CM-728 result toxic for the cell at concentrations as low as 1 μM, inhibiting cell cycle normal progression. The mechanism of action remains to be elucidated, although the behavior it presents at higher doses may indicate oxidative stress, which trigger degradation or loss of fluorescence of fluorescent proteins derived from GFP and hypercompaction of the histone, tagged with the red fluorescent variant mCherry. To conclude, our yeast model

proved to be useful to easily evaluate nuclear morphology and chromatin segregation under the fluorescent microscope. The importance of this approach for future studies relies on the importance of nuclear shape relative to cell health, both in yeast and in higher eukaryotes, in which is a hallmark of cancer.

Taken all together, this work has given new insight into the maintenance of nuclear shape, a feature of uttermost important to maintain cell health, related to several diseases upon disturbance. A thorough microscopic analysis details the relevance of the vacuole and lipid synthesis regarding nuclear morphology in mitotic delays, although the molecular mechanism by which the vacuole shapes the nucleus remains to be solved. Besides, the apparent increase in autophagy levels when Nz is removed may be a sign of nucleophagy, proposing a possible mechanism to explain how cells deal with nuclear membrane excess, allowing the regular continuation of mitosis without an evident loss in cell viability. Continuation of this work will shed light on how cells respond to nuclear membrane imbalances, especially by combining live cell imaging of strains with multiple fluorescent makers to observe protein and organelle interactions *in vivo*.

A watercolor illustration featuring a central blue bird-like figure with a long neck and tail. The bird is surrounded by several large, textured red flowers. Grey, brush-stroke-like branches or stems are scattered around the composition. The background is a light, off-white color.

5. CONCLUSIONS

1. The rDNA loop in a mid-M block is a highly dynamic structure, with many intermediate states, ranging from a protruding bar to the full rDNA handle, which can arise from at least two main developmental pathways.
2. The establishment of the rDNA loop depends on phospholipid biosynthesis and the absence of microtubules.
3. The space under the rDNA loop in a mid-M block caused by microtubule depletion is occupied by the vacuole, which serves as a template for nuclear expansion, and shapes the nucleus as a toroid.
4. Nuclear projections caused by a Nz arrest remain present when they are released, although cells recover a spherical nucleus between later stages of mitosis and the beginning of the new cycle.
5. There is an increase in autophagy levels in a Nz release, presumably to recycle the excess of membrane accumulated in the arrest.
6. The recovery of spherical nuclei occurs faster in mid-M blocks triggered by APC inhibition than it does due to microtubule depletion, most likely for the need in the latter to reassemble and correctly reposition the mitotic spindle to allow segregation.
7. Aberrant nuclear morphologies generated by the Nz-induced mitotic block do not apparently increase genome instability or affect cell viability.
8. The close proximity of nuclear projections to vacuoles in the Nz-induced mid-M block and in a mid-M block induced by APC inhibition, suggest a possible functional role associated to the contact between the rDNA and the vacuole.
9. CEAMED S.A. compounds CM-568 and CM-728 result highly toxic to yeast cells at concentrations as low as 1 μ M, inhibiting cell cycle progression.

A watercolor illustration of a blue, bird-like creature with a long neck and a crest of red flowers. The creature is perched on a grey branch. The background is white with faint grey branches and red flowers. The text "6. REFERENCES" is centered in the middle of the page, underlined with a red line.

6. REFERENCES

-
- Aitchison, J. D., & Rout, M. P. (2012). The yeast nuclear pore complex and transport through it. *Genetics*, *190*(3), 855–883. <https://doi.org/10.1534/genetics.111.127803>
- Akey, C. W., Singh, D., Ouch, C., Echeverria, I., Nudelman, I., Varberg, J. M., Yu, Z., Fang, F., Shi, Y., Wang, J., Salzberg, D., Song, K., Xu, C., Gumbart, J. C., Suslov, S., Unruh, J., Jaspersen, S. L., Chait, B. T., Sali, A., ... Rout, M. P. (2022). Comprehensive structure and functional adaptations of the yeast nuclear pore complex. *Cell*, *185*(2), 361–378.e25. <https://doi.org/10.1016/j.cell.2021.12.015>
- Alber, F., Dokudovskaya, S., Veenhoff, L. M., Zhang, W., Kipper, J., Devos, D., Suprpto, A., Karni-Schmidt, O., Williams, R., Chait, B. T., Sali, A., & Rout, M. P. (2007). The molecular architecture of the nuclear pore complex. *Nature*, *450*(7170), 695–701. <https://doi.org/10.1038/nature06405>
- Albert, B., Léger-Silvestre, I., Normand, C., Ostermaier, M. K., Pérez-Fernández, Panov, K. I., Zomerdijk, J. C. B. M., Schultz, P., & Gadad, O. (2011). RNA polymerase I-specific subunits promote polymerase clustering to enhance the rRNA gene transcription cycle. *Journal of Cell Biology*, *192*(2), 277–293. <https://doi.org/10.1083/JCB.201006040>
- Alexandru, G., Uhlmann, F., Mechtler, K., Poupart, M. A., & Nasmyth, K. (2001). Phosphorylation of the cohesin subunit Scc1 by Polo/Cdc5 kinase regulates sister chromatid separation in yeast. *Cell*, *105*(4), 459–472. [https://doi.org/10.1016/S0092-8674\(01\)00362-2](https://doi.org/10.1016/S0092-8674(01)00362-2)
- Almacellas, E., Pelletier, J., Day, C., Ambrosio, S., Tauler, A., & Mauvezin, C. (2021). Lysosomal degradation ensures accurate chromosomal segregation to prevent chromosomal instability. *Autophagy*, *17*(3), 796–813. <https://doi.org/10.1080/15548627.2020.1764727>
- Andersen, S. L., & Petes, T. D. (2012). Reciprocal uniparental disomy in yeast. *Proceedings of the National Academy of Sciences*, *109*(25), 9947–9952. <https://doi.org/10.1073/PNAS.1207736109>
- Andrulis, E. D., Zappulla, D. C., Ansari, A., Perrod, S., Laiosa, C. V., Gartenberg, M. R., & Sternglanz, R. (2002). Esc1, a Nuclear Periphery Protein Required for Sir4-Based Plasmid Anchoring and Partitioning. *Molecular and Cellular Biology*, *22*(23), 8292–8301. <https://doi.org/10.1128/MCB.22.23.8292-8301.2002>
- Arnone, J. T., Walters, A. D., & Cohen-Fix, O. (2013). The dynamic nature of the nuclear envelope. *Nucleus*, *4*(4), 261–266. <https://doi.org/10.4161/nucl.25341>
- Ayra-Plasencia, J., & Machín, F. (2019). DNA double-strand breaks in telophase lead to coalescence between segregated sister chromatid loci. *Nature Communications*, *10*(1). <https://doi.org/10.1038/s41467-019-10742-8>
- Baba, M., Takeshige, K., Baba, N., & Ohsumi, Y. (1994). Ultrastructural analysis of the autophagic process in yeast: detection of autophagosomes and their characterization. *The Journal of Cell Biology*, *124*(6), 903–913. <https://doi.org/10.1083/JCB.124.6.903>
- Backues, S. K., & Klionsky, D. J. (2022). *Quantification of Autophagosome Size and Formation Rate by Electron and Fluorescence Microscopy in Baker's Yeast*. 1–12. https://doi.org/10.1007/978-1-0716-1589-8_1

6. References

- Banday, S., Farooq, Z., Rashid, R., Abdullah, E., & Altaf, M. (2016). Role of inner nuclear membrane protein complex Lem2-Nur1 in heterochromatic gene silencing. *Journal of Biological Chemistry*, 291(38), 20021–20029. <https://doi.org/10.1074/jbc.M116.743211>
- Banta, L. M., Robinson, J. S., Klionsky, D. J., & Emr, S. D. (1988). Organelle assembly in yeast: characterization of yeast mutants defective in vacuolar biogenesis and protein sorting. *The Journal of Cell Biology*, 107(4), 1369–1383. <https://doi.org/10.1083/JCB.107.4.1369>
- Barbera, M. A., & Petes, T. D. (2006). Selection and analysis of spontaneous reciprocal mitotic cross-overs in *Saccharomyces cerevisiae*. *Proceedings of the National Academy of Sciences*, 103(34), 12819–12824. <https://doi.org/10.1073/pnas.0605778103>
- Barbosa, A. D., Lim, K., Mari, M., Edgar, J. R., Gal, L., Sterk, P., Jenkins, B. J., Koulman, A., Savage, D. B., Schuldiner, M., Reggiori, F., Wigge, P. A., & Siniossoglou, S. (2019). Compartmentalized Synthesis of Triacylglycerol at the Inner Nuclear Membrane Regulates Nuclear Organization. *Developmental Cell*, 50(6), 755–766.e6. <https://doi.org/10.1016/j.devcel.2019.07.009>
- Barbosa, A. D., Sembongi, H., Su, W.-M., Abreu, S., Reggiori, F., Carman, G. M., & Siniossoglou, S. (2015). Lipid partitioning at the nuclear envelope controls membrane biogenesis. *Molecular Biology of the Cell*, 26(20), 3641–3657. <https://doi.org/10.1091/mbc.E15-03-0173>
- Barbosa, A. D., & Siniossoglou, S. (2017). Function of lipid droplet-organelle interactions in lipid homeostasis. In *Biochimica et Biophysica Acta - Molecular Cell Research* (Vol. 1864, Issue 9, pp. 1459–1468). Elsevier B.V. <https://doi.org/10.1016/j.bbamcr.2017.04.001>
- Barbosa, A. D., & Siniossoglou, S. (2020). New kid on the block: lipid droplets in the nucleus. *The FEBS Journal*, febs.15307. <https://doi.org/10.1111/febs.15307>
- Bensidoun, P., Reiter, T., Montpetit, B., Zenklusen, D., & Oeffinger, M. (2022). Nuclear mRNA metabolism drives selective basket assembly on a subset of nuclear pore complexes in budding yeast. *Molecular Cell*, 82(20), 3856–3871. <https://doi.org/10.1016/j.molcel.2022.09.019>
- Bogerd, A. M., Hoffman, J. A., Amberg, D. C., Fink, G. R., & Davis, L. I. (1994). nup1 mutants exhibit pleiotropic defects in nuclear pore complex function. *Journal of Cell Biology*, 127(2), 319–332. <https://doi.org/10.1083/JCB.127.2.319>
- Boisvert, F. M., Van Koningsbruggen, S., Navascués, J., & Lamond, A. I. (2007). The multifunctional nucleolus. *Nature Reviews Molecular Cell Biology* 2007 8:7, 8(7), 574–585. <https://doi.org/10.1038/nrm2184>
- Brewer, B. J., Lockshon, D., & Fangman, W. L. (1992). The arrest of replication forks in the rDNA of yeast occurs independently of transcription. *Cell*, 71(2), 267–276. [https://doi.org/10.1016/0092-8674\(92\)90355-G](https://doi.org/10.1016/0092-8674(92)90355-G)
- Budovskaya, Y. V., Stephan, J. S., Deminoff, S. J., & Herman, P. K. (2005). An evolutionary proteomics approach identifies substrates of the cAMP-dependent protein kinase. *Proceedings of the National Academy of Sciences of the United States of America*, 102(39), 13933. <https://doi.org/10.1073/PNAS.0501046102>

-
- Bupp, J. M., Martin, A. E., Stensrud, E. S., & Jaspersen, S. L. (2007). Telomere anchoring at the nuclear periphery requires the budding yeast Sad1-UNC-84 domain protein Mps3. *The Journal of Cell Biology*, *179*(5), 845. <https://doi.org/10.1083/JCB.200706040>
- Bystricky, K., Heun, P., Gehlen, L., Langowski, J., & Gasser, S. M. (2004). Long-range compaction and flexibility of interphase chromatin in budding yeast analyzed by high-resolution imaging techniques. *Proceedings of the National Academy of Sciences of the United States of America*, *101*(47), 16495–16500. <https://doi.org/10.1073/pnas.0402766101>
- Bystricky, K., Laroche, T., van Houwe, G., Blaszczyk, M., & Gasser, S. M. (2005). Chromosome looping in yeast. *Journal of Cell Biology*, *168*(3), 375–387. <https://doi.org/10.1083/jcb.200409091>
- Campbell, J. L., Lorenz, A., Witkin, K. L., Hays, T., Loidl, J., & Cohen-Fix, O. (2006). Yeast nuclear envelope subdomains with distinct abilities to resist membrane expansion. *Molecular Biology of the Cell*, *17*(4), 1768–1778. <https://doi.org/10.1091/mbc.E05-09-0839>
- Cantwell, H., & Nurse, P. (2019a). A systematic genetic screen identifies essential factors involved in nuclear size control. *PLOS Genetics*, *15*(2), e1007929. <https://doi.org/10.1371/JOURNAL.PGEN.1007929>
- Cantwell, H., & Nurse, P. (2019b). Unravelling nuclear size control. *Current Genetics* *2019* *65*:6, *65*(6), 1281–1285. <https://doi.org/10.1007/S00294-019-00999-3>
- Capella, M., Mandemaker, I. K., Martín Caballero, L., den Brave, F., Pfander, B., Ladurner, A. G., Jentsch, S., & Braun, S. (2021). Nucleolar release of rDNA repeats for repair involves SUMO-mediated untethering by the Cdc48/p97 segregase. *Nature Communications* *2021* *12*:1, *12*(1), 1–16. <https://doi.org/10.1038/s41467-021-25205-2>
- Carman, G. M., & Han, G.-S. (2019). Fat-regulating phosphatidic acid phosphatase: a review of its roles and regulation in lipid homeostasis. *Journal of Lipid Research*, *60*(1), 2. <https://doi.org/10.1194/JLR.S087452>
- Carman, G. M., & Han, G. S. (2018). Phosphatidate phosphatase regulates membrane phospholipid synthesis via phosphatidylserine synthase. In *Advances in Biological Regulation* (Vol. 67, pp. 49–58). Elsevier Ltd. <https://doi.org/10.1016/j.jbior.2017.08.001>
- Cavalier-Smith, T. (2005). Economy, Speed and Size Matter: Evolutionary Forces Driving Nuclear Genome Miniaturization and Expansion. *Annals of Botany*, *95*(1), 147. <https://doi.org/10.1093/AOB/MCI010>
- Caydasi, A. K., Khmelinskii, A., Duenas-Sanchez, R., Kurtulmus, B., Knop, M., & Pereira, G. (2017). Temporal and compartment-specific signals coordinate mitotic exit with spindle position. *Nature Communications* *2017* *8*:1, *8*(1), 1–14. <https://doi.org/10.1038/ncomms14129>
- Caydasi, A. K., & Pereira, G. (2012). SPOC alert—When chromosomes get the wrong direction. *Experimental Cell Research*, *318*(12), 1421–1427. <https://doi.org/10.1016/J.YEXCR.2012.03.031>

6. References

- Chan, J. N. Y., Poon, B. P. K., Salvi, J., Olsen, J. B., Emili, A., & Mekhail, K. (2011). Perinuclear cohibin complexes maintain replicative life span via roles at distinct silent chromatin domains. *Developmental Cell*, 20(6), 867–879. <https://doi.org/10.1016/j.devcel.2011.05.014>
- Chen, L., & Madura, K. (2014). Degradation of specific nuclear proteins occurs in the cytoplasm in *Saccharomyces cerevisiae*. *Genetics*, 197(1), 193–197. <https://doi.org/10.1534/GENETICS.114.163824/-/DC1>
- Choi, H.-S., Su, W.-M., Morgan, J. M., Han, G.-S., Xu, Z., Karanasios, E., Siniossoglou, S., & Carman, G. M. (2011). Phosphorylation of Phosphatidate Phosphatase Regulates Its Membrane Association and Physiological Functions in *Saccharomyces cerevisiae*. *Journal of Biological Chemistry*, 286(2), 1486–1498. <https://doi.org/10.1074/jbc.m110.155598>
- Choi, H. S., Su, W. M., Han, G. S., Plote, D., Xu, Z., & Carman, G. M. (2012). Pho85p-Pho80p phosphorylation of yeast pah1p phosphatidate phosphatase regulates its activity, location, abundance, and function in lipid metabolism. *Journal of Biological Chemistry*, 287(14), 11290–11301. <https://doi.org/10.1074/jbc.M112.346023>
- Clemente-Blanco, A., Mayán-Santos, M., Schneider, D. A., Machín, F., Jarmuz, A., Tschochner, H., & Aragón, L. (2009). Cdc14 inhibits transcription by RNA polymerase I during anaphase. *Nature*, 458(7235), 219–222. <https://doi.org/10.1038/nature07652>
- Cohen-Fix, O., Peters, J. M., Kirschner, M. W., & Koshland, D. (1996). Anaphase initiation in *Saccharomyces cerevisiae* is controlled by the APC-dependent degradation of the anaphase inhibitor Pds1p. *Genes & Development*, 10(24), 3081–3093. <https://doi.org/10.1101/GAD.10.24.3081>
- D'Amours, D., & Amon, A. (2004). At the interface between signaling and executing anaphase--Cdc14 and the FEAR network. *Genes & Development*, 18(21), 2581–2595. <https://doi.org/10.1101/gad.1247304>
- D'Angelo, M. A., & Hetzer, M. W. (2008). Structure, dynamics and function of nuclear pore complexes. In *Trends in Cell Biology* (Vol. 18, Issue 10, pp. 456–466). NIH Public Access. <https://doi.org/10.1016/j.tcb.2008.07.009>
- Dawaliby, R., & Mayer, A. (2010). Microautophagy of the nucleus coincides with a vacuolar diffusion barrier at nuclear-vacuolar junctions. *Molecular Biology of the Cell*, 21(23), 4173–4183. <https://doi.org/10.1091/mbc.E09-09-0782>
- Dawson, T. R., Lazarus, M. D., Hetzer, M. W., & Wente, S. R. (2009). ER membrane-bending proteins are necessary for de novo nuclear pore formation. *The Journal of Cell Biology*, 184(5), 659. <https://doi.org/10.1083/JCB.200806174>
- De Magistris, P., & Antonin, W. (2018). The Dynamic Nature of the Nuclear Envelope. *Current Biology*, 28(8), R487–R497. <https://doi.org/10.1016/J.CUB.2018.01.073>
- Dechat, T., Pflieger, K., Sengupta, K., Shimi, T., Shumaker, D. K., Solimando, L., & Goldman, R. D. (2008). Nuclear lamins: major factors in the structural organization and function of the nucleus and chromatin. *Genes & Development*, 22(7), 832–853. <https://doi.org/10.1101/GAD.1652708>

-
- Denholtz, M., Zhu, Y., He, Z., Lu, H., Isoda, T., Döhrmann, S., Nizet, V., & Murre, C. (2020). Upon microbial challenge, human neutrophils undergo rapid changes in nuclear architecture and chromatin folding to orchestrate an immediate inflammatory gene program. *Genes and Development*, *34*(3–4), 149–165. <https://doi.org/10.1101/GAD.333708.119/-/DC1>
- Deolal, P., Male, G., & Mishra, K. (2021). The challenge of staying in shape: nuclear size matters. *Current Genetics*, *67*(4), 605–612. <https://doi.org/10.1007/S00294-021-01176-1/FIGURES/3>
- Deolal, P., & Mishra, K. (2021). Regulation of diverse nuclear shapes: pathways working independently, together. *Communicative & Integrative Biology*, *14*(1), 158–175. <https://doi.org/10.1080/19420889.2021.1939942>
- Dey, G., & Baum, B. (2021). Nuclear envelope remodelling during mitosis. *Current Opinion in Cell Biology*, *70*, 67–74. <https://doi.org/10.1016/J.CEB.2020.12.004>
- Dey, G., Culley, S., Curran, S., Schmidt, U., Henriques, R., Kukulski, W., & Baum, B. (2020). Closed mitosis requires local disassembly of the nuclear envelope. *Nature*, *585*(7823), 119–123. <https://doi.org/10.1038/s41586-020-2648-3>
- Dion, V., Kalck, V., Horigome, C., Towbin, B. D., & Gasser, S. M. (2012). Increased mobility of double-strand breaks requires Mec1, Rad9 and the homologous recombination machinery. *Nature Cell Biology* 2012 *14*:5, *14*(5), 502–509. <https://doi.org/10.1038/ncb2465>
- Drin, G., Casella, J. F., Gautier, R., Boehmer, T., Schwartz, T. U., & Antonny, B. (2007). A general amphipathic α -helical motif for sensing membrane curvature. *Nature Structural & Molecular Biology* 2007 *14*:2, *14*(2), 138–146. <https://doi.org/10.1038/nsmb1194>
- Duan, Z., Andronescu, M., Schutz, K., McIlwain, S., Kim, Y. J., Lee, C., Shendure, J., Fields, S., Blau, C. A., & Noble, W. S. (2010). A three-dimensional model of the yeast genome. *Nature* 2010 *465*:7296, *465*(7296), 363–367. <https://doi.org/10.1038/nature08973>
- Dubots, E., Cottier, S., Péli-Gulli, M. P., Jaquenoud, M., Bontron, S., Schneiter, R., & De Virgilio, C. (2014). TORC1 Regulates Pah1 Phosphatidate Phosphatase Activity via the Nem1/Spo7 Protein Phosphatase Complex. *PLOS ONE*, *9*(8), e104194. <https://doi.org/10.1371/JOURNAL.PONE.0104194>
- Engler, C., Gruetzner, R., Kandzia, R., & Marillonnet, S. (2009). Golden Gate Shuffling: A One-Pot DNA Shuffling Method Based on Type II Restriction Enzymes. *PLoS ONE*, *4*(5), e5553. <https://doi.org/10.1371/journal.pone.0005553>
- Engler, C., Kandzia, R., & Marillonnet, S. (2008). A One Pot, One Step, Precision Cloning Method with High Throughput Capability. *PLoS ONE*, *3*(11), e3647. <https://doi.org/10.1371/journal.pone.0003647>
- Expósito-Serrano, M., Sánchez-Molina, A., Gallardo, P., Salas-Pino, S., & Daga, R. R. (2020). Selective Nuclear Pore Complex Removal Drives Nuclear Envelope Division in Fission Yeast. *Current Biology*, *30*(16), 3212–3222.e2. <https://doi.org/10.1016/j.cub.2020.05.066>
- Fan, J., Jin, H., Koch, B. A., & Yu, H. G. (2020). Mps2 links Csm4 and Mps3 to form a

6. References

- telomere-associated LINC complex in budding yeast. *Life Science Alliance*, 3(12). <https://doi.org/10.26508/LSA.202000824>
- Freeman, L., Aragon-Alcaide, L., & Strunnikov, A. (2000). The Condensin Complex Governs Chromosome Condensation and Mitotic Transmission of Rdna. *Journal of Cell Biology*, 149(4), 811–824. <https://doi.org/10.1083/JCB.149.4.811>
- Friederichs, J. M., Ghosh, S., Smoyer, C. J., McCroskey, S., Miller, B. D., Weaver, K. J., Delventhal, K. M., Unruh, J., Slaughter, B. D., & Jaspersen, S. L. (2011). The SUN Protein Mps3 Is Required for Spindle Pole Body Insertion into the Nuclear Membrane and Nuclear Envelope Homeostasis. *PLOS Genetics*, 7(11), e1002365. <https://doi.org/10.1371/JOURNAL.PGEN.1002365>
- Garapati, H. S., & Mishra, K. (2018). Comparative genomics of nuclear envelope proteins. *BMC Genomics*, 19(1), 823. <https://doi.org/10.1186/s12864-018-5218-4>
- Garcia, M., Kumanski, S., Elías-Villalobos, A., Cazevielle, C., Soulet, C., & Moriel-Carretero, M. (2022). Nuclear ingress of cytoplasmic bodies accompanies a boost in autophagy. *Life Science Alliance*, 5(9), e202101160. <https://doi.org/10.26508/LSA.202101160>
- Gasser, S. M. (2002). Visualizing chromatin dynamics in interphase nuclei. *Science (New York, N.Y.)*, 296(5572), 1412–1416. <https://doi.org/10.1126/SCIENCE.1067703>
- Geng, J., Baba, M., Nair, U., & Klionsky, D. J. (2008). Quantitative analysis of autophagy-related protein stoichiometry by fluorescence microscopy. *Journal of Cell Biology*, 182(1), 129–140. <https://doi.org/10.1083/JCB.200711112>
- Goldstein, A. L., Snay, C. A., Heath, C. V., & Cole, C. N. (1996). Pleiotropic nuclear defects associated with a conditional allele of the novel nucleoporin Rat9p/Nup85p. *Molecular Biology of the Cell*, 7(6), 917. <https://doi.org/10.1091/MBC.7.6.917>
- Gomar-Alba, M., Pozharskaia, V., Cichocki, B., Schaal, C., Kumar, A., Jacquél, B., Charvin, G., Igual, J. C., & Mendoza, M. (2022). Nuclear pore complex acetylation regulates mRNA export and cell cycle commitment in budding yeast. *The EMBO Journal*, 41(15), e110271. <https://doi.org/10.15252/EMBJ.2021110271>
- Gonzalez, Y., Saito, A., & Sazer, S. (2012). Fission yeast Lem2 and Man1 perform fundamental functions of the animal cell nuclear lamina. *Nucleus*, 3(1), 60–76. <https://doi.org/10.4161/nucl.18824>
- Gregory, T. (2005). Genome Size Evolution in Animals. *London: Elsevier Academic Press*, 1, 4–87.
- Grimsey, N., Han, G. S., O'Hara, L., Rochford, J. J., Carman, G. M., & Siniosoglou, S. (2008). Temporal and spatial regulation of the phosphatidate phosphatases lipin 1 and 2. *Journal of Biological Chemistry*, 283(43), 29166–29174. <https://doi.org/10.1074/jbc.M804278200>
- Guacci, V., Hogan, E., & Koshland, D. (1994). Chromosome condensation and sister chromatid pairing in budding yeast. *The Journal of Cell Biology*, 125(3), 517. <https://doi.org/10.1083/JCB.125.3.517>
- Guacci, V., Hogan, E., & Koshland, D. (1997). Centromere position in budding yeast: evidence for anaphase A. *Molecular Biology of the Cell*, 8(6), 957. <https://doi.org/10.1091/MBC.8.6.957>

- Güttinger, S., Laurell, E., & Kutay, U. (2009). Orchestrating nuclear envelope disassembly and reassembly during mitosis. *Nature Reviews Molecular Cell Biology* 2009 10:3, 10(3), 178–191. <https://doi.org/10.1038/nrm2641>
- Ha, C. W., & Huh, W. K. (2011). Rapamycin increases rDNA stability by enhancing association of Sir2 with rDNA in *Saccharomyces cerevisiae*. *Nucleic Acids Research*, 39(4), 1336–1350. <https://doi.org/10.1093/NAR/GKQ895>
- Han, G. S., O'Hara, L., Carman, G. M., & Siniosoglou, S. (2008). An unconventional diacylglycerol kinase that regulates phospholipid synthesis and nuclear membrane growth. *Journal of Biological Chemistry*, 283(29), 20433–20442. <https://doi.org/10.1074/jbc.M802903200>
- Han, G. S., Wu, W. I., & Carman, G. M. (2006). The *Saccharomyces cerevisiae* lipin homolog is a Mg²⁺-dependent phosphatidate phosphatase enzyme. *Journal of Biological Chemistry*, 281(14), 9210–9218. <https://doi.org/10.1074/jbc.M600425200>
- Hariri, H., Rogers, S., Ugrankar, R., Liu, Y. L., Feathers, J. R., & Henne, W. M. (2018). Lipid droplet biogenesis is spatially coordinated at ER–vacuole contacts under nutritional stress. *EMBO Reports*, 19(1), 57–72. <https://doi.org/10.15252/EMBR.201744815>
- Harris, B., Bose, T., Lee, K. K., Wang, F., Lu, S., Ross, R. T., Zhang, Y., French, S. L., Beyer, A. L., Slaughter, B. D., Unruh, J. R., & Gerton, J. L. (2014). Cohesion promotes nucleolar structure and function. *Molecular Biology of the Cell*, 25(3), 337–346. <https://doi.org/10.1091/mbc.e13-07-0377>
- Harris, T. E., Huffman, T. A., Chi, A., Shabanowitz, J., Hunt, D. F., Kumar, A., & Lawrence, J. C. (2007). Insulin controls subcellular localization and multisite phosphorylation of the phosphatidic acid phosphatase, lipin 1. *Journal of Biological Chemistry*, 282(1), 277–286. <https://doi.org/10.1074/jbc.M609537200>
- Hattier, T., Andrulis, E. D., & Tartakoff, A. M. (2007). Immobility, inheritance and plasticity of shape of the yeast nucleus. *BMC Cell Biology*, 8(1), 47. <https://doi.org/10.1186/1471-2121-8-47>
- Henne, W. M., Zhu, L., Balogi, Z., Stefan, C., Pleiss, J. A., & Emr, S. D. (2015). Mdm1/Snx13 is a novel ER–endolysosomal interorganelle tethering protein. *Journal of Cell Biology*, 210(4), 541–551. <https://doi.org/10.1083/JCB.201503088>
- Henry, S. A., Kohlwein, S. D., & Carman, G. M. (2012). Metabolism and regulation of glycerolipids in the yeast *Saccharomyces cerevisiae*. *Genetics*, 190(2), 317–349. <https://doi.org/10.1534/genetics.111.130286>
- Hernandez-Verdun, D., Roussel, P., & Gébrane-Younès, J. (2002). Emerging concepts of nucleolar assembly. *Journal of Cell Science*, 115(11), 2265–2270. <https://doi.org/10.1242/JCS.115.11.2265>
- Heun, P., Laroche, T., Shimada, K., Furrer, P., & Gasser, S. M. (2001). Chromosome dynamics in the yeast interphase nucleus. *Science*, 294(5549), 2181–2186. <https://doi.org/10.1126/science.1065366>
- Hinterndorfer, K., Laporte, M. H., Mikus, F., Tafur, L., Bourgoing, C., Prouteau, M., Dey, G., Loewith, R., Guichard, P., & Hamel, V. (2022). Ultrastructure expansion

6. References

- microscopy reveals the cellular architecture of budding and fission yeast. *Journal of Cell Science*, 135(24). <https://doi.org/10.1242/JCS.260240/286062>
- Hirano, T. (2000). Chromosome cohesion, condensation, and separation. *Annual Review of Biochemistry*, 69, 115–144. <https://doi.org/10.1146/ANNUREV.BIOCHEM.69.1.115>
- Hoffmann, K., Dreger, C. K., Olins, A. L., Olins, D. E., Shultz, L. D., Lucke, B., Karl, H., Kaps, R., Müller, D., Vayá, A., Aznar, J., Ware, R. E., Sotelo Cruz, N., Lindner, T. H., Herrmann, H., Reis, A., & Sperling, K. (2002). Mutations in the gene encoding the lamin B receptor produce an altered nuclear morphology in granulocytes (Pelger–Huët anomaly). *Nature Genetics* 2002 31:4, 31(4), 410–414. <https://doi.org/10.1038/ng925>
- Horigome, C., & Mizuta, K. (2012). Ribosome biogenesis factors working with a nuclear envelope SUN domain protein. *Http://Dx.Doi.Org/10.4161/Nucl.18930*, 3(1), 22–28. <https://doi.org/10.4161/NUCL.18930>
- Horigome, C., Okada, T., Shimazu, K., Gasser, S. M., & Mizuta, K. (2011). Ribosome biogenesis factors bind a nuclear envelope SUN domain protein to cluster yeast telomeres. *The EMBO Journal*, 30(18), 3799–3811. <https://doi.org/10.1038/EMBOJ.2011.267>
- Houseley, J., & Tollervey, D. (2011). Repeat expansion in the budding yeast ribosomal DNA can occur independently of the canonical homologous recombination machinery. *Nucleic Acids Research*, 39(20), 8778–8791. <https://doi.org/10.1093/NAR/GKR589>
- Huang, J., & Moazed, D. (2003). Association of the RENT complex with nontranscribed and coding regions of rDNA and a regional requirement for the replication fork block protein Fob1 in rDNA silencing. *Genes & Development*, 17(17), 2162–2176. <https://doi.org/10.1101/GAD.1108403>
- Huff, J. (2015). The Airyscan detector from ZEISS: confocal imaging with improved signal-to-noise ratio and super-resolution. *Nature Methods* 2015 12:12, 12(12), i–ii. <https://doi.org/10.1038/nmeth.f.388>
- Huffman, T. A., Mothe-Satney, I., & Lawrence, J. C. (2002). Insulin-stimulated phosphorylation of lipin mediated by the mammalian target of rapamycin. *Proceedings of the National Academy of Sciences*, 99(2), 1047–1052. <https://doi.org/10.1073/pnas.022634399>
- Hwang, L. H., Lau, L. F., Smith, D. L., Mistrot, C. A., Hardwick, K. G., Hwang, E. S., Amon, A., & Murray, A. W. (1998). Budding Yeast Cdc20: A Target of the Spindle Checkpoint. *Science*, 279(5353), 1041–1044. <https://doi.org/10.1126/SCIENCE.279.5353.1041>
- Inokoshi, J., Tomoda Hideaki Hashimoto Akemi Watanabe Hideo Takeshima, H., Omura, S., Inokoshi, J., Tomoda, H., Takeshima -S Omura, H., Hashimoto, H., & Watanabe, A. (1994). *Cerulenin-resistant mutants of Saccharomyces cerevisiae with an altered fatty acid synthase gene*. 244, 90–96.
- Irniger, S., Piatti, S., Michaelis, C., & Nasmyth, K. (1995). Genes involved in sister chromatid separation are needed for B-type cyclin proteolysis in budding yeast. *Cell*, 81(2), 269–277. [https://doi.org/10.1016/0092-8674\(95\)90337-2](https://doi.org/10.1016/0092-8674(95)90337-2)

-
- Jacobs, C. W., Adams, A. E., Szaniszló, P. J., & Pringle, J. R. (1988). Functions of microtubules in the *Saccharomyces cerevisiae* cell cycle. *Journal of Cell Biology*, *107*(4), 1409–1426. <https://doi.org/10.1083/JCB.107.4.1409>
- Jaspersen, S. L., Giddings, T. H., & Winey, M. (2002). Mps3p is a novel component of the yeast spindle pole body that interacts with the yeast centrin homologue Cdc31p. *Journal of Cell Biology*, *159*(6), 945–956. <https://doi.org/10.1083/JCB.200208169>
- Jaspersen, S. L., & Winey, M. (2004). The budding yeast spindle pole body: structure, duplication, and function. *Annual Review of Cell and Developmental Biology*, *20*, 1–28. <https://doi.org/10.1146/ANNUREV.CELLBIO.20.022003.114106>
- Jevtić, P., & Levy, D. L. (2014). Mechanisms of Nuclear Size Regulation in Model Systems and Cancer. In *Advances in Experimental Medicine and Biology* (Vol. 773, pp. 537–569). Springer New York LLC. https://doi.org/10.1007/978-1-4899-8032-8_25
- Jin, Q. W., Trelles-Sticken, E., Scherthan, H., & Loidl, J. (1998). Yeast nuclei display prominent centromere clustering that is reduced in nondividing cells and in meiotic prophase. *Journal of Cell Biology*, *141*(1), 21–29. <https://doi.org/10.1083/jcb.141.1.21>
- Jin, Y., & Weisman, L. S. (2015). The vacuole/lysosome is required for cell-cycle progression. *ELife*, *4*(AUGUST2015). <https://doi.org/10.7554/ELIFE.08160>
- Jorgensen, P., Edgington, N. P., Schneider, B. L., Rupeš, I., Tyers, M., & Futcher, B. (2007). The Size of the Nucleus Increases as Yeast Cells Grow. *Molecular Biology of the Cell*, *18*, 3523–3532. <https://doi.org/10.1091/mbc.E06>
- Jovtchev, G., Schubert, V., Meister, A., Barow, M., & Schubert, I. (2006). Nuclear DNA content and nuclear and cell volume are positively correlated in angiosperms. *Cytogenetic and Genome Research*, *114*(1), 77–82. <https://doi.org/10.1159/000091932>
- Karanasios, E., Han, G.-S., Xu, Z., Carman, G. M., & Siniosoglou, S. (2010). A phosphorylation-regulated amphipathic helix controls the membrane translocation and function of the yeast phosphatidate phosphatase. *Proceedings of the National Academy of Sciences*, *107*(41), 17539–17544. <https://doi.org/10.1073/pnas.1007974107>
- Kim, D. I., Kc, B., & Roux, K. J. (2015). Making the LINC: SUN and KASH protein interactions. *Biological Chemistry*, *396*(4), 295. <https://doi.org/10.1515/HSZ-2014-0267>
- Kim, S. J., Fernandez-Martinez, J., Nudelman, I., Shi, Y., Zhang, W., Raveh, B., Herricks, T., Slaughter, B. D., Hogan, J. A., Upla, P., Chemmama, I. E., Pellarin, R., Echeverria, I., Shivaraju, M., Chaudhury, A. S., Wang, J., Williams, R., Unruh, J. R., Greenberg, C. H., ... Rout, M. P. (2018). Integrative structure and functional anatomy of a nuclear pore complex. *Nature* *2018* *555*:7697, *555*(7697), 475–482. <https://doi.org/10.1038/nature26003>
- Kim, S. J., Fernandez-Martinez, J., Sampathkumar, P., Martel, A., Matsui, T., Tsuruta, H., Weiss, T. M., Shi, Y., Markina-Inarrairaegui, A., Bonanno, J. B., Sauder, J. M., Burley, S. K., Chait, B. T., Almo, S. C., Rout, M. P., & Sali, A. (2014). Integrative Structure–Function Mapping of the Nucleoporin Nup133 Suggests a Conserved

6. References

- Mechanism for Membrane Anchoring of the Nuclear Pore Complex. *Molecular & Cellular Proteomics*, 13(11), 2911–2926. <https://doi.org/10.1074/MCP.M114.040915>
- Klinge, S., & Woolford, J. L. (2018). Ribosome assembly coming into focus. *Nature Reviews Molecular Cell Biology* 20:2, 20(2), 116–131. <https://doi.org/10.1038/s41580-018-0078-y>
- Kobayashi, T. (2003). The Replication Fork Barrier Site Forms a Unique Structure with Fob1p and Inhibits the Replication Fork. *Molecular and Cellular Biology*, 23(24), 9178–9188. <https://doi.org/10.1128/MCB.23.24.9178-9188.2003>
- Kobayashi, T., Heck, D. J., Nomura, M., & Horiuchi, T. (1998). Expansion and contraction of ribosomal DNA repeats in *Saccharomyces cerevisiae*: requirement of replication fork blocking (Fob1) protein and the role of RNA polymerase I. *Genes & Development*, 12(24), 3821. <https://doi.org/10.1101/GAD.12.24.3821>
- Kobayashi, T., Hidaka, M., Nishizawa, M., & Horiuchi, T. (1992). Identification of a site required for DNA replication fork blocking activity in the rRNA gene cluster in *Saccharomyces cerevisiae*. *MGG Molecular & General Genetics*, 233(3), 355–362. <https://doi.org/10.1007/BF00265431/METRICS>
- Kobayashi, T., & Horiuchi, T. (1996). A yeast gene product, Fob1 protein, required for both replication fork blocking and recombinational hotspot activities. *Genes to Cells*, 1(5), 465–474. <https://doi.org/10.1046/J.1365-2443.1996.D01-256.X>
- Kobayashi, T., & Nagata, S. (2014). Ribosomal RNA gene repeats, their stability and cellular senescence. *Proceedings of the Japan Academy, Series B*, 90(4), 119–129. <https://doi.org/10.2183/PJAB.90.119>
- Kohler, V., & Büttner, S. (2021). Remodelling of Nucleus-Vacuole Junctions During Metabolic and Proteostatic Stress. *Contact*, 4, 251525642110166. <https://doi.org/10.1177/25152564211016608>
- Krick, R., Muehe, Y., Prick, T., Bremer, S., Schlotterhose, P., Eskelinen, E. L., Millen, J., Goldfarb, D. S., & Thumm, M. (2008). Piecemeal microautophagy of the nucleus requires the core macroautophagy genes. *Molecular Biology of the Cell*, 19(10), 4492–4505. <https://doi.org/10.1091/mbc.E08-04-0363>
- Krick, R., Mühe, Y., Prick, T., Bredschneider, M., Bremer, S., Wenzel, D., Eskelinen, E. L., & Thumm, M. (2009). Piecemeal microautophagy of the nucleus: Genetic and morphological traits. *Autophagy*, 5(2), 270–272. <https://doi.org/10.4161/auto.5.2.7639>
- Kume, K., Cantwell, H., Neumann, F. R., Jones, A. W., Snijders, A. P., & Nurse, P. (2017). A systematic genomic screen implicates nucleocytoplasmic transport and membrane growth in nuclear size control. *PLOS Genetics*, 13(5), e1006767. <https://doi.org/10.1371/JOURNAL.PGEN.1006767>
- Kvam, E., Gable, K., Dunn, T. M., & Goldfarb, D. S. (2005). Targeting of Tsc13p to nucleus-vacuole junctions: A role for very-long-chain fatty acids in the biogenesis of microautophagic vesicles. *Molecular Biology of the Cell*, 16(9), 3987–3998. <https://doi.org/10.1091/mbc.E05-04-0290>
- Kvam, E., & Goldfarb, D. S. (2006). Structure and function of nucleus-vacuole junctions:

-
- outer-nuclear-membrane targeting of Nvj1p and a role in tryptophan uptake. *Journal of Cell Science*, 119(17), 3622–3633. <https://doi.org/10.1242/JCS.03093>
- Kvam, E., & Goldfarb, D. S. (2007). Nucleus-Vacuole Junctions and Piecemeal Microautophagy of the Nucleus in *S. cerevisiae*. *Autophagy*. <https://doi.org/10.4161/auto.3586>
- Kwiatek, J. M., Han, G. S., & Carman, G. M. (2020). Phosphatidate-mediated regulation of lipid synthesis at the nuclear/endoplasmic reticulum membrane. In *Biochimica et Biophysica Acta - Molecular and Cell Biology of Lipids* (Vol. 1865, Issue 1, p. 158434). Elsevier B.V. <https://doi.org/10.1016/j.bbailip.2019.03.006>
- Lai, L. A., Morabito, L., & Holloway, S. L. (2003). A novel yeast mutant that is defective in regulation of the Anaphase-Promoting Complex by the spindle damage checkpoint. *Molecular Genetics and Genomics*, 270(2), 156–164. <https://doi.org/10.1007/s00438-003-0912-5>
- Laloraya, S., Guacci, V., & Koshland, D. (2000). Chromosomal Addresses of the Cohesin Component Mcd1p. *The Journal of Cell Biology*, 151(5), 1047. <https://doi.org/10.1083/JCB.151.5.1047>
- Lamothe, R., Costantino, L., & Koshland, D. E. (2020). The spatial regulation of condensin activity in chromosome condensation. *Genes and Development*, 34(11–12), 819–831. <https://doi.org/10.1101/GAD.335471.119/-/DC1>
- Laporte, D., Courtout, F., Salin, B., Ceschin, J., & Sagot, I. (2013). An array of nuclear microtubules reorganizes the budding yeast nucleus during quiescence. *Journal of Cell Biology*, 203(4), 585–594. <https://doi.org/10.1083/JCB.201306075>
- Lara-Gonzalez, P., Westhorpe, F. G., & Taylor, S. S. (2012). The Spindle Assembly Checkpoint. *Current Biology*, 22(22), R966–R980. <https://doi.org/10.1016/J.CUB.2012.10.006>
- Lavoie, B. D., Hogan, E., & Koshland, D. (2002). In vivo dissection of the chromosome condensation machinery: reversibility of condensation distinguishes contributions of condensin and cohesin. *The Journal of Cell Biology*, 156(5), 805. <https://doi.org/10.1083/JCB.200109056>
- Lavoie, B. D., Hogan, E., & Koshland, D. (2004). In vivo requirements for rDNA chromosome condensation reveal two cell-cycle-regulated pathways for mitotic chromosome folding. *Genes & Development*, 18(1), 76–87. <https://doi.org/10.1101/GAD.1150404>
- Lazar-Stefanita, L., Scolari, V. F., Mercy, G., Muller, H., Guérin, T. M., Thierry, A., Mozziconacci, J., & Koszul, R. (2017). Cohesins and condensins orchestrate the 4D dynamics of yeast chromosomes during the cell cycle. *The EMBO Journal*, 36(18), 2684–2697. <https://doi.org/10.15252/EMBJ.201797342>
- Lee, C. W., Wilfling, F., Ronchi, P., Allegretti, M., Mosalaganti, S., Jentsch, S., Beck, M., & Pfander, B. (2020). Selective autophagy degrades nuclear pore complexes. *Nature Cell Biology* 2020 22:2, 22(2), 159–166. <https://doi.org/10.1038/s41556-019-0459-2>
- Lee, L., Klee, S. K., Evangelista, M., Boone, C., & Pellman, D. (1999). Control of Mitotic Spindle Position by the *Saccharomyces cerevisiae* Formin Bni1p. *The Journal of*

6. References

- Cell Biology*, 144(5), 947. <https://doi.org/10.1083/JCB.144.5.947>
- Lee, M. E., DeLoache, W. C., Cervantes, B., & Dueber, J. E. (2015). A Highly Characterized Yeast Toolkit for Modular, Multipart Assembly. *ACS Synthetic Biology*, 4(9), 975–986. <https://doi.org/10.1021/sb500366v>
- Lee, P. S., Greenwell, P. W., Dominska, M., Gawel, M., Hamilton, M., & Petes, T. D. (2009). A Fine-Structure Map of Spontaneous Mitotic Crossovers in the Yeast *Saccharomyces cerevisiae*. *PLOS Genetics*, 5(3), e1000410. <https://doi.org/10.1371/JOURNAL.PGEN.1000410>
- Lee, P. S., & Petes, T. D. (2010). Mitotic gene conversion events induced in G1-synchronized yeast cells by gamma rays are similar to spontaneous conversion events. *Proceedings of the National Academy of Sciences*, 107(16), 7383–7388. <https://doi.org/10.1073/pnas.1001940107>
- Lenz-Böhme, B., Wismar, J., Fuchs, S., Reifegerste, R., Buchner, E., Betz, H., & Schmitt, B. (1997). Insertional Mutation of the *Drosophila* Nuclear Lamin Dm0 Gene Results in Defective Nuclear Envelopes, Clustering of Nuclear Pore Complexes, and Accumulation of Annulate Lamellae. *The Journal of Cell Biology*, 137(5), 1001. <https://doi.org/10.1083/JCB.137.5.1001>
- Li, H., Tsang, C. K., Watkins, M., Bertram, P. G., & Zheng, X. F. S. (2006). Nutrient regulates Tor1 nuclear localization and association with rDNA promoter. *Nature* 2006 442:7106, 442(7106), 1058–1061. <https://doi.org/10.1038/nature05020>
- Li, Z., Chen, S., Zhao, L., Huang, G., Pi, X., Sun, S., Wang, P., & Sui, S. F. (2022). Near-atomic structure of the inner ring of the *Saccharomyces cerevisiae* nuclear pore complex. *Cell Research*, 32(5), 437. <https://doi.org/10.1038/S41422-022-00632-Y>
- Lindström, M. S., Jurada, D., Bursac, S., Orsolich, I., Bartek, J., & Volarevic, S. (2018). Nucleolus as an emerging hub in maintenance of genome stability and cancer pathogenesis. *Oncogene* 2018 37:18, 37(18), 2351–2366. <https://doi.org/10.1038/s41388-017-0121-z>
- Lisby, M., Barlow, J. H., Burgess, R. C., & Rothstein, R. (2004). Choreography of the DNA Damage Response: Spatiotemporal Relationships among Checkpoint and Repair Proteins. *Cell*, 118(6), 699–713. <https://doi.org/10.1016/J.CELL.2004.08.015>
- Liu, J., Ben-Shahar, T. R., Riemer, D., Treinin, M., Spann, P., Weber, K., Fire, A., & Gruenbaum, Y. (2000). Essential Roles for *Caenorhabditis elegans* Lamin Gene in Nuclear Organization, Cell Cycle Progression, and Spatial Organization of Nuclear Pore Complexes. *Molecular Biology of the Cell*, 11(11), 3937–3947. <https://doi.org/10.1091/mbc.11.11.3937>
- Liu, S., Kwon, M., Mannino, M., Yang, N., Renda, F., Khodjakov, A., & Pellman, D. (2018). Nuclear envelope assembly defects link mitotic errors to chromothripsis. *Nature*, 561(7724), 551–555. <https://doi.org/10.1038/s41586-018-0534-z>
- Loewith, R., & Hall, M. N. (2011). Target of rapamycin (TOR) in nutrient signaling and growth control. *Genetics*, 189(4), 1177–1201. <https://doi.org/10.1534/genetics.111.133363>
- Lord, C. L., & Wente, S. R. (2020). Nuclear envelope–vacuole contacts mitigate nuclear

-
- pore complex assembly stress. *Journal of Cell Biology*, 219(12). <https://doi.org/10.1083/jcb.202001165>
- Machín, F., Torres-Rosell, J., De Piccoli, G., Carballo, J. A., Cha, R. S., Jarmuz, A., & Aragón, L. (2006). Transcription of ribosomal genes can cause nondisjunction. *Journal of Cell Biology*, 173(6), 893–903. <https://doi.org/10.1083/jcb.200511129>
- Machín, F., Torres-Rosell, J., Jarmuz, A., & Aragón, L. (2005). Spindle-independent condensation-mediated segregation of yeast ribosomal DNA in late anaphase. *The Journal of Cell Biology*, 168(2), 209–219. <https://doi.org/10.1083/jcb.200408087>
- Makarova, M., Gu, Y., Chen, J.-S., René E Beckley, J., & Gould, K. L. (2016). Temporal Regulation of Lipin Activity Diverged to Account for Differences in Mitotic Programs. *Current Biology*, 26, 237–243. <https://doi.org/10.1016/j.cub.2015.11.061>
- Makarova, M., & Oliferenko, S. (2016). Mixing and matching nuclear envelope remodeling and spindle assembly strategies in the evolution of mitosis. *Current Opinion in Cell Biology*, 41, 43–50. <https://doi.org/10.1016/j.ceb.2016.03.016>
- Male, G., Deolal, P., Manda, N. K., Yagnik, S., Mazumder, A., & Mishra, K. (2020). Nucleolar size regulates nuclear envelope shape in *Saccharomyces cerevisiae*. *Journal of Cell Science*, 133(20). <https://doi.org/10.1242/JCS.242172>
- Manley, H. R., Keightley, M. C., & Lieschke, G. J. (2018). The Neutrophil Nucleus: An Important Influence on Neutrophil Migration and Function. *Frontiers in Immunology*, 9, 2867. <https://doi.org/10.3389/FIMMU.2018.02867/BIBTEX>
- Marelli, M., Lusk, C. P., Chan, H., Aitchison, J. D., & Wozniak, R. W. (2001). A Link between the Synthesis of Nucleoporins and the Biogenesis of the Nuclear Envelope. *Journal of Cell Biology*, 153(4), 709–724. <https://doi.org/10.1083/JCB.153.4.709>
- Marnef, A., Finoux, A. L., Arnould, C., Guillou, E., Daburon, V., Rocher, V., Mangeat, T., Mangeot, P. E., Ricci, E. P., & Legube, G. (2019). A cohesin/HUSH- And LINC-dependent pathway controls ribosomal DNA double-strand break repair. *Genes and Development*, 33(17–18), 1175–1190. <https://doi.org/10.1101/GAD.324012.119-/DC1>
- Marshall, W. F., Straight, A., Marko, J. F., Swedlow, J., Dernburg, A., Belmont, A., Murray, A. W., Agard, D. A., & Sedat, J. W. (1997). Interphase chromosomes undergo constrained diffusional motion in living cells. *Current Biology*, 7(12), 930–939. [https://doi.org/10.1016/S0960-9822\(06\)00412-X](https://doi.org/10.1016/S0960-9822(06)00412-X)
- Martin, D. E., Powers, T., & Hall, M. N. (2006). Regulation of ribosome biogenesis: Where is TOR? *Cell Metabolism*, 4(4), 259–260. <https://doi.org/10.1016/j.cmet.2006.09.002>
- Matellán, L., & Monje-Casas, F. (2020). Regulation of mitotic exit by cell cycle checkpoints: Lessons from *Saccharomyces cerevisiae*. In *Genes* (Vol. 11, Issue 2, p. 195). MDPI AG. <https://doi.org/10.3390/genes11020195>
- Matos-Perdomo, E., & Machín, F. (2017). The ribosomal DNA metaphase loop of *Saccharomyces cerevisiae* gets condensed upon heat stress in a Cdc14-independent TORC1-dependent manner. *Cell Cycle*, 1–39. <https://doi.org/10.1080/15384101.2017.1407890>
- Matos-Perdomo, E., & Machín, F. (2018). The ribosomal DNA metaphase loop of

6. References

- Saccharomyces cerevisiae* gets condensed upon heat stress in a Cdc14-independent TORC1-dependent manner. *Cell Cycle*, 17(2), 200. <https://doi.org/10.1080/15384101.2017.1407890>
- Matos-Perdomo, E., & Machín, F. (2019). Nucleolar and Ribosomal DNA Structure under Stress: Yeast Lessons for Aging and Cancer. *Cells*, 8(8), 779. <https://doi.org/10.3390/cells8080779>
- Matos-Perdomo, E., Santana-Sosa, S., Ayra-Plasencia, J., Medina-Sú Arez, S., & Elix Machín, F. (2022). The vacuole shapes the nucleus and the ribosomal DNA loop during mitotic delays. *Life Science Alliance*, 5(10), e202101161. <https://doi.org/10.26508/LSA.202101161>
- Mayer, C., Bierhoff, H., & Grummt, I. (2005). The nucleolus as a stress sensor: JNK2 inactivates the transcription factor TIF-IA and down-regulates rRNA synthesis. *Genes & Development*, 19(8), 933–941. <https://doi.org/10.1101/GAD.333205>
- Meister, P., & Taddei, A. (2013). Building silent compartments at the nuclear periphery: a recurrent theme. *Current Opinion in Genetics & Development*, 23(2), 96–103. <https://doi.org/10.1016/J.GDE.2012.12.001>
- Mekhail, K., & Moazed, D. (2010). The nuclear envelope in genome organization, expression and stability. *Nature Reviews Molecular Cell Biology* 2010 11:5, 11(5), 317–328. <https://doi.org/10.1038/nrm2894>
- Mekhail, K., Seebacher, J., Gygi, S. P., & Moazed, D. (2008). Role for perinuclear chromosome tethering in maintenance of genome stability. *Nature* 2008 456:7222, 456(7222), 667–670. <https://doi.org/10.1038/nature07460>
- Meseroll, R. A., & Cohen-Fix, O. (2016). The Malleable Nature of the Budding Yeast Nuclear Envelope: Flares, Fusion, and Fenestrations. *Journal of Cellular Physiology*, 231(11), 2353–2360. <https://doi.org/10.1002/jcp.25355>
- Mészáros, N., Cibulka, J., Mendiburo, M. J., Romanauska, A., Schneider, M., & Köhler, A. (2015). Nuclear Pore Basket Proteins Are Tethered to the Nuclear Envelope and Can Regulate Membrane Curvature. *Developmental Cell*, 33(3), 285–298. <https://doi.org/10.1016/j.devcel.2015.02.017>
- Michaelis, C., Ciosk, R., & Nasmyth, K. (1997). Cohesins: Chromosomal proteins that prevent premature separation of sister chromatids. *Cell*, 91(1), 35–45. [https://doi.org/10.1016/S0092-8674\(01\)80007-6](https://doi.org/10.1016/S0092-8674(01)80007-6)
- Michaillat, L., & Mayer, A. (2013). Identification of Genes Affecting Vacuole Membrane Fragmentation in *Saccharomyces cerevisiae*. *PLOS ONE*, 8(2), e54160. <https://doi.org/10.1371/JOURNAL.PONE.0054160>
- Mijaljica, D., & Klionsky, D. J. (2022). The necessity of nucleophagic modality. *Autophagy*, 18(2), 443. <https://doi.org/10.1080/15548627.2021.1971380>
- Mijaljica, D., Prescott, M., & Devenish, R. J. (2012). A Late Form of Nucleophagy in *Saccharomyces cerevisiae*. *PLoS ONE*, 7(6), e40013. <https://doi.org/10.1371/journal.pone.0040013>
- Millen, J. I., Krick, R., Prick, T., Thumm, M., & Goldfarb, D. S. (2009). *Measuring piecemeal microautophagy of the nucleus in Saccharomyces cerevisiae*. <https://doi.org/10.4161/auto.5.1.7181>

-
- Miné-Hattab, J., & Taddei, A. (2019). Physical principles and functional consequences of nuclear compartmentalization in budding yeast. In *Current Opinion in Cell Biology* (Vol. 58, pp. 105–113). Elsevier Ltd. <https://doi.org/10.1016/j.ceb.2019.02.005>
- Miyazaki, T., & Kobayashi, T. (2011). Visualization of the dynamic behavior of ribosomal RNA gene repeats in living yeast cells. *Genes to Cells*, 16(5), 491–502. <https://doi.org/10.1111/J.1365-2443.2011.01506.X>
- Mochida, K., Oikawa, Y., Kimura, Y., Kirisako, H., Hirano, H., Ohsumi, Y., & Nakatogawa, H. (2015). Receptor-mediated selective autophagy degrades the endoplasmic reticulum and the nucleus. *Nature*, 522(7556), 359–362. <https://doi.org/10.1038/nature14506>
- Mori, R., & Oliferenko, S. (2020). Cell Biology: An Open Solution for Closed Mitosis. *Current Biology*, 30(16), R942–R944. <https://doi.org/10.1016/j.cub.2020.06.067>
- Morshed, S., Sharmin, T., & Ushimaru, T. (2020). TORC1 regulates ESCRT-0 complex formation on the vacuolar membrane and microautophagy induction in yeast. *Biochemical and Biophysical Research Communications*, 522(1), 88–94. <https://doi.org/10.1016/j.bbrc.2019.11.064>
- Mostofa, M. G., Morshed, S., Shibata, R., Takeichi, Y., Rahman, M. A., Hosoyamada, S., Kobayashi, T., & Ushimaru, T. (2019). rDNA Condensation Promotes rDNA Separation from Nucleolar Proteins Degraded for Nucleophagy after TORC1 Inactivation. *Cell Reports*, 28(13), 3423–3434.e2. <https://doi.org/10.1016/j.celrep.2019.08.059>
- Mostofa, M. G., Rahman, M. A., Koike, N., Yeasmin, A. M. S. T., Islam, N., Waliullah, T. M., Hosoyamada, S., Shimobayashi, M., Kobayashi, T., Hall, M. N., & Ushimaru, T. (2018). CLIP and cohibin separate rDNA from nucleolar proteins destined for degradation by nucleophagy. *Journal of Cell Biology*, 217(8), 2675–2690. <https://doi.org/10.1083/jcb.201706164>
- Muller, M., Lucchini, R., & Sogo, J. M. (2000). Replication of Yeast rDNA Initiates Downstream of Transcriptionally Active Genes. *Molecular Cell*, 5(5), 767–777. [https://doi.org/10.1016/S1097-2765\(00\)80317-2](https://doi.org/10.1016/S1097-2765(00)80317-2)
- Nagai, S., Dubrana, K., Tsai-Pflugfelder, M., Davidson, M. B., Roberts, T. M., Brown, G. W., Varela, E., Hediger, F., Gasser, S. M., & Krogan, N. J. (2008). Functional Targeting of DNA Damage to a Nuclear Pore–Associated SUMO-Dependent Ubiquitin Ligase. *Science (New York, N.Y.)*, 322(5901), 597. <https://doi.org/10.1126/SCIENCE.1162790>
- Nair, U., Thumm, M., Klionsky, D. J., & Krick, R. (2011). GFP-Atg8 protease protection as a tool to monitor autophagosome biogenesis. [Http://Dx.Doi.Org/10.4161/Auto.7.12.18424](http://Dx.Doi.Org/10.4161/Auto.7.12.18424), 7(12), 1546–1550. <https://doi.org/10.4161/AUTO.7.12.18424>
- Nakatogawa, H., & Mochida, K. (2015). Reticulophagy and nucleophagy: New findings and unsolved issues. *Autophagy*, 11(12), 2377–2378. <https://doi.org/10.1080/15548627.2015.1106665>
- Nakatogawa, H., Suzuki, K., Kamada, Y., & Ohsumi, Y. (2009). Dynamics and diversity in autophagy mechanisms: lessons from yeast. *Nature Reviews Molecular Cell*

6. References

- Biology* 2009 10:7, 10(7), 458–467. <https://doi.org/10.1038/nrm2708>
- Neumann, F. R., & Nurse, P. (2007). Nuclear size control in fission yeast. *Journal of Cell Biology*, 179(4), 593–600. <https://doi.org/10.1083/jcb.200708054>
- Nishimura, K., Fukagawa, T., Takisawa, H., Kakimoto, T., & Kanemaki, M. (2009). An auxin-based degron system for the rapid depletion of proteins in nonplant cells. *Nature Methods*, 6(12), 917–922. <https://doi.org/10.1038/nmeth.1401>
- Noda, T. (2017). Regulation of autophagy through TORC1 and mTORC1. In *Biomolecules* (Vol. 7, Issue 3, p. 52). MDPI AG. <https://doi.org/10.3390/biom7030052>
- Noda, T., & Ohsumi, Y. (1998). Tor, a phosphatidylinositol kinase homologue, controls autophagy in yeast. *Journal of Biological Chemistry*, 273(7), 3963–3966. <https://doi.org/10.1074/jbc.273.7.3963>
- O'Hara, L., Han, G. S., Sew, P. C., Grimsey, N., Carman, G. M., & Siniosoglou, S. (2006). Control of phospholipid synthesis by phosphorylation of the yeast lipin Pah1p/Smp2p Mg²⁺-dependent phosphatidate phosphatase. *Journal of Biological Chemistry*, 281(45), 34537–34548. <https://doi.org/10.1074/jbc.M606654200>
- Oakes, M., Nogi, Y., Clark, M. W., & Nomura, M. (1993). Structural alterations of the nucleolus in mutants of *Saccharomyces cerevisiae* defective in RNA polymerase I. *Molecular and Cellular Biology*, 13(4), 2441. <https://doi.org/10.1128/MCB.13.4.2441>
- Otto, F. B., & Thumm, M. (2020). Nucleophagy—Implications for Microautophagy and Health. *International Journal of Molecular Sciences* 2020, Vol. 21, Page 4506, 21(12), 4506. <https://doi.org/10.3390/IJMS21124506>
- Otto, F. B., & Thumm, M. (2021). Mechanistic dissection of macro- and micronucleophagy. *Autophagy*, 17(3), 626–639. <https://doi.org/10.1080/15548627.2020.1725402>
- Ouspenski, I. I., Cabello, O. A., & Brinkley, B. R. (2000). Chromosome Condensation Factor Brn1p Is Required for Chromatid Separation in Mitosis. *Molecular Biology of the Cell*, 11(4), 1305–1313. <https://doi.org/10.1091/mbc.11.4.1305>
- Palladino, F., Laroche, T., Gilson, E., Axelrod, A., Pillus, L., & Gasser, S. M. (1993). SIR3 and SIR4 proteins are required for the positioning and integrity of yeast telomeres. *Cell*, 75(3), 543–555. [https://doi.org/10.1016/0092-8674\(93\)90388-7](https://doi.org/10.1016/0092-8674(93)90388-7)
- Palmer, R. E., Koval, M., & Koshland, D. (1989). The dynamics of chromosome movement in the budding yeast *Saccharomyces cerevisiae*. *Journal of Cell Biology*, 109(6), 3355–3366. <https://doi.org/10.1083/JCB.109.6.3355>
- Palmer, R. E., Sullivan, D. S., Huffaker, T., & Koshland, D. (1992). Role of astral microtubules and actin in spindle orientation and migration in the budding yeast, *Saccharomyces cerevisiae*. *Journal of Cell Biology*, 119(3), 583–593. <https://doi.org/10.1083/JCB.119.3.583>
- Pan, X., Roberts, P., Chen, Y., Kvam, E., Shulga, N., Huang, K., Lemmon, S., & Goldfarb, D. S. (2000). Nucleus–Vacuole Junctions in *Saccharomyces cerevisiae* Are Formed Through the Direct Interaction of Vac8p with Nvj1p. *Molecular Biology of the Cell*, 11(7), 2445. <https://doi.org/10.1091/MBC.11.7.2445>

-
- Papandreou, M. E., & Tavernarakis, N. (2019). Nucleophagy: from homeostasis to disease. *Cell Death & Differentiation* 2019 26:4, 26(4), 630–639. <https://doi.org/10.1038/s41418-018-0266-5>
- Papandreou, M. E., & Tavernarakis, N. (2020). Nucleophagy mediators and mechanisms. *Progress in Molecular Biology and Translational Science*, 172, 1–14. <https://doi.org/10.1016/BS.PMBTS.2020.01.003>
- Pascual, F., & Carman, G. M. (2013). Phosphatidate phosphatase, a key regulator of lipid homeostasis. In *Biochimica et Biophysica Acta - Molecular and Cell Biology of Lipids* (Vol. 1831, Issue 3, pp. 514–522). Elsevier. <https://doi.org/10.1016/j.bbalip.2012.08.006>
- Pasero, P., & Marilley, M. (1993). Size variation of rDNA clusters in the yeasts *Saccharomyces cerevisiae* and *Schizosaccharomyces pombe*. *Molecular and General Genetics MGG* 1993 236:2, 236(2), 448–452. <https://doi.org/10.1007/BF00277147>
- Passmore, L. A., Booth, C. R., Vénien-Bryan, C., Ludtke, S. J., Fioretto, C., Johnson, L. N., Chiu, W., & Barford, D. (2005). Structural analysis of the anaphase-promoting complex reveals multiple active sites and insights into polyubiquitylation. *Molecular Cell*, 20(6), 855–866. <https://doi.org/10.1016/j.molcel.2005.11.003>
- Passmore, L. A., McCormack, E. A., Au, S. W. N., Paul, A., Willison, K. R., Harper, J. W., & Barford, D. (2003). Doc1 mediates the activity of the anaphase-promoting complex by contributing to substrate recognition. *The EMBO Journal*, 22(4), 786–796. <https://doi.org/10.1093/EMBOJ/CDG084>
- Patel, S. S., & Rexach, M. F. (2008). Discovering Novel Interactions at the Nuclear Pore Complex Using Bead Halo. *Molecular & Cellular Proteomics*, 7(1), 121–131. <https://doi.org/10.1074/mcp.M700407-MCP200>
- Peters, J. M. (2006). The anaphase promoting complex/cyclosome: a machine designed to destroy. *Nature Reviews Molecular Cell Biology* 2006 7:9, 7(9), 644–656. <https://doi.org/10.1038/nrm1988>
- Petes, T. D. (1980). Unequal meiotic recombination within tandem arrays of yeast ribosomal DNA genes. *Cell*, 19(3), 765–774. [https://doi.org/10.1016/S0092-8674\(80\)80052-3](https://doi.org/10.1016/S0092-8674(80)80052-3)
- Prunuske, A. J., & Ullman, K. S. (2006). The nuclear envelope: Form and reformation. *Current Opinion in Cell Biology*, 18(1), 108–116. <https://doi.org/10.1016/j.ceb.2005.12.004>
- Raab, M., Gentili, M., de Belly, H., Thiam, H.-R., Vargas, P., Jimenez, A. J., Lautenschlaeger, F., Voituriez, R., Lennon-Duménil, A.-M., Manel, N., & Piel, M. (2016). ESCRT III repairs nuclear envelope ruptures during cell migration to limit DNA damage and cell death. *Science*, 352(6283), 359–362. <https://doi.org/10.1126/science.aad7611>
- Rahman, M. A., Mostofa, M. G., & Ushimaru, T. (2018). The Nem1/Spo7–Pah1/lipin axis is required for autophagy induction after TORC 1 inactivation. *The FEBS Journal*, 285(10), 1840–1860. <https://doi.org/10.1111/febs.14448>
- Rahman, M. A., Terasawa, M., Mostofa, M. G., & Ushimaru, T. (2018). The TORC1–

6. References

- Nem1/Spo7–Pah1/lipin axis regulates microautophagy induction in budding yeast. *Biochemical and Biophysical Research Communications*, 504(2), 505–512. <https://doi.org/10.1016/j.bbrc.2018.09.011>
- Rai, U., Najm, F., & Tartakoff, A. M. (2017). Nucleolar asymmetry and the importance of septin integrity upon cell cycle arrest. *PLOS ONE*, 12(3), e0174306. <https://doi.org/10.1371/JOURNAL.PONE.0174306>
- Reggiori, F., & Klionsky, D. J. (2013). Autophagic processes in yeast: Mechanism, machinery and regulation. *Genetics*, 194(2), 341–361. <https://doi.org/10.1534/genetics.112.149013>
- Roberts, P., Moshitch-Moshkovitz, S., Kvam, E., O’Toole, E., Winey, M., & Goldfarb, D. S. (2003). Piecemeal microautophagy of nucleus in *Saccharomyces cerevisiae*. *Molecular Biology of the Cell*, 14(1), 129–141. <https://doi.org/10.1091/mbc.E02-08-0483>
- Romanauska, A., & Köhler, A. (2018). The Inner Nuclear Membrane Is a Metabolically Active Territory that Generates Nuclear Lipid Droplets. *Cell*, 174(3), 700–715.e18. <https://doi.org/10.1016/j.cell.2018.05.047>
- Rothballer, A., & Kutay, U. (2013). The diverse functional LINC’s of the nuclear envelope to the cytoskeleton and chromatin. *Chromosoma*, 122(5), 415. <https://doi.org/10.1007/S00412-013-0417-X>
- Rout, M. P., Aitchison, J. D., Suprapto, A., Hjertaas, K., Zhao, Y., & Chait, B. T. (2000). The Yeast Nuclear Pore Complex: Composition, Architecture, and Transport Mechanism. *Journal of Cell Biology*, 148(4), 635–652. <https://doi.org/10.1083/JCB.148.4.635>
- Rowat, A. C., Jaalouk, D. E., Zwerger, M., Ung, W. L., Eydelnant, I. A., Olins, D. E., Olins, A. L., Herrmann, H., Weitz, D. A., & Lammerding, J. (2013). Nuclear envelope composition determines the ability of neutrophil-type cells to passage through micron-scale constrictions. *Journal of Biological Chemistry*, 288(12), 8610–8618. <https://doi.org/10.1074/jbc.M112.441535>
- Sanchez, Y., Desany, B. A., Jones, W. J., Liu, Q., Wang, B., & Elledge, S. J. (1996). Regulation of RAD53 by the ATM-Like Kinases MEC1 and TEL1 in Yeast Cell Cycle Checkpoint Pathways. *Science*, 271(5247), 357–360. <https://doi.org/10.1126/SCIENCE.271.5247.357>
- Santocanale, C., & Diffley, J. F. (1998). A Mec1- and Rad53-dependent checkpoint controls late-firing origins of DNA replication. *Nature*, 395(6702), 615–618. <https://doi.org/10.1038/27001>
- Santos-Rosa, H., Leung, J., Grimsey, N., Peak-Chew, S., & Siniosoglou, S. (2005). The yeast lipin Smp2 couples phospholipid biosynthesis to nuclear membrane growth. *The EMBO Journal*, 24(11), 1931–1941. <https://doi.org/10.1038/SJ.EMBOJ.7600672>
- Sasser, T., Qiu, Q. S., Karunakaran, S., Padolina, M., Reyes, A., Flood, B., Smith, S., Gonzales, C., & Fratti, R. A. (2012). Yeast lipin 1 orthologue Pah1p regulates vacuole homeostasis and membrane fusion. *Journal of Biological Chemistry*, 287(3), 2221–2236. <https://doi.org/10.1074/jbc.M111.317420>

-
- Scaffidi, P., & Misteli, T. (2006). Lamin A-Dependent Nuclear Defects in Human Aging. *Science (New York, N.Y.)*, *312*(5776), 1059. <https://doi.org/10.1126/SCIENCE.1127168>
- Schindelin, J., Arganda-Carreras, I., Frise, E., Kaynig, V., Longair, M., Pietzsch, T., Preibisch, S., Rueden, C., Saalfeld, S., Schmid, B., Tinevez, J. Y., White, D. J., Hartenstein, V., Eliceiri, K., Tomancak, P., & Cardona, A. (2012). Fiji - an Open Source platform for biological image analysis. *Nature Methods*, *9*(7), 676–682. <https://doi.org/10.1038/NMETH.2019>
- Schmid, M., Arib, G., Laemmli, C., Nishikawa, J., Durussel, T., & Laemmli, U. K. (2006). Nup-PI: The nucleopore-promoter interaction of genes in yeast. *Molecular Cell*, *21*(3), 379–391. <https://doi.org/10.1016/j.molcel.2005.12.012>
- Schneider, J. L., & Cuervo, A. M. (2014). Autophagy and human disease: emerging themes. *Current Opinion in Genetics & Development*, *26*, 16–23. <https://doi.org/10.1016/J.GDE.2014.04.003>
- Schreiner, S. M., Koo, P. K., Zhao, Y., Mochrie, S. G. J., & King, M. C. (2015). The tethering of chromatin to the nuclear envelope supports nuclear mechanics. *Nature Communications 2015 6:1*, *6*(1), 1–13. <https://doi.org/10.1038/ncomms8159>
- Scorrano, L., De Matteis, M. A., Emr, S., Giordano, F., Hajnóczky, G., Kornmann, B., Lackner, L. L., Levine, T. P., Pellegrini, L., Reinisch, K., Rizzuto, R., Simmen, T., Stenmark, H., Ungermann, C., & Schuldiner, M. (2019). Coming together to define membrane contact sites. *Nature Communications 2019 10:1*, *10*(1), 1–11. <https://doi.org/10.1038/s41467-019-09253-3>
- Shen, D., & Skibbens, R. V. (2017). Temperature-dependent regulation of rDNA condensation in *Saccharomyces cerevisiae*. *Cell Cycle*, *16*(11), 1118–1127. <https://doi.org/10.1080/15384101.2017.1317409>
- Shintani, T., & Klionsky, D. J. (2004). Cargo proteins facilitate the formation of transport vesicles in the cytoplasm to vacuole targeting pathway. *Journal of Biological Chemistry*, *279*(29), 29889–29894. <https://doi.org/10.1074/jbc.M404399200>
- Shou, W., Seol, J. H., Shevchenko, A., Baskerville, C., Moazed, D., Susan Chen, Z. W., Jang, J., Shevchenko, A., Charbonneau, H., & Deshaies, R. J. (1999). Exit from Mitosis Is Triggered by Tem1-Dependent Release of the Protein Phosphatase Cdc14 from Nucleolar RENT Complex. *Cell*, *97*(2), 233–244. [https://doi.org/10.1016/S0092-8674\(00\)80733-3](https://doi.org/10.1016/S0092-8674(00)80733-3)
- Shpilka, T., Welter, E., Borovsky, N., Amar, N., Mari, M., Reggiori, F., & Elazar, Z. (2015). Lipid droplets and their component triglycerides and steryl esters regulate autophagosome biogenesis. *The EMBO Journal*, *34*(16), 2117–2131. <https://doi.org/10.15252/EMBJ.201490315>
- Sinclair, D. A., & Guarente, L. (1997). Extrachromosomal rDNA circles - A cause of aging in yeast. *Cell*, *91*(7), 1033–1042. [https://doi.org/10.1016/S0092-8674\(00\)80493-6](https://doi.org/10.1016/S0092-8674(00)80493-6)
- Siniosoglou, S. (1998). A novel complex of membrane proteins required for formation of a spherical nucleus. *The EMBO Journal*, *17*(22), 6449–6464. <https://doi.org/10.1093/emboj/17.22.6449>

6. References

- Siniossoglou, S. (2009). Lipins, Lipids and Nuclear Envelope Structure. *Traffic*, *10*(9), 1181–1187. <https://doi.org/10.1111/J.1600-0854.2009.00923.X>
- St-Pierre, J., Douziech, M., Bazile, F., Pascariu, M., Bonneil, É., Sauvé, V., Ratsima, H., & D'Amours, D. (2009). Polo Kinase Regulates Mitotic Chromosome Condensation by Hyperactivation of Condensin DNA Supercoiling Activity. *Molecular Cell*, *34*(4), 416–426. <https://doi.org/10.1016/j.molcel.2009.04.013>
- St. Charles, J., Hazkani-Covo, E., Yin, Y., Andersen, S. L., Dietrich, F. S., Greenwell, P. W., Malc, E., Mieczkowski, P., & Petes, T. D. (2012). High-Resolution Genome-Wide Analysis of Irradiated (UV and γ -Rays) Diploid Yeast Cells Reveals a High Frequency of Genomic Loss of Heterozygosity (LOH) Events. *Genetics*, *190*(4), 1267–1284. <https://doi.org/10.1534/GENETICS.111.137927>
- St Charles, J., & Petes, T. D. (2013). High-resolution mapping of spontaneous mitotic recombination hotspots on the 1.1 Mb arm of yeast chromosome IV. *PLoS Genetics*, *9*(4), e1003434. <https://doi.org/10.1371/journal.pgen.1003434>
- Stephan, J. S., Yeh, Y. Y., Ramachandran, V., Deminoff, S. J., & Herman, P. K. (2009). The Tor and PKA signaling pathways independently target the Atg1/Atg13 protein kinase complex to control autophagy. *Proceedings of the National Academy of Sciences of the United States of America*, *106*(40), 17049. <https://doi.org/10.1073/PNAS.0903316106>
- Stephens, A. D., Banigan, E. J., & Marko, J. F. (2019). Chromatin's physical properties shape the nucleus and its functions. *Current Opinion in Cell Biology*, *58*, 76. <https://doi.org/10.1016/J.CEB.2019.02.006>
- Stone, E. M., Heun, P., Laroche, T., Pillus, L., & Gasser, S. M. (2000). MAP kinase signaling induces nuclear reorganization in budding yeast. *Current Biology*, *10*(7), 373–382. [https://doi.org/10.1016/S0960-9822\(00\)00413-9](https://doi.org/10.1016/S0960-9822(00)00413-9)
- Straight, A. F., Shou, W., Dowd, G. J., Turck, C. W., Deshaies, R. J., Johnson, A. D., & Moazed, D. (1999). Net1, a Sir2-associated nucleolar protein required for rDNA silencing and nucleolar integrity. *Cell*, *97*(2), 245–256. [https://doi.org/10.1016/S0092-8674\(00\)80734-5](https://doi.org/10.1016/S0092-8674(00)80734-5)
- Strunnikov, A. V., Larionov, V. L., & Koshland, D. (1993). SMC1: an essential yeast gene encoding a putative head-rod-tail protein is required for nuclear division and defines a new ubiquitous protein family. *The Journal of Cell Biology*, *123*(6), 1635. <https://doi.org/10.1083/JCB.123.6.1635>
- Strunnikov, A. V., Hogan, E., & Koshland, D. (1995). SMC2, a *Saccharomyces cerevisiae* gene essential for chromosome segregation and condensation, defines a subgroup within the SMC family. *Genes & Development*, *9*(5), 587–599. <http://www.ncbi.nlm.nih.gov/pubmed/7698648>
- Su, W. M., Han, G. S., Casciano, J., & Carman, G. M. (2012). Protein kinase A-mediated phosphorylation of Pah1p phosphatidate phosphatase functions in conjunction with the Pho85p-Pho80p and Cdc28p-Cyclin B kinases to regulate lipid synthesis in yeast. *Journal of Biological Chemistry*, *287*(40), 33364–33376. <https://doi.org/10.1074/jbc.M112.402339>
- Sun, Z., Fay, D. S., Marini, F., Foiani, M., & Stern, D. F. (1996). Spk1/Rad53 is regulated by Mec1-dependent protein phosphorylation in DNA replication and damage

- checkpoint pathways. *Genes & Development*, 10(4), 395–406. <https://doi.org/10.1101/gad.10.4.395>
- Taddei, A., & Gasser, S. M. (2012). Structure and function in the budding yeast nucleus. *Genetics*, 192(1), 107–129. <https://doi.org/10.1534/genetics.112.140608>
- Taimen, P., Pflieger, K., Shimi, T., Möller, D., Ben-Harush, K., Erdos, M. R., Adam, S. A., Herrmann, H., Medalia, O., Collins, F. S., Goldman, A. E., & Goldman, R. D. (2009). A progeria mutation reveals functions for lamin A in nuclear assembly, architecture, and chromosome organization. *Proceedings of the National Academy of Sciences of the United States of America*, 106(49), 20788. <https://doi.org/10.1073/PNAS.0911895106>
- Takeuchi, Y., Horiuchi, T., & Kobayashi, T. (2003). Transcription-dependent recombination and the role of fork collision in yeast rDNA. *Genes & Development*, 17(12), 1497–1506. <https://doi.org/10.1101/GAD.1085403>
- Tanny, J. C., Kirkpatrick, D. S., Gerber, S. A., Gygi, S. P., & Moazed, D. (2004). Budding Yeast Silencing Complexes and Regulation of Sir2 Activity by Protein-Protein Interactions. *Molecular and Cellular Biology*, 24(16), 6931–6946. <https://doi.org/10.1128/MCB.24.16.6931-6946.2004>
- Tercero, J. A., & Diffley, J. F. (2001). Regulation of DNA replication fork progression through damaged DNA by the Mec1/Rad53 checkpoint. *Nature*, 412(6846), 553–557. <https://doi.org/10.1038/35087607>
- Titus, L. C., Dawson, T. R., Rexer, D. J., Ryan, K. J., & Wentz, S. R. (2010). Members of the RSC chromatin-remodeling complex are required for maintaining proper nuclear envelope structure and pore complex localization. *Molecular Biology of the Cell*, 21(6), 1072–1087. <https://doi.org/10.1091/mbc.e09-07-0615>
- Tomioka, Y., Kotani, T., Kirisako, H., Oikawa, Y., Kimura, Y., Hirano, H., Ohsumi, Y., & Nakatogawa, H. (2020). *TORC1 inactivation stimulates autophagy of nucleoporin and nuclear pore complexes*. <https://doi.org/10.1083/jcb.201910063>
- Torán-Vilarrubias, A., & Moriel-Carretero, M. (2021). Oxidative agents elicit endoplasmic reticulum morphological changes suggestive of alterations in lipid metabolism. *MicroPublication Biology*. <https://doi.org/10.17912/MICROPUB.BIOLOGY.000462>
- Torres-Rosell, J., Machín, F., & Aragón, L. (2005). Cdc14 and the temporal coordination between mitotic exit and chromosome segregation. *Cell Cycle*, 4(1), 109–112. <https://doi.org/10.4161/cc.4.1.1356>
- Torres-Rosell, J., Machín, F., Jarmuz, A., & Aragón, L. (2004). Nucleolar segregation lags behind the rest of the genome and requires Cdc14p activation by the FEAR network. *Cell Cycle (Georgetown, Tex.)*, 3(4), 496–502. <http://www.ncbi.nlm.nih.gov/pubmed/15004526>
- Torres-Rosell, J., Sunjevaric, I., De Piccoli, G., Sacher, M., Eckert-Boulet, N., Reid, R., Jentsch, S., Rothstein, R., Aragón, L., & Lisby, M. (2007). The Smc5-Smc6 complex and SUMO modification of Rad52 regulates recombinational repair at the ribosomal gene locus. *Nature Cell Biology*, 9(8), 923–931. <https://doi.org/10.1038/ncb1619>
- Tosal-Castano, S., Peselj, C., Kohler, V., Habernig, L., Berglund, L. L., Ebrahimi, M.,

6. References

- Vögtle, F. N., Höög, J., Andréasson, C., & Büttner, S. (2021). Snd3 controls nucleus-vacuole junctions in response to glucose signaling. *Cell Reports*, *34*(3), 108637. <https://doi.org/10.1016/j.celrep.2020.108637>
- Traverso, E. E., Baskerville, C., Liu, Y., Shou, W., James, P., Deshaies, R. J., & Charbonneau, H. (2001). Characterization of the Net1 Cell Cycle-dependent Regulator of the Cdc14 Phosphatase from Budding Yeast. *Journal of Biological Chemistry*, *276*(24), 21924–21931. <https://doi.org/10.1074/jbc.M011689200>
- Trumtel, S., Léger-Silvestre, I., Gleizes, P. E., Teulières, F., & Gas, N. (2000). Assembly and Functional Organization of the Nucleolus: Ultrastructural Analysis of *Saccharomyces cerevisiae* Mutants. *Molecular Biology of the Cell*, *11*(6), 2175. <https://doi.org/10.1091/MBC.11.6.2175>
- Tsang, C. K., Bertram, P. G., Ai, W., Drenan, R., & Zheng, X. F. S. (2003). Chromatin-mediated regulation of nucleolar structure and RNA Pol I localization by TOR. *The EMBO Journal*, *22*(22), 6045–6056. <https://doi.org/10.1093/EMBOJ/CDG578>
- Ueda, S., Ozaki, R., Kaneko, A., Akizuki, R., Katsuta, H., Miura, A., Matsuura, A., & Ushimaru, T. (2019). TORC1, Tel1/Mec1, and Mpk1 regulate autophagy induction after DNA damage in budding yeast. *Cellular Signalling*, *62*, 109344. <https://doi.org/10.1016/j.cellsig.2019.109344>
- Uhlmann, F. (2001). Chromosome cohesion and segregation in mitosis and meiosis. *Current Opinion in Cell Biology*, *13*(6), 754–761. [https://doi.org/10.1016/S0955-0674\(00\)00279-9](https://doi.org/10.1016/S0955-0674(00)00279-9)
- Ungricht, R., & Kutay, U. (2017). Mechanisms and functions of nuclear envelope remodelling. In *Nature Reviews Molecular Cell Biology* (Vol. 18, Issue 4, pp. 229–245). Nature Publishing Group. <https://doi.org/10.1038/nrm.2016.153>
- Varshney, N., & Sanyal, K. (2019). Nuclear migration in budding yeasts: position before division. *Current Genetics*, *65*(6), 1341–1346. <https://doi.org/10.1007/S00294-019-01000-X/FIGURES/1>
- Vas, A. C. J., Andrews, C. A., Matesky, K. K., & Clarke, D. J. (2007). In vivo analysis of chromosome condensation in *Saccharomyces cerevisiae*. *Molecular Biology of the Cell*, *18*(2), 557–568. <https://doi.org/10.1091/mbc.e06-05-0454>
- Visintin, R., Hwang, E. S., & Amon, A. (1999). Cfi1 prevents premature exit from mitosis by anchoring Cdc14 phosphatase in the nucleolus. *Nature* *1999* *398*:6730, 398(6730), 818–823. <https://doi.org/10.1038/19775>
- Walters, A. D., Amoateng, K., Wang, R., Chen, J.-H., McDermott, G., Larabell, C. A., Gadal, O., & Cohen-Fix, O. (2019). Nuclear envelope expansion in budding yeast is independent of cell growth and does not determine nuclear volume. *Molecular Biology of the Cell*, *30*(1), 131–145. <https://doi.org/10.1091/mbc.E18-04-0204>
- Walters, A. D., Bommakanti, A., & Cohen-Fix, O. (2012). Shaping the nucleus: Factors and forces. *Journal of Cellular Biochemistry*, *113*(9), 2813–2821. <https://doi.org/10.1002/jcb.24178>
- Walters, A. D., May, C. K., Dauster, E. S., Cinquin, B. P., Smith, E. A., Robellet, X., D'Amours, D., Larabell, C. A., & Cohen-Fix, O. (2014). The yeast polo kinase Cdc5 regulates the shape of the mitotic nucleus. *Current Biology*, *24*(23), 2861–2867.

- <https://doi.org/10.1016/j.cub.2014.10.029>
- Wang, B.-D., Butylin, P., & Strunnikov, A. (2006). Condensin Function in Mitotic Nucleolar Segregation is Regulated by rDNA Transcription. *Cell Cycle*, *5*(19), 2260–2267. <https://doi.org/10.4161/cc.5.19.3292>
- Wang, R., Kamgoue, A., Normand, C., Léger-Silvestre, I., Mangeat, T., & Gadai, O. (2016). High resolution microscopy reveals the nuclear shape of budding yeast during cell cycle and in various biological states. *Journal of Cell Science*, *129*(24), 4480–4495. <https://doi.org/10.1242/jcs.188250>
- Webster, B. M., Colombi, P., Jäger, J., & Patrick Lusk, C. (2014). Surveillance of nuclear pore complex assembly by ESCRT-III/Vps4. *Cell*, *159*(2), 388–401. <https://doi.org/10.1016/j.cell.2014.09.012>
- Webster, B. M., Thaller, D. J., Jäger, J., Ochmann, S. E., Borah, S., & Lusk, C. P. (2016). Chm7 and Heh1 collaborate to link nuclear pore complex quality control with nuclear envelope sealing. *The EMBO Journal*, *35*(22), 2447–2467. <https://doi.org/10.15252/EMBJ.201694574>
- Webster, M. T., McCaffery, J. M., & Cohen-Fix, O. (2010). Vesicle trafficking maintains nuclear shape in *Saccharomyces cerevisiae* during membrane proliferation. *Journal of Cell Biology*, *191*(6), 1079–1088. <https://doi.org/10.1083/jcb.201006083>
- Webster, M., Wikin, K. L., & Cohen-Fix, O. (2009). Sizing up the nucleus: Nuclear shape, size and nuclear-envelope assembly. In *Journal of Cell Science* (Vol. 122, Issue 10, pp. 1477–1486). The Company of Biologists Ltd. <https://doi.org/10.1242/jcs.037333>
- Wei, W., McCusker, J. H., Hyman, R. W., Jones, T., Ning, Y., Cao, Z., Gu, Z., Bruno, D., Miranda, M., Nguyen, M., Wilhelmy, J., Komp, C., Tamse, R., Wang, X., Jia, P., Luedi, P., Oefner, P. J., David, L., Dietrich, F. S., ... Steinmetz, L. M. (2007). Genome sequencing and comparative analysis of *Saccharomyces cerevisiae* strain YJM789. *Proceedings of the National Academy of Sciences of the United States of America*, *104*(31), 12825–12830. <https://doi.org/10.1073/pnas.0701291104>
- Weisman, L. S. (2003). Yeast Vacuole Inheritance and Dynamics. *Annual Review of Genetics*, *37*, 435–460. <https://doi.org/10.1146/annurev.genet.37.050203.103207>
- Wente, S. R., & Blobel, G. (1993). A Temperature-sensitive NUP116 Null Mutant Forms a Nuclear Envelope Seal over the Yeast Nuclear Pore Complex Thereby Blocking Nucleocytoplasmic Traffic. *Journal of Cell Biology*, *123*(2), 275–284. <https://doi.org/10.1083/jcb.123.2.275>
- Wilhelmsen, K., Ketema, M., Truong, H., & Sonnenberg, A. (2006). KASH-domain proteins in nuclear migration, anchorage and other processes. *Journal of Cell Science*, *119*(24), 5021–5029. <https://doi.org/10.1242/JCS.03295>
- Winey, M., Yasar, D., Giddings, T. H., & Mastrorarde, D. N. (1997). Nuclear Pore Complex Number and Distribution throughout the *Saccharomyces cerevisiae* Cell Cycle by Three-Dimensional Reconstruction from Electron Micrographs of Nuclear Envelopes. *Molecular Biology of the Cell*, *8*(11), 2119. <https://doi.org/10.1091/MBC.8.11.2119>
- Witkin, K. L., Chong, Y., Shao, S., Webster, M. T., Lahiri, S., Walters, A. D., Lee, B., Koh, J. L. Y., Prinz, W. A., Andrews, B. J., & Cohen-Fix, O. (2012). The budding

6. References

- yeast nuclear envelope adjacent to the nucleolus serves as a membrane sink during mitotic delay. *Current Biology*, 22(12), 1128–1133. <https://doi.org/10.1016/j.cub.2012.04.022>
- Wright, R., Basson, M., D'Ari, L., & Rine, J. (1988). Increased amounts of HMG-CoA reductase induce “karmellae”: a proliferation of stacked membrane pairs surrounding the yeast nucleus. *The Journal of Cell Biology*, 107(1), 101. <https://doi.org/10.1083/JCB.107.1.101>
- Xu, X., & Okamoto, K. (2018). The Nem1-Spo7 protein phosphatase complex is required for efficient mitophagy in yeast. *Biochemical and Biophysical Research Communications*, 496(1), 51–57. <https://doi.org/10.1016/J.BBRC.2017.12.163>
- Yamamoto, A., Guacci, V., & Koshland, D. (1996). Pds1p, an inhibitor of anaphase in budding yeast, plays a critical role in the APC and checkpoint pathway(s). *Journal of Cell Biology*, 133(1), 99–110. <https://doi.org/10.1083/JCB.133.1.99>
- Yang, C. H., Lambie, E. J., Hardin, J., Craft, J., & Snyder, M. (1989). Higher order structure is present in the yeast nucleus: autoantibody probes demonstrate that the nucleolus lies opposite the spindle pole body. *Chromosoma*, 98(2), 123–128. <https://doi.org/10.1007/BF00291048>
- Zheng, L., Schwartz, C., Magidson, V., Khodjakov, A., & Oliferenko, S. (2007). The Spindle Pole Bodies Facilitate Nuclear Envelope Division during Closed Mitosis in Fission Yeast. *PLOS Biology*, 5(7), e170. <https://doi.org/10.1371/JOURNAL.PBIO.0050170>
- Zink, D., Fischer, A. H., & Nickerson, J. A. (2004). Nuclear structure in cancer cells. *Nature Reviews Cancer* 2004 4:9, 4(9), 677–687. <https://doi.org/10.1038/nrc1430>



APPENDIX I.
MEDIA AND SOLUTIONS

Media

S. cerevisiae culture

- Liquid YPD medium (w/v)
 - 1% Yeast extract
 - 2% Peptone
 - 2% Glucose

- Solid YPD medium (w/v)
 - 1% Yeast extract
 - 2% Peptone
 - 2% Glucose
 - 2% Agar

- Synthetic Complete medium (SC) (w/v)
 - 0.17% Yeast Nitrogen Base (YNB) without ammonium sulphate and amino acids
 - 0.1% Monosodium glutamic acid
 - 0.2% Amino acid mix without the appropriate amino acid or nitrogenous base (see **Table I**)
 - 2% Glucose
 - 2% Agar (only in solid medium)

Table I. Nutrient concentration to prepare drop out media

Nutrient	Concentration (mg/L)	Nutrient	Concentration (mg/L)
Adenine	19	Leucine	379
Alanine	76	Lysine	76
Arginine	76	Methionine	76
Asparagine	76	Para-aminobenzoic acid	7.58
Aspartic acid	76	Phenylalanine	76
Cysteine	76	Proline	76
Glutamine	76	Serine	76
Glutamic acid	76	Threonine	76
Glycine	76	Tryptophan	76
Histidine	76	Tyrosine	76
Inositol	76	Uracil	76
Isoleucine	76	Valine	76

E. coli culture

- Liquid LB medium (w/v)
 - 1% Bacto™ tryptone
 - 0.5% Yeast extract
 - 1% NaCl
- Solid LB medium (w/v)
 - 1% Bacto™ tryptone
 - 0.5% Yeast extract
 - 1% NaCl
 - 1.5% agar

Solutions

Yeast transformation

- SORB solution
 - 100 mM Lithium acetate
 - 10 mM Tris-HCl pH 8.0
 - 1 mM EDTA
 - 1 mM Sorbitol pH 8.0 (adjusted using 1 M acetic acid)

- PEG solution
 - 100 mM Lithium acetate
 - 10 mM Tris-HCl pH 8.0
 - 1 mM EDTA
 - 40% Polyethylene glycol 3350 (w/v)

Yeast gDNA extraction

- Breaking buffer
 - 2% Triton X-100 (v/v)
 - 1% SDS (w/v)
 - 100 mM NaCl
 - 10 mM Tris-HCl pH 8.0
 - 1 mM EDTA pH 8.0

- TE buffer
 - 10 mM Tris-HCl
 - 1 mM EDTA pH 8.0

PFGE and conventional agarose gel electrophoresis

- 1x TBE
 - 89 mM Tris base
 - 89 mM Boric acid

- 2 mM EDTA pH 8.0

- LMPA solution
 - 1% Low melting point agarose (w/v)
 - 0.125 M EDTA

- SCE
 - 1 M Sorbitol
 - 0.1 M Trisodium citrate dihydrate salt
 - 0.06 M EDTA

- Solution I
 - SCE
 - 5 μ L/mL β -mercaptoethanol
 - 1 mg/mL Zymolyase 100T (100 U/mL)

- Solution II
 - 0.45 M EDTA
 - 0.01 M Tris-HCl pH 7
 - 7.5% β -mercaptoethanol (v/v)
 - 10 μ g/mL RNase A

- Solution III
 - 0.25 M EDTA
 - 0.01 M Tris-HCl pH 7
 - 1% N-lauroylsarcosine sodium salt (w/v)
 - 1 mg/mL Proteinase K

- Storage solution
 - 60% Glycerol (v/v)
 - 0.05 M EDTA

Western blot

- Laemmli buffer ready to mix with samples
 - 1x Laemmli buffer (from 4x Laemmli buffer, Bio-Rad)
 - 2.5% β -mercaptoethanol (v/v)
 - 0.75 mM Tris-HCl pH 8.0
- Running buffer
 - 3 g/L Tris base
 - 14.4 g/L Glycine
 - 0.6 g/L SDS
- Transfer buffer
 - 25 mM Tris-HCl pH 8.3
 - 192 mM Glycine
 - 20% Methanol (v/v)
 - 0.1% SDS (w/v)
- TBST
 - 100 mM Tris-HCl pH 7.5
 - 150 mM NaCl
 - 0.1% Tween-20 (v/v)

Other solutions

- PBS pH 7.4
 - 2 mM KH_2PO_4
 - 10 mM NaHPO_4
 - 2.7 mM KCl
 - 137 mM NaCl



APPENDIX II.
SCIENTIFIC CONTRIBUTIONS



OPEN

Topoisomerase II deficiency leads to a postreplicative structural shift in all *Saccharomyces cerevisiae* chromosomes

Jessel Ayra-Plasencia^{1,2,7}, Cristina Ramos-Pérez^{1,3,8}, Silvia Santana-Sosa^{1,2}, Oliver Quevedo^{4,9}, Sara Medina-Suárez^{1,2}, Emiliano Matos-Perdomo^{1,2}, Marcos Zamora-Dorta¹, Grant W. Brown³, Michael Lisby⁴ & Félix Machin^{1,5,6}✉

The key role of Topoisomerase II (Top2) is the removal of topological intertwinings between sister chromatids. In yeast, inactivation of Top2 brings about distinct cell cycle responses. In the case of the conditional *top2-5* allele, interphase and mitosis progress on schedule but cells suffer from a chromosome segregation catastrophe. We here show that *top2-5* chromosomes fail to enter a Pulsed-Field Gel Electrophoresis (PFGE) in the first cell cycle, a behavior traditionally linked to the presence of replication and recombination intermediates. We distinguished two classes of affected chromosomes: the rDNA-bearing chromosome XII, which fails to enter a PFGE at the beginning of S-phase, and all the other chromosomes, which fail at a postreplicative stage. In synchronously cycling cells, this late PFGE retention is observed in anaphase; however, we demonstrate that this behavior is independent of cytokinesis, stabilization of anaphase bridges, spindle pulling forces and, probably, anaphase onset. Strikingly, once the PFGE retention has occurred it becomes refractory to Top2 re-activation. DNA combing, two-dimensional electrophoresis, genetic analyses, and GFP-tagged DNA damage markers suggest that neither recombination intermediates nor unfinished replication account for the postreplicative PFGE shift, which is further supported by the fact that the shift does not trigger the G₂/M checkpoint. We propose that the absence of Top2 activity leads to a general chromosome structural/topological change in mitosis.

Among the physical impediments that preclude sister chromatid segregation in anaphase, there are topological intertwinings (catenanes), unfinished replication and unresolved recombination intermediates. The presence of any of these structures gives rise to anaphase bridges that can seriously compromise the genome integrity of the immediate cell lineage¹⁻³. Surprisingly, cells from most organisms apparently lack specialised checkpoints to detect these aberrant structures and stop anaphase onset. Rather, they rely on indirect ways to supervise putative segregation problems ahead. For instance, during DNA replication, cells check that the replication fork (RF) does not get stalled or blocked, or that long stretches of single-stranded DNA (ssDNA) are not left behind the RF, yet cells can enter anaphase with unfinished replication if it proceeds too slowly compared to the cell division rate^{4,5}. Likewise, cells monitor both DNA double-strand breaks (DSBs) and ssDNA during DNA damage and early steps of its repair through the homologous recombination (HR) pathway, but not the direct presence of recombination intermediates that connect the damaged DNA with its sister template⁶⁻⁸. Catenations also appear invisible to cell cycle checkpoints, although there still exist controversy about putative G₂/M checkpoint(s) that sense these topological problems in higher eukaryotes⁹⁻¹¹.

¹Unidad de Investigación, Hospital Universitario Nuestra Señora de la Candelaria, Ctra del Rosario 145, 38010 Santa Cruz de Tenerife, Spain. ²Escuela de Doctorado y Estudios de Postgrado, Universidad de La Laguna, Santa Cruz de Tenerife, Spain. ³Department of Biochemistry and Donnelly Centre, University of Toronto, Toronto, Canada. ⁴Department of Biology, University of Copenhagen, Copenhagen, Denmark. ⁵Instituto de Tecnologías Biomédicas, Universidad de la Laguna, Santa Cruz de Tenerife, Spain. ⁶Facultad de Ciencias de la Salud, Universidad Fernando Pessoa Canarias, Las Palmas de Gran Canaria, Spain. ⁷Present address: Centro Atlántico del Medicamento (CEAMED) S.A., Santa Cruz de Tenerife, Spain. ⁸Present address: BenchSci Analytics Inc., Toronto, Canada. ⁹Present address: River Stone Biotech, Copenhagen, Denmark. ✉email: fmachin@fciisc.es

Eukaryotic type II topoisomerases (topo II/Top2) are exclusive in removing double-strand DNA (dsDNA) catenations^{10,12}. The yeast *Saccharomyces cerevisiae* has been extensively used as a model organism where to assess the physiological roles of Top2. This has been facilitated by the simplicity of this cell model and its genetic engineering, the presence of just one *TOP2* gene, and the ability to generate simple conditional alleles; e.g., *top2* thermosensitive (ts) alleles. Pioneering work in David Botstein's and Rolf Sternglanz's labs showed that *top2-ts* yeast cells died as a consequence of passing through anaphase^{13,14}. Later work demonstrated that Top2 was needed to avoid anaphase bridges, and that completion of cytokinesis had a major role in killing the cell progeny as it severs these anaphase bridges^{15–17}. While the presence of anaphase bridges comprising sister chromatid inter-twinings is undisputed, several works have suggested the presence of other linkages that could contribute to the sister chromatid segregation defects in *top2-ts*. Thus, unfinished replication has been observed and mapped to chromosome fragile sites, likely coincident with replication termini sites¹⁸. Replication defects have also been seen at the ribosomal DNA array (rDNA), especially when Top2 deficiency is combined with other mutations that affect rDNA metabolism¹⁹. The rDNA locus, located on the chromosome XII right arm, is known to be unique because of its unidirectional replication mechanism, the presence of genetically-programmed RF blocks (RFBs), being highly transcribed by RNA polymerases I and III while mostly epigenetically silent for RNA polymerase II, and for being hyper-recombinogenic and, consequently, expected to present more recombination intermediates than other chromosome regions^{2,20}.

Confounding matters, not all *top2-ts* alleles bring about the same phenotypes. Whereas most of them (but not all) allow a timely anaphase onset, progression beyond this point is more variable, particularly the degree of cytokinetic completion^{14,15,21,22}. The underlying reasons behind these differences are somewhat elusive, although features such as residual Top2-ts activity, the genetic background, and the capability to activate a checkpoint that transiently blocks cytokinesis (NoCut/Abscission checkpoint) might be responsible²². In previous works we showed that *top2-5* cells were excellent in both synchronously entering anaphase and quickly severing anaphase bridges through cytokinetic furrow ingression^{15,23}. In this report, we have studied in more detail the *top2-5* cell cycle and found that all chromosomes fail separation by pulsed-field gel electrophoresis (PFGE). Except for the rDNA-bearing chromosome XII, chromosomes stop entering the PFG not at early S-phase but in mitosis. The use of mutants and mitotic drugs showed that the PFGE behaviour is independent of HR, spindle forces and, probably, anaphase onset. We propose that Top2 deficiency (*top2-5*) gives rise to substantial chromosome topological and/or structural changes that cannot however trigger an efficient G₂/M DNA damage checkpoint. Finally, we show that Top2 actions must take place at the correct time, after which the change in chromosome structure becomes refractory to Top2 activity.

Results

Yeast chromosomes stop entering a pulsed-field electrophoretic gel in *top2-5*. In a previous work, we used genetically-modified *TOP2* and *top2-5* ts strains to analyse their first cell cycle by both population and single-cell fluorescence microscopy¹⁵. Specifically, we GFP-tagged the histone H2A2 (*HTA2* gene) in *bar1* derivatives of the original strains in order to synchronously follow the nuclear cell cycle. We started the current work by adding flow cytometry (FACS) and Pulsed Field Gel Electrophoresis (PFGE) to the microscopic analysis. Whereas fluorescence microscopy assesses cell and nuclear morphology as markers of cell cycle progression and nuclear segregation, FACS allows determination of both bulk DNA replication and of the degree of uneven segregation after cytokinesis. In addition, PFGE, in conjunction with Southern blot analysis, gives insights into the structural integrity of individual chromosomes; i.e., intact vs broken chromosomes, gross chromosomal rearrangements, and presence of DNA-mediated linkages^{7,24–26}. In the case of the latter scenario, affected chromosomes are trapped in the wells of the PFG.

Both strains were arrested in G₁ at permissive temperature (25 °C) for 3 h before being released to 37 °C for 4 h. Every 30', samples were collected for analysis by microscopy, FACS and PFGE. As reported before, fluorescence microscopy showed that the *TOP2* strain proceeded into a normal cell cycle (Fig. 1a, left panel); S-phase entry (budding) occurred between 30' and 90' and anaphase onset (H2A2-GFP segregation) between 90' and 150'. Shortly after anaphase entry, cells completed the first cell cycle and split mother and daughter cells (new rise of unbudded category by 180'). We observed an initially similar cell cycle profile in the case of *top2-5* (Fig. 1a, right panel), yet with an earlier G₁-S transition¹⁵; S-phase entry at 30'–60' and the peak of anaphase onset at 90'. As reported in our previous work, we seldom observed genuine H2A2-GFP anaphase bridges in *TOP2* (< 10%) and they were transient in *top2-5* (~ 60% of cells at 90'). Instead, binucleated cells was the major segregation phenotype by 120', indicative of cytokinetic furrow ingression by that time point¹⁵. This phenotype may encompass either cells in anaphase/telophase or mother and daughter cells in the next G₁ before completing physical separation²³. Strikingly, and unlike *TOP2*, a clear uneven segregation of the H2A2-GFP was evident in *top2-5* (Fig. 1b,c). *TOP2* and *top2-5* also differed in that ~ 20% *top2-5* mother cells rebudded without separation of the first mother and daughter (Fig. 1c)^{15,23}.

FACS analysis confirmed that both strains have a timely cell cycle, at least until anaphase onset (Fig. 1d); S-phase entry (drop of 1C, rise of 2C DNA content) at 30'–60'. Cytokinesis and cell separation took place at 120' in *TOP2* (new rise of 1C peak). Likewise, *top2-5* executed cytokinesis at 150'–180' (drop of 2C peak); however, the outcome of such point-of-no-return was catastrophic. The 2C peak did not revert to the typical 1C DNA content but, instead, extended from < 1C to > 2C DNA content, indicating massive uneven segregation of the genetic material, as suggested by the H2A2-GFP microscopy.

When we performed the PFGE analysis, we observed that the chromosome staining pattern in *TOP2* was constant throughout the time course (Fig. 1e, left). By contrast, there were two waves of decreased chromosome staining in *top2-5* (Fig. 1e, right; Figure S1). In the first wave, the signal for the largest chromosome, chromosome XII (cXII), decreased coincident with the cells transiting through S-phase. The second wave occurred after the

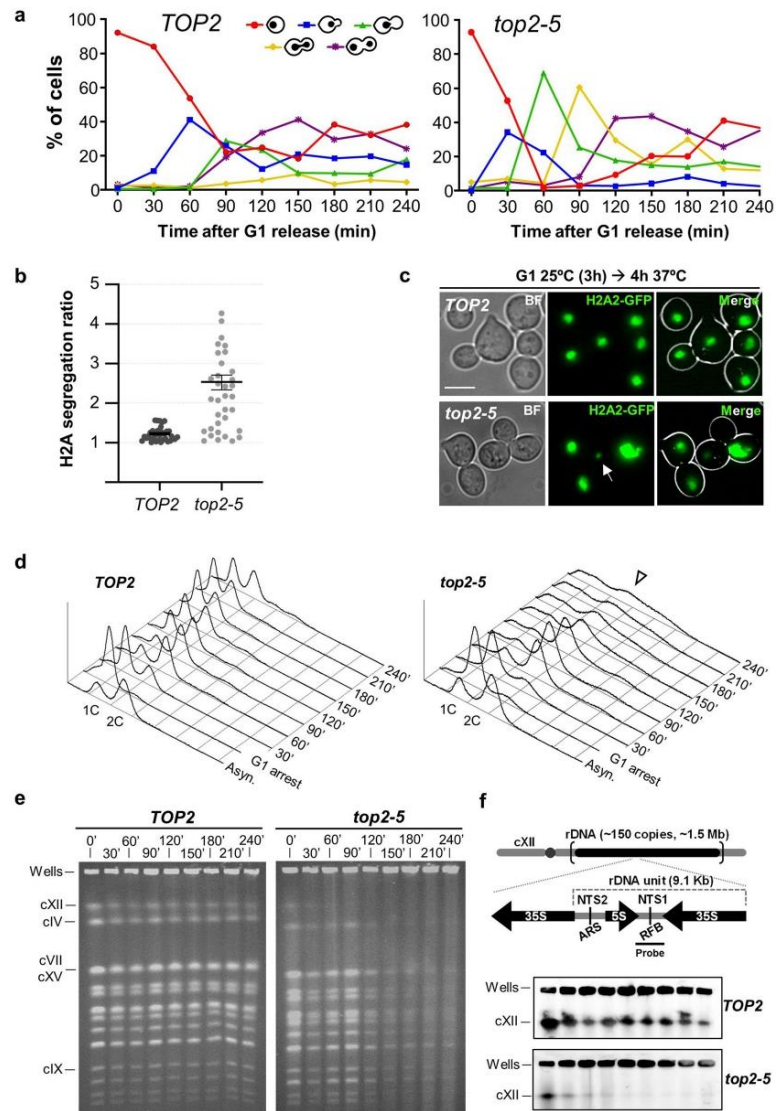


Figure 1. Chromosome integrity is compromised upon inactivation of Top2 with the *top2-5* thermosensitive allele. A synchronous G₁ release experiment was performed for isogenic *TOP2* and *top2-5* strains. **(a)** Charts depicting the cell cycle progression under the microscope (both strains carry H2A2-GFP to label the nuclear masses). **(b)** Ratio of H2A2-GFP segregation among binucleated cells (n = 34; 210'–240' after the G₁ release). The ratio is calculated by dividing the upper by the lower GFP signal in each pair of nuclei. **(c)** Micrographs of representative cells 4 h after the G₁ release. The arrow points to a massive uneven segregation of the H2A2-GFP signal in *top2-5*. **(d)** Flow cytometry (FACS) analysis of the DNA content. Arrowhead highlights the flattened DNA content observed in *top2-5* at later time points. **(e)** Ethidium bromide (EtBr) staining of whole chromosomes resolved by Pulsed-Field Gel Electrophoresis (PFGE). Note how in the *top2-5* strain the cXII in-gel signal disappears shortly after the G₁ release, whereas the other chromosome bands get fainter after 120'. **(f)** Southern blot profiles of the same PFGEs with a probe against the non-transcribed spacer region 1 (NTS1) of the ribosomal DNA array (rDNA) on the cXII (schematic on the top; uncropped blots in Figure S4a).

nuclear division but before the decrease of the 2C peak by FACS ($t = 120' - 240'$), and was marked by a sharp and profound decrease of all chromosome staining (the in-gel signal dropped ~90% in less than 1 h; Figure S1). We found that decrease in chromosome staining in *top2-5* persisted through different sample preparation conditions (Figure S2). Furthermore, the decrease in chromosome staining was not observed if cells were maintained in G₁ through an equivalent incubation regime (6 h from the induction of the G₁ block) (Figure S3).

The lack of visible chromosomes in a PFGE can be due to three major causes: chromosome breakage, chromosome degradation and chromosomes with branched structures that keep them trapped into the loading well^{24,25}. In order to distinguish between these possibilities, we did Southern blots under different stringency conditions with probes for the rDNA in cXII (Figs. 1f and S4). We observed strong hybridization signals in the wells for both strains. No signs of broken chromosomes (fast-migrating smear, e.g.) were noted (Figure S4). We did not observe signs of DNA degradation over the 4 h time course in the *top2-5* mutant, even after the massive missegregation of the genetic material (Figure S5). These results suggest that chromosomes get trapped in the loading well in the *top2-5* mutant.

We previously compared the *top2-5* allele with the broadly-used *top2-4* allele¹⁵. We found that *top2-5* transits through anaphase faster and more synchronously than *top2-4*, so that *top2-5* appears to be a better allele for cell cycle studies at this late stage. However, in order to address if our observations were specific to the *top2-5* allele, we checked the PFGE pattern in an isogenic *top2-4* strain. We found the same steady disappearance of all yeast chromosomes, yet to a lesser extent (Figure S6).

Overall, we conclude that Top2 inactivation brings about an unreported shift in the behaviour of all yeast chromosomes in a PFGE. In a synchronous cell cycle, this shift takes place in late anaphase, near or after cytokinesis.

Cytokinesis is not responsible for the *top2-5* structural chromosome change revealed by PFGE. The general loss of chromosome bands in the *top2-5* PFGE from 120' onwards could simply be due to cells completing a devastating cytokinesis, as both microscopy and FACS strongly suggest. Cytokinesis would break chromosomes at the anaphase bridges; and these broken chromosomes could get trapped in the PFGE well during DSB end resection¹⁵. Of note, we and others have shown that cytokinesis is a point of no return during Top2 inactivation^{15,17}. In order to test this hypothesis, we used a *top2-5 cdc15-2* double ts mutant that blocks cytokinesis and cell progression beyond telophase because of the lack of the Mitotic Exit Network (MEN) kinase Cdc15^{21,25}. We repeated the time course and analysed samples by fluorescence microscopy, FACS and PFGE, comparing *top2-5 cdc15-2* with its *TOP2 cdc15-2* counterpart (Fig. 2). As expected, cells from both strains arrested in telophase, as can be seen by microscopy (dumbbells prevailed) and flow cytometry (2C peak prevailed) (Fig. 2a–c). Incidentally, a minor 4C peak appeared during the time course in both *cdc15-2* strains. This peak correlated to a 2C peak at the G₁ arrest, which stems from incomplete septations at permissive conditions (Figure S7). As previously reported¹⁵, *top2-5 cdc15-2* formed histone-labelled anaphase bridges (up to 90% of cells by 210'), whereas two equally segregated histone masses was the major outcome in the *TOP2 cdc15-2* (Fig. 2a,b). Strikingly though, the PFGE of the *top2-5 cdc15-2* showed the same pattern of decrease in chromosome band intensity (Fig. 2d) as we had observed in *top2-5 CDC15*. Specifically, (i) in-gel cXII quickly disappeared (60'–90'), and (ii) all other chromosome bands decreased at 120'–150'. We therefore conclude that the structural chromosome changes revealed by PFGE are not simply a consequence of the breakage of *top2-5* anaphase bridges by cytokinesis.

Assessment of unfinished replication in *top2-5*. Since cytokinesis is not required for the loss of chromosome bands in PFGE, we tested whether long-lasting DNA-DNA sister chromatid junctions are responsible^{7,24,25}. The timing of the 2C peak by FACS suggests that there is no a major delay in ongoing replication; however, certain late replication intermediates in *top2-5* might change the chromosome structure in such a way that chromosomes cannot enter the PFGE. Indeed, previous results showed that yeast cells deficient in Top2 struggle to complete replication and accumulate late replication intermediates at replication termini sites¹⁸. Thus, we tested whether *top2-5 cdc15-2* accumulates replication intermediates well into the late anaphase block by performing neutral-neutral two-dimensional electrophoresis (NN-2D). This technique can detect the presence of branched DNA structures and classify them into replication-like (Y-shaped) and recombination-like (X-shaped) intermediates²⁷. We studied two replication termini; the well-defined RFB in the rDNA, and a RF converging locus in chromosome III (*TER302*)¹⁸. We found enrichment of Y shapes near the RFB in *top2-5 cdc15-2* (Fig. 3a). The fixed Y-shaped structure at the RFB (spot "a" in Fig. 3a) and other longer Ys that bypass the RFB into the adjacent 3' end of the 35S gene ("b" in Fig. 3a) were particularly enriched. In addition, other spots onto the X-shaped structures also accumulated ("c" and "d" at the spike in Fig. 3a), which might correspond to two very close converging Ys as they cannot branch-migrate along the spike. Conversely, we could not detect unfinished replication at *TER302* (Fig. 3a, rightmost blot).

Even though we could not detect late replication intermediates at the *TER302* locus, we must state that, for chromosomes other than XII, it is difficult to determine where two replication forks converge, which is expected to be variable in the cell population. Thus, we also opted for an alternative technical approach based on measuring underreplicated gaps on extended DNA fibers. These gaps would suggest the presence of two converging RFs (double Ys) in a single-molecule analysis. For that purpose, we transferred the *top2-5* and *cdc15-2* alleles to a strain suitable for the DNA combing technique²⁸. We could not see differences between the *top2-5 cdc15-2* and *TOP2 cdc15-2* strain in late anaphase (Fig. 3b,c). Fibers appeared almost fully replicated in both cases; i.e., green (replicated DNA) and red (DNA) signals extensively overlapped. Although there were some gaps in the BrdU signal on the DNA fibers, there were no differences between the strains in terms of underreplicated percentage (5.85% and 5.34% for *TOP2* and *top2-5*, respectively) and track length (Fig. 3c). The number of gaps (greater than 5 kbp) was also equivalent in the two strains (72 & 69 gaps in 10 Mbp for *TOP2* and *top2-5*, respectively).

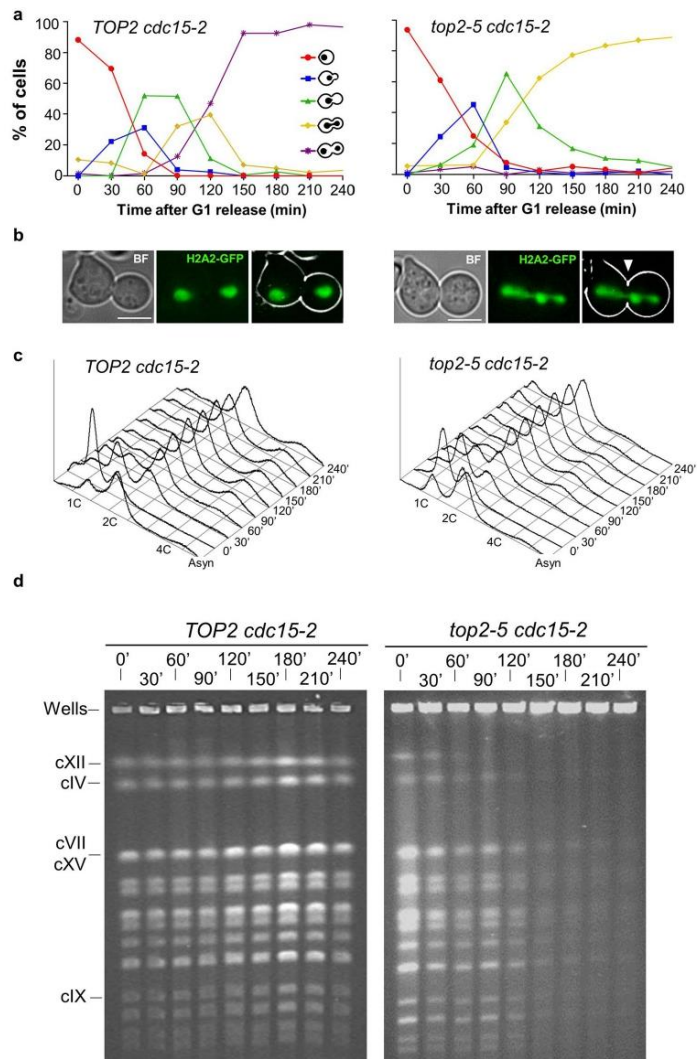


Figure 2. The loss of chromosome integrity in *top2-5* is not a consequence of the mitotic catastrophe that happens upon cytokinesis. A synchronous G₁ release experiment was performed for isogenic *TOP2 cdc15-2* (left panels) and *top2-5 cdc15-2* (right panels) strains. **(a)** Charts depicting the cell cycle progression under the microscope. **(b)** Micrographs of representative cells 4 h after the G₁ release. The arrowhead points to the characteristic massive H2A2-GFP anaphase bridge observed in *top2-5 cdc15-2*. **(c)** FACS analysis of the DNA content. **(d)** EtBr staining of whole chromosomes resolved by PFGE. Note how chromosome behaviour of the *top2-5 cdc15-2* strain resembled that of *top2-5*.

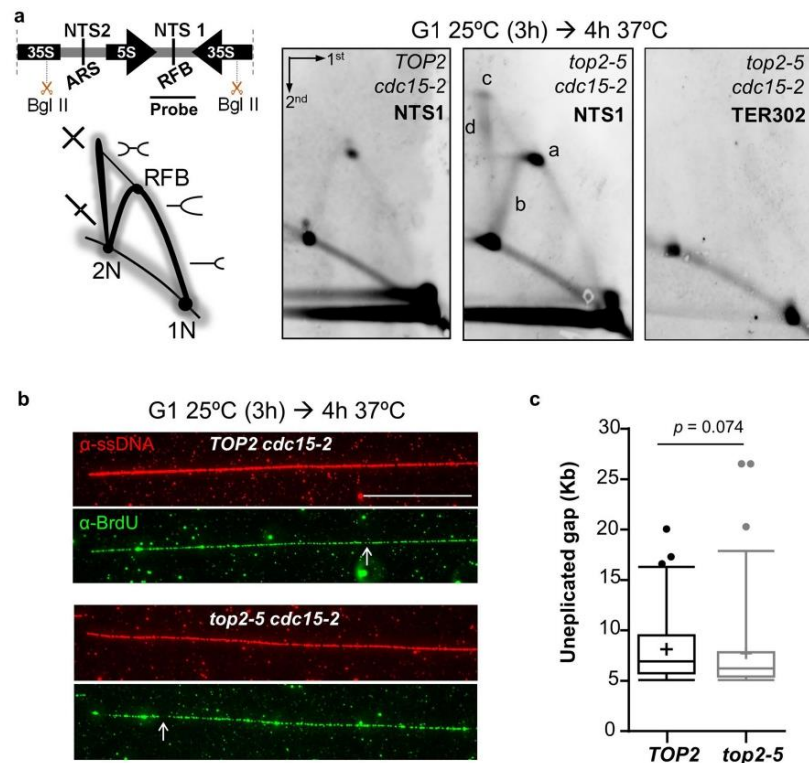


Figure 3. Assessment of the presence of underreplicated chromosomes in *top2-5*. Synchronous G₁ release experiments were performed for isogenic *TOP2 cdc15-2* and *top2-5 cdc15-2* strains. (a) The presence of persistent replication and recombination-like intermediates were evaluated by neutral, neutral two-dimensional electrophoresis (NN-2D) for the NTS1 region of the 9.1 kbp unit of the rDNA and the replication termini site *TER302*. On the left, schematic of the rDNA unit with its main features and relative position of the BglII sites and the probe; a representation of the theoretical branched forms visualized by NN-2D is depicted underneath. NTS1 and 2, non-transcribed regions 1 and 2, respectively; ARS, autonomous replicating sequence; RFB, replication fork block. On the right, NN-2D of both strains 4 h after the G₁ release into 37 °C. Note that four structures were enriched at NTS1 in *top2-5 cdc15-2* relative to *TOP2 cdc15-2*: the Y-shaped intermediate stalled at the RFB (“a”), the long Y-shaped intermediates that pass such block (“b”), the intermediate with highest mass and symmetry (“c” spot, probably a double Y), and the X-shaped spike (“d”). (b) Combing analysis of the completion of replication for DNA fibers obtained 4 h after the G₁ release. Representative pictures of the 4 h immunofluorescence against DNA (red) and incorporated BrdU (green). White arrows point to the small greenless gaps observed in fibers coming from both strains. The scale bar represents 50 kbp. (c) Quantification of the length of gaps greater than 5 kbp.

The data suggest that unreplicated regions larger than 5 kbp do not accumulate in *top2-5*, although Y-structures at the rDNA RFB and X-structures at the rDNA do accumulate.

Assessment of unresolved recombination intermediates in *top2-5*. The X-shaped molecules observed by NN-2D in the *top2-5* rDNA suggest that recombination intermediates might also contribute to the trapping of chromosomes in the PFGE well. HR is known to bypass stalled RFs and might help in completing replication in *top2* mutants²⁹. In order to assess the contribution of recombination intermediates to the *top2-5* PFGE and NN-2D profiles, we used a genetic approach since such intermediates depend on the HR gene *RAD52*³⁰. The triple mutant *top2-5 cdc15-2 rad52Δ* strain showed a similar cell cycle profile than *top2-5 cdc15-2*, including anaphase bridges as the end-point phenotype in telophase (Fig. 4a), similar replication timing by FACS (Fig. 4b), and similar kinetics for PFGE chromosome entrapment (Fig. 4c). Thus, the abrogation of

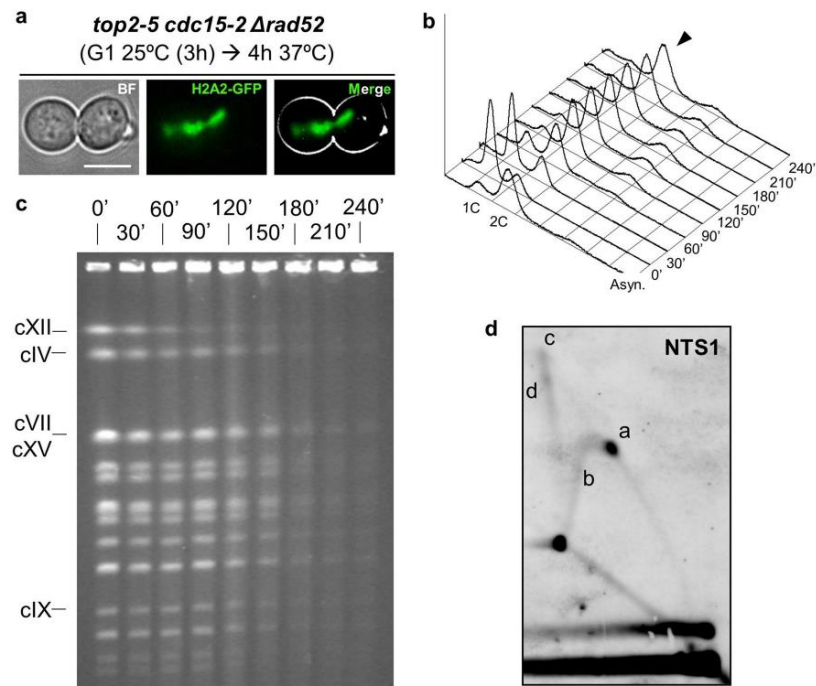


Figure 4. Chromosome integrity loss in *top2-5* is independent of the homologous recombination pathway. A synchronous G₁ release experiment was performed for the *top2-5 cdc15-2 Δrad52* strain. (a) Micrographs of a representative cell 4 h after the G₁ release. Note it resembles *top2-5 cdc15-2* with its characteristic H2A2-GFP anaphase bridge. (b) FACS analysis of the DNA content. (c) EtBr staining of whole chromosomes resolved by PFGE. Note how the late chromosome shift behaviour resembled that of the *top2-5 cdc15-2* strain. (d) NN-2D of the NTS1 region of the rDNA 4 h after the G₁ release.

Rad52 did not prevent the late loss of chromosome bands in the PFGE. Surprisingly, it did not affect the presence of X-shaped intermediates at the rDNA either (Fig. 4d). We conclude that recombination intermediates are unlikely to contribute to the *top2-5* anaphase decrease in chromosome bands by PFGE.

The *top2-5* structural chromosome change revealed by PFGE is independent of CDC14-mediated processes in early anaphase. Since cytokinesis was not responsible for the loss of PFGE chromosome bands in *top2-5*, we wondered whether transition through anaphase played any role. Anaphase starts when all sister kinetochores are attached to opposite spindle pole bodies through the microtubule-based spindle apparatus³¹. At that point, cohesion between sister chromatids is lost and the spindle pulls sisters apart. Once cells enter anaphase, the master cell cycle phosphatase Cdc14 is activated through the FEAR network to promote spindle elongation^{32,33}, as well as resolution and condensation of the rDNA^{34–37}. In addition, Cdc14 targets to the nucleoplasm and activates the structure-specific endonuclease (SSE) Yen1^{38–40}, which can recognize and cut both Y-shaped and X-shaped molecules³⁸. We reasoned that any of these Cdc14-mediated events could be responsible for the loss of chromosome bands observed ~120' after the G₁ release. However, the *top2-5 cdc14-1* strain was indistinguishable from *top2-5 cdc15-2*, ruling out this possibility (Figure S8).

Loss of function of the structure-specific endonucleases Mms4-Mus81 and Yen1 worsens the *top2-5* PFGE shift. The late Rad52-independent X-shaped molecules we observed at the rDNA in *top2-5 cdc15-2* suggests that Top2 could prevent the formation of novel types of four-way DNA-DNA linkages. However, this takes place in the context of active SSEs that should have dealt with these branched structures. Assuming that there are more of these X-shaped linkages in chromosomes other than XII, a connection between these linkages and the late PFGE retention would require one out of these two possibilities: (i) late X-shaped molecules are refractory to SSEs (e.g., they could be hemicatenanes); or (ii) by-products of their processing by SSEs are

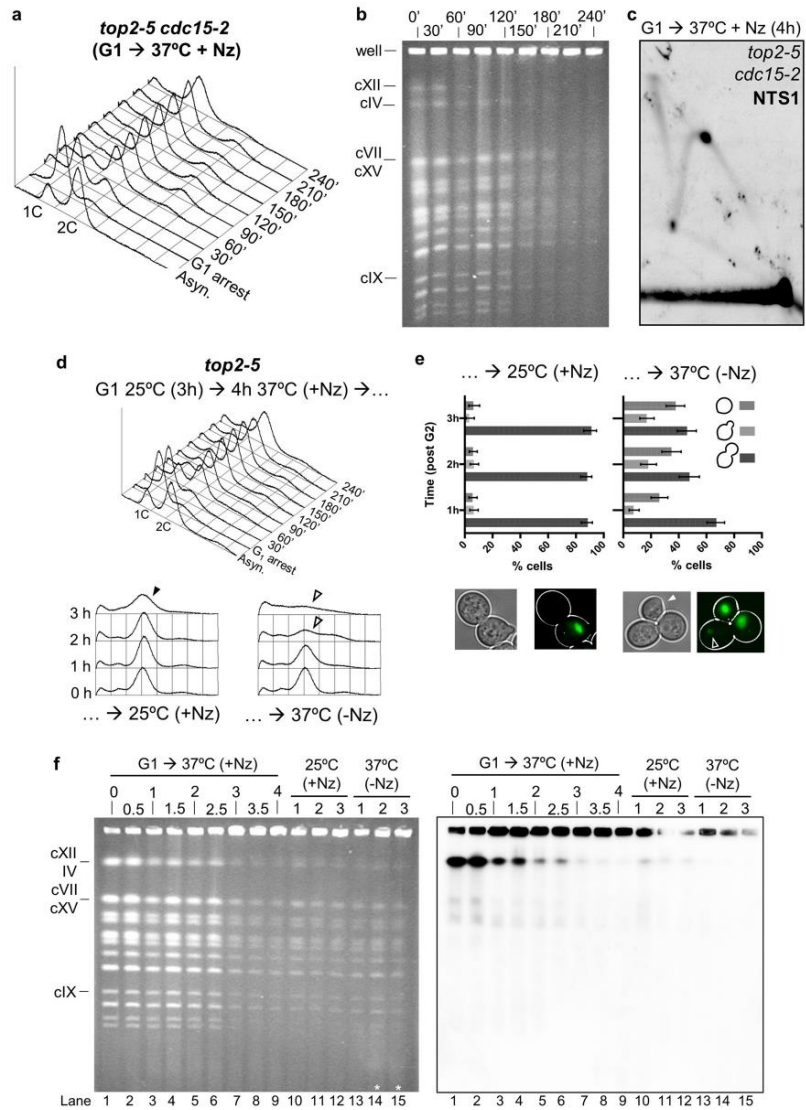


Figure 5. The late change in chromosome structure caused by the absence of Top2 is not a consequence of mitotic spindle forces, is not reversed by Top2, and does not trigger a G₂/M checkpoint. (a–c) A synchronous G₁ release experiment was performed for the *top2-5 cdc15-2* strain under restrictive conditions (37 °C). At the time of the G₁ release, Nocodazole (Nz) was added to depolymerize the spindle and block cells in G₂/M. (a) FACS analysis of the DNA content during the first 4 h of the G₁-to-Nz cell cycle. (b) EtBr-stained PFGE of the time course. (c) NN-2D for the rDNA NTS1 region 4 h after the G₁ release. (d–f) A synchronous G₁ release experiment was performed for the *top2-5* strain as in (a–c). After 4 h, the culture was split in two and incubated for another 3 h. One subculture was shifted back to 25 °C (i.e., re-activate Top2) while keeping the Nz, whereas the other one was kept at 37 °C while removing Nz. (d) FACS analysis of the DNA content during the first 4 h of the G₁-to-Nz cell cycle (on the top) and during the extra 3 h after the culture splitting (underneath). (e) Cell morphology analysis during the extra 3 h incubations. Below the charts, representative micrographs of each subculture after 3 h; i.e., a mononucleated dumbbell versus a dumbbell with an uneven segregation (hollow arrowhead) plus a postcytokinetic G₁-like cell (white arrowhead). (f) EtBr-stained PFGE of the whole experiment (left) and the corresponding Southern blot against the rDNA (right). Note how (i) the late PFGE general shift still occurs in Nz, (ii) how reactivation of Top2-5 does not reshape the chromosomes to enter the gel, and (iii) how the shift does not trigger a G₂/M, so that a mitotic catastrophe still takes place after Nz removal (asterisks in lanes 14 and 15).

responsible for the PFGE retention. In other words, the X-DNA that arises in *top2-5* could be cut by SSEs into another intermediate which, in turn, would be responsible for the late PFGE phenotype. Along with the Cdc14-regulated SSE Yen1, the complex Mus81-Mms4 cuts in metaphase the same anaphase bridge-prone X-DNAs than Yen1 cuts in anaphase⁷. Hence, we checked the PFGE shift in a strain deficient for both SSEs, and any other that may be regulated by Cdc14 in anaphase. However, the hypothesis that SSE by-products were responsible for the late PFGE shift was ruled out genetically through this *top2-5 cdc14-1 yen1Δ mms4Δ* mutant (Figure S9). On the contrary, this quadruple mutant showed more PFGE retention for all chromosomes at earlier time points (from 60' onwards). Because we had not observed a PFGE retention in a *TOP2 yen1Δ mms4Δ* strain in a previous work⁷, it appears that the Top2 absence may indeed increase canonical X-shaped branched structures during S-phase, which are timely processed by SSEs, likely by Mus81-Mms4 as it is the one active before anaphase onset⁴¹. Nevertheless, the late PFGE shift is still present in active SSEs and it is not relieved in their absence. Altogether, we conclude that SSE activity is not responsible for the late PFGE shift.

The *top2-5* structural chromosome change revealed by PFGE does not depend on the spindle force and cannot be reverted by re-activation of Top2. Neither cytokinesis nor Cdc14-controlled anaphase events were responsible for the PFGE phenotype, yet it clearly takes place in anaphase as determined by comparing microscopy and PFGE (Figs. 1, 2 and S8). We next checked whether the force of the mitotic spindle might trigger the loss of chromosome bands. Thus, we added nocodazole (Nz) to depolymerize the microtubules before *top2-5 cdc15-2* (Fig. 5a–c) and *top2-5 CDC15* (Fig. 5d–f) cells reached anaphase. Noteworthy, Nz also elicits the activation of the spindle assembly checkpoint⁴², leading to a transient cell cycle block at metaphase⁴³. The FACS pattern we observed, with the corresponding long lasting 2C peak in both *top2-5* mutants (Fig. 5a,d, upper FACS profile), confirmed this arrest. The presence of >95% of mononucleated dumbbell cells under the microscope (Fig. 5e, lower left) further confirmed the Nz arrest. Strikingly, even though spindle pulling forces were absent, the loss of chromosome bands still occurred (Fig. 5b,f, lanes 1–9). Likewise, the rDNA exhibited Y- and X-shaped intermediates (Fig. 5c).

Having found that the loss of chromosome bands can also happen in Nz-arrested cells after the absence of Top2, we next checked whether re-activation of Top2 could restore the chromosome bands. For that purpose, we shifted the temperature down to 25 °C while maintaining the cells in Nz in the *top2-5* strain (Fig. 5d–f). Cells remained as mononucleated dumbbells with a 2C DNA content for at least 3 h after the temperature shift (Fig. 5d, lower left FACS profile; and Fig. 5e, left chart); however, this did not restore the structural integrity of the chromosomes (Fig. 5f, lanes 10–12). Since cultures were left in Nz for some time, and it is known that the G₂/M arrest is leaky in Nz⁴³, we repeated this experiment in a *top2-5 cdc15-2* with shorter incubation times (Figure S10). In this way, slippage from the Nz arrest was minimized while we further prevented entry into a second cell cycle by *cdc15-2*. We still observed that the PFGE shift was not modified after the temperature downshift. In addition, resuming both Top2 activity (25°C downshift) and spindle forces (Nz removal) did not change the PFGE pattern either.

We conclude that the chromosome structural change upon Top2 depletion can occur in a G₂/M block, is independent of spindle forces and is irreversible.

G₂/M checkpoints are blind to the *top2-5* structural chromosome change. The persistent loss of chromosome bands in Nz-arrested cells allowed us to assess whether the structural chromosome change triggers a G₂/M checkpoint. This question could not be answered in cycling cells as the change happens in anaphase. However, once we observed the loss of chromosome bands in Nz, if a G₂/M checkpoint were triggered we would see a delay in late cell cycle events after Nz removal in the *top2-5* strain. However, when Nz was removed we observed not only anaphase progression but also cytokinesis and the corresponding mitotic catastrophe (Fig. 5d, lower right FACS profile; and 5e, right chart).

In addition, we ruled out that the absence of a checkpoint response after the *top2-5* PFGE shift was a consequence of Top2 itself being a sensor/mediator of such checkpoint(s). Both hydroxyurea (HU) and methyl methanesulfonate (MMS) still arrested the *top2-5* strain in G₂/M in restrictive conditions (Figure S11). HU creates

replicative stress through formation of ssDNA behind the RFs, whereas MMS leads to RF stalling in addition to ssDNA gaps behind the RFs³.

Dysfunctional mitochondria do not alter the PFGE shift in *top2-5*. Lastly, we checked whether the *top2-5* PFGE profile could be modulated by the pleiotropic effects observed in the absence of mitochondrial DNA (*rho*⁰ cells), which renders dysfunctional mitochondria. Mitochondria satisfy the high energy demands require for critical events during cell growth, including replication and condensation. We reasoned that a slower metabolism could slow down or prevent the PFGE shift. In addition, *rho*⁰ cells have altered dNTP pools and inefficient folding of enzymes require for DNA replication and repair⁴⁴. Both deleterious effects may influence the PFGE outcome.

We found that a *top2-5 rho*⁰ strain missegregates the histone-labelled nuclear mass to the same extent as its *top2-5 rho*⁺ counterpart, also showing unequal segregation and a low percentage of visible anaphase bridges (Figure S12a). However, *top2-5 rho*⁰ cells undergo a slower cell cycle, which includes a lengthened S-phase (Figure S12b, compare transposition of 1C to 2C content by FACS with that of Fig. 1b) and an apparent arrest in late anaphase (the 2C peak remains for at least 4 h). Remarkably, though, the postreplicative PFGE shift was still present (Figure S12c). The 30' delay with respect to *top2-5 rho*⁺ correlates well with the delay observed in the accumulation of the 2C content. We conclude those mitochondrial functions compromised in *rho*⁰ cells do not alter the PFGE shift.

A GFP-based candidate screen of DNA damage and checkpoint proteins further indicates that *top2-5* cells do not detect the structural chromosome change as chromosomal damage. In addition to the previous set of experiments, we conducted a GFP-based screen of DNA damage proteins known to either form foci or increase their nuclear content upon DNA damage⁶⁵. This screen was undertaken at the *top2-5 cdc15-2* block and included the Dpb11- γ EmRFP as an additional reporter. Dpb11 is known to get enriched at certain types of anaphase bridges⁴⁶. As a control, we included a *TOP2 cdc15-2* strain also blocked in telophase. We observed an increase in nuclear foci in the *top2-5 cdc15-2* block for the DNA replication stress markers Lcd1/Ddc2, Rfa2 and Rfa3, the latter two belonging to the ssDNA binding RPA complex (Table 1, Figures S13 and S14). The foci were predominantly present along the anaphase bridge. However, there were no differences for other important replication stress reporters such as Ddc1, Dpb11, Dna2 and Rad5. Importantly, there was no increase in foci of proteins involved in HR such as Rad51, Rad52 and Rad54. Altogether, we conclude that more ssDNA is present in cells blocked in telophase after passing through a cell cycle without Top2. However, this higher ssDNA level does not elicit an efficient DDR. Incidentally, there were RPA and Dna2 foci in *TOP2 cdc15-2* cells. Nearly 50% of telophase-blocked *TOP2 cdc15-2* cells had one Rfa2/3 focus.

Discussion

Top2 is the critical enzyme that removes sister chromatid intertwinings prior to chromosome segregation in anaphase. The absence of Top2 is broadly recognized to lead to a type of mitotic catastrophe whereby anaphase bridges, which arise from these intertwined chromatids, are severed during cytokinesis. Altogether, the results shown in this paper confirmed that *top2-5* also leads to a mitotic catastrophe; we here demonstrate this by microscopy, complementing our previous work^{15,23}, but also by FACS and by PFGE. The mitotic catastrophe in *top2-5* seems greater than other previously studied *top2-ts* alleles, at least by FACS analysis and microscopy^{15,17,47}, and might be a feature of either the *top2-5* allele itself or the genetic background it is in¹⁵. However, the most shocking *top2-5* phenotype we introduce here is the disappearance of chromosome bands in a PFGE at a stage prior to the mitotic catastrophe. The overall DNA content we quantified by FACS, as well as the absence of ingel smears and broken rDNA in the Southern blots, strongly suggests that the disappearance of bands correlates with entrapment of chromosomes in the loading well (Figs. 1, 2, 5, S4–S6). Moreover, DNA release from the plug was accomplished by digestion with BglII for the NN-2D analysis (Figs. 3 and 4). We distinguished two classes of chromosomes affected by the PFGE retention: the rDNA-bearing chromosome XII and all the other 15 chromosomes. The former persistently gets well-bound from the beginning of the S phase, which is compatible with, at least, unfinished replication (protracted Y-shaped DNA at the RFB in *top2-5 cdc15-2*; Fig. 3, 4 and 5). By contrast, chromosomes other than XII manifest the same PFGE behaviour much later in the cell cycle; after replication appears to have ended by both FACS and PFGE (Figs. 1, 2, 4, 5, S1, S3–S6, S8 and S12). A closer look at this late PFGE behaviour suggests that it might be independent of transition between cell cycle stages (i.e., S-phase to metaphase to anaphase) and the key spatial and molecular changes that occur in such transitions (e.g., activation of structure-specific endonucleases, spindle pulling forces, hypercondensation by Cdc14, etc.)^{2,48}. Rather, it seems there is a fixed time window between the end of S-phase (as determined by FACS) and the PFGE shift (~1–2 h). Thus, in synchronous cell cycle cultures the loss of chromosome bands takes place well within anaphase (Figs. 1, 2 and S8), and the loss of chromosome bands is present in Nz-treated cells as well (Fig. 5 and S10). Importantly, these latter experiments led us to conclude two important features of the loss of chromosome bands in PFGE; (i) no G₂/M checkpoint is activated after the loss of chromosome bands; and (ii) the loss of chromosome bands is irreversible with respect to Top2 activity.

There are four known causes of chromosomes entrapment in the loading well during PFGE: linear chromosomes larger than 10 Mbp⁴⁹, relaxed circular chromosomes larger than 100 kbp⁵⁰, the presence of chromosomes with branched structures^{24,25,51}, and the presence of large portions of ssDNA^{52,53}. Branched structures and ssDNA physiologically arise during replication and DNA repair through HR. Whereas a theoretical and experimental framework exists to explain the relationship between PFGE trapping and chromosome size⁵⁴, the causes of why chromosomes carrying DNA branches or ssDNA gaps do not enter PFGE remain undetermined. Because of this lack of knowledge on the PFGE technique, we cannot fully draw at present the postreplicative pathway to

Protein ^a	Lab#1 ^b		Lab#2 ^c		At the telophase block (37°C × 3 h)	
	As	As	HU	MMS	<i>top2-5 cdc15-2</i>	<i>TOP2 cdc15-2</i>
Rfa2	+	+	+	++	+++ (S)	++
Rfa3	+	+	+	++	+++ (S)	++
Lcd1 (Ddc2)	-	+	++ (f)	++	++ (29%); NAI	-
Ddc1	-	-	++ (f)	++	-	-
Dbp11	-	-	-	++	-	-
Dna2	-	+	-	+	+	+
Elg1	-	-	-; NAI	-; NAI	-	-
Mrc1	-	+(f)	+(f)	-	-	-
Ctf18	-	-	+(f)	-	-	n.d. (w) ^d
Cdc28	-	+	+	+	-	-
Rad9	-	-	-	+(f)	-	-
Rad53	-	-	+(f)	++ (f)	-	-
Chk1	-	-	-; NLI	-; NLI	-	-
Dbf4	-	-	-; NAI	-; NAI	-	-
Cdc7	-	-	-; NAI	-; NAI	-	-
Dun1	-	-	-	-; NAI	-	-
Rad5	-	-	+(f)	++ (f)	-	-
Rad6	-	-	-	-	-	-
Rad50	-	-	-	-	-	-
Xrs2	-	-	+(f)	+(f)	-	n.d. (w)
Yku70	-	-	-	-	-	n.d. (w)
Yku80	-	-	-	-	-	-
Irc20	-	-	-	-	-	-
Exo1	-	-	++ (f)	-	-	-
Sac2	-	++ (f)	++ (f)	++ (f)	-	-
Rad51	-	-	-	-	-	-
Rad52	-	-	-	-	+(6.4%)	+(6.5%)
Rad54	-	-	-	++	-	-
Rad55	-	-	-	-	-	-
Rad57	-	-	-	-	-	-
Rad59	-	-	-	+	-	-
Rad10	-	-	+(f)	-; NAI	-	-
Cdc13	-	-	-	+	-	-
Mms21	-	+	+	+	-	-
Nse4	-	+	+	+	-	-
Esc2	-	-	-; NAI	-; NAI	-	-
Mph1	-	-	-	+(f)	-	-
Rmi1	-	-	-	-	-	-
Slx4	+(f)	+	++ (f)	++ (f)	-	-

Table 1. Location pattern in telophase-blocked cells of DNA damage checkpoint and repair proteins after going through a synchronous cell cycle with or without Top2. ^aProteins are sorted according to the approximate order of action after replication stress⁵. Most proteins inform about replication stress (or DNA damage) by the formation of nuclear foci. Other proteins may concentrate in the nucleus upon replication stress (e.g., Elg1; Chk1; Dbf4-Cdc7; Dun1; Esc2). Cells with foci? -, <5%; +, 5–25%; ++, 25–60%; +++, >60%. In some instances, the actual percentage is between brackets. Foci intensity? (f), faint; (S), strong. Location/abundance? NLI, higher cell number with nuclear location; NAI, nuclear abundance increased. ^bLab#1: As seen at <https://yeastfp.yeastgenome.org/>. ^cLab#2: As seen at http://images.yeastrc.org/tkach_brown/repliation_stress. ^dn.d. (w) = not determined because wrong protein location.

whatever structures preclude the affected chromosomes from entering the PFGE. From results we present in this work (Figs. 3, S13 and S14; Table 1), it appears that both ssDNA and replicative branched structures are already present in chromosomes that, nonetheless, enter a PFGE. For instance, gaps of unreplicated DNA were observed by combing in the *TOP2 cdc15-2* block (Fig. 3). Although this may reflect a limitation of the combing technique for the purpose of quantifying underreplication, it is remarkable that a recent report shows that chromosomes are not fully replicated in a *TOP2 cdc15-2* block⁵⁵. Likewise, we have shown that sister chromatids are somehow

connected with each other in the *TOP2 cdc15-2* block and form retrograde anaphase bridges after DSBs⁵⁶. In addition, cytological markers of ssDNA and replication stress are present in the *TOP2 cdc15-2* block, although there is an increase in the *top2-5 cdc15-2* block (Table 1; Figures S13 and S14). One of these markers, the RPA complex, has been recently seen by others in the *TOP2 cdc15-2* block⁵⁵. Because we could not see a difference in the amount of underreplicated material between *TOP2 cdc15-2* and *top2-5 cdc15-2* (Fig. 3), we speculate that a late modification of remaining Y-shaped branches in the absence of Top2 might trigger the PFGE shift. This modification would not be sensed as DNA damage (Figs. 1, 2, 5 and S11) and would not depend on Rad52-driven HR (Fig. 4). An interesting possibility is the eventual regression of converging RFs into four-way HJ-like chicken foot structures (Figure S15a), which are particularly enriched when cells cannot sense RF problems⁵⁷. This scenario is compatible with the presence of Rad52-independent NN-2D X-shaped signals we observed in the rDNA (Fig. 4). Moreover, RF regression is expected for *top2* mutants as positive supercoiling accumulates ahead of the converging RFs at replication termini^{58,59}. Where are these persistent RFs? We have shown that the RFB at the rDNA locus is one of these (Figs. 3, 4 and 5), but this only accounts for chromosomes XII. We envisage that other difficult-to-replicate regions shared by all chromosomes may be involved. These regions would include centromeres, G-quadruplex, fragile sites, transposable elements, non-coding RNAs and subtelomeric regions^{18,55,60–62}. However, we checked one of such regions, the replication temini locus *TER302* in chromosome III, but could not detect persistent RFs in *top2-5 cdc15-2*. Recently, another paper has shown that pericentromeric regions accumulate DNA damage markers during S-phase⁶³. Again, this damage does not appear to arrest the cell cycle⁶⁴. A corollary of these assertions is that the traditional claim for ongoing replication as one cause of chromosome entrapment during PFGE should be revised. Perhaps, chromosomes get entrapped not by having RFs but by ensuing RF modifications. Alternatively, cumulative topological stress could promote dsDNA unwinding towards ssDNA that, followed by ectopic or sister re-annealing, would create four-way DNA origamis. In addition, ssDNA tracks may be interlocked by type IA topoisomerases (Top3), forming hemicatenanes. These solutions are indeed compatible with the presence of more ssDNA in *top2-5 cdc15-2* while not observing larger underreplication gaps than the control *TOP2 cdc15-2*. In addition, it predicts Rad52-independent X-shaped molecules at the rDNA and lack of sensing by the DNA damage checkpoints. Another possibility compatible with more ssDNA tracks but the same levels of underreplication is partial re-replication taking place in the absence of Top2. Perhaps, the perturbed topology at the replication origin deregulates how many times they can fire within a single cell cycle. However, it is difficult to envisage how re-replication can proceed in such topological jumble without triggering a DNA damage checkpoint.

Finally, we cannot rule other explanations for the PFGE shift such as massive topological intertwinings, or even knots, between different chromosomes after prolonged Top2 absence (Figure S15b). Catenations between the replicated sister chromatids is the immediate consequence of the Top2 absence; however, within the constrained space of the nucleus, and with other important dynamic events taking place in G₂/M/anaphase, such as transcription and condensation, it is difficult to envisage how cells avoid cumulative topological problems without Top2. Of note, previous studies with *top2-ts* showed vastly interlocked/knotted plasmids^{56,17,65}. Massive interchromosomal intertwinings/knotting may form a chromosome web that trap chromosomes. The presence of persistent late replication intermediates and complex topological intertwinings as explanations of the PFGE are not mutually exclusive. Indeed, knotting and hemicatenanes have been related to failure to finish replication^{66,67}.

In conclusion, the lack of Top2 postreplicatively modifies the structure of all yeast chromosomes in a way that diminish their ability to run in a PFGE. Future work on the actual physical nature of the DNA molecules trapped in the PFGE, together with genetic screenings of modifiers, should clarify this late chromosome structural change and perhaps assign a novel role for Top2 in the chromosome biology field.

Materials and methods

Yeast strains and experimental conditions. All the strains used in this work are listed in Table S1. All strains were grown overnight in air orbital incubators at 25 °C in YEPD. Time course experiments were performed as follows: asynchronous cultures were adjusted to OD₆₀₀ = 0.3 and then synchronized in G1 at 25 °C for 3 h by adding 50 ng/ml of alpha-factor. The G₁ release was induced by washing the cells twice and resuspending them in fresh media containing 0.1 mg/ml of pronase E. Then, they were incubated at 37 °C for 3–4 h. In time course experiments, samples were taken every 30 min for microscopy, FACS and PFGE.

Microscopy and flow cytometry (FACS). H2A2-GFP was analyzed by wide-field fluorescence microscopy as reported before¹⁵. Briefly, series of z-focal plane images (15–20 planes, 0.15–0.3 μm depth) were collected on a Leica DMI6000, using a 63×/1.30 immersion objective and an ultrasensitive DFC 350 digital camera, and processed with the AF6000 software (Leica). Scale bars in micrographs depict 5 μm; BF stands for bright field.

DNA content by flow cytometry analysis (FACS) was done as previously described using a BD FACS caliber equipment⁷. An asynchronous culture of each strain growing at permissive temperature was used to calibrate the 1C and 2C peaks before reading the samples. Strains carrying the *cdc15-2* and *cdc14-1* alleles rendered a minor 2C peak at the G1 arrest. This peak corresponded to 10–20% of G1 samples and comprised cells responsive to alpha-factor but that remain attached as pairs (Figure S7). This phenotype likely stems from delayed septation at permissive temperatures. This minor 2C transposes into a 4C peak when cells are released from the G1 arrest, giving the false impression of re-replication.

Pulsed-field gel electrophoresis (PFGE) and neutral, neutral two-dimensional electrophoresis (NN-2D). Yeast DNA for PFGE and NN-2D was extracted in low-melting agarose (LMA) plugs in conditions known to avoid branch migration⁷. Briefly, 4 OD₆₀₀ equivalents were embedded into a 0.5% (w/v) LMA plug and then digested with zymolyase (2 units, day 1), RNaseA (10 μg/ml; day 1) and Proteinase K (1 mg/ml; day 2).

All digestions were carried out at 37 °C (including the Proteinase K step). Yeast DNA for combing analysis was also extracted in LMA but in different conditions (see below). In case of subsequent overnight treatment of the agarose plugs with 250 units of BglII (R0144M, New England Biolabs), Proteinase K was first inactivated with 1 mg/ml Pefabloc (11429868001, Roche).

PFGEs were carried out using a CHEF DR-III system (Bio-Rad) and we followed standard conditions with minor modifications: 1% agarose gel in 0.5×TBE buffer and run at 14 °C for 40 h at 5 V/cm with an initial switching time of 47 s, a final of 170 s, and an angle of 120°. The chromosome bands in the gels were visualized with EtBr staining. For Southern blots we used a fluorescein-labelled probe (Sigma-Aldrich, #11585622910) against the NTS1 region within the rDNA^{7,26}. Detection was performed by chemiluminescence (Amersham Hyperfilm ECL film) using an anti-fluorescein antibody coupled to alkaline phosphatase (Sigma-Aldrich, #11426338910) and using CDP-star (Sigma-Aldrich, #11759051001) as the substrate.

NN-2Ds for NTS1 were also performed from agarose plugs. These were digested with BglII, run in two dimensions, and transferred to positively charged nylon membranes for Southern analysis as described before²⁶. Comparison between samples was based on expositions that render equivalent 1N/2N linear spots. The NN-2Ds for *TER302* was carried out according to the CTAB DNA extraction protocol¹⁸, as 1N and 2N spots from this single-copy genomic region were not strong enough from plugs.

DNA combing and immunodetection. DNA combing experiments were performed as described before⁴⁸. Firstly, *top2-5* and *cdc15-2* alleles were transferred by PCR methods to a strain suitable for BrdU DNA labelling (Table S1)²⁸. The resulting strains were first arrested in G₁ at 25 °C by incubating with 5 µg/mL alpha-factor (*BARI* genotype) for 3 h. Cells were then released from G₁ by adding Pronase E (100 µg/mL final concentration) and incubated 4 h at 37 °C. Half an hour before Pronase addition, BrdU was added to the cultures at 400 µg/mL final concentration. Samples were taken 4 h after the release and immediately treated with 0.1% w/v sodium azide and cooled down to 0 °C. DNA for combing was extracted in LMA plugs. Relative to the plugs prepared for PFGE and NN-2Ds, these plugs used the following settings: 4×10^7 cells ($\sim 1 \text{ OD}_{600}$ equivalents), 0.5 U Zymolyase (2 days of incubation), no RNase, and 3 days incubation with Proteinase K at 50 °C.

For DNA combing, the plugs were incubated at RT for 30 min with 1 µL of YOYO-1 (Molecular Probes, Y3601) in 150 µL of TE50 buffer (10 mM Tris-HCl pH 7.0, 50 mM EDTA). Then, they were washed 3 times in TE50 buffer, and incubated twice for 5 min in 2 mL MES buffer (7:3 v/v MES hydrate: MES sodium salt 50 mM pH 5.7). After that, the plugs were melted at 72 °C for 20 min. The solution was transferred to 42 °C for 15 min and incubated overnight in 3 U of β -agarase I (New England Biolabs, M0392). Next, the solution was heated to 72 °C for 10 min, cooled to room temperature (RT) and poured into the reservoir of the combing device. The silanized combing coverslips were incubated into the solution for at least 5 min, and then pulled out at a constant speed of 710 µm/s. Finally, they were incubated for 90 min at 60 °C, and mounted on a glass slide.

For immunodetection, the slides were dehydrated by sequential 5 min incubations with 70%, 90%, and 100% v/v ethanol at RT. They were air dried and the DNA was denatured in 1 M NaOH for 25 min at RT. Next, the slides were washed 5 times in PBS and incubated for 5 min in PBS-T (PBS plus 0.05% v/v Tween-20). After that, 21 µL of blocking buffer (PBS-T plus 10% w/v BSA) were added and dispersed on the coverslip and the slides were incubated in a humidity chamber for 30 min at 37 °C. Next, the coverslips were removed by dipping the slides into PBS-T, and 21 µL of anti-BrdU solution (1:40 dilution in blocking buffer of the rat anti-BrdU antibody [AbD Serotec, MCA2060]) were added, dispersed and incubated (1 h) as the previous step. The same steps were carried out after that with the anti-DNA solution (1:50 dilution of the anti-DNA antibody [Millipore, MAB3034]) and the secondary antibodies solution (1:75 dilutions of Alexa Fluor 488 goat anti-rat and Alexa Fluor 546 goat anti-mouse [Molecular probes, A11006 & A11030, respectively]), always washing with PBS-T in between. Finally, 10 µL of ProLong Gold antifade reagent (Molecular Probes, 36930) were added and the samples were covered with a fresh coverslip.

Only DNA fibers larger than 100 kbp and markedly labelled with BrdU were included in the analyses. A low number of fibers (1% in *TOP2 cdc15-2* and 9% in *top2-5 cdc15-2*) were wholly devoid of BrdU. We considered that these fibers came from cells that did not enter S-phase after the G₁ release, as we previously showed that ~10% of the *top2-5* progeny at 25 °C may be inviable²³.

Mini-screening of fluorescent DNA stress markers. The GFP-fusion library (Invitrogen, catalog number: 95702) was used as the basis for the mini-screening⁶⁹. To introduce both the *top2-5* and *cdc15-2* alleles into the library, a series of PCR-based transformations were carried out to obtain the strain OQR84. This strain was also designed to carry the anaphase bridge reporter Dpb11-yEmRFP. The strain OQR84 was crossed with preselected strains from the GFP-fusion library and then haploids were selected for two genotypes: *DPB11-yEmRFP gene-GFP TOP2 cdc15-2* and *DPB11-yEmRFP gene-GFP top2-5 cdc15-2* (Table S1).

To carry out the screen, cells were grown overnight in 96-well plates at permissive temperature (25 °C) in synthetic complete medium supplemented with 100 µg/ml adenine. The following day, cells were diluted 1/10 and grown for 2 h at 25 °C. Next, cells were incubated at restrictive temperature (37 °C) for 3 h and finally transferred to 384-well CellCarrier plates (PerkinElmer, 6007550) for imaging on an Opera QEHS high-content screening microscope (PerkinElmer). Single planes of 5 different fields were taken per each strain of the library using a 60× water immersion objective and CCD cameras with the proper filter sets to visualise either GFP or RFP. The exposure time for each channel was 1 s. Data analysis to determine the presence of GFP-tagged proteins on Dpb11-labeled anaphase bridges was performed manually. Foci number was also determined by eye.

Data availability

The datasets supporting the conclusions of this article are included within the article and its additional files.

Received: 23 June 2021; Accepted: 1 July 2021
Published online: 22 July 2021

References

- Bizard, A. H. & Hickson, I. D. Anaphase: A fortune-teller of genomic instability. *Curr. Opin. Cell Biol.* **52**, 112–119 (2018).
- Machin, F., Quevedo, O., Ramos-Pérez, C. & García-Luis, J. Cdc14 phosphatase: Warning, no delay allowed for chromosome segregation. *Curr. Genet.* **62**, 7–13 (2016).
- Ly, P. & Cleveland, D. W. Rebuilding chromosomes after catastrophe: Emerging mechanisms of chromothripsis. *Trends Cell Biol.* **27**, 917–930 (2017).
- Giannattasio, M. & Branzei, D. S-phase checkpoint regulations that preserve replication and chromosome integrity upon dNTP depletion. *Cell. Mol. Life Sci.* **74**, 2361–2380 (2017).
- Pardo, B., Crabbé, L. & Pasero, P. Signaling pathways of replication stress in yeast. *FEMS Yeast Res.* **17**, 1–11 (2017).
- Symington, L. S., Rothstein, R. & Lisby, M. Mechanisms and regulation of mitotic recombination in *Saccharomyces cerevisiae*. *Genetics* **198**, 795–835 (2014).
- García-Luis, J. & Machin, F. Mus81-Mms4 and Yen1 resolve a novel anaphase bridge formed by noncanonical Holliday junctions. *Nat. Commun.* **5**, 5652 (2014).
- Chan, Y. W., Fugger, K. & West, S. C. Unresolved recombination intermediates lead to ultra-fine anaphase bridges, chromosome breaks and aberrations. *Nat. Cell Biol.* **20**, 92–103 (2018).
- Damelin, M. & Bestor, T. H. The decatenation checkpoint. *Br. J. Cancer* **96**, 201–205 (2007).
- Nitiss, J. L. DNA topoisomerase II and its growing repertoire of biological functions. *Nat. Rev. Cancer* **9**, 327–337 (2009).
- Pommier, Y., Sun, Y., Huang, S. N. & Nitiss, J. L. Roles of eukaryotic topoisomerases in transcription, replication and genomic stability. *Nat. Rev. Mol. Cell Biol.* **17**, 703–721 (2016).
- Piskadlo, E. & Oliveira, R. A. A topology-centric view on mitotic chromosome architecture. *Int. J. Mol. Sci.* **18**, 1–21 (2017).
- DiNardo, S., Voelkel, K. & Sternglanz, R. DNA topoisomerase II mutant of *Saccharomyces cerevisiae*. Topoisomerase II is required for segregation of daughter molecules at the termination of DNA replication. *Proc. Natl. Acad. Sci. USA.* **81**, 2616–2620 (1984).
- Holm, C., Goto, T., Wang, J. C. & Botstein, D. DNA topoisomerase II is required at the time of mitosis in yeast. *Cell* **41**, 553–563 (1985).
- Ramos-Pérez, C. *et al.* Genome-scale genetic interactions and cell imaging confirm cytokinesis as deleterious to transient topoisomerase II deficiency in *Saccharomyces cerevisiae*. *G3* **7**, 3379–3391 (2017).
- Holm, C., Stearns, T. & Botstein, D. DNA topoisomerase II must act at mitosis to prevent nondisjunction and chromosome breakage. *Mol. Cell Biol.* **9**, 159–168 (1989).
- Baxter, J. & Diffley, J. F. X. Topoisomerase II inactivation prevents the completion of DNA replication in budding yeast. *Mol. Cell* **30**, 790–802 (2008).
- Fachinetti, D. *et al.* Replication termination at eukaryotic chromosomes is mediated by Top2 and occurs at genomic loci containing pausing elements. *Mol. Cell* **39**, 595–605 (2010).
- Mundbjerg, K. *et al.* Top2 and Sgs1-Top3 act redundantly to ensure rDNA replication termination. *PLoS Genet.* **11**, 1–24 (2015).
- Kobayashi, T. Regulation of ribosomal RNA gene copy number and its role in modulating genome integrity and evolutionary adaptability in yeast. *Cell. Mol. Life Sci.* **68**, 1395–1403 (2011).
- Andrews, C. A. *et al.* A mitotic topoisomerase II checkpoint in budding yeast is required for genome stability but acts independently of Pds1/securin. *Genes Dev.* **20**, 1162–1174 (2006).
- Amaral, N. *et al.* The Aurora-B-dependent NoCut checkpoint prevents damage of anaphase bridges after DNA replication stress. *Nat. Cell Biol.* **18**, 516–526 (2016).
- Ramos-Pérez, C. *et al.* Cytological and genetic consequences for the progeny of a mitotic catastrophe provoked by Topoisomerase II deficiency. *Aging* **11**, 11686–11721 (2019).
- Hennessy, K. M., Lee, A., Chen, E. & Botstein, D. A group of interacting yeast DNA replication genes. *Genes Dev.* **5**, 958–969 (1991).
- Ho, C. K., Mazón, G., Lam, A. F. & Symington, L. S. Mus81 and Yen1 promote reciprocal exchange during mitotic recombination to maintain genome integrity in budding yeast. *Mol. Cell* **40**, 988–1000 (2010).
- Quevedo, O., García-Luis, J., Matos-Perdomo, E., Aragón, L. & Machin, F. Nondisjunction of a single chromosome leads to breakage and activation of DNA damage checkpoint in g2. *PLoS Genet.* **8**, e1002509 (2012).
- Brewer, B. J. & Fangman, W. L. A replication fork barrier at the 3' end of yeast ribosomal RNA genes. *Cell* **55**, 637–643 (1988).
- Lengronne, A., Pasero, P., Bensimon, A. & Schwob, E. Monitoring S phase progression globally and locally using BrdU incorporation in TK(+) yeast strains. *Nucleic Acids Res.* **29**, 1433–1442 (2001).
- Branzei, D. & Szakal, B. DNA damage tolerance by recombination: Molecular pathways and DNA structures. *DNA Repair* **44**, 68–75 (2016).
- Pâques, F. & Haber, J. E. Multiple pathways of recombination induced by double-strand breaks in *Saccharomyces cerevisiae*. *Microbiol. Mol. Biol. Rev.* **63**, 349–404 (1999).
- Rudner, A. D. & Murray, A. W. The spindle assembly checkpoint. *Curr. Opin. Cell Biol.* **8**, 773–780 (1996).
- Stegmeier, F., Visintin, R. & Amon, A. Separase, polo kinase, the kinetochore protein Slk19, and Spo12 function in a network that controls Cdc14 localization during early anaphase. *Cell* **108**, 207–220 (2002).
- Rocuzzo, M., Visintin, C., Tili, F. & Visintin, R. FEAR-mediated activation of Cdc14 is the limiting step for spindle elongation and anaphase progression. *Nat. Cell Biol.* **17**, 251–261 (2015).
- D'Amours, D., Stegmeier, F. & Amon, A. Cdc14 and condensin control the dissolution of cohesin-independent chromosome linkages at repeated DNA. *Cell* **117**, 455–469 (2004).
- Sullivan, M., Higuchi, T., Katis, V. L. & Uhlmann, F. Cdc14 phosphatase induces rDNA condensation and resolves cohesin-independent cohesion during budding yeast anaphase. *Cell* **117**, 471–482 (2004).
- Torres-Rosell, J., Machin, F., Jarmuz, A. & Aragón, L. Nucleolar segregation lags behind the rest of the genome and requires Cdc14p activation by the FEAR network. *Cell Cycle* **3**, 496–502 (2004).
- Machin, F., Torres-Rosell, J., Jarmuz, A. & Aragón, L. Spindle-independent condensation-mediated segregation of yeast ribosomal DNA in late anaphase. *J. Cell Biol.* **168**, 209–219 (2005).
- Blanco, M. G., Matos, J. & West, S. C. Dual control of Yen1 nuclease activity and cellular localization by Cdk and Cdc14 prevents genome instability. *Mol. Cell* **54**, 94–106 (2014).
- Eissler, C. L. *et al.* The Cdk/Cdc14 module controls activation of the Yen1 Holliday junction resolvase to promote genome stability. *Mol. Cell* **54**, 80–93 (2014).
- García-Luis, J., Clemente-Blanco, A., Aragón, L. & Machin, F. Cdc14 targets the Holliday junction resolvase Yen1 to the nucleus in early anaphase. *Cell Cycle* **13**, 1392–1399 (2014).
- Wild, P. & Matos, J. Cell cycle control of DNA joint molecule resolution. *Curr. Opin. Cell Biol.* **40**, 74–80 (2016).
- Hoyt, M. A., Totis, L. & Roberts, B. T. S. *cerevisiae* genes required for cell cycle arrest in response to loss of microtubule function. *Cell* **66**, 507–517 (1991).
- Bonaiuti, P. *et al.* Cells escape an operational mitotic checkpoint through a stochastic process. *Curr. Biol.* **28**, 28–37.e7 (2018).
- Kaniak-Golik, A. & Skoneczna, A. Mitochondria-nucleus network for genome stability. *Free Radic. Biol. Med.* **82**, 73–104 (2015).

45. Tkach, J. M. *et al.* Dissecting DNA damage response pathways by analysing protein localization and abundance changes during DNA replication stress. *Nat. Cell Biol.* **14**, 966–976 (2012).
46. Germann, S. M. *et al.* TopBP1/Dpb11 binds DNA anaphase bridges to prevent genome instability. *J. Cell Biol.* **204**, 45–59 (2014).
47. Bermejo, R. *et al.* Genome-organizing factors Top2 and Hmo1 prevent chromosome fragility at sites of S phase transcription. *Cell* **138**, 870–884 (2009).
48. Falquet, B. & Rass, U. Structure-specific endonucleases and the resolution of chromosome underreplication. *Genes* **10**, 1–22 (2019).
49. Cantor, C. R., Smith, C. L. & Mathew, M. K. Pulsed-field gel electrophoresis of very large DNA molecules. *Annu. Rev. Biophys. Biophys. Chem.* **17**, 287–304 (1988).
50. Wang, M. & Lai, E. Pulsed field separation of large supercoiled and open-circular DNAs and its application to bacterial artificial chromosome cloning. *Electrophoresis* **16**, 1–7 (1995).
51. Heichman, K. A. & Roberts, J. M. The yeast CDC16 and CDC27 genes restrict DNA replication to once per cell cycle. *Cell* **85**, 39–48 (1996).
52. Bendich, A. J. Structural analysis of mitochondrial DNA molecules from fungi and plants using moving pictures and pulsed-field gel electrophoresis. *J. Mol. Biol.* **255**, 564–588 (1996).
53. Maleszka, R. Single-stranded regions in yeast mitochondrial DNA revealed by pulsed-field gel electrophoresis. *Appl. Theor. Electrophoresis* **3**, 259–263 (1993).
54. Bustamante, C., Gurrieri, S. & Smith, S. B. Towards a molecular description of pulsed-field gel electrophoresis. *Trends Biotechnol.* **11**, 23–30 (1993).
55. Ivanova, T. *et al.* Budding yeast complete DNA synthesis after chromosome segregation begins. *Nat. Commun.* **11**, 2267 (2020).
56. Ayra-Plasencia, J. & Machin, F. DNA double-strand breaks in telophase lead to coalescence between segregated sister chromatid loci. *Nat. Commun.* **10**, 2862 (2019).
57. Sogo, J. M., Lopes, M. & Fojani, M. Fork reversal and ssDNA accumulation at stalled replication forks owing to checkpoint defects. *Science* **297**, 599–602 (2002).
58. Atkinson, J. & McGlynn, P. Replication fork reversal and the maintenance of genome stability. *Nucleic Acids Res.* **37**, 3475–3492 (2009).
59. Postow, L. *et al.* Positive torsional strain causes the formation of a four-way junction at replication forks. *J. Biol. Chem.* **276**, 2790–2796 (2001).
60. Hashash, N., Johnson, A. L. & Cha, R. S. Topoisomerase II- and condensin-dependent breakage of MEC1 (ATR)-sensitive fragile sites occurs independently of spindle tension, anaphase, or cytokinesis. *PLoS Genet.* **8**, e1002978 (2012).
61. Song, W., Dominska, M., Greenwell, P. W. & Petes, T. D. Genome-wide high-resolution mapping of chromosome fragile sites in *Saccharomyces cerevisiae*. *Proc. Natl. Acad. Sci. USA* **111**, E2210–E2218 (2014).
62. Szilard, R. K. *et al.* Systematic identification of fragile sites via genome-wide location analysis of γ -H2AX. *Nat. Struct. Mol. Biol.* **17**, 299–305 (2010).
63. Minchell, N. E., Keszhelyi, A. & Baxter, J. Cohesin causes replicative DNA damage by trapping DNA topological stress. *Mol. Cell* **78**, 739–751 (2020).
64. Schalbeter, S. A., Mansoubi, S., Chambers, A. L., Downs, J. A. & Baxter, J. Fork rotation and DNA precatenation are restricted during DNA replication to prevent chromosomal instability. *Proc. Natl. Acad. Sci. USA* **112**, E4565–E4570 (2015).
65. Valdés, A., Segura, J., Dyson, S., Martínez-García, B. & Roca, J. DNA knots occur in intracellular chromatin. *Nucleic Acids Res.* **46**, 650–660 (2018).
66. Lucas, I. & Hyrien, O. Hemicatenanes form upon inhibition of DNA replication. *Nucleic Acids Res.* **28**, 2187–2193 (2000).
67. Olavarrieta, L., Hernández, P., Krimer, D. B. & Schwartzman, J. B. DNA knotting caused by head-on collision of transcription and replication. *J. Mol. Biol.* **322**, 1–6 (2002).
68. Gallo, D., Wang, G., Yip, C. M. & Brown, G. W. Single-molecule analysis of replicating yeast chromosomes. *Cold Spring Harb. Protoc.* **2016**, 104–106 (2016).
69. Huh, W. K. *et al.* Global analysis of protein localization in budding yeast. *Nature* **425**, 686–691 (2003).

Acknowledgements

We thank other members of the lab for fruitful discussions and help. This work was supported by the Spanish Ministry of Science and Innovation research grants BFU2015-63902-R and BFU2017-83954-R to F.M., the Danish Council for Independent Research, the Carlsberg Foundation and the Villum Foundation to M.L. and O.Q., and Canadian Institutes of Health Research grant FDN-159913 to G.W.B. High-throughput imaging was performed at the Center for Advanced Bioimaging, University of Copenhagen. Agencia Canaria de Investigación, Innovación y Sociedad de la Información supported C.R-P., S.S-S., and S.M-S. through predoctoral fellowships (TESIS20120109, TESIS2018010034 and TESIS2020010028, respectively). Grants to F.M. and predoctoral fellowships were co-financed with the European Commission's ERDF structural funds.

Author contributions

J.A-P., C.R-P., M.L., G.W.B. and F.M. conceived and designed the experiments. J.A-P., C.R-P., S.S-S., O.Q., S.M-S. and M.Z-D. made the strains and performed the experiments. J.A-P., C.R-P., O.Q., E.M-P. and F.M. prepared the figures and tables. F.M. wrote the manuscript. All authors reviewed the manuscript.

Competing interests

The authors declare no competing interests.

Additional information

Supplementary Information The online version contains supplementary material available at <https://doi.org/10.1038/s41598-021-93875-5>.

Correspondence and requests for materials should be addressed to F.M.

Reprints and permissions information is available at www.nature.com/reprints.

Publisher's note Springer Nature remains neutral with regard to jurisdictional claims in published maps and institutional affiliations.

www.nature.com/scientificreports/



Open Access This article is licensed under a Creative Commons Attribution 4.0 International License, which permits use, sharing, adaptation, distribution and reproduction in any medium or format, as long as you give appropriate credit to the original author(s) and the source, provide a link to the Creative Commons licence, and indicate if changes were made. The images or other third party material in this article are included in the article's Creative Commons licence, unless indicated otherwise in a credit line to the material. If material is not included in the article's Creative Commons licence and your intended use is not permitted by statutory regulation or exceeds the permitted use, you will need to obtain permission directly from the copyright holder. To view a copy of this licence, visit <http://creativecommons.org/licenses/by/4.0/>.

© The Author(s) 2021

Topoisomerase II deficiency leads to a postreplicative structural shift in all *Saccharomyces cerevisiae* chromosomes.

Jessel Ayra-Plasencia^{1,2,a}, Cristina Ramos-Pérez^{1,3,b}, Silvia Santana-Sosa^{1,2}, Oliver Quevedo^{4,c}, Sara Medina-Suarez^{1,2}, Emiliano Matos-Perdomo^{1,2}, Marcos Zamora-Dorta¹, Grant W Brown³, Michael Lisby⁴ and Félix Machín^{1,5,6*}

¹ Unidad de Investigación, Hospital Universitario Nuestra Señora de Candelaria, Tenerife, Spain.

² Escuela de Doctorado y Estudios de Postgrado, Universidad de La Laguna, Tenerife, Spain

³ Department of Biochemistry and Donnelly Centre, University of Toronto, Canada

⁴ Department of Biology, University of Copenhagen, Denmark.

⁵ Instituto de Tecnologías Biomédicas, Universidad de la Laguna, Tenerife, Spain.

⁶ Facultad de Ciencias de la Salud, Universidad Fernando Pessoa Canarias, Las Palmas de Gran Canaria, Spain.

^a Present address: CEAMED S.A., Tenerife, Spain.

^b Present address: BenchSci Analytics Inc., Toronto, Canada.

^c Present address: River Stone Biotech, Copenhagen, Denmark.

* Corresponding author: Félix Machín. Unidad de Investigación, Hospital Universitario Nuestra Señora de la Candelaria, Ctra del Rosario 145, 38010 Santa Cruz de Tenerife, Spain. Tfno: +34 922 602 951. E-mail: fmachin@fciisc.es

SUPPLEMENTAL MATERIAL

SUPPLEMENTAL FIGURES.

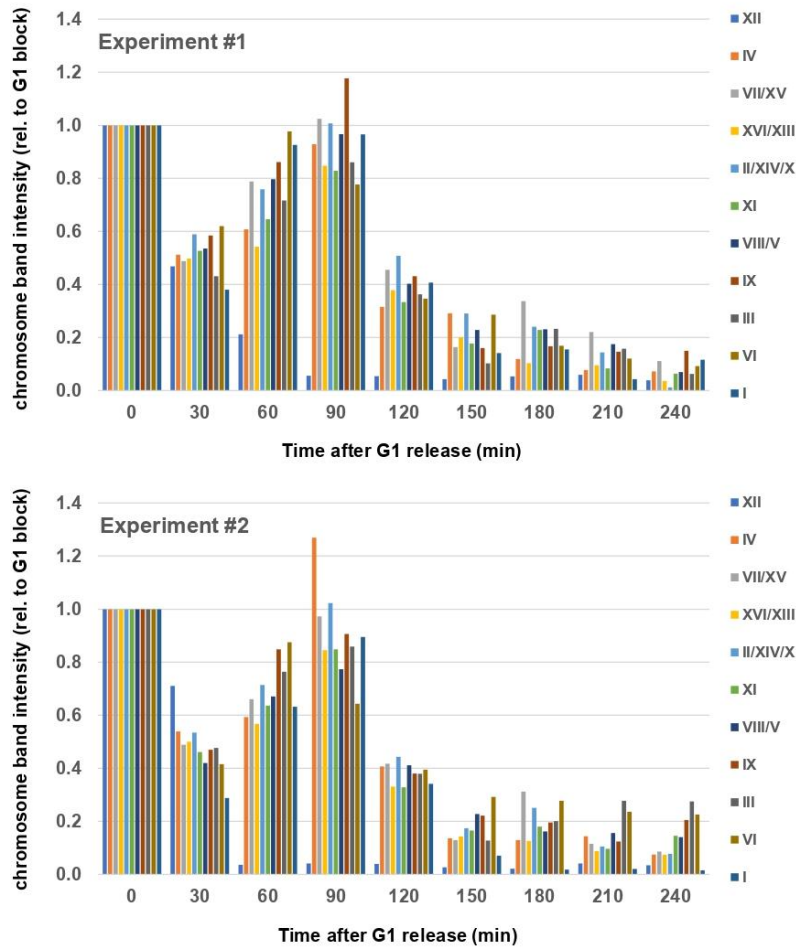


Figure S1. Quantification of PFG chromosome bands after the *top2-5* release from G1. After the PFGEs obtained from time course experiments as shown in Figure 1, gels were stained with ethidium bromide, photographed, each band quantified by Fiji/ImageJ (<https://imagej.net/Fiji>), and represented against the band value at G1. The experiment #1 corresponds to the PFGE shown in Figure 1e.

	<i>TOP2</i>	<i>top-5</i>		
~OD ₆₀₀ /plug	6	6	3	1.5
Zymo (Units/plug)	1	2	2	2
Zymo/OD ratio	0.17	0.33	0.66	1.3

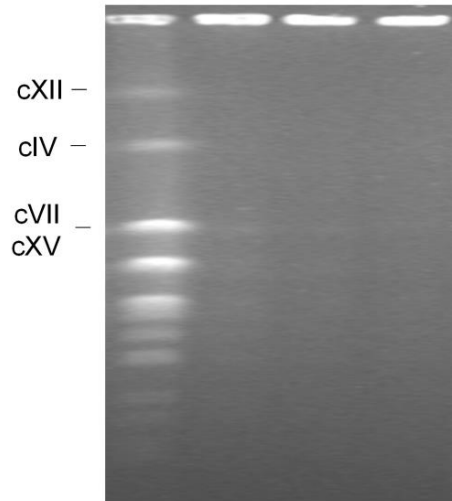


Figure S2. Well entrapment of *top2-5* is not due to special wall digestion requirements in this mutant. A time course experiment was carried out as stated in Figure 1. Four hours after the G1 release, samples from the *TOP2* and *top2-5* strains were taken from plug preparation under different cell wall digestion treatments. In general, the number of cells (OD₆₀₀ equivalents) and the amount of zymolyase were changed. The standard values in all other plug preparations of this article were 4 OD₆₀₀ and 2 units zymolyase. Note how increasing ODs and decreasing zymolyase unit in *TOP2* plugs still allowed chromosome migration, whereas decreasing ODs in *top2-5* did not ameliorate chromosome entrapment. The image of the PFG is vertically squeezed to half of its actual length.

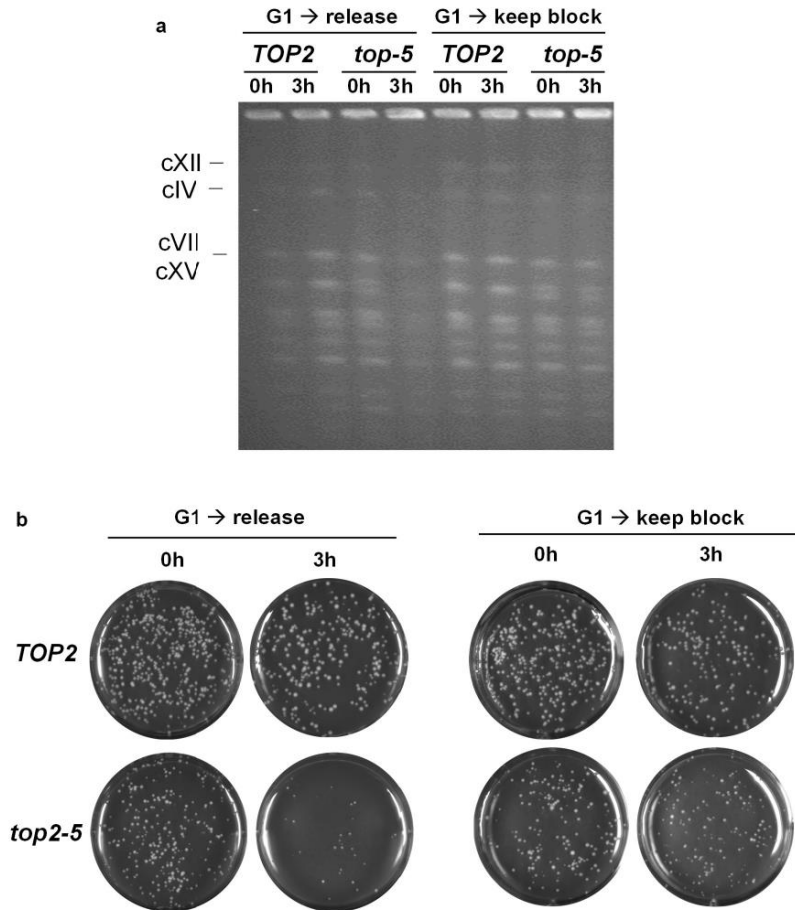


Figure S3. Maintaining the G1 block prevents chromosomes from well-entrapment in *top2-5*. The *TOP2* and *top2-5* strains were arrested in G1 for 3h at 25 °C. Then the cultures were split in two, one of them was released into a synchronous cycle (G1 → release) and the second one was kept in the G1 block. All four cultures were incubated at 37 °C for 3 more hours before stopping the experiment. At the time of the G1 block at 25 °C and after 3h at 37 °C, samples were taken for PFGE and assessment of clonogenic survivability. **(a)** PFGE. The image of the PFG is vertically squeezed to half of its actual length. Note that chromosomes do not get entrapped in *top2-5* cells kept in G1. **(b)** Clonogenic survivability. Note that *top2-5* cells do not loose viability when kept in G1.

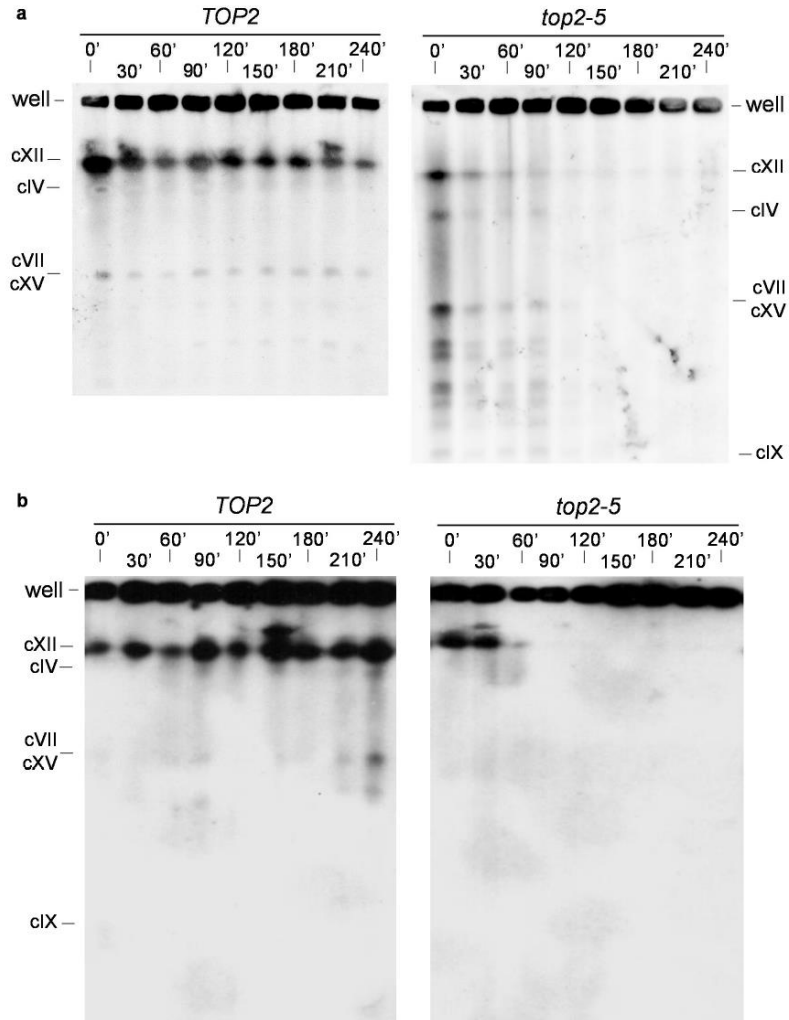


Figure S4. No sign of fast-migrating broken chromosomes after Top2-5 inactivation. Two synchronous G1 release experiments were performed at 37 °C for isogenic *TOP2* and *top2-5* strains. At the indicated time points, samples were taken for microscopy, FACS and PFGE (shown in Figure 1 for experiment #1). After PFGEs, Southern blots were undertaken with probes against the NTS1 region of the rDNA (chromosome XII, cXII). (a) Southern blots from experiment #1 (*top2-5* under lower stringency conditions). (b) Southern blots from experiment #2. Each experiment used independent NTS1 probes.

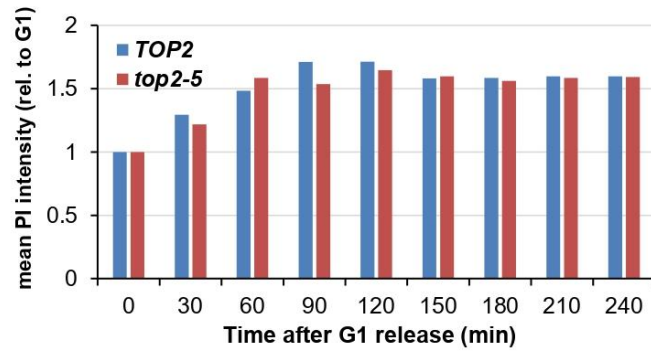


Figure S5. Quantification of the average DNA content after the *top2-5* G1 release. Area under the curve was quantified for the FACS profiles shown in Figure 1d. Note that *TOP2* and *top2-5* have an equivalent DNA content during the time course despite the extremely flattened profile of *top2-5* at the latest time points (180'-240'). The values never reached the theoretical 2xG1 content, probably because propidium iodide stains budded cells less efficiently.

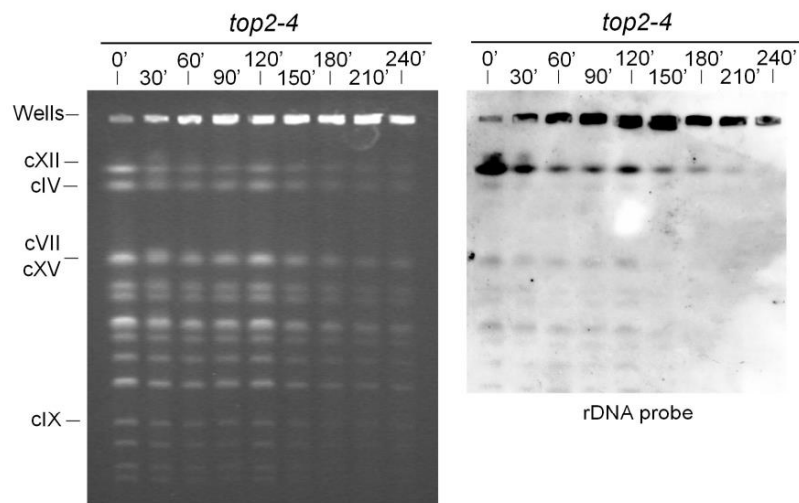


Figure S6. The mutant *top2-4* also entraps chromosomes after the mitotic catastrophe. An isogenic strain carrying the *top2-4* ts allele was subjected to the same experiment shown in Figure 1. A PFGE was run and a Southern blot against the rDNA was performed in the same conditions. Note how *top2-4* led to entrapment from 150' onwards, although the phenotype was slightly milder, including for chromosome XII.

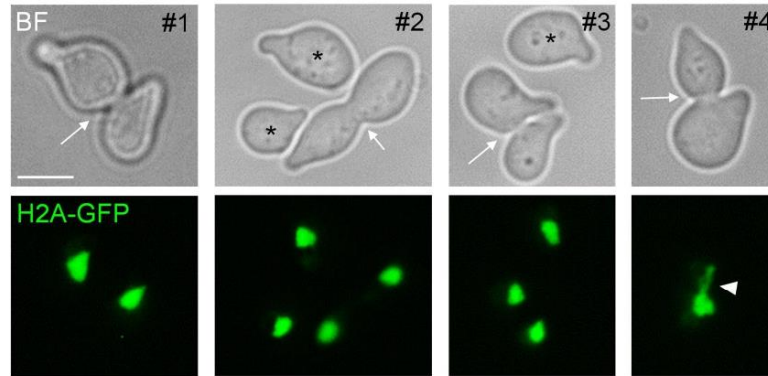


Figure S7. Incomplete cytokinesis and septation in *cdc15-2* derivatives of *top2-5* and *TOP2* blocked in G1. Four representative micrographs are shown from the Figure 2 experiment. Note how G1-blocked cells (they all responded to alpha-factor as reported by the characteristic pear-like morphology) can appear as either singlets (asterisks) or doublets. The latter stems from incomplete septation (white arrows) and/or cytokinesis in the previous cell cycle. At least in the example #4, a defect in cytokinesis is evident since the doublet shows a chromatin bridge (white arrowhead in the GFP channel). These doublets likely account for the minor 2C peaks observed at time 0 in the corresponding FACS, and the ensuing minor 4C peaks during the release. The scale bar depicts 5 μm . BF, bright field.

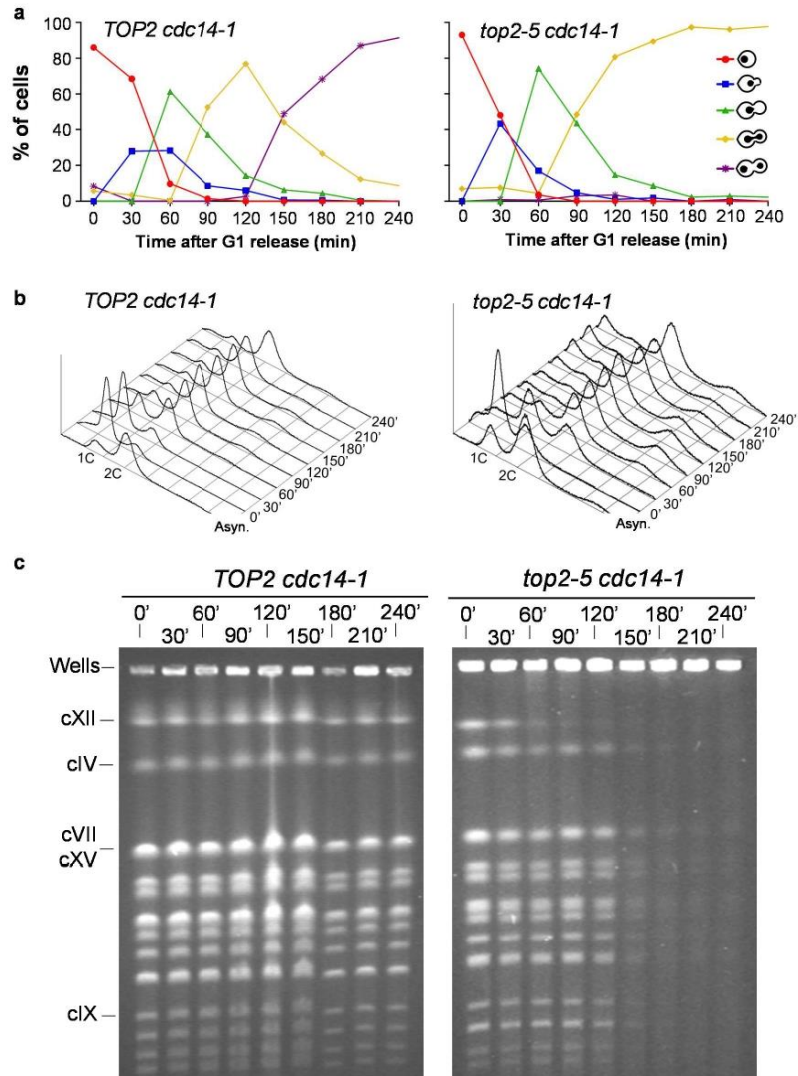


Figure S8. The loss of chromosome integrity in *top2-5* is not a consequence of Cdc14-driven activities in anaphase. A synchronous G1 release experiment was performed for isogenic *TOP2 cdc14-1* (left panels) and *top2-5 cdc14-1* (right panels) strains. **(a)** Charts depicting the cell cycle progression under the microscope. **(b)** FACS analysis of the DNA content. **(c)** EtBr staining of whole chromosomes resolved by PFGE. Note how chromosome behaviour of the *top2-5 cdc14-1* strain fully resembled that of *top2-5 cdc15-2*.

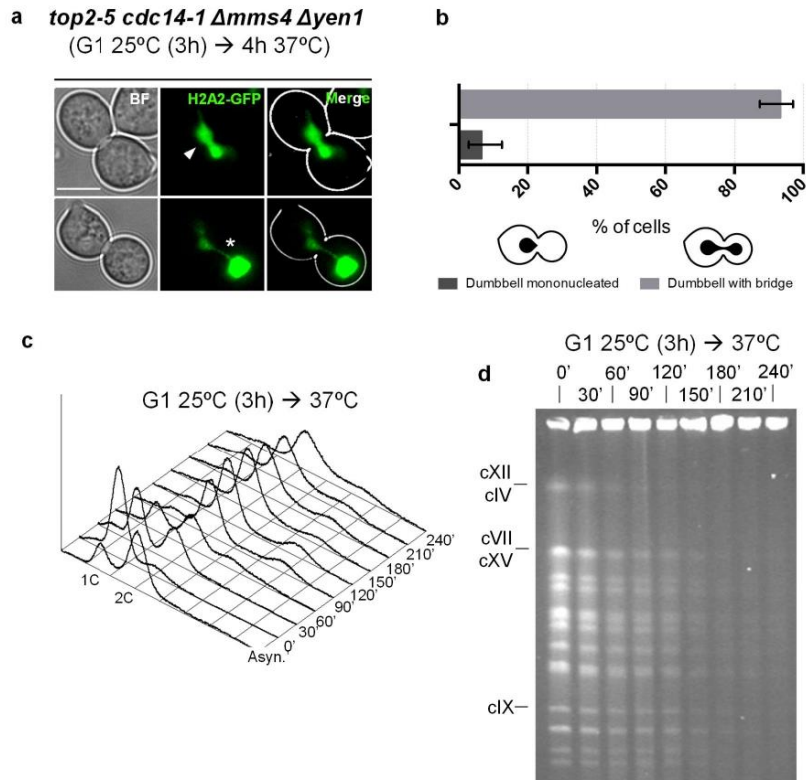


Figure S9. The loss of chromosome integrity in *top2-5* occurs earlier in mutants for the major HR structure-specific endonucleases. A synchronous G1 release experiment was performed for the *top2-5 cdc14-1 Δmms4 Δyen1* strain. **(a)** Micrographs of representative cells 4 h after the G1 release. This strain resembles the previously characterized *top2-5 cdc14-1* anaphase bridge: a mixture of *top2-5 cdc15-2* bridges (arrow), and dumbbells with most of the histone signal in the daughter body (asterisk) [Ramos-Pérez et al. G3 (Bethesda). 7, 3379–3391 (2017)]. The scale bar depicts 5 μ m. BF, bright field. **(b)** Chart of the proportion of the sum of these two phenotypes in the population. **(c)** FACS analysis of the DNA content. **(d)** EtBr staining of whole chromosomes resolved by PFGE. Note how the general chromosome shift starts taking place earlier than in other mutants and growth conditions (at around 60').

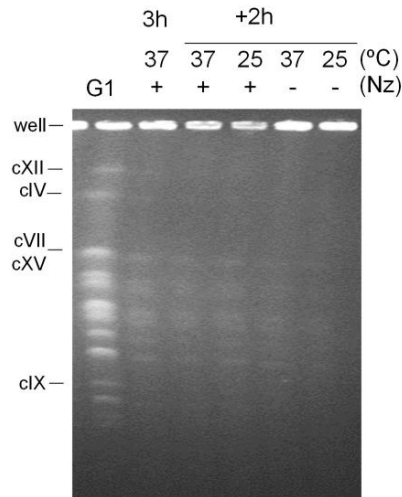


Figure S10. The change in chromosome structure caused by the absence of Top2 is neither modified by previous treatment with Nocodazole nor restored by Top2 reactivation. A synchronous G1 release experiment was performed for the *top2-5 cdc15-2* strain under restrictive conditions (37 °C). At the time of the G1 release, Nocodazole (Nz) was added to depolymerize the spindle and transiently block cells in G2/M. After 3 h, the culture was split in four and incubated for another 2 h. One subculture was kept in Nz and at 37°C; one kept the Nz but was shift back to 25 °C (i.e., re-activate Top2); one was kept at 37 °C while removing Nz; whereas the fourth one was treated to re-activate Top2 (25°C shift) and remove the Nz. The PFGE of all intermediate and end point conditions is shown (the photo has been squeezed 1:2 vertically to fit in the figure). Note that chromosome structural shift was not reverted once established. This experiment relates to those in Figure 5.

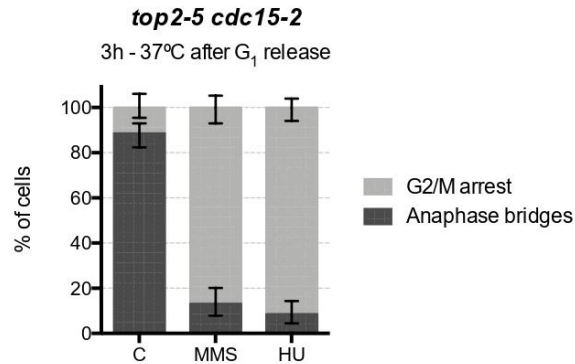


Figure S11. The replication stress checkpoints are functional in the absence of Top2. Synchronous G₁ release experiments were performed for the *top2-5 cdc15-2* strain. At the time of the G₁ release into 37 °C, the culture was split in three. 2M Hydroxyurea (HU) was added to one subculture; 0.01 % w/v MMS to another one; and the third one was incubated without exogenous replication stress (C). Three hours after the G₁ release, samples were observed under the microscope and classified as G₂/M (mononucleated dumbbells) or with anaphase bridges (H2A2-GFP stretched across the dumbbell's neck). Error bars depict 95% confidence intervals.

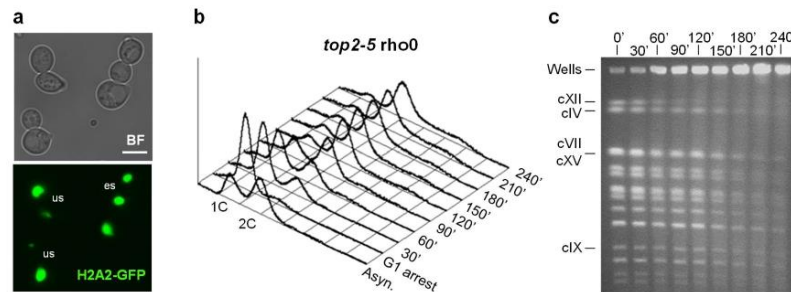


Figure S12. Lack of mitochondrial function does not prevent the PFGE chromosome shift in *top2-5*. A synchronous G₁ release experiment was performed for a *top2-5 [rho0]* strain. (a) Micrograph of representative cells 4 h after the G₁ release. Note the massive uneven segregation events of the H2A2-GFP signal, as in *top2-5* in Figure 1c; us, uneven/unequal segregation; es, even/equal segregation. (b) Flow cytometry (FACS) analysis of the DNA content. Note that, unlike *top2-5* in Figure 1d, the 2C peak remains at later time points, indicating a late anaphase/telophase arrest. (c) Ethidium bromide (EtBr) staining of whole chromosomes resolved by Pulsed-Field Gel Electrophoresis (PFGE). Note how the cXII in-gel signal is first to disappear and the other chromosome bands still get fainter after 150'.

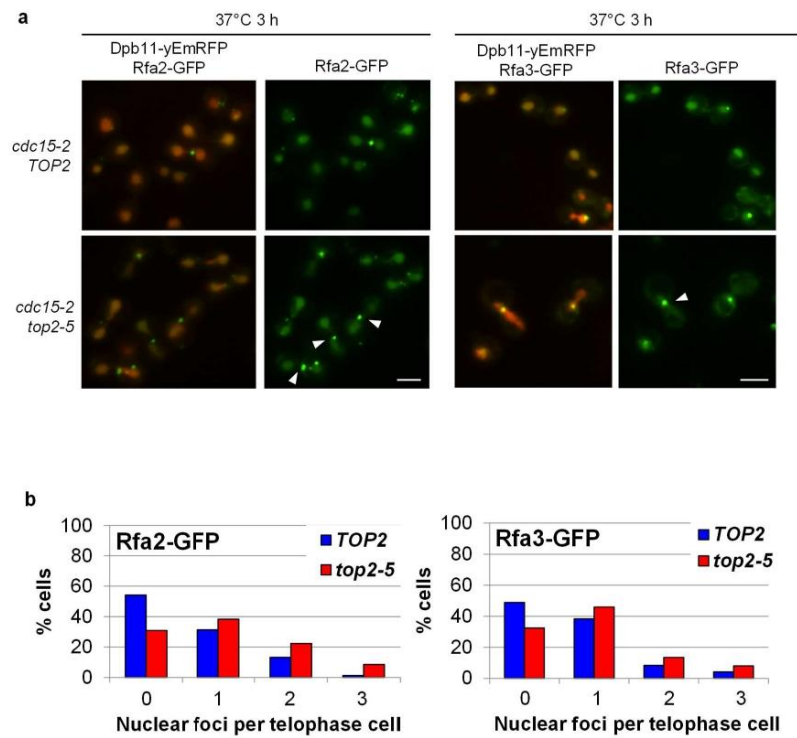


Figure S13. There is more ssDNA in the *top2-5 cdc15-2* telophase block. *TOP2* and *top2-5* strains bearing *cdc15-2*, the ultrafine anaphase bridge marker Dpb11-yEmRFP and one RPA component labelled with GFP (either Rfa2 or Rfa3) were blocked in telophase at 37 °C. (a) Representative micrographs. Note how *top2-5* has more foci and they are more intense. Scale bars depict 5 μ m. Arrowheads point to foci located at anaphase bridges. (b) Quantification of foci number per telophase cell (N>200). See also Table 1.

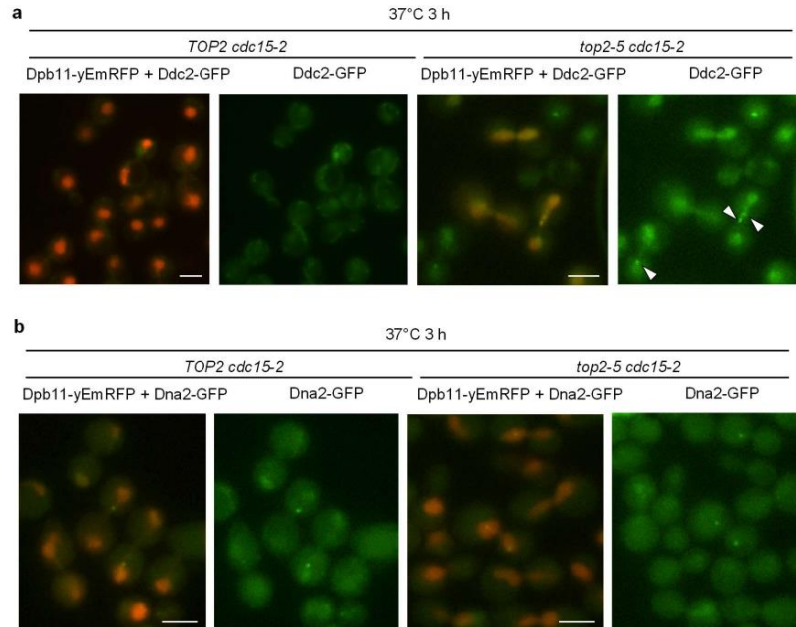


Figure S14. The replication stress marker Ddc2 gets enriched in *top2-5 cdc15-2* telophase nuclei. (a) Representative micrograph of the *TOP2 cdc15-2 DPB11-yEmRFP DDC2-GFP* and *top2-5 cdc15-2 DPB11-yEmRFP DDC2-GFP* strains blocked in in telophase at 37 °C. Note that nuclear abundance of Ddc2 increases in *top2-5*, where it also forms foci. (b) Representative micrograph of the *TOP2 cdc15-2 DPB11-yEmRFP DNA2-GFP* and *top2-5 cdc15-2 DPB11-yEmRFP DNA2-GFP* strains blocked in in telophase at 37 °C. Note that Dna2 forms foci in both telophase blocks, regardless the Top2 activity. Scale bars depict 5 μm. Arrowheads point to foci located at anaphase bridges. See also Table 1.

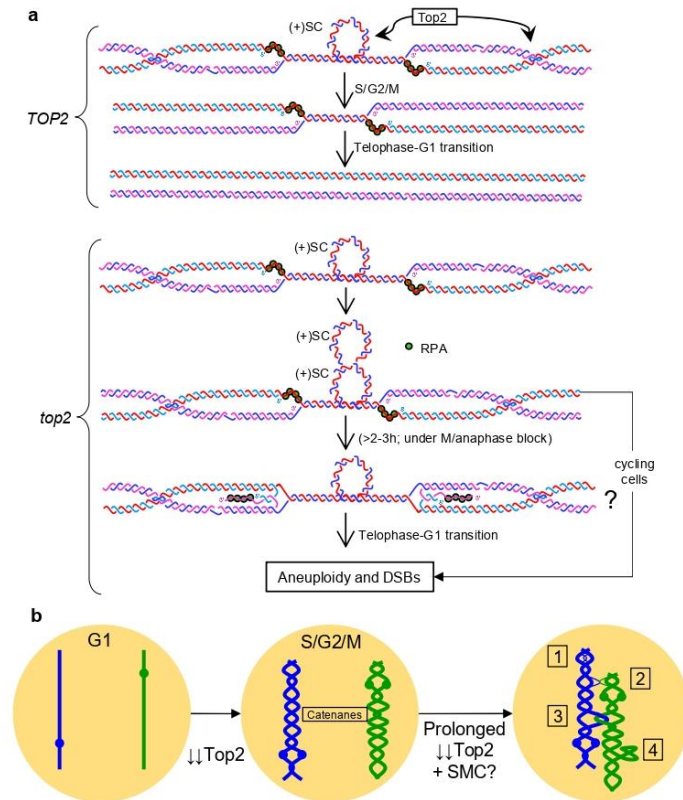


Figure S15. Two putative models of how changes on the chromosome structure occur upon prolonged Top2 deficiency. (a) When replication is ending and two converging forks are approaching, critical positive supercoiling arises ((+)SC) in between and precatenanes behind. Supercoiling interferes with replication completion, especially in difficult-to-replicate regions. Top2 deals with both topological problems, replication can finish, and sister chromatids are resolved for segregation. Part of these regions finish replication during the telophase-G1 transition, according to a recent report. In the prolonged absence of Top2, these regions accumulate an excess of topological problems that shift the chromosome structure so that chromosomes get trapped in a PFGE. Based on previous literature and the findings shown herein, we speculate that an excess of (+)SC may turn into reversed forks, and that these structures, or derivatives thereof, lead to PFGE entrapment. (b) Sister chromatid catenations arise during replication. Without Top2, this class of intertwining persists. Meanwhile, other DNA metabolic processes go on, such as transcription, DNA repair, cohesion and condensation, and these might exacerbate topological problems and other intertwining classes arise: 1, sister chromatid hemicatenanes; 2, chromosome hemicatenanes; 3, inter-chromosome knots; and 4, intra-chromosome knots. Unscheduled re-replication may also contribute to these problems. Both models are not mutually exclusive. RPA, replication protein A complex.

SUPPLEMENTAL TABLES.

Table S1. Strains used in this work.

Strain name	Relevant genotype ^a	Origin
CH326	(S288C) <i>MATa ura3-52 his4-539am lys2-801am SUC2+ top2-5</i>	1
CH325	(S288C) <i>MATa ura3-52 his4-539am lys2-801am SUC2+ top2-4</i>	1
CH335	(S288C) <i>MATa ura3-52 his4-539am lys2-801am SUC2+ TOP2</i>	1
FM1386	CH326; <i>H2A2(YBL003c):GFP:BLEMX; Δbar1::URA3</i>	2
CH325	<i>H2A2(YBL003c):GFP:BLEMX; Δbar1::URA3</i>	2
FM1419	CH335; <i>H2A2(YBL003c):GFP:BLEMX; Δbar1::URA3</i>	2
FM2021	FM1386; <i>cdc15-2:9myc:Hph</i>	2
FM2086	FM1419; <i>cdc15-2:9myc:Hph</i>	2
FM2154	FM1386; <i>cdc14-1:9myc:Hph</i>	2
FM2152	FM1419; <i>cdc14-1:9myc:Hph</i>	2
FM2170	FM2154; <i>Δmms4::natMX4; Δyen1::KanMX4</i>	This work
FM2268	FM2021; <i>Δrad52::KanMX4</i>	This work
FM2305	FM1386 [<i>rho</i> ⁰]	This work ^b
E1670	(W303) <i>MATa ade2-1 trp1-1 can1-100 his3-11,15 leu2-3,112 RAD5 + GAL psi+ura3::URA3/GPD-TK_{TK}</i>	3
FM2128	E1670; <i>cdc15-2:9myc:Hph</i>	This work ^c
FM2129	E1670; <i>top2-5:NAT; cdc15-2:9myc:Hph</i>	This work ^c
FM2241	<i>MATa can1Δ::STE2pr-Sp_his5 lyp1Δ his3Δ1 leu2Δ0 ura3Δ0 met15Δ0 top2-5::natMX</i>	2
ML532	<i>MATa can1Δ::STE2pr-LEU2 lyp1Δ his3Δ1 leu2Δ0 ura3Δ0 TRP1 LYS2 MET15 KanMX:tTA(tetR-VP16)-tetO2-DPB11</i>	4
OQR84	ML532; <i>KanMX:tTA(tetR-VP16)-tetO2-DPB11-yEmRFP; top2-5:NAT; cdc15-2:9myc:Hph</i>	This work ^{c,d}
OQR-TOP2-Xs-GFP (39 strains)	<i>MATa can1Δ::STE2pr-LEU2 lyp1Δ his3Δ1 leu2Δ0 ura3Δ0 MET15 KanMX:tTA(tetR-VP16)-tetO2-DPB11-yEmRFP; TOP2; cdc15-2:9myc:Hph; X-GFP:His3MX</i>	This work ^e
OQR-top2-5-Xs-GFP (39 strains)	<i>MATa can1Δ::STE2pr-LEU2 lyp1Δ his3Δ1 leu2Δ0 ura3Δ0 MET15 KanMX:tTA(tetR-VP16)-tetO2-DPB11-yEmRFP; top2-5:NAT; cdc15-2:9myc:Hph; X-GFP:His3MX</i>	This work ^e

^a Semicolons separate independent transformation events during strain construction. Intermediate strains are omitted.

^b The mitochondrial DNA was eliminated by growing the strain under the presence of ethidium bromide as reported previously in ⁵.

^c The ts alleles were transferred after PCR amplification from strains where they had been tagged downstream with the corresponding markers according to ⁶.

^d The yEmRFP was tagged to DPB11 through an adaptor-mediated PCR fusion methodology described in ⁷.

^e These strains were selected after crossing OQR84 with the GFP tagged collection reported in ⁸, whose basic genotype is *MATa his3Δ1 leu2Δ0 met15Δ0 ura3Δ0 X-GFP(S65T):His3MX* (*X* being the gene of interest). Individual genotypes are omitted for the sake of space. The haploids were selected on minimum media plates supplemented with canavanine, thialysine, G418 and hygromycin, and in the absence of histidine, leucine and methionine. Then, the presence of either *TOP2* or *top2-5:NAT* was checked by nourseothricin sensitivity or resistance, respectively.

SUPPLEMENTAL REFERENCES

1. Holm, C., Goto, T., Wang, J. C. & Botstein, D. DNA topoisomerase II is required at the time of mitosis in yeast. *Cell* **41**, 553–63 (1985).
2. Ramos-Pérez, C. *et al.* Genome-Scale Genetic Interactions and Cell Imaging Confirm Cytokinesis as Deleterious to Transient Topoisomerase II Deficiency in *Saccharomyces cerevisiae*. *G3 (Bethesda)*. **7**, 3379–3391 (2017).
3. Lengronne, A., Pasero, P., Bensimon, A. & Schwob, E. Monitoring S phase progression globally and locally using BrdU incorporation in TK(+) yeast strains. *Nucleic Acids Res.* **29**, 1433–42 (2001).
4. Germann, S. M. *et al.* Dpb11/TopBP1 plays distinct roles in DNA replication, checkpoint response and homologous recombination. *DNA Repair (Amst)*. **10**, 210–24 (2011).
5. Anaissi-Afonso, L. *et al.* Lawsone, Juglone, and β -Lapachone Derivatives with Enhanced Mitochondrial-Based Toxicity. *ACS Chem. Biol.* **13**, 1950–1957 (2018).
6. Smith, J. S. & Burke, D. J. *Yeast Genetics: Methods and Protocols*. **1205**, (Springer New York, 2014).
7. Reid, R. J. D., Lisby, M. & Rothstein, R. Cloning-free genome alterations in *Saccharomyces cerevisiae* using adaptamer-mediated PCR. *Methods Enzymol.* **350**, 258–77 (2002).
8. Huh, W. K. *et al.* Global analysis of protein localization in budding yeast. *Nature* **425**, 686–691 (2003).

Published Online: 12 August, 2022 | Supp Info: <http://doi.org/10.26508/lsa.202101161>
Downloaded from life-science-alliance.org on 18 November, 2022

Research Article



The vacuole shapes the nucleus and the ribosomal DNA loop during mitotic delays

Emiliano Matos-Perdomo^{1,2} , Sílvia Santana-Sosa^{1,2} , Jessel Ayra-Plasencia^{1,2} , Sara Medina-Suárez^{1,2} , Félix Machín^{1,3,4}

The ribosomal DNA (rDNA) array of *Saccharomyces cerevisiae* has served as a model to address chromosome organization. In cells arrested before anaphase (mid-M), the rDNA acquires a highly structured chromosomal organization referred to as the rDNA loop, whose length can double the cell diameter. Previous works established that complexes such as condensin and cohesin are essential to attain this structure. Here, we report that the rDNA loop adopts distinct presentations that arise as spatial adaptations to changes in the nuclear morphology triggered during mid-M arrests. Interestingly, the formation of the rDNA loop results in the appearance of a space under the loop (SUL) which is devoid of nuclear components yet colocalizes with the vacuole. We show that the rDNA-associated nuclear envelope (NE) often reshapes into a ladle to accommodate the vacuole in the SUL, with the nucleus becoming bilobed and doughnut-shaped. Finally, we demonstrate that the formation of the rDNA loop and the SUL require TORC1, membrane synthesis and functional vacuoles, yet is independent of nucleus–vacuole junctions and rDNA–NE tethering.

DOI 10.26508/lsa.202101161 | Received 15 July 2021 | Revised 20 July 2022 | Accepted 20 July 2022 | Published online 12 August 2022

Introduction

One of the most remarkable visual events in cell biology is chromosome condensation, which takes place when cells transit from G2 into the prophase and metaphase (M phase). In higher eukaryotes, chromosomes are condensed over a central scaffold formed by topoisomerase II α , condensin I and condensin II (Paulson et al, 2021). Condensation requires the reorganization of the chromatin fiber into nested loops (Losada & Hirano, 2001; Gibcus et al, 2018; Paulson et al, 2021), so that chromosomes progressively shorten their length while becoming wider. The formation and expansion of these loops continues until chromosomes acquire their characteristic rod-like appearance by late metaphase.

The yeast *Saccharomyces cerevisiae* has served as an instrumental model for understanding fundamental processes of the eukaryotic cell. Its powerful genetic tools enable precise characterization of protein function. Condensin (there is a unique condensin complex in yeast) has not been an exception and has been scrutinized extensively (Strunnikov et al, 1995; Freeman et al, 2000; Lavoie et al, 2000, 2002; Bhalla et al, 2002). However, whereas in higher eukaryotes chromosome condensation is cytologically evident, this is not in yeast, where most of the nuclear mass remains visually amorphous throughout the cell cycle. The only exception to this is the ribosomal DNA (rDNA) array, located on the right arm of chromosome XII (cXIIr), and whose repetitive nature facilitates its visualization by FISH and fluorescence microscopy through specific rDNA binding proteins (e.g., Net1, Fob1, Cdc14, etc.) tagged with GFP variants. Previous studies showed that the rDNA of wild type cells appears unstructured in interphase, with a spotted and diffuse morphology by FISH, referred to as puff, and a crescent/oval shape at the nuclear periphery when labelled with GFP-tagged coating proteins (Guacci et al, 1994; Lavoie et al, 2002; Machín et al, 2005; Shen & Skibbens, 2017; Matos-Perdomo & Machín, 2018). As cells enter G2/M, this disorganized rDNA becomes a highly organized bar-like structure. In cells arrested in the late metaphase (sometimes referred to as mid-M in yeast) by the microtubule-depolymerizing drug nocodazole (Nz), the rDNA bar bends out of the rest of the chromosomal mass to become a horseshoe-like loop. This rDNA loop has been considered a condensed state of the repetitive locus and depends on active condensin for its establishment and maintenance (Freeman et al, 2000; Lavoie et al, 2002, 2004).

Condensin is not the only factor involved in the establishment and maintenance of the rDNA loop. Cohesin, which keeps sister chromatids together until anaphase, and the Polo-like kinase Cdc5 are also involved, yet their role is thought to regulate condensin activity on the rDNA (St-Pierre et al, 2009; Harris et al, 2014; Lamothe et al, 2020). Besides these, we previously reported that the rDNA loop requires an active Target of Rapamycin Complex 1 (TORC1) (Matos-Perdomo & Machín, 2018). TORC1 is the master complex that regulates cell growth and metabolism, controlling anabolic processes in the cell such as ribosome biogenesis, protein synthesis, and lipid synthesis (Wullschleger et al, 2006; Laplante &

¹Unidad de Investigación, Hospital Universitario Nuestra Señora de Candelaria, Santa Cruz de Tenerife, Spain ²Escuela de Doctorado y Estudios de Postgrado, Universidad de La Laguna, Santa Cruz de Tenerife, Spain ³Instituto de Tecnologías Biomédicas, Universidad de La Laguna, Santa Cruz de Tenerife, Spain ⁴Facultad de Ciencias de la Salud, Universidad Fernando Pessoa Canarias, Santa María de Guía, Spain

Correspondence: fmachin@fciisc.es

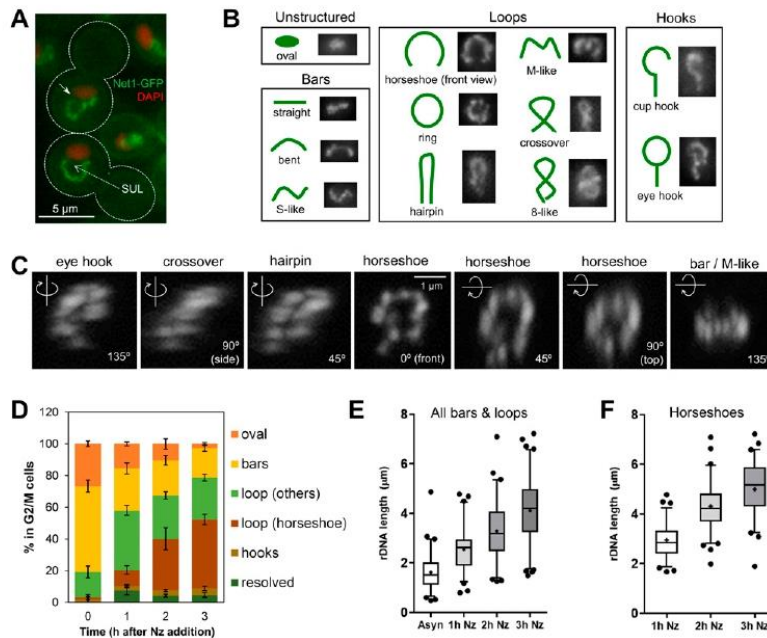


Figure 1. Mid-M ribosomal DNA (rDNA) morphologies.

(A) Prototypical examples of the rDNA loop in the mid-M (nocodazole) arrest. The rDNA is labelled by Net1-GFP and the main nuclear mass by DAPI. The dotted arrow points to the space under the loop (SUL). The white arrow on the upper cell points to a small gap observed sometimes on one flank of the loop.

(B) Morphological patterns of the rDNA. Loops, especially the horseshoe loop, are common in mid-M blocks with Nz. (C) The morphology of the rDNA also depends on the visual perspective. A front view of a horseshoe loop (central image, 0°), captured by confocal superresolution microscopy and reconstructed in 3D from 0.15- μ m-thick z-planes, was rotated on the y-axis (images to the left) or the x-axis (images to the right). (D) Proportion of rDNA morphologies during an Nz time-course experiment (mean \pm SEM; n = 3). (E) Length of rDNA bars and loops during an Nz time-course experiment (n > 100 cells per condition). (F) As in (E) but only measuring horseshoe loops.

be quite stable over the course of short time-lapse video-microscopy (Video 1).

The bases of the rDNA horseshoe loop are the flanking sequences of the rDNA array

We reasoned that the tracts of two twisting threads observed in some loops by CSM may comprise either the cohesed sister chromatids, resolved at 120 nm laterally, or domains of topologically packed/knotted rDNA units. In either case, the horseshoe loop would comprise the two sister chromatids travelling all along its length, with the first and the last unit of the repetitive locus at each edge of the loop (Fig 2E; “a” configuration). Alternatively, these two-thread tracts may expose the two halves of a coiled coil rDNA array (Fig 2B; “b”). In support that the latter (“b”) could occur, we often found small gaps between one edge of the Net1 signal and the DAPI (Fig 1A, arrow). To differentiate between these two models, we combined into a single Net1-eCFP strain two bacterial *tetO*s arrays that we have previously designed to flank the rDNA array; *tetO:450* (rDNA proximal flank) and *tetO:487* (rDNA distal flank). This strain also carries the *tetO*-specific binding protein TetR-YFP. If the rDNA loop comprised an extended array that coils back (“b”), we should see both *tetO*s localizing at the same loop edge. On the contrary, if the rDNA follows the “a” configuration, we should see each *tetO* at each edge of the loop. We observed the “a” configuration in all cases (Fig 2F). This flanking positioning is in agreement with previous FISH data for the rDNA borders at the chromosome XII right arm (cXIIr) (Fuchs & Loidl, 2004). Aside from the frontal views of

horseshoe loops, the “a” configuration for the *tetO:450/487* partner was almost always seen for other rDNA loops and bars.

Similar configuration results were observed for horseshoe loops when we used a partner comprising *tetO:450* and a *tetO:1061*, which localizes near the cXIIr telomere. Even though the *tetO:1061* showed a looser localization, it was often close to the opposite *tetO:450* base (Fig 3A). The distance between the *tetO:1061* and the distal rDNA flank ranged from 0.2 to 4 μ m (Fig S1A). In short time-lapse movies, the *tetO:450* remained immobile and attached to the loop base, whereas the *tetO:1061* moved rapidly and extensively (Video 2). Shorter distances to the nearest rDNA flank were measured for the *tetO:194*, which settles next to the chromosome XII centromere (Fig S1A). However, relative distances (μ m/kbp) were the opposite, as the *tetO:194* is ~200 Kbs away from the proximal rDNA flank, whereas the *tetO:1061* is ~600 Kbs away from the distal rDNA flank (mean relative distances of 0.0025 and 0.0017 μ m/kbp, respectively). The resulting mean apparent compaction ratio was 205 for the centromere-proximal flank tract, and 280 for the distal rDNA flank-telomere tract (Fig S1B). Previously, the axial compaction of chromosome arms in mid-M was estimated to be ~140 (Guacci et al, 1994). This implies that both tracts are probably curly or eventually fold back, especially the distal rDNA flank-telomere tract (Fig S1C; see below for further insights).

Next, we addressed the configuration of the rDNA horseshoe loop relative to the rest of nuclear DNA. To do so, we made use of the histone H2A2 (Hta2) labelled with mCherry to visualize the bulk of the chromatin. A close look at the Net1-GFP Hta2-mCherry strain showed that the Hta2 forms a protruding loop in ~55% of the

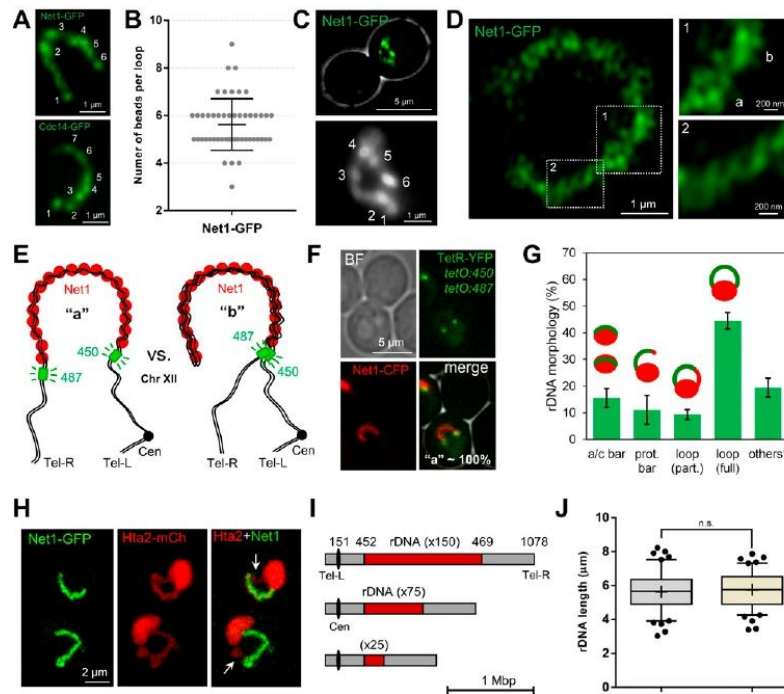


Figure 2. Fine characterization of the mid-M ribosomal DNA (rDNA) horseshoe loop.

(A) The rDNA loop comprises domains with distinctly enriched markers. Examples of rDNA loops with two specific markers: Net1 and Cdc14 (both deconvolved z-stack 2D projections). Numbers indicate counted “beads.” (B) Counted beads for the Net1-GFP rDNA loop ($n = 50$ cells). Central horizontal solid line represents the mean and outer horizontal solid lines represent one SD. (C) The loop and its beads as seen by TIRF microscopy. (D) 120 nm superresolution of the rDNA loop. Inlet “1” features a section with two tight braided threads (“a” and “b”) separated with a constriction. Inlet “2” features a spring-like section. (E) Schematics of two possible and mutually exclusive spatial configurations of the rDNA loop: (a), the loop has two bases, each comprising one of the rDNA flanks; and (b) the loop folds back, having both flanks residing on a single base. The green boxes indicate the *tetO* arrays inserted at 450 (rDNA proximal flank) and 487 (rDNA distal flank). (F) The rDNA loop in a strain with both 450 and 487 *tetO*s, the TetR-YFP and the Net1-ECFP (pseudo-coloured in red). All loops presented the configuration (a). BF, bright field. (G) Quantification of rDNA morphologies (Net1-GFP) relative to the main nuclear mass (Hta2-mCherry) as observed from z-stack 2D projections (mean \pm SEM; $n = 3$); a/c, attached/crossing bar; prot bar, protruding bar. Others* mostly include oval and resolved into two rDNA signals. (H) Examples of partial horseshoe rDNA loops as seen by confocal superresolution

microscopy (Net1 looks like a protruding bar but Hta2 forms a closed handle); white arrows point to where Net1 and the Hta2 do not overlap. (I) Scale drawing of chromosome XII with rDNA arrays bearing different numbers of its basic repetitive unit. The numbers above indicate Saccharomyces Genome Database (SGD) coordinates. (J) Length of rDNA loops from arrays with ~ 75 ($n = 100$ cells) and ~ 25 ($n = 100$ cells) copies.

Nz-blocked cells (Fig 2G). In about four fifth of these horseshoe loops, the rDNA (Net1-GFP) overlapped entirely with the Hta2 loop; however, in one fifth of the cases, the overlapping was partial, suggesting that flanking regions of the rDNA in cXIIr can belong to horseshoe loops (Fig 2H). Single-cell time lapse of these two presentations of the horseshoe loop showed they are interchangeable (Video 3; e.g., nuclei 2, 4, 6, and 13). These, together with the fact that attached/crossed bars ($\sim 15\%$ of all Hta2/Net1 morphologies; Fig 2G) can represent top views of horseshoe loops (Fig 1C and Video 3, nuclei 3 and 15; Video 4, nuclei 3–5), imply that horseshoe loops are even more frequent than what can be observed at first glance in 2D projections. Another $\sim 10\%$ of Nz mid-M nuclei presented a protruding bar-like Hta2/Net1 signal, which appear to be anchored to the bulk of the nuclear mass through one base only, with no visible signs of them being perfect side views of horseshoe loops (yet a bunch of cases could be so; see Video 3, nuclei #5).

The size of the rDNA array does not determine the length of the mid-M rDNA loop

Whereas it is undisputed that the rDNA is highly organized in mid-M, previous studies raised concerns about whether the loop is a

condensed state of the locus, at least from a longitudinal point of view (Sullivan et al, 2004; Machín et al, 2005). We have repeatedly measured loop lengths in a Net1-GFP strain with ~ 150 copies of the 9.137-kbp rDNA unit and obtained mean values of $\sim 5 \mu\text{m}$ (Fig 1F) (Matos-Perdomo & Machín, 2018). This translates into a relative length of $\sim 275 \text{ kbp}/\mu\text{m}$ ($150 \times 9.137/5$). Considering that the length of one bp of naked B-form DNA is 0.34 nm, the estimated axial compaction ratio of the rDNA loop results in ~ 93 (275×0.34). In some instances, the loop reached $\sim 9 \mu\text{m}$ ($\sim 152 \text{ kbp}/\mu\text{m}$; compaction ratio ~ 52) (Matos-Perdomo & Machín, 2018). Hence, the rDNA loop actually appears less compacted than a normal chromosome arm.

We questioned whether the loop length could be shortened by reducing the number of units of the rDNA array. We analyzed the rDNA length in two strains with the rDNA size fixed at around 75 and 25 copies (Figs 2I and S2A and B). This was achieved through the deletion of the *FOB1* gene, responsible for the change in size of the array (Kobayashi et al, 1998). Both strains were blocked in mid-M and the length of their rDNA loops was measured. We found no differences in their lengths (Figs 2J and S2C). The length was also equivalent to that of a ~ 150 copies rDNA (Fig 1E) (Matos-Perdomo & Machín, 2018). This implies that the compaction ratio of the rDNA can be lowered to, at least, ~ 10 (a loop of 25 copies reached $7.9 \mu\text{m}$ [$0.34 \times 25 \times 9.137/7.9$]). Theoretically, this packing ratio is close to



frontal views of horseshoe loops (Fig 3A, see saturated TetR-YFP images, and Fig S3A). We hypothesized that this space may comprise other parts of the nucleolus, which could be somehow free of the TetR, perhaps through liquid–liquid phase separation (Feric et al, 2016; Matos-Perdomo & Machín, 2019). However, we found neither rRNA-processing proteins (Fig S3B) nor RNA (Fig S3C). In both cases, the mid-M arrest made these markers adopt a horseshoe-like morphology as well. Alternatively, the SUL could be filled up by part of the nucleus devoid of freely circulating proteins; for instance, heterochromatinized DNA. However, we did not find histone-coated (Hta2-mCherry) DNA, DAPI (after overexposing), or ultrasensitive YOYO-1 DNA stain within that space (Fig S3D and E).

In light of these negative labelling, we next questioned whether the SUL was nuclear. For addressing this, we added a third fluorescent marker to the previous set of strains, the ER membrane translocator Sec61, which labels the perinuclear ER, this being a continuum with the outer nuclear membrane of the nuclear envelope (NE). We found that the Net1 loop was surrounded both externally and internally by Sec61 (Figs 3B and C and S3F; see also Video 5 for a full appreciation of the spatial orientation of the second example). A similar pattern was obtained when an EGFP-NLS replaced TetR-YFP as the nucleoplasm reporter (Fig 3D). This was further confirmed by another NE marker, the nuclear pore complex (NPC) protein Nup49. Nup49 is more specific for the NE than Sec61, but its labelling shows a punctate distribution and is more challenging to interpret (Belgareh & Doye, 1997). Nonetheless, we could confirm that Nup49 labels the internal face of the loop as well (Figs 3E and S3G and H). To get further support for the claim that the SUL is not nuclear, we performed transmission electron microscopy (TEM). We found examples where the nucleus appears as a handbag, with a thin handle surrounded by a double membrane, and with the electrodense nucleolus close to or within this handle (Figs 3F and S3I).

The nucleoplasm labelling with both TetR-YFP and EGFP-NLS pinpointed that the nucleus is arranged as a ring-shaped doughnut, with a tendency to asymmetrically distribute the nucleoplasm towards a bulge, where most of the non-rDNA chromatin resides (Fig 3A–D). Frequently, a constriction in the bulge was evident (Fig S3J), which can be deep enough to separate the nucleoplasm signal in two (Fig 3G). 2D projections and 3D reconstructions of the NE (Sec61 and Nup49) showed that in these cases the bulge is made up of two lobes that overlap to various degrees (Figs 3H and S3J and K and Video 6). In addition, in most 3D reconstructions (80%; 16 of 20), the Sec61 signal distributed in depth as a hemisphere in the SUL (Fig 3I and Video 6, top two cells), suggesting that the NE (or the ER) could be ladle-shaped in lateral views, in addition to being doughnut-shaped in frontal views. This ladle was also seen with Nup49, which supports that it is made up of NE; however, Nup49 was much less abundant there, pointing out that NPCs may have restrictions to access the ladle (Fig S3H, arrows).

The space under the rDNA loop is occupied by the vacuole

After realizing that the SUL was not nuclear, we added a cytosolic EGFP to a Sec61-eCFP Net1-mCherry strain to confirm the SUL was cytosolic. To our surprise, the EGFP signal was weaker in the SUL (Fig 4A). A key hint to understand the nature of the SUL came from the

visual comparison of the Net1 loop and the Hta2 handle with the entire mid-M cell as seen through the transmission light (bright field). We noticed that most large horseshoe loops appear to either entirely or partially surround the vacuole, which otherwise appears to sit on these loops in partial side views (Fig 4A–C). Hence, we checked whether the vacuole was occupying the SUL. We used several specific vacuolar markers, including the vacuolar lumen vital dyes Blue CMAC and carboxy-DCFDA, the vacuolar membrane (VM) non-vital dye MDY-64, and the VM marker Vph1-GFP. In all cases, at least one vacuole co-localized with the SUL (Figs 4D–I and S4A–D). There were instances where the co-localization of the SUL from a front view horseshoe loop and a sole vacuole was almost perfect, whereas in other cases the vacuole was too large for the SUL, or the SUL was filled with multiple smaller vacuoles (Fig S4A). VM markers such as Vph1-GFP gave the best signal at the equatorial central plane, which in large vacuoles was in a different z plane relative to frontal views of the rDNA horseshoe loop, making them to appear as if they were crossing the vacuole in 2D z-stack projections (Fig 4D). However, 3D reconstructions showed that part of the vacuole was sitting on the SUL (Fig 4G and H). With smaller vacuoles, at least one of them occupies the SUL (Figs 4E and I and S4A–D). Z-stack imaging, fluorescence intensity profiles and orthogonal projections of the vacuolar lumen confirm that the SUL was indeed occupied by these small vacuoles (Figs 4I and S4B–D).

The rDNA horseshoe loop stems from small rDNA loops and bars that grow and bend around vacuoles

Next, we focused on the origin of the horseshoe rDNA loop with the vacuole in the SUL. To do so, we performed both time-course experiments and time-lapse video-microscopy after Nz addition. We observed that in an asynchronous population, most nuclei were spherical or slightly oval in cells transiting through S/G2/M (counting only the pre-anaphase budded cell subpopulation) (Figs 5A and S5A). Of note, in ~20% of these S/G2/M cells, the nucleus may appear squeezed between the vacuole and the plasma membrane, as if the NE is a malleable body that must seek allocation between two other stiffer bodies, the vacuole and the cell wall (Fig S5A, S/G2/M example). Shortly after Nz addition, budded cells elongate their nucleus (Fig 5A and Video 7), and this occurred with different degrees of symmetry in relation to the amount of nucleoplasm present along the extended nucleus (from pool noodles to finger-like projections; Fig S5B–G) and could carry or not primordial constrictions, which makes nuclei look like cashew nuts (Fig 5B, Video 7 and Video 8, and Fig S5B–F). These nuclear constrictions indicate that bilobulation could be a primordial event in the reshaping of the nucleus in Nz.

Nuclear elongation and constriction presentation could occur in two axes relative to the rDNA. The first and more abundant axis entails the spatial separation of the rDNA/nucleolus from the rest of the nuclear material, with the rDNA on one side or lobe (Fig 5B, upper two cells; Fig 5C and Video 7 and Video 8, upper cell). This configuration of having the nucleolus into protruding nuclear fingers/lobes was also confirmed by TEM (Fig S5B), and is in full agreement with the nucleolus-containing NE “flare” previously described by the Cohen-Fix’s laboratory (Campbell et al, 2006; Witkin et al, 2012). In its early presentation, the rDNA often appears

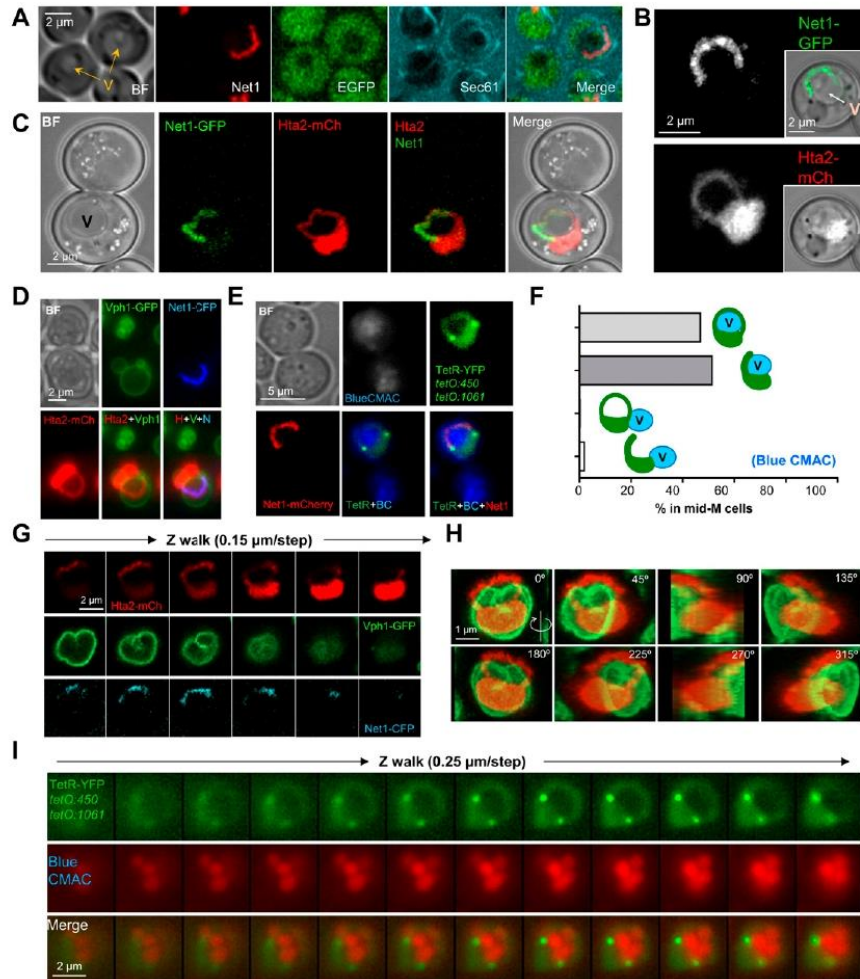


Figure 4. The space under the ribosomal DNA (rDNA) loop is occupied by vacuoles.

(A) Cytosolic EGFP weakly stains the SUL. The strain also bears Sec61-eCFP and Net1-mCherry to delimit the SUL (black holes within cell bodies). In the BF, vacuoles (V, pointed by arrows) may appear as balls of different density. Note how SULs and vacuoles colocalize. (B, C, D, E, F, G, H, I) Vacuoles reside in the SUL. (B) The rDNA loop (Net1-GFP and Hta2-mCherry handle) partly surrounds the vacuole (V), pointed with the arrow in the inlet BF image. (C) An example in which the vacuole (V in the BF) sits on a horseshoe loop. (D) A horseshoe loop, too small to engulf the vacuole (labelled with the vacuole membrane reporter Vph1-GFP), appears to cross the organelle in z-stack 2D projections. (E) Vacuole content (labelled with the vacuolar lumen vital dye Blue CMAC) is found in the SUL. (F) For a representative experiment as in (E), quantification of colocalization (for SUL) or juxtaposition (for nuclear flares) of rDNA bars and loops with vacuoles. Nuclear extensions (“flares”) may correspond to either SUL side views or early stages before SUL formation (see below). (G) A walk through z planes of a horseshoe loop with a large vacuole on top. (H) A 3D reconstruction of (G) with serial 45° anticlockwise rotation on the y-axis. Note how the horseshoe loop leans onto the vacuole. (I) Z-plane walk-through of a TetR doughnut-like nucleus where vacuole lumens have been stained with Blue CMAC. In micrographs: BF, bright field; V, vacuole; BC, blue CMAC.

packed (oval or any of the small loop morphologies). However, as the nucleus becomes enlarged, this rDNA loop gets larger as well, either blooming into a horseshoe loop (compare the upper cell of Fig 5B with Fig 3C and Video 5; Video 9 for horseshoe bloom) or recoiling entirely one flank of cXII to become a protruding bar (see below for a detailed description of the latter).

The second axis of elongation leads to the formation of an rDNA bar that goes across the extended nucleus (Fig 5B and Video 8, lower cell). More evolved morphologies observed later in Nz suggest that these nuclei continue growing in length while bending, eventually forming a nucleoplasmic bridge that connects the two lobes (also as inferred from Video 7, lower cell). The rDNA is mostly

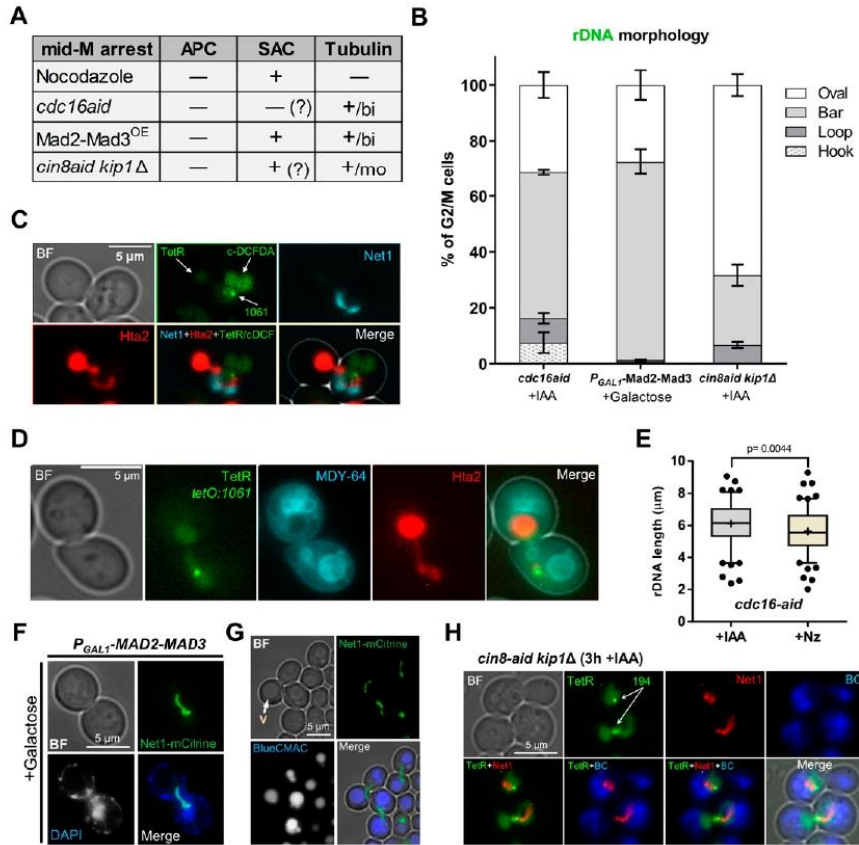


Figure 6. The ribosomal DNA (rDNA) in mid-M arrests that preserve the microtubules. (A) Summary of the differences between four mid-M arrests (Nz, depletion of Cdc16, overexpression of the Mad2-Mad3 chimera, and depletion of kinesin motor proteins Cin8 and Kip1). APC, anaphase-promoting complex; SAC, spindle assembly checkpoint; OE, overexpression. The plus sign indicates either active (APC, SAC) or present (spindle); the minus sign indicates the opposite; the question mark indicates that the corresponding activation state is assumed, but there are contradictory data in the literature; bi, bipolar spindle; mo, monopolar spindle. (B) Morphology of the rDNA after the non-Nz mid-M arrests (mean ± SEM, n = 3). (C, D) Representative micrographs of the mid-M arrest observed after depleting Cdc16-aid. (C) An example with labels for the bulk of chromatin (Hta2), the rDNA (Net1), the nucleoplasm (free TetR-YFP), the cXIIr telomere (*tetO:1061*) and the vacuolar lumen (c-DCFDA). In the green channel, the three latter structures are labelled and differentiated by intensity and morphology; nucleoplasm is the weak signal on the left, the cXIIr telomere is the spot, and the vacuolar lumen is the stronger signal on the right. (D) Like in (C) but with the vacuolar membrane labelled with MDY-64. The strain is the same, but Net1-CFP is completely masked by the much stronger MDY-64 signal. Note in both examples the nuclear disposition across the neck, with the rDNA and the bulk of the DNA mass residing in different cell bodies, and how the rDNA interacts with vacuoles in the receiving body. (E) Length of the rDNA (Net1) in Cdc16-aid plus IAA (>100 cells) versus Cdc16-aid plus Nz (>100 cells). (F, G) Representative micrographs of the neck-crossing rDNA bars observed after overexpressing Mad2-Mad3. (F) Net1 together with DAPI staining. (G) Net1 together with BC staining. (H) Representative micrograph of the mid-M arrest observed after depleting Cin8-aid in a *kip1Δ* background. The upper cell shows a case where the nucleus and the rDNA remain in the same cell body; note that there is no horseshoe loop. The lower cell shows a neck-crossing rDNA bar, as in other non-Nz mid-M arrests. In micrographs: BF, bright field; V, vacuole; BC, Blue CMAC.

the morphological patterns described above. As stated, the horseshoe rDNA loop is the most remarkable morphology of the rDNA array in mid-M, but protruding rDNA bars are observed as well in 10% of the arrested cells (Figs 2G and 5B, mid cell). These protruding bars often contained a brighter Hta2 spot at the tip (Fig 5F, arrow), which must correspond to one of the flanks of cXII, probably up to the corresponding telomere. To precisely determine the arrangement of the chromosome in these protruding bars, we looked at the location of the four *tetOs* along cXIIr (Fig 5G). We

observed that the distal flank of the rDNA (*tetO:487*) tended to be significantly present in the nuclear projections (~65% of the cases, mostly in an apical position), although in ~18% of the bars we found the proximal flank (*tetO:450*) in there; and even the centromere in ~10% of bars. The fact that the distal rDNA flank was more frequently found than the proximal flank suggests that distal cXIIr regions are more prone to get into the growing extension. Compared with the rDNA distal flank, we found fewer examples of the cXIIr telomere (*tetO:1061*) in the projection, strongly pointing out that about half of

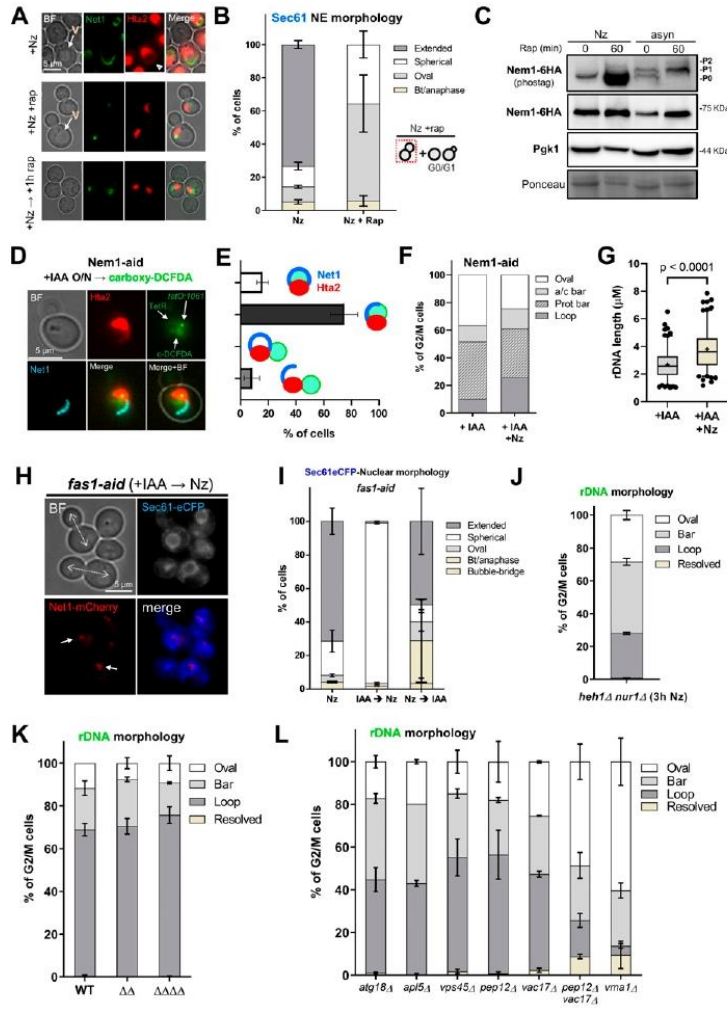


Figure 7. The ribosomal DNA (rDNA) loop requires TORC1, membrane synthesis and functional vacuoles.

(A, B) Rapamycin prevents formation and maintenance of the rDNA loop in Nz-treated cells.

(A) Representative cells upon Nz alone, Nz plus rapamycin co-treatment, and 1 h rapamycin after a previous Nz mid-M arrest. The arrowhead points to the Hta2 handle in the Net1 horseshoe loop in Nz alone. **(B)** Morphology of the NE (Sec61) in Nz and Nz plus rapamycin (mean ± SEM; n = 3; only mid-M cells counted). **(C, D, E, F, G)** Over-synthesis of NE leads to nuclear and rDNA extensions morphologically distinct to those observed in Nz mid-M arrest. **(C)** Western blot of Nem1-6HA under Nz alone and Nz followed by 1 h rapamycin. An equivalent rapamycin regime over an asynchronous culture was performed as well for reference. The position of the three expected bands is indicated in the electrophoresis run with Phos-tag (top image). The others were standard SDS-PAGE controls. **(D)** A representative G2/M cell in asynchronous cultures growing with a depleted Nem1. Note it comprises a seeming protruding bar, which is actually a closed cXIIr loop as deduced from the cXIIr telomere position, into a finger-like flare nuclear projection. Five subcellular structures are labelled: the bulk of chromatin (Hta2), the rDNA (Net1), the nucleoplasm (free TetR-YFP), the cXIIr telomere (tetO:1061), and the vacuolar lumen (c-DCFDA). In the green channel, the three latter structures are labelled and differentiated by intensity and morphology; nucleoplasm is the weak signal on the top that colocalizes with Hta2, the cXIIr telomere is the spot, and the vacuolar lumen is the stronger signal underneath. **(E)** Quantification of rDNA morphology (loop versus bars) and vacuole juxtaposition in asynchronous cells with depleted Nem1 (mean ± SEM; n = 3). **(F)** Quantification of rDNA morphologies in a representative experiment where Nz was added to cells depleted of Nem1. Note that the proportion of loops doubled after Nz, yet it does not reach that of Nz alone (from 40% to 70% in other Nz experiments in this work). **(G)** Length of the rDNA loops and bars in cells depleted of Nem1 before and after Nz addition. Note the additive Nz effect. **(H, I)** Depletion of the fatty acid synthetase beta subunit Fas1 prevents nuclear extension upon Nz treatment. **(H)** Representative micrograph with two mid-M cells (whose polar axes are indicated by double dotted arrows in the BF) in which the NE is round and the rDNA are small bent bars (white arrows). **(I)** Morphology of the NE (Sec61) in Nz (control), IAA → Nz (establishment) and Nz → IAA (maintenance) (mean ± SEM; n = 2; only mid-M cells

counted). **(J)** Quantification of the rDNA morphology in the Nz mid-M arrest in a mutant that does not tether the rDNA to the NE (mean ± SEM; n = 2). **(K)** Quantification of rDNA morphologies upon Nz in mutants for nucleus-vacuole junctions (mean ± SEM; n = 2). Nucleus-vacuole junction mutants: $\Delta\Delta$, $mdm1\Delta$, $nvj1\Delta$, $nvj2\Delta$, $nvj3\Delta$ quadruple mutant. **(L)** Quantification of the rDNA morphology in the Nz mid-M arrest in mutants that affect vacuole size, inheritance, and function (mean ± SEM; n = 2). In micrographs: BF, bright field; V, vacuole.

the rDNA protruding bars are still cXIIr loops (likely side views of the partial rDNA loops we reported in Fig 2G and H). However, as Nz incubation goes by, the cXIIr telomere did move to the tip (Fig 5H and I). Remarkably, these rDNA bars, and their surrounding nucleoplasmic flares, showed extensive bending, which were clearly reminiscent of incomplete states of the horseshoe loop and the overlapping bilobed nucleus described above (Fig 5I, left nucleus; Fig S5C and G); there were also cases where the protruding bar crossed the neck into the bud (Fig 5I, right nucleus).

The horseshoe rDNA loop requires the absence of microtubules

Previous works demonstrated that nuclear extensions and flares are characteristic of cells blocked in mid-M (Witkin et al, 2012). Nz is the most common experimental tool to achieve the mid-M arrest. Nz depolymerizes microtubules, which dismantles the spindle apparatus and activates the spindle assembly checkpoint (SAC) (Jacobs et al, 1988; Hoyt et al, 1991). With an active SAC, the anaphase-promoting complex (APC) activator Cdc20 is tightly bound and inhibited by the SAC components Mad2 and Mad3



(Peters, 2006; Musacchio & Salmon, 2007). Considering the effect of Nz on microtubules and the SAC, we next chose to study the effect of arresting cells in mid-M by other means. We planned two different strategies that preserved the bipolar spindle, yet they differ in the activation state of the SAC (Fig 6A). On the one hand, we depleted Cdc16, an essential component of the APC, by creating a *cdc16-aid* conditional allele. We used this strategy because thermosensitive alleles require incubation at 37°C, and we and others previously showed that this triggers a mild heat stress response that impinges on the rDNA loop (Shen & Skibbens, 2017; Matos-Perdomo & Machín, 2018). Degradation of Cdc16-aid can be triggered by adding the auxin indole-3 acetic acid (IAA) to the medium (Fig S6A and B) (Nishimura et al, 2009). Under this condition, the APC can be inactivated without interfering with the spindle and/or the SAC, although there is a report about a possible activation of the SAC upon APC inactivation (Lai et al, 2003). On the other hand, we made use of another strain carrying a *P_{GAL1}-MAD2-MAD3* construction, which overexpresses a fusion protein of these two key SAC players (Mad2-Mad3^{OE}), yielding an active SAC in galactose. Under this condition, the active SAC maintains the mid-M arrest by keeping the APC inactive (Lau & Murray, 2012; Thadani et al, 2018).

We observed a general pattern that was shared by both non-Nz mid-M strategies, and that greatly differed from Nz-arrested cells. Despite an organized bar-like rDNA (Net1-GFP) was seen in all conditions, the horseshoe loop was largely absent and, instead, either a straight bar or a hook that crossed the bud neck orientated in the chromosome division axis (polar axis) was the major outcome (Figs 6B–F and S6C and D). This shift in the rDNA morphology was not a consequence of the newly introduced alleles, as Nz still leads to horseshoe loops in these strains (Fig S6C and E). Importantly, the crossing bar and the hook appear to bend to interact with and wrap around vacuoles in the second body (either the mother or the bud) (Fig 6C, D, and G). The rDNA length was slightly larger in the *cdc16* crossing bars than in the Nz horseshoe loops, pointing out that the rDNA is even more stretched in such configuration (Fig 6E). In the *P_{GAL1}-MAD2-MAD3* strain, the bar was shorter (Fig S6F); however, this was due to the incubation with galactose, as Nz-induced horseshoe loops were also shorter in galactose (Fig S6G).

In addition to these two strains, we included a third approach to arrest cells in mid-M, while keeping polymerized microtubules. This was based in a *cin8-aid kip1Δ* strain; Cin8 and Kip1 are partly redundant kinesins required for the assembly of the mitotic spindle (Singh et al, 2018). Unlike the previous strains, which are able to form a bipolar spindle, depletion of both kinesins renders cells with a monopolar spindle (Fig 6A). Thermosensitive *cin8 kip1* double mutants have been shown to arrest in mid-M at the restrictive condition (Hoyt et al, 1992; Roof et al, 1992). *Cin8-aid* can be efficiently depleted with IAA (Ayra-Plasencia & Machín, 2019), and we accordingly found that this leads to a similar mid-M arrest (Fig S6H). In terms of the relative position of the nucleus, this arrest was intermediate between what was observed for *cdc16* and Mad2-Mad3^{OE} and what was seen with Nz, that is, ~45% of cells had a nucleus tightly stretched across the neck (bow-tie phenotype), with the rDNA oriented in the polar axis, and ~35% had the nucleus entirely in one cell body (Figs 6H and S6H). Remarkably, horseshoe loops were scarcely present, even in cells where the nucleus

locates in a single cell body as in Nz (Fig 6B, last bar; and Fig 6H, upper cell).

We conclude that the absence of microtubules is a prerequisite to acquire the horseshoe rDNA loop. However, the mid-M arrest is sufficient to change the rDNA morphology into an organized bar.

The rDNA protrusion and the nuclear extension depend on active TORC1 and membrane phospholipid synthesis

We have previously shown that conditions that inactivate TORC1 dismantle the rDNA loop (Matos-Perdomo & Machín, 2018). Intriguingly, many reports have demonstrated that TORC1 inactivation activates autophagy, including nucleophagy, thereby promoting the nuclear-vacuolar interaction (Kvam & Goldfarb, 2007; Dawaliby & Mayer, 2010). According to the results shown above, it appears counterintuitive that the horseshoe rDNA loop is absent when the influence of the vacuole on the nucleus should be maximum. To get further insights, we studied the rDNA and nuclear mass morphologies in cells transiting through stationary phase, when TORC1 activity is expected to be low, autophagy high, and most cells appear swollen and with a large vacuole compressing the rest of the cell organelles. In this condition, the rDNA (Net1-GFP) was hyper-compacted, and its structure was barely modified by the vacuole (Fig S7A). Moreover, we could not observe any histone (Hta2-mCherry) handles. The addition of Nz did not change this pattern, demonstrating that Nz only elicits its effects on the rDNA in growing cells, when Nz leads to the mid-M arrest.

Next, we studied the effect of rapamycin addition, a well-known inhibitor of the TORC1 (Heitman et al, 1991; Barbet et al, 1996; Urban et al, 2007). For this, we compared an Nz arrest to both a concomitant Nz plus rapamycin treatment and adding rapamycin to cells previously arrested in Nz. On the two latter, we found that the rDNA morphology was mainly oval without histone handles (Figs 7A and S7B). Alternatively, some mini-loops/handles of Net1/Hta2 (<2 μm) were also visible (Fig 7A, +Nz → rap condition), as we have shown before (Matos-Perdomo & Machín, 2018). We showed above that horseshoe loops and bars are associated with extended nuclei, as seen by rDNA, histone, and NE markers. Thus, we studied nuclear morphology under Nz treatment and TORC1 inhibition by following the NE shape with Sec61-eCFP. In growing cells, most nuclei appear either spherical or oval shaped (Fig S5A and D), except in those cells transiting M phase where the nucleus is stretched along the mother-daughter axis. In such cases, two morphologies are distinguished. The first one is bow-tie shaped, which is shared by cells that are in the late metaphase and early anaphase (Dotiwala et al, 2007). The second one is dumbbell shaped and corresponds to cells in late anaphase. Upon Nz treatment, the NE appears extended, but rarely in the mother-daughter axis (Figs 7B and S5D and E). However, under Nz plus rapamycin the nuclear morphology was mainly spherical/oval again (Fig 7B). Similarly, cells in stationary phase presented a spherical/oval morphology and, once again, the addition of Nz did not change this pattern (Fig S7C).

In a mid-M block, phospholipid synthesis is unabated, and the nuclear membrane expands around the region that contains the nucleolus (Campbell et al, 2006; Witkin et al, 2012). Several lines of evidence pinpoint the Nem1-Spo7/Pah1 complex as a central player



for the control of nuclear membrane expansion. This complex is involved in the balance between membrane phospholipids during growth conditions and lipid droplets during starving conditions; an active Nem1-Spo7/Pah1 complex shifts the balance towards the latter (Siniouoglou et al, 1998; Pascual & Carman, 2013). TORC1 regulates the activity of Nem1-Spo7/Pah1 by keeping Nem1 unphosphorylated and inactive, so that the phospholipid synthesis is favored (Dubots et al, 2014). Accordingly, Nem1-Spo7/Pah1 mutants display nuclear flares and extensions in growing cells (Santos-Rosa et al, 2005; Campbell et al, 2006). For this reason, we studied the phosphorylation status of Nem1 under Nz treatment and TORC1 inhibition. We arrested cells in either Nz alone or Nz followed by rapamycin addition for 1 h, and further compared these conditions with rapamycin treatment in asynchronous cultures (Fig 7C). We observed the same pattern of major phosphorylation shifts that have been described before in asynchronous exponentially growing cells: two bands, P0 and P1, and a third band, P2, after rapamycin addition (Dubots et al, 2014). Strikingly, only the P0 band was seen in Nz. This un(hypo)phosphorylated state suggests a strong Nem1 inhibition in Nz, which was modified only modestly by rapamycin, either after or concomitant to Nz addition (Figs 7C and S7D and E).

Next, we studied the nuclear and rDNA morphologies in cells depleted of Nem1. Instead of using a knockout mutant, we chose a *nem1-aid* allele (Fig S7F), so that we could control when to elicit NE elongation, and thus avoid carryover effects on the nuclear shape during many generations. We found that an overnight culture (~6 generations) with IAA was sufficient for G2/M nuclei in growing cells to exhibit finger-like nucleolar extensions (flares), in agreement with previous reports (Siniouoglou et al, 1998; Witkin et al, 2012). However, this morphology was more fixed than the plethora of morphologies described above for Nz mid-M arrests. In particular, horseshoe loops were seen in less than 20% of G2/M cells and, instead, protruding bars were the main morphological pattern (Figs 7D-F and S7G). Bars and loops were also shorter than in Nz (Fig 7G; mean length of ~2.5 μ m). However, protruding bars turned out to be thicker, and there were examples in which they could be distinguished as hairpin loops (Fig S7G). The position of the *cXIIr* telomere in the nuclear mass further confirmed that these *nem1* protruding bar are in fact rDNA/*cXIIr* loops. This indicates that *nem1* forms rDNA loops that are retrained to blossom into horseshoes. This was partly confirmed as Nz addition doubled the presence of horseshoe loops as well as the overall length of loops and bars (Fig 7F and G). Whether open horseshoe or closed hairpin loops, vacuoles were principally juxtaposed to *nem1* flares as well (Fig 7E).

The fact that the rDNA was always found in the nuclear extensions seen in both Nz and *nem1*, raised the question of whether NE tethering of the rDNA was a prerequisite for this phenotype. Thus, we checked both rDNA morphologies and colocalization with nucleoplasm extensions in the *nur1 Δ heh1 Δ* double mutant, in which rDNA-NE tethering is compromised (Mekhail et al, 2008). We still observed loops and bars (Figs 7J and S7L). The overall proportion of the sum of loops and bars was equivalent to that of the wild type strain, although horseshoe loops were less frequent. They both were found within nuclear extension, including finger-like flares, in 62% of all bars and loops. We did not observe extensions without the rDNA; hence, the rDNA-NE tethering is a prerequisite for neither

the presence of nuclear extensions nor the rDNA being in these extensions.

In addition to addressing the effects of an excess in phospholipids for membrane synthesis, we decided to investigate the consequences of a defect in these lipids on the phenotypes described here. It has been shown that mRNAs encoding lipogenic enzymes (Acc1, Fas1 and Fas2), all involved in fatty acid synthesis, increased in G2/M (Blank et al, 2017b). Previous studies have also shown that biosynthesis of fatty acids is necessary for the extension of the nuclear membrane (Witkin et al, 2012; Walters et al, 2014, 2019; Male et al, 2020). Thus, we drew our attention to fatty acid synthesis and its relation to nuclear membrane growth in Nz. We made a Fas1-aid chimera and tested both NE (Sec61-eCFP) and rDNA (Net1-mCherry) morphologies when Fas1 was depleted before Nz addition. Degradation of Fas1-aid in IAA was partial (~66% drop in protein levels; Fig S7H and I); however, this was sufficient to prevent NE extensions upon Nz addition (Fig 7H and I). In these round nuclei, neither horseshoe loops nor protruding bars were observed, with the rDNA mostly seen as extremely short bars and loops (Fig 7H, white arrows). When Fas1 depletion was triggered after the Nz mid-M arrest, most mid-M cells maintained an extended nucleus (Fig 7I, subtracting bow-ties and anaphases), implying that lipid biosynthesis is required to attain the NE expansion in mid-M arrests but not for its maintenance. Finally, we corroborated these findings by using cerulenin, a specific inhibitor of fatty acid biosynthesis (Inokoshi et al, 1994). We treated cells with cerulenin, 1 h before the addition of Nz, which also resulted in spherical nuclei (Sec61-eCFP) and compacted Net1-mCherry signals (Fig S7J). Incidentally, we also observed for both Fas1 depletion and cerulenin more spherical NE morphologies within the bow-tie subgroup (Fig 7I and S7J and K, “bubble bridge”), suggesting a stiffer NE when fatty acid biosynthesis is inhibited.

The rDNA loop does not depend on known nuclear–vacuolar interactions

From our previous results, the shape of the malleable NE appears to be highly influenced by the stiffer vacuole. When the NE becomes enlarged in mid-M blocks, the vacuole serves as a template on which the extended NE bends around. In this context, the length of the rDNA in protruding bars and horseshoe loops may depend on how intimate the nuclear–vacuole relationship is. For this reason, we decided to study the role of the nucleus–vacuole junctions (NVJs) in the morphology of the rDNA. The NVJs are formed through the formation of Velcro-like interactions between the vacuolar protein Vac8 and the outer nuclear membrane protein Nvj1, which mediate piecemeal microautophagy of the nucleus (Pan et al, 2000; Roberts et al, 2003). Similarly, NE–vacuole contacts are established as sites for lipid droplet biogenesis, which include the proteins Nvj1, Mdm1, Nvj3, Nvj2, and Vac8 (Henne et al, 2015; Hariri et al, 2018). We tagged the Net1-GFP in wild type, double (*mdm1 Δ nvj3 Δ*) and quadruple (*mdm1 Δ nvj1 Δ nvj2 Δ nvj3 Δ*) “*Anvj*” mutants, of which the latter is known to increase the NE–vacuole inter-organellar distance (Hariri et al, 2018). Cells were arrested in Nz for 3 h and the rDNA structure visualized as before. Surprisingly, we still found that most mid-M cells presented an rDNA loop, even in the quadruple *Anvj* mutant (Fig 7K). Moreover, when we stained the cells with Blue CMAC

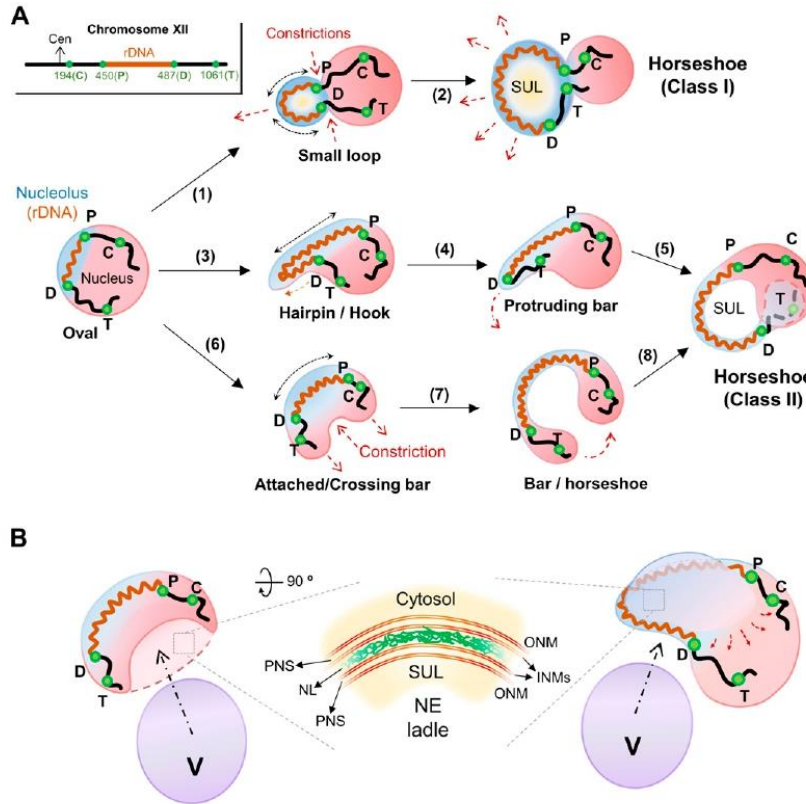


Figure 8. Classes and origin of ribosomal DNA (rDNA) loops in mid-M arrests.

(A) Relationships between rDNA and nuclear morphologies during the Nz-induced mid-M arrest. Upon Nz addition, the round nucleus expands the NE next to the nucleolus in G2/M cells, so that the rDNA acquires bar-like morphologies distinct to the packed oval shape seen in interphase. Three main reshaping pathways can be drawn. First pathway: (1) the NE grows outwards forming a nuclear bud for the nucleolus, with the corresponding basal constrictions; (2) the NE continues expanding symmetrically in all directions, making possible the flourishing of the class I horseshoe loop, characterized by a unilobed nucleus and a NE ladle at the SUL (yellow). Second pathway: (3) the nucleolus grows outwards as a finger-like projection; (4) its subsequent growth pulls the distal cXIIr arm into the projection; (5) the resulting protruding bar leads to a bi-lobed nucleus that bends until both lobes touch each other, giving rise to the class II horseshoe loop. Third pathway: (6) The NE expands laterally, creating an opposing nuclear constriction; (7) the expanding rDNA bar/handle connects a bi-lobed nucleus; (8) the bar bends and both lobes touch each other, giving rise to the class II horseshoe loop. The rDNA array is depicted as a dark red spring, the rest of the chromosome XII (cXII) as a black thick line, the nucleolus is in blue, and the main nuclear DNA mass is in red. The four cXII regions followed by tetOs arrays in this work are indicated as green dots (C, next to the centromere; P, proximal or centromeric rDNA flank; D, distal or telomeric rDNA flank; T, next to telomere; a

cXII schematic is also depicted on the left top corner). Black arrows with a number indicate morphological transitions, dashed black double arrows indicate the direction of NE expansion, and red dashed arrows the motion of nuclear subdomains during transitions. **(B)** Models of how the vacuole may serve as a template for the SUL NE ladle. Two different nucleus-vacuole spatial configurations are shown. On the left, the vacuole serves as a scaffold for nuclear reshaping when the NE grows laterally at the nucleolus. This may explain the presence of NE ladles in cashew nuclei (proto-SUL; see Fig 5B). On the right, the expanding NE in a class I horseshoe form an NE ladle at the SUL. Vacuolar engulfment by the NE may explain the ladle shaped of these SULs; At the centre, a zoom-in of the putative NE ladle, showing that it may comprise two very close NE sheets that run in parallel, leaving an extremely narrow nuclear lumen in between. SUL, Space under the rDNA loop; NE, nuclear envelope; NL, nuclear lumen; PNS, perinuclear space; ONM, outer nuclear membrane; INM, inner nuclear membrane.

in the *Anvj* mutant, the loops still wrap the vacuole (Fig S7M). We conclude that NE-vacuole contacts are not a prerequisite for the formation of the horseshoe rDNA loop.

The rDNA loop depends on functional vacuoles

We then checked whether vacuole mutants that impinge on their size, shape, or functionality undermine the ability to form the horseshoe loop. Vacuoles grow and shrink through fusion and fission of vesicles, respectively (Chan & Marshall, 2014). The quick dynamics of such events can be appreciated in the Video 10. Atg18 favors vacuole fission, whereas *Apl5*, *Vps45*, and *Pep12* are factors involved in delivering vesicles from Golgi to fuse with vacuoles; single knockout mutants for these genes alter vacuolar size and functionality (Becherer et al, 1996; Burd et al, 1997; Cowles et al, 1997; Bryant et al, 1998; Efe et al, 2007). Despite these alterations, we still

observed horseshoe loops and all the other bar-like morphologies in proportions equivalent to the wild-type strain (Figs 7L and S8A).

We next checked the *vac17Δ* mutant, which dampens vacuole maturation and inheritance, and the *vac17Δ pep12Δ* double mutant, which enhances these phenotypes and even make 40% of cells lack normal vacuoles (Jin & Weisman, 2015). We found a clear drop in the proportion of cells with horseshoe loops in the double mutant (Fig 7L; loops in only ~10% of mid-M cells). In addition, the rDNA array in those loops were less organized than in the wild type (Fig S8B).

Last, we checked the effect of suppressing the vacuolar H⁺-ATPase (V-ATPase), responsible for vacuolar acidification and thus correct vacuolar function (Stevens & Forgac, 1997). We used the *vma1Δ* knockout mutant; *Vma1* is one V-ATPase subunit. This mutant grew more slowly than wild type cells and only half of the cell population reached a mid-M arrest after 3 h in Nz. However, in these mid-M cells, the horseshoe loop was barely present, and oval and



Table 1. Strains used in this work.

Strain ^a	Genotype ^b	Origin
AS499	<i>MATa ura3-52 lys2-801 ade2-101 trp1-Δ63 his3-Δ200 leu2-Δ1 bar1-Δ</i>	Strunnikov lab
CCG771	{AS499} <i>NET1-GFP::LEU2</i>	Aragon lab
CCG918	{AS499} <i>CDC14-GFP::KanMX</i>	Aragon lab
CCG1297	{AS499} <i>TetR-YFP::ADE2; TetO(5.6 Kb)::194Kb-ChrXII::HIS3</i>	Aragon lab
CCG1300	{AS499} <i>TetR-YFP ADE2; TetO(5.6 Kb)::487Kb-ChrXII::HIS3</i>	Aragon lab
CCG1326	{CCG1297} <i>NET1-CFP::kanMX4</i>	Aragon lab
CCG1327	{AS499} <i>TetR-YFP::ADE2; TetO(5.6 Kb)::450Kb-ChrXII::URA3; NET1-CFP::kanMX4</i>	Aragon lab
CCG1328	{CCG1300} <i>NET1-CFP::kanMX4</i>	Aragon lab
CCG1329	{AS499} <i>TetR-YFP::ADE2; TetO(5.6 Kb)::1061Kb-ChrXII::HIS3; NET1-CFP::kanMX4</i>	Aragon lab
CCG1582	{AS499} <i>NET1-CFP::HygB; NUP49-GFP::URA3</i>	Aragon lab
CCG2306	{AS499} <i>TetR-YFP::ADE2; TetO(5.6 Kb)::450Kb-ChrXII::URA3; TetO(5.6 Kb)::487Kb-ChrXII::HIS3</i>	Aragon lab
CCG2309	{AS499} <i>TetR-YFP::ADE2; TetO(5.6 Kb)::450Kb-ChrXII::URA3; TetO(5.6 Kb)::1061Kb-ChrXII::HIS3</i>	Aragon lab
CCG2570 (x75)	<i>MATa leu2-3,112 ura3-1 his3-11 trp1-1 ade2-1 can1-100; fob1Δ::his3::HygB (rDNA ~ 75 copies); NET1-GFP::LEU2</i>	Aragon lab
CCG2572	<i>MATa leu2-3,112 ura3-1 his3-11 trp1-1 ade2-1 can1-100; fob1Δ::his3::HygB (rDNA ~ 25 copies); NET1-GFP::LEU2</i>	Aragon lab
SEY6210	<i>MATa ura3-52 leu2-3,112 his3-Δ100 trp1-Δ901 lys2-801 suc2-Δ9</i>	Henne lab
SEY6210 <i>mdm1Δ nvj3Δ</i>	{SEY6210} <i>mdm1Δ::KanMX nvj3Δ::NatMX (MATa)</i>	Henne lab
SEY6210 <i>ΔNVJ</i>	{SEY6210} <i>nvj1Δ::TRP1 nvj2Δ::HIS3 mdm1Δ::KanMX nvj3Δ::NatMX (MATa)</i>	Henne lab
W303-K699	<i>MATa trp1-1 can1-100 leu2-3,112, his3-11,15, ura3-1 GAL phi+ ade2-1::OsTir1-9Myc::ADE2 smc4-3HA::TRP1 Net1-yEmCitrine::HIS3 leu2-3,112::P_{GAL}--MAD2-MAD3::LEU2</i>	Uhlmann lab
yED233	<i>Mata ura3-1 HTA2-mCherry::URA3 ade2-1 his3-11,15 leu2-3,112 trp1-1 can1-100</i>	Pelet lab
YNK54	<i>Mata ura3-1::ADH1-OsTIR1-9Myc::URA3 ade2-1 his3-11,15 leu2-3,112 trp1-1 can1-100</i>	Kanemaki lab ^c
DMY3284- W303a	{W303a} <i>leu2::mURA3 heh1Δ::KANR nur1Δ::HPHR</i>	Moazed Lab
FM931	{YNK54} <i>NET1-GFP::LEU2</i>	Machín lab
FM2113	{YNK54} <i>cdc14-aid*-9myc::Hph; SPC42-RedStar::KanMX; [NOP1-CFP(LEU2)]</i>	Machín lab
FM2301	{CCG2309}; <i>NET1-eCFP::KanMX4</i>	This work
FM2361	{CCG1297}; <i>NET1-eCFP::KanMX4</i>	This work
FM2383	{FM931}; <i>NEM1-6HA::natNT2</i>	This work
FM2394	{YNK54}; <i>SEC61-eCFP::kanMX4</i>	This work
FM2396	{FM931}; <i>cdc16-aid*-9myc::hphNT</i>	This work
FM2398	{CCG1300} <i>ura3-52::ADH1-OsTIR1-9Myc::URA3; net1-aid*-9myc::hphNT; FOB1-eCFP::KanMX4</i>	This work
FM2399	{FM2394}; <i>NET1-eYFP::Hph</i>	This work
FM2438	{CCG2306}; <i>NET1-eCFP::KanMX4</i>	This work
FM2474	{CCG1297}; <i>cdc15-2.9myc::Hph; cin8::cin8-AID*-9myc::KanMX; ura3-52::ADH1-OsTIR1-9myc::URA3; Δkip1::HIS3MX4</i>	Machín lab
FM2614	{yED233}; <i>NET1-GFP::LEU2</i>	This work

(Continued on following page)



Table 1. Continued

Strain ^a	Genotype ^b	Origin
FM2619	{YAT1735}; NET1-GFP::LEU2	This work
FM2620	{FM2398} <i>ura3-52</i> (-OstIR1)	This work ^d
FM2639	{FM2394}; NET1-mCherry::natNT2; <i>trp1-1::P_{ADH1}-EGFP-IAA17-NLS::TRP1</i>	This work ^{e,f}
FM2641	{FM2394}; NET1-mCherry::natNT2; <i>trp1-1::P_{ADH1}-EGFP-IAA17::TRP1</i>	This work ^{e,f}
FM2658	{CCG2309}; SEC61-eCFP::kanMX4; NET1-mCherry::natNT2	This work
FM2659	{FM2396}; <i>ura3-1</i> (-OstIR1)	This work ^d
FM2696	{SEY6210}; NET1-GFP::LEU2	This work
FM2697	{SEY6210 <i>mdm1Δ nvj3Δ</i> }; NET1-GFP::LEU2	This work
FM2698	{SEY6210 ΔNV} (<i>nvj1Δ,nvj2Δ,mdm1Δ,nvj3Δ</i>); NET1-GFP::LEU2	This work
FM2707	{AS499} TetR-YFP::ADE2; TetO(5.6 Kb)::1061Kb-ChrXII::HIS3; <i>cdc15-2::9myc:Hph</i> ; <i>ura3-52::ADH1-OstIR1-9myc::URA3</i> ; HTA2-mCherry::natNT2; NET1-ECFP::klTRP1	This work
FM2735	{FM2707} <i>cdc16-AID*-9myc::KanMX</i>	This work
FM2743	{yED233}; SEC61-EYFP::kanMX4	This work
FM2748	{FM2707} <i>nem1-AID*-9myc::KanMX</i>	This work
FM2799	{yED233}; NET1-ECFP::klTRP1; SEC61-EYFP::kanMX4	This work
FM2800	{FM2639}; <i>fast1-aid*-9myc::hphNT</i>	This work
FM2913	{FM2696}; <i>apl5Δ::HIS3MX6</i>	This work
FM2923	{FM2696}; <i>atg18Δ::HIS3MX6</i>	This work
FM2924	{FM2696}; <i>vps45Δ::HIS3MX6</i>	This work
FM2945	{FM2696}; <i>pep12Δ::HIS3MX6</i>	This work
FM2951	{FM2696}; <i>vma1Δ::HIS3MX6</i>	This work
FM2959	{FM2474}; NET1-mCherry::natNT2	This work
FM2960	{DMY3284-W303a}; <i>trp1-1::P_{ADH1}-EGFP-IAA17-NLS::TRP1</i> ; NET1-mCherry::natNT2	This work
FM2965	{yED233}; NET1-ECFP::LEU2; VPH1-GFP::kanMX4	This work
FM2973	{FM2945}; <i>vac17Δ::TRP1</i>	This work
FM2977	{FM2696}; <i>vac17Δ::TRP1</i>	This work

^aStrains are sorted alphabetically, and then by number, starting from strains reported in previous works.

^bCurly brackets indicate parental strains used for successive strain construction. Semicolons separate independent transformation events during strain construction; intermediate strains are omitted. Square brackets indicate episomal elements.

^cThis strain was obtained from the NBRP repository (<http://yeastlab.nig.ac.jp/yeast/>).

^dThese strains were obtained by counterselecting for the *ura⁻* phenotype in five-FOA, which results in the pop out of the OstIR1:URA3 segment.

^eThese strains express EGFP reporters for the nucleoplasm and the cytoplasm, respectively. These EGFPs are chimeras that contain the auxin-responsive degron peptide IAA17 from *Arabidopsis thaliana*. In most figures, the reference to the IAA17 is omitted for the sake of space because it is experimentally irrelevant. In those cases where cells were treated with IAA, the IAA17 epitope is indicated.

^fThe integrative plasmids for making these strains were also obtained from the NBRP repository (pMK42 and pMK72; originally from Kanemaki lab). To target pop-in integration into the *TRP1* locus, both plasmids were digested with MfeI before transformation.

SULs. Sec61 labels both NE and ER, so we cannot completely rule out that the ladle is formed of ER. Two findings suggest otherwise though; we observed traces of nucleoplasm and Nup49 (NPCs) in a subset of ladles (Figs 5B and S3H).

The horseshoe loop requires nuclear extensions in the absence of microtubules (Nz treatment). When mid-M arrests are accomplished by means that preserve microtubules (APC inactivation, ectopic activation of SAC or monopolar spindles), other rDNA morphologies are seen (Figs 6 and S6). Despite some of them (bars and hooks) can be envisaged as

incomplete horseshoe loops because the bipolar spindle pulling forces pose a barrier to vacuole wrapping, non-horseshoe morphologies were seen with a monopolar spindle as well. This points out that the absence of microtubules per se is a requirement for the nuclear reshaping that leads to the horseshoe loop, establishing a connection between the cytoskeleton and the way the nucleus is extended during mid-M arrests.

We also show that membrane phospholipid biosynthesis is required, yet not sufficient, for the horseshoe rDNA loop (Fig 7C-I). It is



vol/vol. Cerulenin was added at a final concentration of 2 $\mu\text{g}/\text{ml}$ (from a 5 mg/ml stock in EtOH).

Wide field fluorescence microscopy, staining, and image processing

Two epifluorescence inverted microscopes were used. A Leica DMI6000B with an ultrasensitive DFC350 digital camera was used for single cell visualization with a 63X/1.30 immersion objective as we have reported before (Quevedo et al, 2012; Matos-Perdomo & Machín, 2018). A Zeiss Axio Observer.Z1/7 was also used; this microscope was equipped with an Axiocam 702 sCMOS camera, the Colibri-7 LED excitation system, narrow band filter cubes for co-visualization of CFP, YFP/GFP, and mCherry without emission crosstalk, and a 63X/1.40 immersion objective.

Whenever possible cells were imaged alive. Briefly, 250 μl of cell culture was collected at each time point, centrifuged at 300g for 1 min at room temperature, the supernatant carefully retired, and ~ 1.5 μl of the pellet was added on the microscope slide. Samples were visualized directly using the appropriate filter cube for each tag/stain. For each field, we first captured either single planes or a series of 10–20 z-focal plane images (0.2–0.6 μm depth between each consecutive image), and then we processed images with the Leica AF6000, Zeiss Zen Blue and ImageJ software. For z-stack 2D projections, we used the maximum intensity method. Deconvolution was performed on z-stacks using Leica AF6000 software (method: blind deconvolution algorithm, 10 total iterations, fast processing). Orthogonal projections were generated using ImageJ. Fluorescence intensity profiles were generated using Leica AF6000 and Zeiss Zen 3.1 lite (blue edition) software. For short time-lapse movies of living cells, Nz-blocked cells were pelleted and spread at a high density onto the slide. Specific conditions are described in the video legends.

Stains: DAPI, YOYO-1, SYTO RNaselect, MDY-64, Blue CMAC, carboxy-DCFDA. Nz-blocked cells were stained as follows:

For DAPI staining, the cell pellet was frozen for at least 24 h at -20°C before thawing at room temperature, and then ~ 1.5 μl of the pellet was added to ~ 1 μl of 4 $\mu\text{g}/\text{ml}$ of DAPI on the microscope slide.

For YOYO-1, we followed a previously described procedure (Ivanova et al, 2020). Briefly, cells were fixed in 4% formaldehyde for 30 min, washed once in PBS, and re-suspended in 5 mg/ml zymolyase in P solution (1.2 M sorbitol, 0.1 M potassium phosphate buffer, pH: 6.2) for 1 min. Cells were spun down, taken up in P-Solution +0.2% Tween 20 + 100 $\mu\text{g}/\text{ml}$ RNase A and incubated for 1 h at 37°C . After digestion, cells were pelleted and taken up in P-Solution containing 25 μM YOYO-1 and visualized as before.

For SYTO RNaselect, cells were pelleted and stained according to manufacturer's procedures. Briefly, a solution of RNaselect green fluorescent stain (final concentration 500 nM) in YPD medium was added to the cells and incubated for 30 min. After this, cells were washed twice with fresh YPD, let rest for 5 min and visualized as before.

For carboxy-DCFDA and Blue CMAC, 1 ml of cells were incubated for ~ 15 –30 min in either carboxy-DCFDA (final concentration of 10 μM from a 10 mM DMSO stock solution) or Blue CMAC (final concentration of 100 μM from a 10 mM DMSO stock solution). Then, the cells were pelleted, washed in YPD (PBS if fixed), and visualized

accordingly. For MDY-64, cells were incubated for ~ 3 –5 min in 10 μl from a 10 mM DMSO stock solution.

CSM

Nz-blocked cells were pelleted and imaged in two Zeiss Axio Observer.Z1/7 inverted microscopes equipped for super-resolution confocal microscopy with live cell capabilities (LSM880 with Airyscan and LSM980 with Airyscan 2). The resolution provided in Airyscan mode is lateral (x/y) resolution to 120 nm for 2D and 3D data sets (z-stacks) and 350-nm axial (z) resolution for z-stacks, with an improved resolution up to 1.7X compared with standard confocal (Huff, 2015). The super-resolution images were taken with either a C-Apochromat 63x/NA 1.20 W M27 DICII objective for the LSM880 or a Plan-Apochromat 63x/NA 1.40 Oil M27 DIC objective for the LSM980. The Airyscan detector was used for all single and multiple labellings, with the pinhole automatically set to correct opening according to the selected Airyscan mode. The super-resolution mode of the Airyscan detector was used throughout. We used the following laser lines for excitation of fluorescent tags: 405 nm for CFP; 514 nm for YFP; 488 nm for GFP; and 561 nm for mCherry. The bright field (BF) image was acquired with T-PMT detectors (pinhole 1 AU). After imaging, Airyscan processing was conducted. Z-stack 2D projections were generated by either applying the processing "extended depth of focus" using Zeiss Zen Blue 3.2 software or the sum intensity method in ImageJ.

For 3D reconstructions, ~ 45 –50 z planes (0.15 μm thick) were obtained across the entire cell. Both alive and fixed cells were photographed, although fixed cells were generally used in the presented experiments. For cell fixation, cells were incubated in 3.7% wt/vol formaldehyde on a nutating mixer at room temperature for 15–30 min, spun down at 6,800g for 30 s, the pellet washed in 500 μl of filtered PBS 1 \times , resuspended in another 500 μl of PBS 1 \times , and stored at 4°C in the dark. Before micrographs were taken, suspensions were sonicated for 8 s in a bath sonicator to separate clumps of cells.

Unless stated otherwise in video captions, long (3 h) time-lapse images were acquired on cells immobilized in Nunc Lab-Tek coverglass eight-wells chambers pretreated with concanavalin A (ConA). ConA pretreatment was undertaken the day of filming by adding 50 μl of ConA (1 mg/ml in PBS) to a well, incubate in the dark at 25°C for 20 min, and washed the well twice with synthetic complete (SC) media. For cell adhesion, a log cell culture was concentrated 2 \times in SC and 100 μl of the suspension applied to the well and kept at 25°C for 20 min. Non-attached cells were then washed twice with 100 μl of SC media and finally the well was covered with 250 μl of YPD plus Nz at a final concentration of 22.5 $\mu\text{g}/\text{ml}$ to start live cell imaging. The higher concentration of Nz used in these experiments is actually equal to the initial plus the reinforcement doses applied in liquid cultures growing in an air incubator. We did this to avoid detachment of the cells by pipetting in the middle of the experiment. Aside from photobleaching and phototoxicity, the horseshoe loop was photosensitive in subtoxic conditions (as determined by comparing end points of exposed versus non-exposed fields). Because of that, laser powers were kept to a minimum and number of z planes reduced. With 405-nm UV irradiation (for CFP), the number of total frames (z planes plus t



points) was set to a maximum of 35; without 405 nm, the maximum frame number was 150.

TIRF microscopy

This was adapted from a protocol described before (Barroso-González et al, 2009). Nz-blocked cells were pelleted and imaged with an inverted microscope Zeiss 200 M through a 1.45-numerical aperture objective (α Fluor, 100 \times /1.45; Zeiss). The objective was coupled to the coverslip using an immersion fluid (n(488) 1.518, Zeiss). The expanded beam of an argon ion laser (Lasos; Lasertechnik GmbH) was band-pass filtered (488/10 nm) and used to selectively excite EGFP-tagged proteins, for evanescent field illumination. The laser beam was focused at an off-axis position in the back focal plane of the objective. Light, after entering the coverslip, underwent total internal reflection as it struck the interface between the glass and the cell at a glancing angle. The images were projected onto a back-illuminated CCD camera (AxioCam MRm; Zeiss) through a dichroic (500 LP) and specific band-pass filter (525/50 nm). Each cell was imaged using Axiovision (version 4.9; Zeiss) with 0.5 s exposition. Image analysis: The raw images were low-pass filtered (3×3 pixels) and analyzed with ImageJ.

TEM

The protocol was adapted and modified from Byers and Goetsch (1991). Cells were arrested in nocodazole for 180 min, then pelleted, re-suspended and fixed in phosphate-magnesium buffered (40 mM K_2HPO_4 , and 0.5 mM $MgCl_2$, pH 6.5) 2% glutaraldehyde (EM Grade) + 2% formaldehyde and incubated overnight and stored at 4°C. Then, cells were rinsed twice in 0.1 M phosphate-citrate buffer (170 mM KH_2PO_4 and 30 mM sodium citrate, pH 5.8) and re-suspended in this buffer containing a 1/10 dilution of Lyticase (10 mg/ml 2,000 U stock) + Zymolyase (5 U/ μ l stock) and incubated at 30°C for 2 h, or until cell walls have been removed. For post fixation, cells were washed twice in 0.1 M sodium acetate (pH 6.1), transferred to a 2% osmium tetroxide fixation solution, and incubate for 4 h in a fume hood. Then, cells were washed with double-distilled water (ddH_2O) and transfer to 1% aqueous uranyl acetate for 60 min of incubation in the dark. After this, cells were washed twice in ddH_2O and dehydrate by transferring them through a series of ethanol concentrations (20, 40, 60, 70 [overnight], 96, and 100). Then, cells were pelleted and resuspended in EMBed 812 resin. Finally, semi-thin and ultra-thin sections were cut on an ultramicrotome (Reichert Ultracut S-Leica) and stained with toluidine blue for semi-thin sections and with uranyl acetate and lead salts (Sato's Staining Procedure, 5 min) for ultra-thin sections. EM images were captured by a TEM 100 kV JEOL JEM 1010 electron microscope.

Pulsed field gel electrophoresis and Southern blot

Yeast chromosomes extraction was prepared in low-melting point agarose plugs as reported before (Ayra-Plasencia et al, 2021). For each sample, six OD_{600} equivalents were centrifuged and washed twice in ice-cold sterile 1 \times PBS. Then, cells were re-suspended in Lyticase solution (2,500 U/ml), and embedded into 0.5% (wt/vol) agarose plugs. Finally, full-sized chromosomes were obtained by

digesting overnight in RNase A (10 μ g/ml) and Proteinase K (1 mg/ml) containing solutions at 37°C. Pulsed field gel electrophoresis, used to assess the chromosome XII size, was performed by using the CHEF DR-III system (Bio-Rad). One third of each plug was placed within the corresponding well of a 1% (wt/vol) agarose gel made in 1 \times TBE buffer. Then, the wells were filled-up and sealed with additional 1% (wt/vol) agarose. 0.5 \times TBE was used as the running buffer at 14°C. The electrophoresis was carried out at 3 V/cm for 68 h, including 300 and 900 s of initial and switching time (respectively), and an angle of 120°. The gel was stained with ethidium bromide for 40 min and destained with ddH_2O for 20 min. The chromosomes bands were visualized under UV light using the Gel Doc system (Bio-Rad). To specifically study the chromosome XII, a Southern blot was carried out by a saline downwards transference onto a positively charged nylon membrane (Hybond-N+, Amersham-GE). A DNA probe against the NST1 region within the rDNA was synthesized using the Fluorescein-High Prime kit (Sigma-Aldrich). The fluorescein-labelled probe hybridization was carried out overnight at 68°C. The next day, the membrane was incubated with an anti-fluorescein antibody coupled to alkaline phosphatase (Roche), and the signal was developed using CDP-star (Amersham) as the substrate. The detection was recorded by using the Vilber-Lourmat Fusion Solo S equipment.

Western blotting

Western blotting was carried out as reported before with minor modifications (Matos-Perdomo & Machín, 2018; Ayra-Plasencia & Machín, 2019). Briefly, 5 ml of the yeast liquid culture was collected to extract total protein using the trichloroacetic acid (TCA) method; cell pellets were fixed in 2 ml of 20% TCA. After centrifugation (2,500g for 3 min), cells were resuspended in fresh 100 μ l 20% TCA and ~200 mg of glass beads were added. After 3 min of breakage in a homogenizer (P000062-PEVO0-A; Precellys Evolution-Bertin Instruments), extra 200 μ l 5% TCA were added to the tubes and ~300 μ l of the mix were collected in new 1.5 ml tubes. Samples were then centrifuged (2,500g for 5 min) and pellets were resuspended in 100 μ l of PAGE Laemmli Sample Buffer (1610747; Bio-Rad) mixed with 50 μ l TE 1X pH 8.0. Finally, tubes were boiled for 3 min at 95°C and pelleted again. Total proteins were quantified with a Qubit 4 Fluorometer (Q33227; Thermo Fisher Scientific). Proteins were resolved in 7.5% SDS-PAGE gels and transferred to PVDF membranes (PVM020C-099; Pall Corporation). For protein phosphorylation states, we used the method for Phos-tag acrylamide gel electrophoresis (Kinoshita et al, 2006). The following antibodies were used for immunoblotting: The HA epitope was recognized with a primary mouse monoclonal anti-HA (1:1,000; Sigma-Aldrich); the Myc epitope was recognized with a primary mouse monoclonal anti-Myc (1:5,000; Sigma-Aldrich); the Pgk1 protein was recognized with a primary mouse monoclonal anti-Pgk1 (1:5,000; Thermo Fisher Scientific) and the aid tag was recognized with a primary mouse monoclonal anti-miniaid (1:500; MBL). A polyclonal goat anti-mouse conjugated to horseradish peroxidase (1:5,000, 1:10,000 or 1:20,000; Promega) was used as secondary antibody. Antibodies were diluted in 5% milk TBST (TBS pH 7.5 plus 0.1% Tween 20). Proteins were detected by using the ECL reagent (RPN2232; GE Healthcare) chemiluminescence method, and visualized in a Vilber-Lourmat



Fusion Solo S chamber. The membrane was finally stained with Ponceau S-solution (PanReac AppliChem) for a loading reference.

Quantification and statistical analysis

All experiments presented in this study are representative examples, and where stated, three ($n = 3$) or two ($n = 2$) independent experiments (biological replicates) are shown. In quantifying experiments involving microscopy, number of cells counted for each condition ranged between 100 and 300, depending on the complexity of the data.

For morphological data, cells were categorized, and the corresponding proportions calculated and represented in bar charts. Where indicated, error bars represent Standard Error of the Mean (mean \pm SEM). Unless stated otherwise, only G2/M cells were counted, and these were selected from mononucleated budded cells in which the bud was at least half the size of the mother. In mid-M arrests, the bud size equals that of the mother (dumbbell cell), but we still used the term “G2/M cells” in the y-axis of those charts to make comparisons with experiments where G2/M cells do not necessarily get arrested in mid-M (e.g., Nem1 depletion, rapamycin co-treatments, etc.) Because in dumbbell cells it is difficult to establish which is the mother and which is the bud, we use the term “cell body” to refer to either one.

Quantification of rDNA length and distances was performed with the Leica AF6000 software. These continuous data were represented in box-plots. In these plots, the centre lines depict the medians, box limits indicate the 25th and 75th percentile, and roughly give the 95% confidence intervals for each median. Whiskers represent 5–95 percentile. The mean is shown as “+.” Dots represent outliers. *P*-values are represented on each boxplot when comparing two sets of data. For this, assumption of normality was calculated by applying a Shapiro Test. For equality of variances, an *F* test was used before a *t* test analysis when needed. Unpaired *t* test with Welch’s correction was used for the equality of two means. When necessary, a nonparametric Wilcoxon Mann–Whitney *U* test was applied. Significance level was established at $P < 0.05$ (two tailed). Nonsignificant is denoted by “ns.” Statistical analyses were performed with GraphPad Prism (<https://www.graphpad.com/>) and R software (<https://www.r-project.org/>).

Cross section profiles of fluorescence intensity were obtained with either the Leica AF6000 or the Zeiss Zen Blue software and represented using GraphPad Prism.

Quantification of bands on Western blots was performed by measuring the intensity of each band in non-saturated conditions using the Bio1D software. The relative amount of aid^{*}-9myc tagged protein (target protein) was estimated using Pkg1 as an internal housekeeping control (loading control protein). Normalization of the target protein relative to the loading control protein was carried out for each lane, and then the fold difference calculated (relative target protein levels) for each lane:

$$\text{Normalized density} = \text{Target protein} \times \frac{\text{Loading control (lane 1)}}{\text{Loading control (each lane)}}$$

$$\text{Fold difference} = \frac{\text{Normalized density (each lane)}}{\text{Normalized density (lane 1)}}$$

Supplementary Information

Supplementary Information is available at <https://doi.org/10.26508/lsa.202101161>.

Acknowledgements

We kindly thank the Luis Aragón, Frank Uhlmann, Mike Henne, Danesh Moazed, Joris Winderickx and Patricia Kane labs for yeast strains and plasmids. We thank María Moriel-Carretero for sharing unpublished results as well as critical reading of the manuscript. We also thank David Machado from the Pharmacology Unit at Universidad de La Laguna for support on TIRF microscopy and José Manuel Pérez Galván from Servicio Investigación Microscopía Avanzada Confocal y Electrónica-SIMACE—at Universidad de Las Palmas de Gran Canaria for support on confocal and electron microscopy. This work was supported by the Spanish Ministry of Science grant BFU2017-83954-R to F Machín. The Agencia Canaria de Investigación, Innovación y Sociedad de la Información supported S Santana-Sosa and S Medina-Suárez through the predoctoral fellowships TESIS2018010034 and TESIS2020010028, respectively

Author Contributions

E Matos-Perdomo: conceptualization, data curation, formal analysis, investigation, visualization, methodology, and writing—original draft, review, and editing

S Santana-Sosa: formal analysis, investigation, visualization, and methodology.

J Ayra-Plasencia: formal analysis, investigation, visualization, and methodology.

S Medina-Suárez: methodology.

F Machín: conceptualization, data curation, formal analysis, supervision, funding acquisition, validation, investigation, visualization, methodology, project administration, and writing—original draft, review, and editing.

Conflict of Interest Statement

The authors declare that they have no conflict of interest.

References

- Albert B, Mathon J, Shukla A, Saad H, Normand C, Léger-Silvestre I, Villa D, Kamgoue A, Mozziconacci J, Wong H, et al (2013) Systematic characterization of the conformation and dynamics of budding yeast chromosome XII. *J Cell Biol* 202: 201–210. doi:10.1083/jcb.201208186
- Almacellas E, Pelletier J, Day C, Ambrosio S, Tauler A, Mauvezin C (2021) Lysosomal degradation ensures accurate chromosomal segregation to prevent chromosomal instability. *Autophagy* 17: 796–813. doi:10.1080/15548627.2020.1764727
- Ayra-Plasencia J, Ramos-Pérez C, Santana-Sosa S, Quevedo O, Medina-Suárez S, Matos-Perdomo E, Zamora-Dorta M, Brown GW, Lisby M,



- Machín F (2021) Topoisomerase II deficiency leads to a postreplicative structural shift in all *Saccharomyces cerevisiae* chromosomes. *Sci Rep* 11: 14940. doi:10.1038/s41598-021-93875-5
- Ayra-Plasencia J, Machín F (2019) DNA double-strand breaks in telophase lead to coalescence between segregated sister chromatid loci. *Nat Commun* 10: 2862. doi:10.1038/s41467-019-10742-8
- Barbet NC, Schneider U, Helliwell SB, Stansfield I, Tuite MF, Hall MN (1996) TOR controls translation initiation and early G1 progression in yeast. *Mol Biol Cell* 7: 25–42. doi:10.1091/mbc.7.1.25
- Barbosa AD, Lim K, Mari M, Edgar JR, Gal L, Sterk P, Jenkins BJ, Koulman A, Savage DB, Schuldiner M, et al (2019) Compartmentalized synthesis of triacylglycerol at the inner nuclear membrane regulates nuclear organization. *Dev Cell* 50: 755–766.e6. doi:10.1016/j.devcel.2019.07.009
- Barbosa AD, Sembongi H, Su W-M, Abreu S, Reggiori F, Carman GM, Siniosoglou S (2015) Lipid partitioning at the nuclear envelope controls membrane biogenesis. *Mol Biol Cell* 26: 3641–3657. doi:10.1091/mbc.e15-03-0173
- Barroso-González J, Machado J-D, García-Expósito L, Valenzuela-Fernández A (2009) Moesin regulates the trafficking of nascent clathrin-coated vesicles. *J Biol Chem* 284: 2419–2434. doi:10.1074/jbc.M80531200
- Bauer DE, Hatzivassiliou G, Zhao F, Andreadis C, Thompson CB (2005) ATP citrate lyase is an important component of cell growth and transformation. *Oncogene* 24: 6314–6322. doi:10.1038/sj.onc.1208773
- Becherer KA, Rieder SE, Emr SD, Jones EW (1996) Novel syntaxin homologue, Pep12p, required for the sorting of luminal hydrolases to the lysosome-like vacuole in yeast. *Mol Biol Cell* 7: 579–594. doi:10.1091/mbc.7.4.579
- Belgareh N, Doye V (1997) Dynamics of nuclear pore distribution in nucleoporin mutant yeast cells. *J Cell Biol* 136: 747–759. doi:10.1083/jcb.136.4.747
- Bhalla N, Biggins S, Murray AW (2002) Mutation of YCS4, a budding yeast condensin subunit, affects mitotic and nonmitotic chromosome behavior. *Mol Biol Cell* 13: 632–645. doi:10.1091/mbc.01-05-0264
- Blank HM, Maitra N, Polymenis M (2017a) Lipid biosynthesis: When the cell cycle meets protein synthesis? *Cell Cycle* 16: 905–906. doi:10.1080/15384101.2017.1312851
- Blank HM, Perez R, He C, Maitra N, Metz R, Hill J, Lin Y, Johnson CD, Bankaitis VA, Kennedy BK, et al (2017b) Translational control of lipogenic enzymes in the cell cycle of synchronous, growing yeast cells. *EMBO J* 36: 487–502. doi:10.15252/embj.201695050
- Bryant NJ, Piper RC, Weisman LS, Stevens TH (1998) Retrograde traffic out of the yeast vacuole to the TGN occurs via the prevacuolar/endosomal compartment. *J Cell Biol* 142: 651–663. doi:10.1083/jcb.142.3.651
- Burd CG, Peterson M, Cowles CR, Emr SD (1997) A novel Sec18p/NSF-dependent complex required for Golgi-to-endosome transport in yeast. *Mol Biol Cell* 8: 1089–1104. doi:10.1091/mbc.8.6.1089
- Byers B, Goetsch L (1991) Preparation of yeast cells for thin-section electron microscopy. *Methods Enzymol* 194: 602–608. doi:10.1016/0076-6879(91)94044-d
- Campbell JL, Lorenz A, Witkin KL, Hays T, Loidl J, Cohen-Fix O (2006) Yeast nuclear envelope subdomains with distinct abilities to resist membrane expansion. *Mol Biol Cell* 17: 1768–1778. doi:10.1091/mbc.e05-09-0839
- Cantwell H, Nurse P (2019) Unravelling nuclear size control. *Curr Genet* 65: 1281–1285. doi:10.1007/s00294-019-00999-3
- Chan Y-HM, Marshall WF (2014) Organelle size scaling of the budding yeast vacuole is tuned by membrane trafficking rates. *Biophys J* 106: 1986–1996. doi:10.1016/j.bpj.2014.03.014
- Clemente-Blanco A, Mayán-Santos M, Schneider DA, Machín F, Jarmuz A, Tschochner H, Aragón L (2009) Cdc14 inhibits transcription by RNA polymerase I during anaphase. *Nature* 458: 219–222. doi:10.1038/nature07652
- Cowles CR, Odorizzi G, Payne GS, Emr SD (1997) The AP-3 adaptor complex is essential for cargo-selective transport to the yeast vacuole. *Cell* 91: 109–118. doi:10.1016/s0092-8674(01)80013-1
- D'Amours D, Amon A (2004) At the interface between signaling and executing anaphase-Cdc14 and the FEAR network. *Genes Dev* 18: 2581–2595. doi:10.1101/gad.1247304
- Dauban L, Kamgoué A, Wang R, Léger-Silvestre I, Beckouët F, Cantaloube S, Gadal O (2019) Quantification of the dynamic behaviour of ribosomal DNA genes and nucleolus during yeast *Saccharomyces cerevisiae* cell cycle. *J Struct Biol* 208: 152–164. doi:10.1016/j.jsb.2019.08.010
- Dawaliby R, Mayer A (2010) Microautophagy of the nucleus coincides with a vacuolar diffusion barrier at nuclear-vacuolar junctions. *Mol Biol Cell* 21: 4173–4183. doi:10.1091/mbc.e09-09-0782
- Deolal P, Male G, Mishra K (2021) The challenge of staying in shape: Nuclear size matters. *Curr Genet* 67: 605–612. doi:10.1007/s00294-021-01176-1
- Dotiwala F, Haase J, Arbel-Eden A, Bloom K, Haber JE (2007) The yeast DNA damage checkpoint proteins control a cytoplasmic response to DNA damage. *Proc Natl Acad Sci U S A* 104: 11358–11363. doi:10.1073/pnas.0609636104
- Dubots E, Cottier S, Péli-Gulli M-P, Jaquenoud M, Bontron S, Schneiter R, De Virgilio C (2014) TORC1 regulates Pah1 phosphatidate phosphatase activity via the Nem1/Spo7 protein phosphatase complex. *PLoS One* 9: e104194. doi:10.1371/journal.pone.0104194
- Dunham M, Gartenberg M, Brown GW (2015) *Methods in Yeast Genetics and Genomics, 2015 Edition: A CSHL Course Manual*. New York: Cold Spring Harbor Laboratory Press.
- Düvel K, Yecies JL, Menon S, Raman P, Lipovsky AI, Souza AL, Triantafellow E, Ma Q, Gorski R, Cleaver S, et al (2010) Activation of a metabolic gene regulatory network downstream of mTOR complex 1. *Mol Cell* 39: 171–183. doi:10.1016/j.molcel.2010.06.022
- Efe JA, Botelho RJ, Emr SD (2007) Atg18 regulates organelle morphology and Fab1 kinase activity independent of its membrane recruitment by phosphatidylinositol 3, 5-bisphosphate. *Mol Biol Cell* 18: 4232–4244. doi:10.1091/mbc.e07-04-0301
- Falchook G, Infante J, Arkenau H-T, Patel MR, Dean E, Borazanci E, Brenner A, Cook N, Lopez J, Pant S, et al (2021) First-in-human study of the safety, pharmacokinetics, and pharmacodynamics of first-in-class fatty acid synthase inhibitor TVB-2640 alone and with a taxane in advanced tumors. *EClinicalMedicine* 34: 100797. doi:10.1016/j.eclinm.2021.100797
- Felsenfeld G, Groudine M (2003) Controlling the double helix. *Nature* 421: 448–453. doi:10.1038/nature01411
- Feric M, Vaidya N, Harmon TS, Mitrea DM, Zhu L, Richardson TM, Kriwacki RW, Pappu RV, Brangwynne CP (2016) Coexisting liquid phases underlie nucleolar subcompartments. *Cell* 165: 1686–1697. doi:10.1016/j.cell.2016.04.047
- Foster DA (2009) Phosphatidic acid signaling to mTOR: Signals for the survival of human cancer cells. *Biochim Biophys Acta* 1791: 949–955. doi:10.1016/j.bbali.2009.02.009
- Freeman L, Aragon-Alcaide L, Strunnikov A (2000) The condensin complex governs chromosome condensation and mitotic transmission of rDNA. *J Cell Biol* 149: 811–824. doi:10.1083/jcb.149.4.811
- Fuchs J, Loidl J (2004) Behaviour of nucleolus organizing regions (NORs) and nucleoli during mitotic and meiotic divisions in budding yeast. *Chromosome Res* 12: 427–438. doi:10.1023/b:chro.0000034726.05374.db
- García M, Kumanski S, Elías-Villalobos A, Cazeville C, Soulet C, Moriel-Carretero M (2022) Nuclear ingress of cytoplasmic bodies accompanies a boost in autophagy. *Life Sci Alliance* 5: e202101160. doi:10.26508/lsa.202101160
- Gibcus JH, Samejima K, Goloborodko A, Samejima I, Naumova N, Nuebler J, Kanemaki MT, Xie L, Paulson JR, Earnshaw WC, et al (2018) A pathway for mitotic chromosome formation. *Science* 359: eaao6135. doi:10.1126/science.aao6135



- Guacci V, Hogan E, Koshland D (1994) Chromosome condensation and sister chromatid pairing in budding yeast. *J Cell Biol* 125: 517–530. doi:10.1083/jcb.125.3.517
- Ha CW, Huh WK (2011) Rapamycin increases rDNA stability by enhancing association of Sir2 with rDNA in *Saccharomyces cerevisiae*. *Nucleic Acids Res* 39: 1336–1350. doi:10.1093/nar/gkq895
- Hariri H, Rogers S, Ugrankar R, Liu YL, Feathers JR, Henne WM (2018) Lipid droplet biogenesis is spatially coordinated at ER-vacuole contacts under nutritional stress. *EMBO Rep* 19: 57–72. doi:10.15252/embr.201744815
- Harris B, Bose T, Lee KK, Wang F, Lu S, Ross RT, Zhang Y, French SL, Beyer AL, Slaughter BD, et al (2014) Cohesion promotes nucleolar structure and function. *Mol Biol Cell* 25: 337–346. doi:10.1091/mbc.e13-07-0377
- Heitman J, Movva NR, Hall MN (1991) Targets for cell cycle arrest by the immunosuppressant rapamycin in yeast. *Science* 253: 905–909. doi:10.1126/science.1715094
- Henne WM, Zhu L, Balogi Z, Stefan C, Pleiss JA, Emr SD (2015) Mdm1/Snx13 is a novel ER-endolysosomal interorganelle tethering protein. *J Cell Biol* 210: 541–551. doi:10.1083/jcb.201503088
- Hoyt MA, He L, Loo KK, Saunders WS (1992) Two *Saccharomyces cerevisiae* kinesin-related gene products required for mitotic spindle assembly. *J Cell Biol* 118: 109–120. doi:10.1083/jcb.118.1.109
- Hoyt MA, Totis L, Roberts BT (1991) *S. cerevisiae* genes required for cell cycle arrest in response to loss of microtubule function. *Cell* 66: 507–517. doi:10.1016/0092-8674(81)90014-3
- Huff J (2015) The airyscan detector from ZEISS: Confocal imaging with improved signal-to-noise ratio and super-resolution. *Nat Methods* 12: i–ii. doi:10.1038/nmeth.f.388
- Hult C, Adalsteinsson D, Vasquez PA, Lawrimore J, Bennett M, York A, Cook D, Yeh E, Forest MG, Bloom K (2017) Enrichment of dynamic chromosomal crosslinks drive phase separation of the nucleolus. *Nucleic Acids Res* 45: 11159–11173. doi:10.1093/nar/gkx741
- Inokoshi J, Tomoda H, Hashimoto H, Watanabe A, Takeshima H, Omura S (1994) Cerulenin-resistant mutants of *Saccharomyces cerevisiae* with an altered fatty acid synthase gene. *Mol Gen Genet* 244: 90–96. doi:10.1007/bf00280191
- Ivanova T, Maier M, Missarova A, Ziegler-Birling C, Dam M, Gomar-Alba M, Carey LB, Mendoza M (2020) Budding yeast complete DNA synthesis after chromosome segregation begins. *Nat Commun* 11: 2267. doi:10.1038/s41467-020-16100-3
- Jacobs CW, Adams AE, Szaniszlo PJ, Pringle JR (1988) Functions of microtubules in the *Saccharomyces cerevisiae* cell cycle. *J Cell Biol* 107: 1409–1426. doi:10.1083/jcb.107.4.1409
- Jin Y, Weisman LS (2015) The vacuole/lysosome is required for cell-cycle progression. *Elife* 4: 1–19. doi:10.7554/elife.08160
- Kinoshita E, Kinoshita-Kikuta E, Takiyama K, Koike T (2006) Phosphate-binding tag, a new tool to visualize phosphorylated proteins. *Mol Cell Proteomics* 5: 749–757. doi:10.1074/mcp.1500024-mcp200
- Kobayashi T, Heck DJ, Nomura M, Horiuchi T (1998) Expansion and contraction of ribosomal DNA repeats in *Saccharomyces cerevisiae*: Requirement of replication fork blocking (Fob1) protein and the role of RNA polymerase I. *Genes Dev* 12: 3821–3830. doi:10.1101/gad.12.24.3821
- Kvam E, Goldfarb DS (2007) Nucleus-vacuole junctions and piecemeal microautophagy of the nucleus in *S. cerevisiae*. *Autophagy* 3: 85–92. doi:10.4161/auto.3586
- Lai LA, Morabito L, Holloway SL (2003) A novel yeast mutant that is defective in regulation of the anaphase-promoting complex by the spindle damage checkpoint. *Mol Genet Genomics* 270: 156–164. doi:10.1007/s00438-003-0912-5
- Lamothé R, Costantino L, Koshland DE (2020) The spatial regulation of condensin activity in chromosome condensation. *Genes Dev* 34: 819–831. doi:10.1101/gad.33547.1.119
- Laplante M, Sabatini DM (2009) An emerging role of mTOR in lipid biosynthesis. *Curr Biol* 19: R1046–R1052. doi:10.1016/j.cub.2009.09.058
- Lau DTC, Murray AW (2012) Mad2 and Mad3 cooperate to arrest budding yeast in mitosis. *Curr Biol* 22: 180–190. doi:10.1016/j.cub.2011.12.029
- Lavoie BD, Hogan E, Koshland D (2002) In vivo dissection of the chromosome condensation machinery: Reversibility of condensation distinguishes contributions of condensin and cohesin. *J Cell Biol* 156: 805–815. doi:10.1083/jcb.200109056
- Lavoie BD, Hogan E, Koshland D (2004) In vivo requirements for rDNA chromosome condensation reveal two cell-cycle-regulated pathways for mitotic chromosome folding. *Genes Dev* 18: 76–87. doi:10.1101/gad.1150404
- Lavoie BD, Tuffo KM, Oh S, Koshland D, Holm C (2000) Mitotic chromosome condensation requires Brn1p, the yeast homologue of Barren. *Mol Biol Cell* 11: 1293–1304. doi:10.1091/mbc.11.4.1293
- Lawrimore J, Kolbin D, Stanton J, Khan M, de Larmminat SC, Lawrimore C, Yeh E, Bloom K (2021) The rDNA is biomolecular condensate formed by polymer-polymer phase separation and is sequestered in the nucleolus by transcription and R-loops. *Nucleic Acids Res* 49: 4586–4598. doi:10.1093/nar/gkab229
- Lazar-Stefanita L, Scolari VF, Mercy G, Muller H, Guérin TM, Thierry A, Mozziconacci J, Koszul R (2017) Cohesins and condensins orchestrate the 4D dynamics of yeast chromosomes during the cell cycle. *EMBO J* 36: 2684–2697. doi:10.15252/embj.201797342
- Li H, Tsang CK, Watkins M, Bertram PG, Zheng XFS (2006) Nutrient regulates Tor1 nuclear localization and association with rDNA promoter. *Nature* 442: 1058–1061. doi:10.1038/nature05020
- Loewith R, Hall MN (2011) Target of rapamycin (TOR) in nutrient signaling and growth control. *Genetics* 189: 1177–1201. doi:10.1534/genetics.111.133363
- Losada A, Hirano T (2001) Shaping the metaphase chromosome: Coordination of cohesion and condensation. *Bioessays* 23: 924–935. doi:10.1002/bies.1133
- Machín F, Torres-Rosell J, De Piccoli G, Carballo JA, Cha RS, Jarmuz A, Aragón L (2006) Transcription of ribosomal genes can cause nondisjunction. *J Cell Biol* 173: 893–903. doi:10.1083/jcb.200511129
- Machín F, Torres-Rosell J, Jarmuz A, Aragón L (2005) Spindle-independent condensation-mediated segregation of yeast ribosomal DNA in late anaphase. *J Cell Biol* 168: 209–219. doi:10.1083/jcb.200408087
- Male G, Deolal P, Manda NK, Yagnik S, Mazumder A, Mishra K (2020) Nucleolar size regulates nuclear envelope shape in *Saccharomyces cerevisiae*. *J Cell Sci* 133: jcs242172. doi:10.1242/jcs.242172
- Martin DE, Powers T, Hall MN (2006) Regulation of ribosome biogenesis: Where is TOR? *Cell Metab* 4: 259–260. doi:10.1016/j.cmet.2006.09.002
- Matos-Perdomo E, Machín F (2019) Nucleolar and ribosomal DNA structure under stress: Yeast lessons for aging and cancer. *Cells* 8: 779. doi:10.3390/cells8080779
- Matos-Perdomo E, Machín F (2018) The ribosomal DNA metaphase loop of *Saccharomyces cerevisiae* gets condensed upon heat stress in a Cdc14-independent TORC1-dependent manner. *Cell Cycle* 17: 200–215. doi:10.1080/15384101.2017.1407890
- Mekhalik K, Moazed D (2010) The nuclear envelope in genome organization, expression and stability. *Nat Rev Mol Cell Biol* 11: 317–328. doi:10.1038/nrm2894
- Mekhalik K, Seebacher J, Gygi SP, Moazed D (2008) Role for perinuclear chromosome tethering in maintenance of genome stability. *Nature* 456: 667–670. doi:10.1038/nature07460
- Menendez JA, Lupu R (2007) Fatty acid synthase and the lipogenic phenotype in cancer pathogenesis. *Nat Rev Cancer* 7: 763–777. doi:10.1038/nrc2222
- Menon D, Salloum D, Bernfeld E, Gorodetsky E, Akselrod A, Frias MA, Sudderth J, Chen P-H, DeBerardinis R, Foster DA (2017) Lipid sensing by mTOR



- complexes via de novo synthesis of phosphatidic acid. *J Biol Chem* 292: 6303–6311. doi:10.1074/jbc.m116.72988
- Mochida K, Oikawa Y, Kimura Y, Kirisako H, Hirano H, Ohsumi Y, Nakatogawa H (2015) Receptor-mediated selective autophagy degrades the endoplasmic reticulum and the nucleus. *Nature* 522: 359–362. doi:10.1038/nature14506
- Moreno-Torres M, Jaquenoud M, Péli-Gulli M-P, Nicastro R, De Virgilio C (2017) TORC1 coordinates the conversion of Sic1 from a target to an inhibitor of cyclin-CDK-Cks1. *Cell Discov* 3: 17012. doi:10.1038/celldisc.2017.12
- Mostofa MG, Rahman MA, Koike N, Yeasmin AM, Islam N, Waliullah TM, Hosoyamada S, Shimobayashi M, Kobayashi T, Hall MN, et al (2018) CLIP and cohibin separate rDNA from nucleolar proteins destined for degradation by nucleophagy. *J Cell Biol* 217: 2675–2690. doi:10.1083/jcb.201706164
- Musacchio A, Salmon ED (2007) The spindle-assembly checkpoint in space and time. *Nat Rev Mol Cell Biol* 8: 379–393. doi:10.1038/nrm2163
- Nakashima A, Maruki Y, Imamura Y, Kondo C, Kawamata T, Kawanishi I, Takata H, Matsuura A, Lee KS, Kikkawa U, et al (2008) The yeast Tor signaling pathway is involved in G2/M transition via polo-kinase. *PLoS One* 3: e2223. doi:10.1371/journal.pone.0002223
- Nishimura K, Fukagawa T, Takisawa H, Kakimoto T, Kanemaki M (2009) An auxin-based degen system for the rapid depletion of proteins in nonplant cells. *Nat Methods* 6: 917–922. doi:10.1038/nmeth.1401
- Palmer RE, Koval M, Koshland D (1989) The dynamics of chromosome movement in the budding yeast *Saccharomyces cerevisiae*. *J Cell Biol* 109: 3355–3366. doi:10.1083/jcb.109.6.3355
- Pan X, Roberts P, Chen Y, Kvam E, Shulga N, Huang K, Lemmon S, Goldfarb DS (2000) Nucleus-vacuole junctions in *Saccharomyces cerevisiae* are formed through the direct interaction of Vac8p with Nvj1p. *Mol Biol Cell* 11: 2445–2457. doi:10.1091/mbc.11.7.2445
- Pascual F, Carman GM (2013) Phosphatidate phosphatase, a key regulator of lipid homeostasis. *Biochim Biophys Acta* 1831: 514–522. doi:10.1016/j.bbalip.2012.08.006
- Paulson JR, Hudson DF, Cisneros-Soberanis F, Earnshaw WC (2021) Mitotic chromosomes. *Semin Cell Dev Biol* 117: 7–29. doi:10.1016/j.semcdb.2021.03.014
- Pérez-Hidalgo L, Moreno S (2017) Coupling TOR to the cell cycle by the greatwall-endosulfine-PP2A-B55 pathway. *Biomolecules* 7: 59. doi:10.3390/biom7030059
- Peters J-M (2006) The anaphase promoting complex/cyclosome: A machine designed to destroy. *Nat Rev Mol Cell Biol* 7: 644–656. doi:10.1038/nrm1988
- Peterson TR, Sengupta SS, Harris TE, Carmack AE, Kang SA, Balderas E, Gurtin DA, Madden KL, Carpenter AE, Finck BN, et al (2011) mTOR complex 1 regulates lipin 1 localization to control the SREBP pathway. *Cell* 146: 408–420. doi:10.1016/j.cell.2011.06.034
- Quevedo O, García-Luis J, Matos-Perdomo E, Aragón L, Machín F (2012) Nondisjunction of a single chromosome leads to breakage and activation of DNA damage checkpoint in g2. *PLoS Genet* 8: e1002509. doi:10.1371/journal.pgen.1002509
- Rai U, Najm F, Tartakoff AM (2017) Nucleolar asymmetry and the importance of septin integrity upon cell cycle arrest. *PLoS One* 12: e0174306. doi:10.1371/journal.pone.0174306
- Roberts P, Moshitch-Moshkovitz S, Kvam E, O'Toole E, Winey M, Goldfarb DS (2003) Piecemeal microautophagy of nucleus in *Saccharomyces cerevisiae*. *Mol Biol Cell* 14: 129–141. doi:10.1091/mbc.e02-08-0483
- Roof DM, Meluh PB, Rose MD (1992) Kinesin-related proteins required for assembly of the mitotic spindle. *J Cell Biol* 118: 95–108. doi:10.1083/jcb.118.1.95
- Sanchez-Alvarez M, Zhang Q, Finger F, Wakelam MJO, Bakal C (2015) Cell cycle progression is an essential regulatory component of phospholipid metabolism and membrane homeostasis. *Open Biol* 5: 150093. doi:10.1098/rsob.150093
- Santos-Rosa H, Leung J, Grimsey N, Peak-Chew S, Siniouoglou S (2005) The yeast lipin Smp2 couples phospholipid biosynthesis to nuclear membrane growth. *EMBO J* 24: 1931–1941. doi:10.1038/sj.emboj.7600672
- Shen D, Skibbens RV (2017) Temperature-dependent regulation of rDNA condensation in *Saccharomyces cerevisiae*. *Cell Cycle* 16: 1118–1127. doi:10.1080/15384101.2017.1317409
- Shou W, Seol JH, Shevchenko A, Baskerville C, Moazed D, Chen ZW, Jang J, Shevchenko A, Charbonneau H, Deshaies RJ (1999) Exit from mitosis is triggered by Tem1-dependent release of the protein phosphatase Cdc14 from nucleolar RENT complex. *Cell* 97: 233–244. doi:10.1016/s0092-8674(00)80733-3
- Singh SK, Pandey H, Al-Bassam J, Gheber L (2018) Bidirectional motility of kinesin-5 motor proteins: Structural determinants, cumulative functions and physiological roles. *Cell Mol Life Sci* 75: 1757–1771. doi:10.1007/s00018-018-2754-7
- Siniouoglou S (2009) Lipins, lipids and nuclear envelope structure. *Traffic* 10: 1181–1187. doi:10.1111/j.1600-0854.2009.00923.x
- Siniouoglou S, Santos-Rosa H, Rappsilber J, Mann M, Hurt E (1998) A novel complex of membrane proteins required for formation of a spherical nucleus. *EMBO J* 17: 6449–6464. doi:10.1093/emboj/17.22.6449
- St-Pierre J, Douziech M, Bazile F, Pascariu M, Bonneil E, Sauvè V, Ratsima H, D'Amours D (2009) Polo kinase regulates mitotic chromosome condensation by hyperactivation of condensin DNA supercoiling activity. *Mol Cell* 34: 416–426. doi:10.1016/j.molcel.2009.04.013
- Stevens TH, Forgac M (1997) Structure, function and regulation of the vacuolar (H⁺)-ATPase. *Annu Rev Cell Dev Biol* 13: 779–808. doi:10.1146/annurev.cellbio.13.1.779
- Strunnikov AV, Hogan E, Koshland D (1995) SMC2, a *Saccharomyces cerevisiae* gene essential for chromosome segregation and condensation, defines a subgroup within the SMC family. *Genes Dev* 9: 587–599. doi:10.1101/gad.9.5.587
- Sullivan M, Higuchi T, Katis VL, Uhlmann F (2004) Cdc14 phosphatase induces rDNA condensation and resolves cohesin-independent cohesion during budding yeast anaphase. *Cell* 117: 471–482. doi:10.1016/s0092-8674(04)00415-5
- Taddei A, Gasser SM (2012) Structure and function in the budding yeast nucleus. *Genetics* 192: 107–129. doi:10.1534/genetics.112.140608
- Takemoto A, Kawashima SA, Li J-J, Jeffery L, Yamatsugu K, Elemento O, Nurse P (2016) Nuclear envelope expansion is crucial for proper chromosomal segregation during a closed mitosis. *J Cell Sci* 129: 1250–1259. doi:10.1242/jcs.181560
- Tatchell K, Makrantonis V, Stark MJR, Robinson LC (2011) Temperature-sensitive *ipl1-2/Aurora B* mutation is suppressed by mutations in TOR complex 1 via the Glc7/PP1 phosphatase. *Proc Natl Acad Sci U S A* 108: 3994–3999. doi:10.1073/pnas.1014406108
- Thadani R, Kamenz J, Heeger S, Muñoz S, Uhlmann F (2018) Cell-cycle regulation of dynamic chromosome association of the condensin complex. *Cell Rep* 23: 2308–2317. doi:10.1016/j.celrep.2018.04.082
- Thiry M, Lafontaine DLJ (2005) Birth of a nucleolus: The evolution of nucleolar compartments. *Trends Cell Biol* 15: 194–199. doi:10.1016/j.tcb.2005.02.007
- Tsang CK, Bertram PG, Ai W, Drenan R, Zheng XFS (2003) Chromatin-mediated regulation of nucleolar structure and RNA Pol I localization by TOR. *EMBO J* 22: 6045–6056. doi:10.1093/emboj/cdg578
- Urban J, Souillard A, Huber A, Lippman S, Mukhopadhyay D, Deloche O, Wanke V, Anrather D, Ammerer G, Riezman H, et al (2007) Sch9 is a major target of TORC1 in *Saccharomyces cerevisiae*. *Mol Cell* 26: 663–674. doi:10.1016/j.molcel.2007.04.020



- Visintin R, Hwang ES, Amon A (1999) Cfi1 prevents premature exit from mitosis by anchoring Cdc14 phosphatase in the nucleolus. *Nature* 398: 818–823. doi:10.1038/19775
- Walters AD, Amoateng K, Wang R, Chen J-H, McDermott G, Larabell CA, Gadal O, Cohen-Fix O (2019) Nuclear envelope expansion in budding yeast is independent of cell growth and does not determine nuclear volume. *Mol Biol Cell* 30: 131–145. doi:10.1091/mbc.e18-04-0204
- Walters AD, May CK, Dauster ES, Cinquin BP, Smith EA, Robellet X, D'Amours D, Larabell CA, Cohen-Fix O (2014) The yeast polo kinase Cdc5 regulates the shape of the mitotic nucleus. *Curr Biol* 24: 2861–2867. doi:10.1016/j.cub.2014.10.029
- Wang R, Mozziconacci J, Bancaud A, Gadal O (2015) Principles of chromatin organization in yeast: Relevance of polymer models to describe nuclear organization and dynamics. *Curr Opin Cell Biol* 34: 54–60. doi:10.1016/j.ceb.2015.04.004
- Wang X, Proud CG (2009) Nutrient control of TORC1, a cell-cycle regulator. *Trends Cell Biol* 19: 260–267. doi:10.1016/j.tcb.2009.03.005
- Wilms T, Swinnen E, Eskes E, Dolz-Edo L, Uwineza A, Van Essche R, Rosseels J, Zabrocki P, Camerini E, Franssens V, et al (2017) The yeast protein kinase Sch9 adjusts V-ATPase assembly/disassembly to control pH homeostasis and longevity in response to glucose availability. *PLoS Genet* 13: e1006835. doi:10.1371/journal.pgen.1006835
- Witkin KL, Chong Y, Shao S, Webster MT, Lahiri S, Walters AD, Lee B, Koh JLY, Prinz WA, Andrews BJ, et al (2012) The budding yeast nuclear envelope adjacent to the nucleolus serves as a membrane sink during mitotic delay. *Curr Biol* 22: 1128–1133. doi:10.1016/j.cub.2012.04.022
- Wullschleger S, Loewith R, Hall MN (2006) TOR signaling in growth and metabolism. *Cell* 124: 471–484. doi:10.1016/j.cell.2006.01.016



License: This article is available under a Creative Commons License (Attribution 4.0 International, as described at <https://creativecommons.org/licenses/by/4.0/>).

